Origin and Effects of the Non-Thermal Components in Large-Scale Structures of the Universe

Dissertation

zur Erlangung des Doktorgrades
an der Fakultät für Mathematik, Informatik und Naturwissenschaften
Fachereich Physik
der Universität Hamburg

vorgelegt von

Denis Wittor

Hamburg, Wintersemester 2017/18

Gutachter/innen der Dissertation:	Prof. Dr. Marcus Brüggen Prof. Dr. Thomas W. Jones
Zusammensetzung der Prüfungskommission:	Prof. Dr. Marcus Brüggen Prof. Dr. Jochen Liske Prof. Dr. Robi Banerjee Prof. Dr. Peter Hauschildt Dr. Franco Vazza
Vorsitzende/r der Prüfungskommission:	Prof. Dr. Jochen Liske
Datum der Disputtation:	15.12.2017
Vorsitzender Fach-Promotionsausschusses PHYSIK:	Prof. Dr. Wolfgang Hansen
Leiter des Fachbereichs PHYSIK:	Prof. Dr. Michael Potthoff
Dekan der Fakultät MIN:	Prof. Dr. Heinrich Graener

Zusammenfassung

Galaxienhaufen, Anhäufungen von hunderten bis zu tausenden von Galaxien, bestehen nicht nur aus Galaxien selbst, sondern auch aus dunkler Materie und einem heißen Plasma, dem intracluster Medium (ICM). Beobachtungen beweisen die Existenz nicht-thermische Phänomene in Form von: kosmischer Strahlung, Magnetfeldern und Turbulenz im ICM. Obwohl zahlreiche Beobachtung und Simulationen benutzt werden, um diese nicht-thermischen Komponenten zu studieren, gibt es noch zahlreiche ungelöste Probleme. Das Studium der nicht-thermischen Komponenten ist eine komplexe Angelegenheit, da sich die einzelnen Komponenten gegenseitig beeinflussen.

Im Rahmen dieser Dissertation wurde der lagrange'sche Teilchen Code `CRaTer` geschrieben. `CRaTer` ist ein Werkzeug, das mit passiven Testteilchen die Daten von Gittercodes analysiert. Diese originelle Herangehensweise erlaubt es, die numerischen Vorteile von Gittercodes zu bewahren und gleichzeitig lagrange'sche Informationen über die nicht-thermischen Komponenten zu sammeln. Wir benutzen `CRaTer`, um verschiedene kosmologische Simulation, die mit gitter-basierten Code `ENZO` produziert wurden, zu analysieren

Mit `CRaTer` verfolgen wir die Ausbreitung kosmischer Strahlung im ICM und suchen Erklärungen für die bisher unbeobachtete γ-Strahlung, ein Nebenprodukt der Beschleunigung von Protonen durch groß-skalige Stoßwellen. Wenn die Effizienz der Beschleunigung zusätzlich von der Obliquität abhängt, verringert sich die beobachtete γ-Emission, jedoch nicht genug, um nicht mehr detektiert zu werden. Um die fehlende γ-Strahlung zu erklären, müssen die Effizienzen durchschnittlich kleiner als $\leq 10^{-3}$ sein.

Wir untersuchen mit `CRaTer` die Polarisation von Radio Relikten. Bei hohen Frequenzen entsteht die beobachtete Depolarisation hauptsächlichen zwischen der Quelle und dem Beobachter. Bei niedrigen Frequenzen jedoch kommt zu gleichermaßen zur Depolarisation an der Quelle und im ICM zwischen Beobachter und Quelle. Außerdem zeigen wir, dass Radio Beobachtungen die höheren Mach Zahlen stärker gewichten. Dies könnte die Diskrepanz zwischen Radio- und Röntgenbeobachtung bei der Bestimmung der Stoßwellenstärke erklären.

Zuletzt folgen wir der Entwicklung der Enstrophy im ICM. Wir beobachten, dass hauptsächlich kompressive Bewegungen für die Verstärkung der Enstrophy verantwortlich sind. Die Amplifikation durch sich ausdehnende Bewegungen wird durch eine starke Dissipation unterdrückt. Jedoch reicht ein geringer Anteil der Dissipation des turbulenten, kinetischen Energie Flusses, um die Magnetfeldsträrken im Einklang mit Beobachtungen zu erzeugen.

Summary

Galaxy clusters are assemblies of a few hundred to thousands of galaxies. Furthermore they consists of dark matter and a hot, dilute plasma called the intracluster medium (ICM). The ICM hosts non-thermal phenomena in form of cosmic rays, magnetic fields and turbulence. Even though, several observations and simulations are devoted to their study, the non-thermal components are a complex matter as they influence each other, and still a lot of unsolved problems remain.

In the scope of this thesis, the Lagrangian tracer code `CRaTer` is developed. `CRaTer` is a post-processing tool that injects tracer particles on top of grid codes and advects them passively with the underlying fluid flow. This novel approach allows us to keep the numerical advantages of grid codes while studying the Lagrangian properties of the non-thermal components. We use `CRaTer` to analyse the evolution of the non-thermal components in several cosmological simulations produced with the mesh refinement code `ENZO`.

`CRaTer` is used to follow the propagation of cosmic rays in the ICM and to tackle the problem of the unobserved γ-rays, an unavoidable by-product of the acceleration of cosmic-ray protons by large-scale shocks. We find that using the shock obliquity as an additional parameter for computing the shock acceleration efficiencies releases some of the tensions but it does not solve the problem completely. Furthermore, we estimate that on average the shock acceleration efficiencies for cosmic-ray protons must be smaller than $\leq 10^{-3}$, to explain the missing γ-rays.

With the help of `CRaTer`, we provide new insights on the observed polarized emission of radio relics. We estimate that most of the depolarization at high frequencies happens in the ICM between the source and the observer, while at low frequencies the depolarization happens to similar amounts at the source and in the intermediate space. Furthermore, our findings suggest that radio observations are typically biased towards higher Mach numbers and therefore overestimate the shock strength. This can possibly explain the discrepancy in the Mach number estimates from radio and X-ray observations.

Finally, `CRaTer` is used to follow the evolution of enstrophy within the ICM. We discover that the amplification of enstrophy is mostly due to compressive motions. The amplification by stretching motions is overwhelmed by strong dissipation and enstrophy decays fast. Yet, a few percent of the corresponding dissipation of the turbulent kinetic energy flux is enough to produce magnetic fields that agree with current estimates from radio observations.

Eidesstattliche Versicherung

Hiermit versichere ich an Eides statt, die vorliegende Dissertationsschrift selbst verfasst und keine anderen als die angegebenen Hilfsmittel und Quellen benutzt zu haben.

Die eingereichte schriftliche Fassung entspricht der auf dem elektronischen Speichermedium.

Die Dissertation wurde in der vorgelegten oder einer ähnlichen Form nicht schon einmal in einem früheren Promotionsverfahren angenommen oder als ungenügend beurteilt.

(Denis Wittor)
Hamburg, den 09.11.2017

"Equipped with his five senses, man explores the universe around him and calls the adventure science."
Edwin Powell Hubbel

Contents

1 Introduction **1**

1.1 Motivation . . . 1

1.2 Astrophysical Context . . . 4

1.2.1 Growth of Galaxy Clusters . . . 4

1.2.2 A Thermal View on Galaxy Clusters . . . 7

1.2.3 A High-Energy View on Galaxy Clusters . . . 9

1.3 Non-Thermal Phenomena in the Intracluster Medium . . . 13

1.3.1 Cosmic-Ray Shock Acceleration . . . 13

1.3.2 Turbulence in Galaxy Clusters . . . 19

1.3.3 Magnetic Fields . . . 21

1.4 Numerical Simulations . . . 22

2 Methods and Algorithms **27**

2.1 ENZO . . . 27

2.2 CRaTer: A Versatile Lagrangian Analysis Tool . . . 27

2.2.1 Particle Injection . . . 29

2.2.2 Particle Advection . . . 30

2.2.3 Following Cosmic Rays . . . 36

2.2.4 Parallelization with `openMP` . . . 39

3 The Role of Shock Obliquity in the Acceleration of Cosmic Rays. **43**

3.1 Testing Cosmic-Ray Acceleration with Radio Relics: a High-Resolution Study using MHD and Tracers . . . 43

3.1.1 Introduction . . . 43

3.1.2 Simulation Setup . . . 45

3.1.3 Results . . . 49

3.1.4 Discussion & Conclusions . . . 63

3.1.A Density Distribution . . . 68

3.1.B Accretion Shocks and Filaments . . . 69

3.1.C Computing the γ-Ray Emission . . . 73

3.2 Studying the Effect of Shock Obliquity on the γ-ray and Diffuse Radio Emission in Galaxy Cluster . . . 74
3.2.1 Introduction . . . 74
3.2.2 Methods . . . 74
3.2.3 Results . . . 78
3.2.4 Discussion . . . 80
3.3 Additional Material Relation $\theta_{\rm pre}$ and $\theta_{\rm post}$ . . . 83

4 Constraining the Efficiency of Cosmic-Ray Acceleration by Cluster Shocks 85
4.1 Introduction . . . 85
4.2 Methods . . . 86
4.2.1 Cosmic-Ray Physics . . . 87
4.2.2 Gas Physics . . . 88
4.2.3 Adaptive Mesh Refinement Resimulations of MACSJ1752.0+0440 . . . 89
4.2.4 γ-Ray Observation of MACSJ1752.0+0440 . . . 89
4.3 Results . . . 90
4.3.1 Cluster Properties . . . 90
4.3.2 Cosmic-Ray Properties . . . 94
4.3.3 Hadronic γ-Ray Emission from Simulated Cluster Samples . . . 98
4.3.4 Hadronic γ-Ray Emission from MACSJ1752 . . . 100
4.4 Discussion . . . 105
4.5 Conclusions . . . 108
4.A Effects of Resolution and Additional Physics . . . 110
4.B Impact of CR Physics on Cluster Scaling Relations . . . 111

5 Polarization of Radio Relics: an on-going Study 115
5.1 Introduction . . . 115
5.2 Polarization in `CRaTer` . . . 117
5.3 Results . . . 119
5.3.1 Mach Number and Spectral Index Distributions . . . 119
5.3.2 Polarization Properties . . . 121
5.4 Conclusion . . . 127

6 Evolution of Vorticity and Enstrophy in the Intracluster Medium 131
6.1 Introduction . . . 131
6.1.1 Evolution of Enstrophy . . . 132
6.2 Simulation Setup . . . 134
6.2.1 ENZO . . . 134
6.2.2 CRaTer . . . 135

6.3 Results on IT90_3 136
6.3.1 Cluster Properties 136
6.3.2 Evolution of Enstrophy 137
6.3.3 Growth and Decay Timescales 142
6.3.4 Dissipation Term and Magnetic Field Amplification 144
6.4 Discussion & Conclusions 147
6.A Cluster Dynamics 149
6.B Simple Models for Turbulent Dissipation Rates 150

7 Conclusion and Perspective **155**
7.1 Summary of Results 155
7.2 Future Perspectives 157

A Acknowledgements **i**

B List of Figures **iii**

C List of Tables **xv**

D Bibliography **xvii**

1 Introduction

1.1 Motivation

Galaxy clusters are assemblies of a few hundreds to thousands of galaxies that are gravitationally bound. In fact, galaxies only account for a small amount ($\sim$ few %) of the total cluster mass. The rest of the mass consists of a hot, dilute plasma the intracluster medium (ICM) ($\sim 15 - 20\%$) and mostly dark matter ($\sim 80 - 85\%$). The evolution and properties of galaxy clusters highly depend on cosmology, and their abundances and bulk properties can be used to constrain the cosmological parameters (e.g. Haiman et al., 2001; Mantz et al., 2008; Vikhlinin et al., 2009; Benson et al., 2013). Furthermore, galaxy clusters present a large variety of possibilities to study astrophysical processes encompassing galaxy evolution and plasma processes, as well as cosmic-ray acceleration. These processes take place across all scales, ranging all the way from stars, galaxies and active galactic nuclei (AGN) to the ICM itself. (see Sarazin, 1988; Schneider, 2006; Kaastra et al., 2008, for recent textbooks)
Moreover, galaxy clusters host non-thermal components in the form of cosmic rays, magnetic fields and turbulence. During the formation of galaxy clusters, shock waves and turbulence develop in the ICM providing large acceleration sites for cosmic rays (see Brunetti & Jones, 2014; Brüggen & Vazza, 2015, and references therein). The existence of cosmic-ray electrons is revealed by radio observations of large-scale synchrotron emission (see Ferrari et al., 2008, and references therein). This radio emission in form of radio relics and radio halos is observed in a fraction of galaxy clusters, i.e. $\sim$ 30 % of clusters with a mass $> 10^{15}$ $M_{\odot}$ (e.g. Feretti et al., 2012). Radios halos, diffuse sources located at the cluster center, are thought to be connected to turbulence (e.g. Brunetti et al., 2001), while radio relics, seen as elongated sources at the cluster periphery, are most likely connected to shock waves (e.g. Ensslin et al., 1998). So far no detection of cosmic-ray protons has been reported (e.g. Ackermann et al., 2014, 2015, 2016). At the same time, relics and halos give proof for the existence of large-scale magnetic fields. Even though the origin of magnetic fields is still under debate, i.e. either primordial or astrophysical, they are most likely amplified by the turbulent motions of the ICM (see Ryu et al., 2008, and references therein).
Understanding the physics of the non-thermal components in galaxy clusters is important for cosmology because they have a huge impact on the out-of-equilibrium plasma conditions and the mass estimates of galaxy cluster. For example, the additional pressure support from the

non-thermal components yields different cluster masses than the mass estimates from the hydrostatic equilibrium and virial theorem only (e.g. Lau et al., 2010). However, an exact mass estimate is crucial for the fine tuning of the cosmological constants within the ΛCDM-model of cosmology. Furthermore, this will help to better understand the cosmological information embedded into the intergalactic medium. Additionally, the non-thermal components provide probes of the plasma conditions prior to the formation of large-scale structures as they are subjected to longer dynamical timescales. For example, once accelerated cosmic-ray protons are believed to be confined in the ICM and its tangled magnetic fields for longer than a Hubble time (Berezinsky et al., 1997).
Even though galaxy clusters are observed at different wavelengths, the study of the non-thermal components is still an open field and many unsolved problems remain. Numerical cosmological simulations help answering these questions by modelling the multi-wavelength observations.
Nowadays, three numerical approaches are mainly used: Eulerian methods (e.g. Bryan et al., 2014), Lagrangian methods (e.g. Springel, 2005) and moving-mesh methods (e.g. Springel, 2011; Hopkins, 2015). In this thesis, we investigate the non-thermal components of galaxy clusters by combining Eulerian cosmological simulations with the Lagrangian tracer tool `CRaTer`, that has been specifically developed in the scope of this thesis (see Chap. 2). The thesis is divided into the following projects:

- *How are cosmic-ray protons and electrons accelerated in the ICM?* Even though there is evidence for the acceleration of cosmic-ray electrons in galaxy clusters in form of large-scale radio emission, neither direct nor indirect detections of cosmic-ray protons have been reported (e.g. Ackermann et al., 2014). This brings the commonly assumed acceleration efficiencies of low Mach number shocks into question and challenges the validity of applying the shock acceleration mechanisms in supernovae to galaxy clusters. One possibility to overcome this problem is to consider the dependence of the acceleration efficiencies on the shock obliquity. Cosmic-ray electrons and protons require different shock obliquities to be efficiently accelerated by shocks. In this work, we estimate the distribution of shock obliquities in galaxies clusters and how this affects the acceleration of cosmic rays, if the shock acceleration efficiencies also depend on the shock obliquity. We show that the additional dependency on the shock obliquity releases some of the tension with the non-detection of the γ-rays. Yet, it does not solve the problem completely and further assumptions have to be made. See Chap. 3.

- *What is the upper limit for the acceleration efficiencies of cosmic rays?* The non-detection of γ-rays sets upper limits for the amount of cosmic-ray protons found in galaxy clusters. If the cosmic-ray protons are following the radial distribution of the thermal baryons, the upper limit for the amount of cosmic-ray protons in the ICM

is only a few percent. In this work, we use these limits to constrain the acceleration efficiencies of cosmic rays in galaxy clusters. We estimate that the shock acceleration efficiencies must be $\leq 10^{-3}$ on average, in order to match the non-detection of γ-rays. See Chap. 4.

- *What are the causes of the polarization of radio relics?* Radio relics are observed to be highly polarized ($\sim 10 - 50$ %). The degree of polarization is a measurement for the alignment of the magnetic field. Polarization is best observed in the high frequency bands of radio telescopes, where the effect of Faraday depolarization is small. It is still unclear whether depolarization occurs mainly in the ICM between the source and the observer or at the source itself. In this work, we show that at high observing frequencies the depolarization mostly happens in the space between the source and the observer. On the other hand at low frequencies, the depolarization happens to similar amounts at the source and between the source and the observer. See Chap. 5

- *What causes the discrepancy of Mach number estimates based on X-ray and radio observations?* It is commonly assumed that radio relics are connected to the shock acceleration of cosmic-ray electrons. While the synchrotron emission of radio relics is visible at radio wavelengths, the shocks themselves are observed via X-ray telescopes. Yet, Mach number estimates from X-rays, that depend on surface brightness or density jumps, and from radio, that depend on the observed spectral index, do not agree in some cases (e.g. Hong et al., 2015, and references therein). We find that Mach number distributions obtained from radio observations predicts larger values than the real Mach number distributions. This could possibly explain the observed Mach number discrepancy. See Chap. 5

- *How do turbulent gas motions evolve in the ICM?* Turbulence is driven by mergers and accretion in the ICM. Despite its importance for the understanding of the physics in the ICM, the evolution of turbulence is still poorly understood. Using the gas enstrophy as a trustworthy metric for turbulent motions, we follow the evolution of enstrophy and its dependence on various physical source terms. This novel approach provides new insights on the history of turbulent motions in galaxy clusters. We observe that the evolution of enstrophy follows a specific sequence of events: first compressive and baroclinic motions increase. This is followed by a peak of enstrophy. Finally solenoidal motions are increased. Furthermore, we find that the amount of dissipated turbulence would be sufficient to explain today's observed magnetic fields. See Chap. 6.

The thesis is structured as follows: The remainder of this chapter provides physical and methodological backgrounds. The following chapter, Chap. 2, we will present the numerical methods used in this thesis. First, we will give a brief overview on the `ENZO` code that we used for the cosmological simulations, Sec. 2.1. Next, we will give a detailed presentation of

`CRaTer`, the Lagrangian Tracer Code that has been written in the scope of this dissertation and is an important tool for our further analysis, Sec. 2.2.
The following chapters have been or will be individually published and are presented here in their entirety. Chap. 3 contains two papers that deal with the question, if using the shock obliquity as an additional parameter for computing the shock acceleration efficiencies can solve the problem of the non-detection of the γ-rays. In Chap. 4, we constrain the shock acceleration efficiencies based on the non-detection of γ-rays by the Fermi-LAT. In the next chapter, Chap. 5, we compute the polarization of a luminous radio relic at different observing frequencies and estimate the contributions of the different environments to the Faraday depolarization. Furthermore, we provide an explanation for the observed discrepancy of Mach number estimates based on X-ray and radio observations. In the last paper presented here, Chap. 6, we follow the evolution of turbulence and enstrophy in galaxy clusters and we estimate how much the magnetic fields are amplified by turbulence. We will round up this work with a summary, conclusion and outlook in Chapter 7.

1.2 Astrophysical Context

1.2.1 Growth of Galaxy Clusters

It is assumed that shortly after the Big Bang, the beginning of the Universe, small density perturbations were created in a homogeneous Universe by quantum fluctuations during the period of cosmic inflation. The richness of structures in the Universe today has grown from these perturbations (e.g. Planelles et al., 2015), that are characterized by a dimensionless density contrast:

$$\delta\left(\mathbf{x}\right) = \frac{\rho_{\mathrm{DM+BM}}\left(\mathbf{x}\right) - \overline{\rho}_{\mathrm{DM+BM}}}{\overline{\rho}_{\mathrm{DM+BM}}}. \tag{1.1}$$

Here $\rho_{\mathrm{DM+BM}}\left(\mathbf{x}\right)$ is the density at the position $\mathbf{x}$, while $\overline{\rho}_{\mathrm{DM+BM}}$ is the mean density of the Universe. During the evolution of the Universe, the overdense ($\delta > 0$) regions keep on growing by hauling the matter from the underdense ($\delta < 0$) regions. Over time, these overdense regions grow into filaments that form the cosmic web. At the intersections of the filaments, that host about $50 - 60$ % of the total matter in the Universe, we find galaxy clusters. The space between the filaments is populated with underdense regions, called voids. In Fig. 1.1, we show the evolution of the cosmic web in a standard cosmological simulation produced in the scope of this thesis.
At the same time, the Universe is expanding with a rate is given by the *Hubble*-constant $H_0 \approx 70$ km/s/Mpc (Planck Collaboration et al., 2016b). The expansion of the Universe is

described by the Friedmann equation

$$\left(\frac{\dot{a}}{a}\right)^2 = H_0^2 \left[a^{-4}(t)\Omega_r + a^{-3}(t)\Omega_m + a^{-2}(t)(1-\Omega_m-\Omega_\Lambda) + \Omega_\Lambda\right]. \tag{1.2}$$

In the equation above, a is the cosmic-scale factor that is directly connected to the observed redshift as $a = (1+z)^{-1}$. The dimensionless density parameters account for different physical effects, namely radiation Ω_r, dark matter and baryonic matter $\Omega_m = \Omega_{DM} + \Omega_{BM}$ and dark energy Ω_λ. Currently, we are living in a dark energy dominated Universe with $\Omega_\lambda \approx 0.70$ (Planck Collaboration et al., 2016b).

The Universe we live in and its evolution, as summarized above, are explained by the ΛCDM-cosmology. This cosmology has two main ingredients: the cosmological constant Λ, that governs the expansion of the Universe and cold dark matter, that is responsible for the bottom-up growth of structures. As the study of cosmology is no direct objective of this dissertation, we point to textbooks such as Peebles (1993); Peacock (1999); Liddle (1999) and Schneider (2006) for more detailed reviews.

Galaxy cluster, large accumulations of mass in form of dark and baryonic matter, are found at the intersections of the filaments of the cosmic web. They are the youngest structures of the Universe that have formed during structure formation. Galaxy cluster have been observed at different redshifts all the way out to $z > 2.5$ which corresponds to an age of the Universe of roughly ~ 2.6 Gyr. The current record holder is J1001+0220 that has been discovered at $z \approx 2.504$ by Wang et al. (2016), while the galaxy cluster closest to the Milky Way is the Virgo cluster at a distance of $z \approx 0.0036$ (see Mei et al., 2007, and references therein). Furthermore, galaxy clusters are very hot $T_{\rm gas} = 10^7 - 10^8$ K and massive $M = 10^{14} - 10^{15}\ M_\odot$. The most massive cluster known today is the El Gordo cluster at $z \approx 0.87$ and with a mass of $M_{200} \approx (2.16 \pm 0.32) \cdot 10^{15}\ h^{-1}\ M_\odot$ (see Menanteau et al., 2012). The mass of galaxy clusters consists of galaxies ($\sim$ few %), the gas of the ICM ($\sim 15 - 20$ %) and mostly dark matter ($\sim 80 - 85$ %).

One possibility to estimate the total mass within a galaxy cluster is the observation of the velocity dispersion of the cluster galaxies σ_v. Under the assumption of an isolated, spherical symmetric system in dynamical equilibrium, the virial theorem yields for a system of size r a total mass of

$$M = \frac{3\sigma_v^2 r}{G}. \tag{1.3}$$

Here G is the gravitational constant. Another possibility to determine the cluster mass is given by observing the diffuse X-ray emission in galaxy clusters. The bolometric X-ray luminosity is computed as

$$L_X = \int n_e n_i \Lambda(T) \mathrm{d}^3\mathbf{r}, \tag{1.4}$$

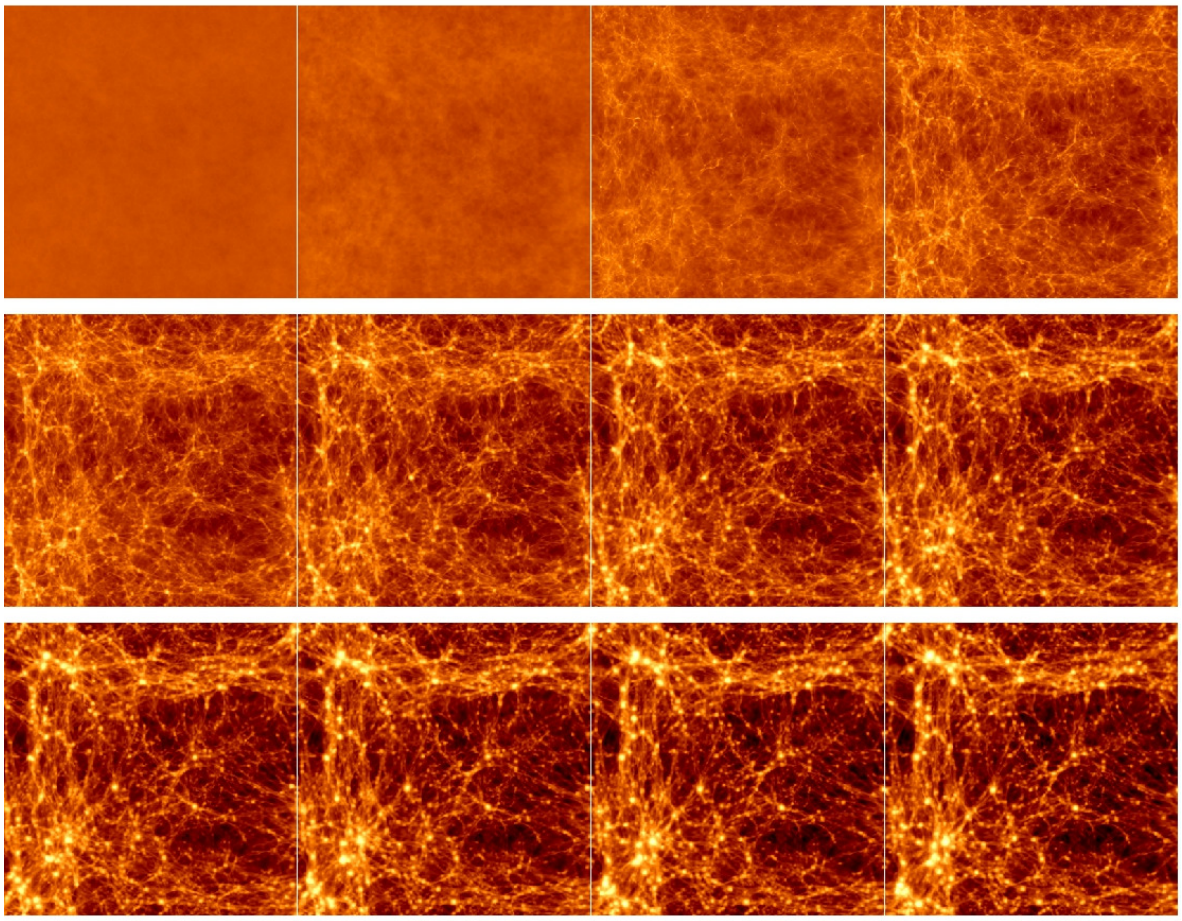

Figure 1.1: Evolution of a cosmological volume in time from redshift $z \approx 30$ to $z \approx 0$. Small density perturbations (left upper panel) collapse over time and form the Universe as it is know today (bottom right panel): Filaments of matter, the cosmic web, permeate the space. Voids, low density regions, are found between the filaments, while galaxy clusters sit at their intersections.

using the cooling function $\Lambda(T) \propto T^{1/2}$ for a fully ionized plasma, e.g. $T > 2$ keV, such as the ICM. In Eq. 1.4, n_i and n_e are the ion and electron number density, respectively. We will focus on the nature and properties of this X-ray emission in Sec. 1.2.2. The observation of hot diffuse X-ray emitting gas indicates that a deep gravitational well keeps the hot gas confined within the cluster. The total mass inside a radius r can be derived under the assumptions of spherical symmetry and hydrostatic equilibrium as

$$M(<r) = \frac{-k_B T_{\rm gas} r^2}{G\mu m_p} \left(\frac{{\rm d}\ln \rho_{\rm gas}}{{\rm d}r} + \frac{{\rm d}\ln T_{\rm gas}}{{\rm d}r} \right). \tag{1.5}$$

In this equation, k_B is the Boltzmann-constant, $T_{\rm gas}$ is the gas temperature, r is the size of the system, G is the gravitational constant, $\mu \sim 0.63$ is the mean molecular mass, m_p is the proton mass and $\rho_{\rm gas}$ is the gas density. Weak and strong gravitational lensing (e.g

Schneider, 2006), the caustic technique (Diaferio, 1999) and the Sunyaev-Zeldovich signal (Bartlett, 2006) provide complementary methods for the mass estimations of galaxy clusters. Under the assumption of clusters being in hydrostatic equilibrium, which is supported at low redshifts by simulations, simple scaling relations between their global properties can be derived (e.g. Planelles et al., 2015). Their mass M, temperature T, radius R, X-ray luminosity L_X and sound speed c_s are related as follows:

$$T \propto \frac{M}{R}, \tag{1.6}$$

$$T \propto M^{\frac{2}{3}}, \tag{1.7}$$

$$L_X \propto T^2, \tag{1.8}$$

$$c_s \propto \sqrt{M^{\frac{2}{3}}}. \tag{1.9}$$

The assumption of hydrostatic equilibrium breaks down in the dense inner cluster regions where the cooling time can be smaller than the Hubble time. As the gas cools, it radiates and therefore it loses internal energy, which again leads to a decrease in pressure and a break in the hydrostatic equilibrium. As a result, the gas will flow towards the cluster centre where it accumulates, known as a cooling flow. Hence, the cores of galaxy clusters should be regions of active star formation, i.e. $> 100\ M_\odot/\mathrm{yr}$. But this is not observed and some mechanism is needed that prevents the gas from cooling. A central engine, for example an AGN, can heat the inner cluster gas and hence prevent the cooling flow (e.g. Brüggen & Kaiser, 2002). Another possibility of heating the plasma is the dissipation of turbulent motions in the ICM.

1.2.2 A Thermal View on Galaxy Clusters

The launch of the *Uhuru* X-ray satellite[1] on the 12th of December 1970 allowed the first survey of the entire X-ray sky. These observations showed that galaxy clusters are typically X-ray bright objects with an extended emission and luminosities in the range of $10^{43} - 10^{45}$ erg/s. The detection of X-ray emission from of the iron line in the Perseus cluster (Mitchell et al., 1976) and in the Coma and Virgo cluster (Serlemitsos et al., 1977) substantiated the idea of a thermal X-ray mechanism. There are two mechanisms producing the observed X-ray emission.

The first is thermal bremsstrahlung. This *free-free* emission is caused during the deacceleration of fast electrons by ions via the electromagnetic force. The X-ray emissivity is computed using a weighted sum over the different ion species n_i:

[1] `https://heasarc.gsfc.nasa.gov/docs/uhuru/uhuru.html`

$$\epsilon_\nu^{ff} = \frac{32\pi e^6}{3m_e c^3}\sqrt{\frac{2\pi}{3m_e k_B T}}\exp\left(-\frac{h\nu}{k_B T}\right) n_e \sum_i Z_i n_i g_{ff}\left(Z_i, T, \nu\right). \tag{1.10}$$

In the equation above, g_{ff} is Gaunt factor, that accounts for quantum mechanical effects, and Z_i is the ion charge. Furthermore e is the electron charge, m_e is the electron mass, c is the speed of light, k_B is the Boltzmann-constant, n_e is the electron number density, h is the Planck-constant, ν is the observation frequency and T is the gas temperature.

The monochromatic X-ray emission is proportional to the inverse square root of the temperature and to the product of ion and electron number density, i.e. $L_X \propto T^{-1/2} n^2$. Therefore, the X-ray luminosity increases highly towards the centre of galaxy clusters. Moreover, due to the selection bias related to the central gas density, X-ray observations tend to pick up more relaxed clusters, whose central density and temperature are higher.

Metal line cooling is the other most important mechanism producing X-rays. There is a forest of keV lines present in the ICM. Using their ratios one can constrain the bulk gas temperature (see Sarazin, 1988, and references therein).

X-ray telescopes are used to study the properties of the thermal gas in galaxy clusters. Both shock waves and turbulence in the ICM that are described in detail in Sec. 1.3 are well observed by modern X-ray telescopes such as the XMM-Newton telescope[2] and the Chandra X-ray Observatory[3].

Both temperature jumps and surface brightness jumps can be used to find shock waves in the ICM and to estimate their strengths. Yet, an identification of a shock structure in X-ray images is difficult, except in the case of major merger. The observation of so called radio relics, see Sec. 1.2.3, helps to constrain the areas where to look for these structures (e.g. Finoguenov et al., 2010) and systematic surveys around radio relics have been carried out to search for shock waves (e.g. Akamatsu & Kawahara, 2013).

Over the last decade the Sunyaev-Zeldovich (SZ) effect, i.e. inverse Compton scattering of the low-energy photons from the cosmic microwave background by the ICM electrons (Sunyaev & Zeldovich, 1972b), has become a complementary tool to observe the thermal properties of the ICM (e.g. Korngut et al., 2011; Erler et al., 2015; Kitayama et al., 2016, and references therein). The search for shock waves in the ICM using the SZ-effect is a powerful complementary method as it is redshift independent (e.g. Basu et al., 2016, and references therein). Additionally, the SZ effect is proportional to the product of density and temperature. Hence, SZ observations tend to pick-up more distributed non cool-core clusters than X-ray observations (Andrade-Santos et al., 2017).

X-ray observations are further used to measure the velocity dispersion of turbulent motions

[2] `https://www.cosmos.esa.int/web/xmm-newton`
[3] `http://chandra.harvard.edu/`

in the ICM. In 2016, Hitomi[4] measured a velocity dispersion of $\sigma_v \approx (164 \pm 10)$ km/s in the XXV iron line of the Perseus cluster (Hitomi Collaboration et al., 2016).
The next generation of X-ray telescopes, that will be launched in the near future, are eRosita[5], expected to be launched in 2018, the X-ray Recovery Mission[6], planned to be launched in 2021, and Athena[7], scheduled for launch in 2028.

1.2.3 A High-Energy View on Galaxy Clusters

The first detection of extended and diffuse radio emission in a galaxy cluster was reported by Large et al. (1959), who detected an extended source in the Coma cluster using the 250-ft. radio telescope at Jodrell Bank[8]. Later on this observation was confirmed by interferometric observations carried out by Willson (1970). The detection of large-scale radio emission, that is interpreted as synchrotron radiation, gives proof for both the existence of large-scale magnetic fields and the acceleration of cosmic-ray electrons to relativistic energies.
Several different radio sources can be observed in galaxy clusters: radio galaxies, radio relics, radio halos and radio mini-halos. To give a very illustrative example from a recent deep radio observation, we show in Fig. 1.2(a) the combined radio continuum of Abell 2744 produced by Pearce et al. (2017). Additionally we present an overlay of optical, X-ray and radio observations of the same cluster in Fig. 1.2(b). The maps show radio relics, radio haloes and radio galaxies. Unlike radio galaxies, both radio relics and radio haloes do not have any optical counterpart and they are most likely caused by some global mechanism. Both of them are believed to be connected to the processes of hierarchical structure formation but to trace different physical processes.
Radio halos, see Fig. 1.3, are unpolarized, diffuse sources on $\sim$ Mpc scales whose intensities follow a power law $I_\nu \propto \nu^{-\alpha}$ ($\alpha \geq 1$) with an uniform spectral index, e.g. see Fig. 1.3(b). Yet. their origin is poorly understood. Either they could be produced by so called *primary electron models* (see Brunetti et al., 2001; Petrosian, 2001) or *secondary models* (see Dennison, 1980).
In the primary model, relativistic electrons with radiative lifetimes of $t \approx 10^7 - 10^8$ yr are locally injected by an AGN or starburst galaxy. Yet, their lifetimes are to short to produce the observed emission. Therefore, either a continuous injection, which is in conflict with the observations, or a re-acceleration mechanism is needed. A promising candidate for the re-acceleration is turbulence. In the secondary model, comic-ray protons and thermal protons

[4] http://global.jaxa.jp/projects/sat/astro_h/
http://astro-h.isas.jaxa.jp/si/index_e.html
[5] http://www.mpe.mpg.de/eROSITA
[6] https://heasarc.gsfc.nasa.gov/docs/xarm/
[7] http://www.the-athena-x-ray-observatory.eu/
[8] http://www.jodrellbank.net/

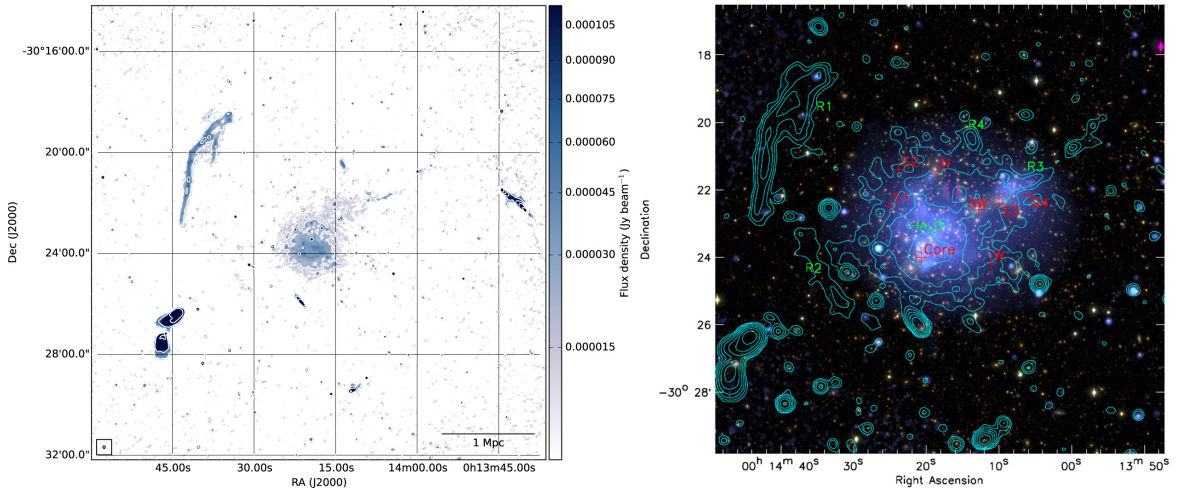

(a) (b)

Figure 1.2: Combined radio continuum from $1 - 4$ GHz taken with the VLA. The image shows the various radio sources in a galaxy cluster: a radio halo at the cluster centre, a radio relic north west of the halo, a tailed radio galaxy just south of the halo and a foreground AGN in the left corner. These pictures are taken from Pearce et al. (2017).

collide and hence produce pions (Blasi & Colafrancesco, 1999):

$$p + p \rightarrow \pi^{+/-} + \pi^0 + \text{anything}. \tag{1.11}$$

Eventually the charged pions will decay into muons that again decay into electrons and positrons

$$\pi^{+/-} \rightarrow \mu^{+/-} + \nu_\mu \tag{1.12}$$

$$\mu^{+/-} \rightarrow e^{+/-} + \bar{\nu}_\mu(\nu_\mu) + \nu_e(\nu_e). \tag{1.13}$$

The neutral pions will decay into γ-rays:

$$\pi^0 \rightarrow 2\gamma. \tag{1.14}$$

Even though the secondary model is not completely ruled out, most observations favour the primary model. The strongest argument against the the secondary model is the non-detection of the γ-rays (e.g. Huber et al., 2013a; Ackermann et al., 2014). Furthermore, the secondary model predicts radio emission in all clusters, yet the correlation of X-ray luminosity and the radio luminosity, $P_{1.4} \sim L_{500}^{2.1\pm0.2}$ (e.g. Cassano et al., 2013), is instead bimodal and clusters without radio halos do not follow it. Finally, some radio halos show a steep spectra at high frequencies (e.g. Brunetti et al., 2008; Dallacasa et al., 2009; Bonafede et al., 2012; Venturi et al., 2013), which hints an inefficient process for the acceleration of electrons and therefore

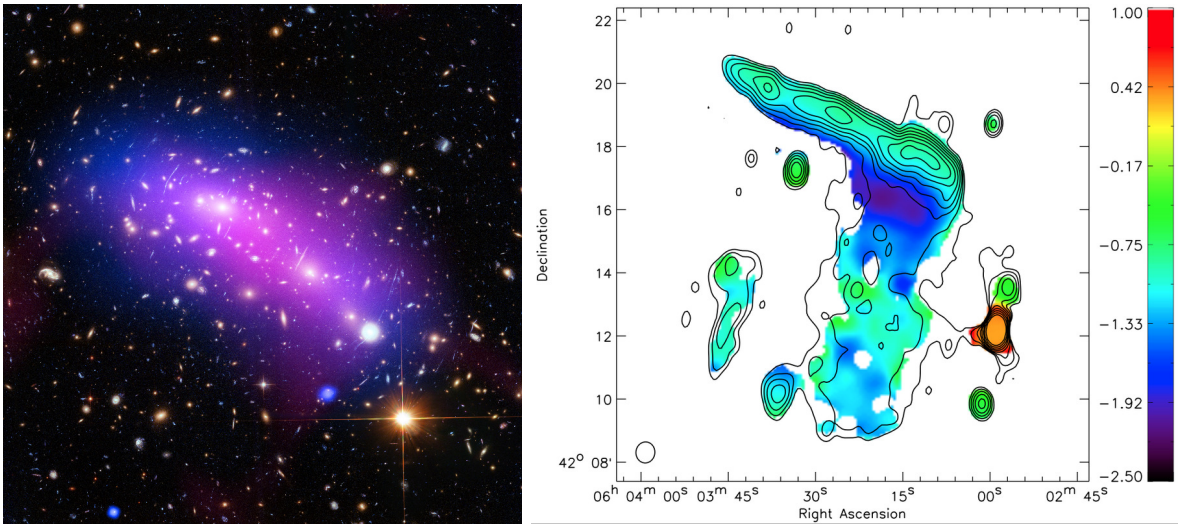

(a) (b)

Figure 1.3: Chandra X-ray data (blue) and VLA radio data of the MACS.J0416.1-2403 cluster, as shown by NASA, ESA, CXC, NRAO/AUI/NSF, STScI, and G. Ogrean (e.g Ogrean et al., 2016). (b) Spectral index map of 1RXS J0603.3+4214, as displayed in van Weeren et al. (2012).

points towards the primary model (e.g. Schlickeiser et al., 1987).

Radio mini-halos are most likely not a rescaled versions of giant radio halo, but they actually seem to trace different physical processes as they are mostly found at the centre of cool core clusters, where they trace high, $\sim$ few μG, magnetic fields. The sloshing of dark matter cores within these systems has been identified as a possible source for the energisation of radio emitting electrons (Giacintucci et al., 2014). Furthermore, as mini-halos are always found in clusters with evidence of AGN activity, the source of gas heating and of the relativistic electrons might be ultimately the same (e.g. Bravi et al., 2016).

The other sources of large-scale radio emission are radio relics, see Fig. 1.4. They are seen as $\sim$ Mpc long and elongated arc-shaped like sources at the cluster periphery. The first kind of these radio sources has been detected in the Coma cluster by Giovannini et al. (1991). The monochromatic radio power of radio relics is of the order of $10^{23} - 10^{25}$ W Hz^{-1}. They possess steep radio spectra $\alpha > 1$ and show spectral index ageing towards the cluster centre as seen in Fig. 1.3(b) and 1.4(b) (e.g. van Weeren et al., 2010, 2012). Radio relics are highly polarized ($10 - 50$ %), too, see Fig. 1.4(b), which suggests the presence of an ordered magnetic fields at their front. The magnetic field could have been aligned for example by a shock wave or compression, (e.g. Rottgering et al., 1997; van Weeren et al., 2016). Radio relics have been found in cool core clusters as well as in merging cluster and they seem to be tracing shock waves, that originated either from a major merger or an off axis merger. These shock waves appear to be able to accelerate cosmic-ray electrons, albeit the details of the mechanism leading to it are still unclear (see Sec. 1.3.1 and Sec. 3). Both simulations

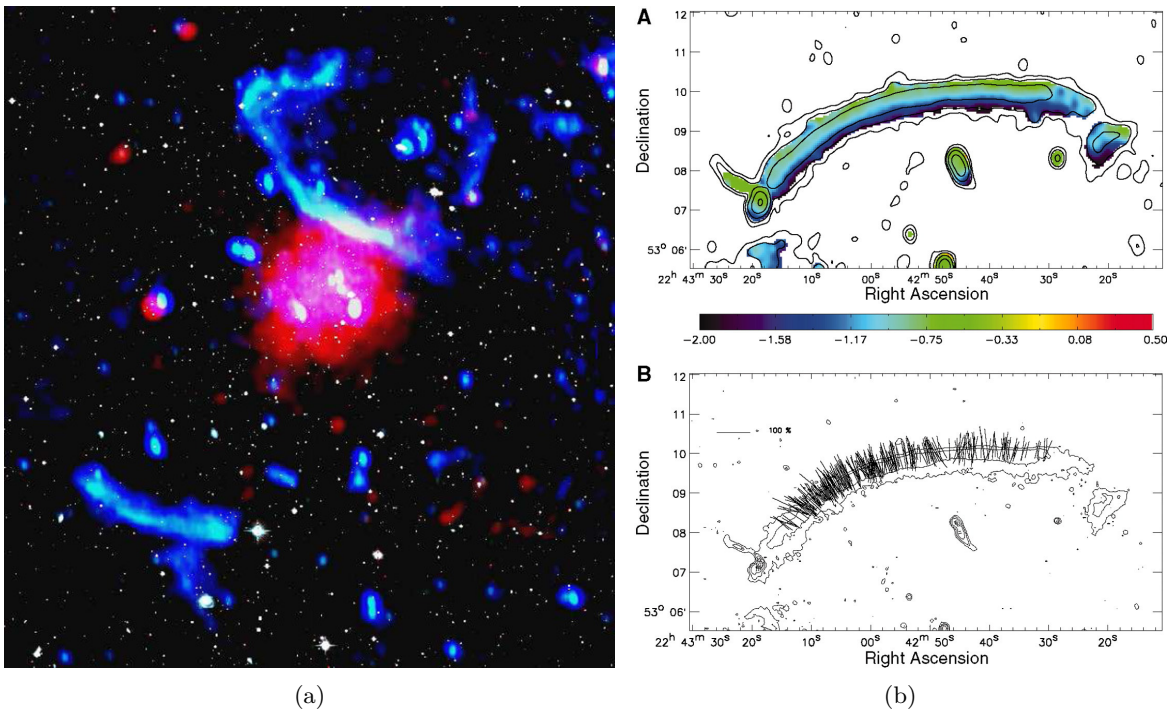

(a) (b)

Figure 1.4: (a) Radio emission of the double radio relic in PLCKG287.0+32.9 at 323 MHz in blue (GMRT) and the X-ray emission in red (XMM-Newton). This picture is taken from Bonafede et al. (2014). (b) Spectral index map (top) and polarized electric field vectors (bottom) in CIZA 2242.8+5301, as displayed in van Weeren et al. (2010).

and observations provide hints pointing towards a connection between radio relics and shock acceleration. Radio relics are mostly located at the position of X-ray surface brightness jumps, i.e. temperature jumps, strengthening the idea of shock acceleration (e.g. Ogrean & Brüggen, 2013; Akamatsu et al., 2015; Botteon et al., 2016; van Weeren et al., 2016). In addition, simulations predict that two symmetric relics can be visible if the merger axis is perpendicular to the line-of-sight (e.g. Brüggen et al., 2012). The actual observation of such double radio relics at opposite sides of the clusters gives additional proof to the shock acceleration model. So far, 17 double relics have been detected (Bonafede et al., 2017) and seven of those host an additional radio halo. Among the known relics, several correlations with other cluster properties can be found. Feretti et al. (2012) found a correlation between the relic radio power at 1.4 GHz and the cluster X-ray luminosity of $P_{1.4} \propto L_X^{1.2}$, while de Gasperin et al. (2014) found a relation between the radio luminosity of double relics and the cluster mass of $L_R \propto M^{2.83}$.

Systematic surveys have been carried out to search for both radio relics, e.g. the NRAO VLA Sky Survey by Condon et al. (1998a), and radio haloes, e.g. the GMRT Radio Halo Survey and Extended GMRT Radio Halo Survey by Venturi et al. (2007) and Kale et al.

(2015) respectively. An example for a modern radio telescope is the Low Frequency Array[9] (LOFAR) that is distributed across all over Europe and operates in a low-, $\nu \sim 30 - 80$ MHz, and a high-frequency band, $\nu \sim 120 - 240$ MHz. The Square Kilometre Array[10] (SKA), that is going to be built in both South Africa and Australia, will cover the total frequency range of $\nu \sim 50$ MHz $- 14$ GHz. The surveys conducted with these facilities are expected to discover hundreds of new radio relics and halos (e.g. Nuza et al., 2012; Cassano et al., 2013) and especially the low-frequency range will provide important information on the older and lower energetic cosmic rays.
In this work, we present work on the emission in radio relics. In Chap. 3 of this thesis, we will discuss the possible role shock obliquity plays in shaping the emission in radio relics, while in Sec. 5 we will discuss the effect of cluster magnetic fields on the polarization properties of radio relics.

1.3 Non-Thermal Phenomena in the Intracluster Medium

1.3.1 Cosmic-Ray Shock Acceleration

The acceleration of cosmic rays by shock waves is observed across all scales, ranging from as small as the bow shock between Sun and Earth over intermediate scales such as supernovae all the way to galaxy clusters. Radio relics, see Sec. 1.2.3, suggest evidence for the shock acceleration of cosmic-ray electrons in galaxy clusters on large scales. In the following, we will describe the physics of these processes.

Shocks Waves in the Intracluster Medium

Shock waves, waves that travel fast than the sound speed of the ambient medium, are naturally induced in the ICM during mergers and matter accretion, the two major processes of forming galaxy clusters in the current paradigm of ΛCDM-cosmology (see Sec. 1.2.1). Since the ICM is a hot tenuous plasmas, these shocks are collisionless, yet they heat the gas, accelerate cosmic rays and induced turbulent flows on Mpc-scales (e.g. Bykov et al., 2008).
Large amount of studies on large-scale structure formation have investigated the properties of shocks in the ICM (e.g. Ryu et al., 2003; Kang et al., 2007; Vazza et al., 2009a). These studies have shown that shocks can basically be classified as *external*, *internal* and *merger* shocks (e.g. following the classification of Ha et al., 2017).
External shocks occur in the cluster outskirts where the cold $T \sim 10^4$ K gas from voids is accreted onto the cluster. Even though external shocks should have high Mach numbers,

[9] http://www.lofar.org/
[10] http://skatelescope.org/

$M \sim 100$, the are energetically unimportant as the only live in low-density regions resulting in a low energy flux.

Internal shocks form inside the inner, already virialized regions of galaxy clusters. They can be caused by turbulent motions and typically have small Mach numbers $M < 2$ (e.g. Porter et al., 2015). Alternatively they form when either gas clumps or the warm-hot intergalactic medium (WHIM) are accreted onto the cluster. In this case, they are estimated to have large Mach numbers of the order of $M \sim 10$ (e.g. Hong et al., 2014).

Merger shocks are energetically most important. They form when two clusters of similar masses merge involving energies up to $\sim 10^{64}$ erg. One of the most famous merger shocks was recorded by Markevitch et al. (2002) in 1E 0657-56, the famous Bullet Cluster. Ever since, dozens of merger shocks have been detected (e.g. Markevitch et al., 2005; Dasadia et al., 2016) and in most cases radio relics are observed at the shock position.

In the following, even though there seems to be a consistent mismatch between the X-ray and radio-based estimates of the Mach number, see Chap. 5, we will give a short overview on the properties of hydrodynamical shocks. The shock divides an upstream ($\rho_1,\ v_1$) and a downstream ($\rho_2,\ v_2$) region with $\rho_2 > \rho_1$. Across the shock front mass, momentum and energy must be conserved:

$$\rho_1 v_1 = \rho_2 v_2 \tag{1.15}$$

$$P_1 + \rho_1 v_1^2 = P_2 + \rho_2 v_2^2 \tag{1.16}$$

$$\frac{1}{2} v_1^2 + \frac{5}{2}\frac{P_1}{\rho_1} = \frac{1}{2} v_2^2 + \frac{5}{2}\frac{P_2}{\rho_2}. \tag{1.17}$$

From the relations above one can derive the density, temperature and entropy jumps across the shock front as follows:

$$\frac{\rho_2}{\rho_1} = \frac{4M^2}{M^2+3} \tag{1.18}$$

$$\frac{T_2}{T_1} = \frac{\left(5M^2-1\right)\left(M^2+3\right)}{16M^2} \tag{1.19}$$

$$\frac{S_2}{S_1} = \frac{T_2}{T_1}\left(\frac{\rho_2}{\rho_1}\right)^{-\frac{2}{3}}. \tag{1.20}$$

For large Mach numbers the compression ratio $r = \rho_2/\rho_1$ in purely hydrodynamic shocks converges towards 4, yielding a maximum velocity ratio of $v_2/v_1 \leq \frac{1}{4}$ (e.g. Landau & Lifshitz, 2013).

Particles that are in the vicinity of shock waves can undergo shock acceleration mechanisms. If a lot of energy is transferred to the cosmic rays, this is the case especially in strong shocks, they back-react on the shock and modify its structure. This modification generates a highly compressed shock precoursor, which drives upstream turbulence and amplifies the magnetic

fields. The precoursor is followed by a subshock. Most of the cosmic-ray acceleration via Diffusive Shock Acceleration in modified shocks happens in the precoursor, while the subshock rather injects seed particles. This whole processes is described by non-linear theory (e.g. Drury, 1983; Jones & Ellison, 1991; Kang & Jones, 2005). While modified shocks are probably relevant to model strong shocks in supernova remnants (e.g. Caprioli, 2012), in the case of the weaker shocks in the ICM a linear test-particle acceleration may be sufficient (e.g Kang & Ryu, 2013). In the following, we will describe two of these acceleration processes, that are of importance for this thesis, in more detail.

Diffusive Shock Acceleration

Shock waves in the ICM can accelerate particles to high energies. This process is described by *Diffusive Shock Acceleration* (DSA) (see Blandford & Ostriker, 1978; Bell, 1978a,b; Drury, 1983; Blandford & Eichler, 1987; Kang & Jones, 1990; Jones & Ellison, 1991; Brunetti & Jones, 2014). The basic idea of DSA is that relativistic particles, in the tail of a Maxwell-Boltzmann distribution, can cross the shock front in both directions multiple times. Particles that travel into the upstream scatter with the incoming particles and are reflected back into the downstream, where they excite waves. These waves reflect them back into the upstream and the process is repeated. Each time the particles cross the shock, they gain energy.
The whole process can be modelled by evolving the cosmic-ray distribution function $f(p,t)$ using a convection-diffusion equation:

$$\frac{\partial f(p,t)}{\partial t} + (\mathbf{v}\cdot\nabla)f(p,t) - \nabla\cdot[\mathbf{n}D(\mathbf{n}\cdot\nabla)f(p,t)] = \frac{1}{3}(\nabla\cdot\mathbf{v})\,p\frac{\partial f(p,t)}{\partial p} \tag{1.21}$$

In the equation above, the second term accounts for convection, the third term accounts for diffusion and the right hand side describes adiabatic changes of the particle energy. A general solution of this problem under realistic conditions does not exist and only solutions in particular regimes have been worked out (e.g. Drury, 1983; Malkov, 1997).
These approaches yield that the actual energy gained by a particle with a velocity v that crosses the shock front j-times has a final energy of:

$$E_j = E_0\beta^j, \tag{1.22}$$

with E_0 being its initial energy and $\beta = (1 + v/c)$. Acceleration processes that accelerate particles by non-random motions, such as DSA, are classified as Fermi-I processes and their energy gain depends linearly, $\propto v/c$, on the shock velocity. In the case of random motions as an accelerator, the energy gain is not as efficient, $\propto (v/c)^2$, and these processes are called Fermi-II processes.

The momentum and energy distributions of injected cosmic rays follow power-laws, depeding on the shock compression ratio r:

$$f(p) \propto p^{-s_p}, \quad \text{with} \quad s_p = \frac{3r}{r-1} \tag{1.23}$$

$$f(E) \propto E^{-s_E}, \quad \text{with} \quad s_E = \frac{r+2}{r-1}. \tag{1.24}$$

For very strong shocks, the slopes converge to $s_p \to 4$ and $s_E \to 2$. According to synchrotron theory, such a population of electrons would produce an emission described by a power law as well. Hence, the observed radio spectra of radio relics take the form $F_\nu \propto \nu^{-\alpha_R}$. From the radio spectral index, the corresponding Mach number can be computed as (see Blandford & Eichler, 1987):

$$\alpha_R = \frac{1}{2} - \frac{M^2+1}{M^2-1}. \tag{1.25}$$

If the relic's lifetime is longer than the electron cooling time, the radio spectral index is directly connect to the energy spectral index as: $s_E = 1 - 2\alpha_R$ (for more details see Trasatti et al., 2015, and references therein). Hence, we expect older particles to be observed at lower frequencies.

Shock Drift Acceleration

Recently, *Shock Drift Acceleration* (SDA) has been suggested as a viable mechanism to accelerate electrons efficiently in low Mach number shocks (Matsukiyo et al., 2011). In SDA, electrons residing in the upstream drift along the shock front due to a magnetic field gradient across the shock front. The velocity due to the *gradient-B*-drift is

$$\mathbf{v}_{\nabla B} = -\frac{p_\perp^2}{2m_e e\gamma B^3} \left(\mathbf{B} \times \nabla B\right). \tag{1.26}$$

The velocity is computed using: the magnetic field, $\mathbf{B}$, the electron mass, m_e, the electron charge, e, the Lorentz-factor of the electron, γ, and the electron momentum perpendicular to the magnetic field, $p_\perp$. While the electrons are drifting along the shock front they gain energy from a motional electric field. Eventually they are reflected back into the upstream with a momentum that is parallel to the upstream magnetic field. This causes a temperature anisotropy $T_\parallel > T_\perp$ which self-consistently generates upstream waves that scatter the upstream moving electrons back to the shock front where they repeat the process. Guo et al. (2014a) identified this process as a first-order Fermi process. The energy gain of the electrons

due to SDA is

$$\Delta\gamma_{\rm SDA} = -\frac{e}{m_e c^2}\int_Z E_d \mathrm{d}z = -\frac{e}{m_e c^2}\frac{v_0}{c} B \sin(\theta_B)\, Z. \tag{1.27}$$

The second equality assumes that the electric field is constant along the drift direction of the electrons $E_d = v_0/cB\sin(\theta_B)$. Therefore the energy gain only depends on the shock obliquity θ_B, the angle between shock normal and underlying magnetic field, B, and the travelled distance Z. The other quantities in Eq. 1.27 are the electron mass, m_e, the electron charge, e, the speed of light, c, and the electron speed, v_0. Hence, SDA is most efficiently in perpendicular shocks. In Chap. 3 we will discuss the first test of SDA in cosmological simulations of galaxy clusters.

The Challenges of Shock Acceleration in Galaxy Clusters

Even though the processes of DSA seem to be well understood for shock waves in supernovae, the extrapolation of the same theory to large-scale shocks in galaxy clusters involves several challenges and problems that have to be solved. In the following, we present an overview on those and provide ideas of overcoming these challenges if possible.

In principle, both cosmic-ray protons and electrons should be accelerated at the shock front. Yet there has not been any observational signature of cosmic-ray protons in form of γ-ray emission (see Sec. 1.2.3 and Huber et al., 2013a; Ackermann et al., 2014, 2015, 2016). The non-detection of γ-rays yields an upper limits for the flux above 500 MeV in the range of $0.5 - 22.2 \cdot 10^{-10}$ ph cm^{-2} sec^{-1} (Ackermann et al., 2014). The analysis of stacked *Fermi*-LAT count maps estimated an upper flux limit of the order of a few 10^{-10} ph cm^{-2} sec^{-1} (Huber et al., 2013a). Deep observations of the Virgo cluster (see Ackermann et al., 2015) and the Coma cluster (see Ackermann et al., 2016) have been performed. The limits for the γ-ray flux above 100 MeV have been estimated to be $1.2 \cdot 10^{-8}$ ph cm^{-2} sec^{-1} for Virgo and $5.2 \cdot 10^{-9}$ ph cm^{-2} sec^{-1} for Coma. Overall, observations constrain the ratio of cosmic-ray to thermal pressure within the virial radius to be below a few percent.

Recently, PIC-simulations have released some of the tension (Caprioli & Spitkovsky, 2014b; Guo et al., 2014a,b), by showing that electrons and protons undergo different shock acceleration mechanisms whose efficiencies highly depend on the shock obliquity, i.e. the angle between the shock normal and the underlying magnetic field. These simulations showed that protons are injected into DSA directly but they are only efficiently accelerated if the shock obliquity is smaller than $\lesssim 45^\circ$ (see Caprioli & Spitkovsky, 2014b). On the other hand electrons cannot participate in DSA directly as they cannot cross the shock front because their gyro-radius is too small compared to the shock front's thickness that again is controlled by the protons. Hence, thermal electrons are tied too closely to the magnetic field lines and are

convected downstream without undergoing any significant DSA. Therefore, electrons have to be pre-accelerated before they can undergo efficient DSA. This is an other unsolved puzzle of shock acceleration in galaxy clusters known as the *electron injection problem*.

Studies of high Mach number shocks have shown that *Shock Surfing Acceleration* (SSA) can accelerate electrons and inject them into DSA (e.g. Dieckmann et al., 2000). In SSA, the Buneman instability, triggered by the interaction of incoming electrons and reflected ions, excites electrostatic waves that trap the electrons in their electrostatic potential. The trapped electrons are then efficiently accelerated by the convective electric field. Yet, in the low Mach number regime ($M < 5$), that is expected in galaxy clusters, SSA cannot work because the Buneman instability that is essential for SSA cannot trigger (Matsumoto et al., 2012). However, electrons can be efficiently pre-accelerated by shock drift acceleration (SDA) in low Mach number regimes (Ball & Melrose, 2001; Bell, 1978a; Park et al., 2013), but only if the shock obliquity is greater than $\gtrsim 45°$ (see Guo et al., 2014a,b). This additional requirement alleviates the problem of the missing γ-ray emission, yet it does not solve it completely (see Sec. 3 this edition).

One unknown in the theory of DSA is the true value of the shock acceleration efficiencies, whose estimation is difficult due to the non-linear nature of the different processes. The acceleration efficiencies for cluster shocks have been inferred from the efficiencies observed in supernovae remnants (e.g. Dyer et al., 2001), that are in the range of a few percent. Yet, the extrapolation to cluster shocks is not trivial as their energy dissipation happens at weak shocks, while young supernovae remnants have high Mach numbers. It is still unclear how the acceleration efficiencies depend on the Mach number or not. For example, Keshet et al. (2004) and Hoeft et al. (2008) assume a constant acceleration efficiency for all Mach numbers, while Kang & Ryu (2013) estimated that they are an increasing function of the Mach number that saturates for strong shocks, see Fig. 1.5(a).

In order to produce the observed radio brightness of relics (see Fig. 1.5(b)) with electrons that have been directly accelerated from the thermal pool large Mach numbers are required (e.g. Ryu et al., 2003; Kang & Ryu, 2013). Yet, the Mach numbers of shock waves in galaxy clusters are very small and the corresponding acceleration efficiencies of DSA are not strong enough, e.g. a $M = 2$ has an acceleration efficiency of about $\sim 6.5 \cdot 10^{-6}$ (see Fig. 1.5(a)). The apparent very efficient acceleration can be explained by considering the presence of relativistic fossil electrons (Markevitch et al., 2005). Due to their short lifetime ($\sim 10^8$ yrs), electrons lose their energy fast and become invisible to radio telescopes. Thus, the lifetimes of these fossil electrons with Lorentz factors of $\gamma \geq 10^2$ are of the order of $\sim$ Gyr and they can survive long enough in the cluster to be re-accelerated. It has been proposed that these fossil electrons can be efficiently re-accelerated at shocks and therefore make radio relics visible again (e.g. Pinzke et al., 2013; Kang & Ryu, 2015). The Mach numbers required for the re-acceleration of fossil electrons are much smaller than required by the acceleration from

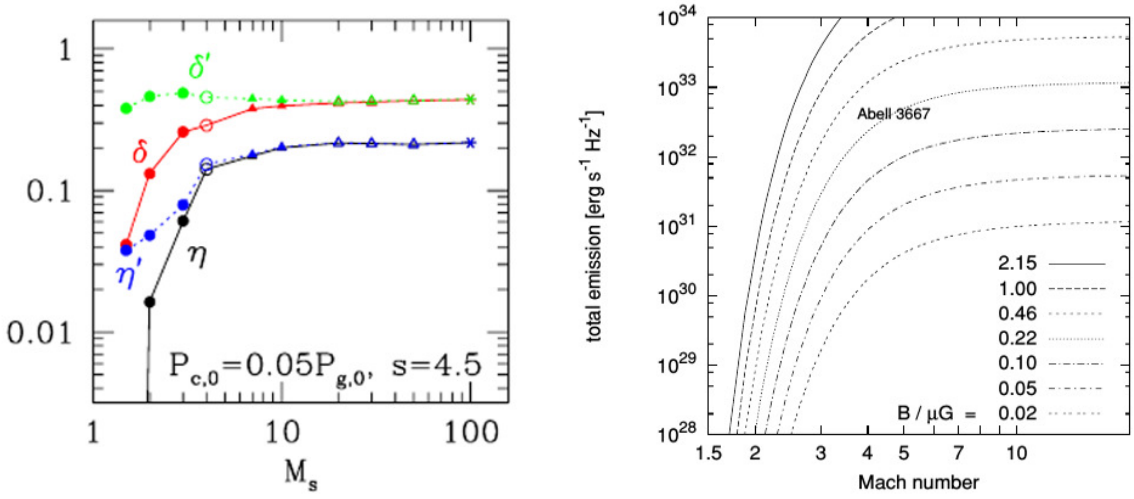

(a) (b)

Figure 1.5: 1.5(a) Shock dissipation efficiencies for the gas, δ, and the cosmic rays, η, taken from Kang & Ryu (2013). The green and blue line display the cases without adiabatic compression. 1.5(b) Radio power as a function of Mach number at different field strengths taken from Hoeft et al. (2008).

the thermal pool, see Fig. 1.5(a). In particular, typical shocks in the ICM, $M < 3$, should predominantly re-accelerate existing cosmic-ray electrons, rather than injecting new ones (e.g. Kang & Ryu, 2013). The re-acceleration of fossil electrons could also explain the discrepancy in Mach numbers derived by radio and X-ray observations that are, in principle, much smaller (e.g. Hong et al., 2015, and references therein). Possible candidates for the fossil electrons are remnants of previous shock acceleration by large-scale shocks as well as old lobes and tails of radio galaxies. Recently, van Weeren et al. (2017) have reported the first discovery of a direct connection between a radio relic and a radio galaxy in Abell 3411-3412. Also Bonafede et al. (2014) found evidence for the connection between radio galaxies and radio relics in PLCKG287.0+32.9.

Another challenge is that shocks are found without a corresponding radio relic, as for example the eastern temperature jump in 1RXS J0603.3+4214 (e.g. Ogrean et al., 2013). Yet, as in the case of Abell 2146 this might be simply due to a low surface brightness of the relic itself (see Russell et al., 2011; Hlavacek-Larrondo et al., 2017).

1.3.2 Turbulence in Galaxy Clusters

Understanding the nature and evolution of turbulence in galaxy clusters is crucial as it can account for a variety of physical processes in the ICM. Turbulence provides and additional pressure support to the thermal pressure, with $P_{\rm turbulent} \sim (10 - 20)$ % $P_{\rm thermal}$, against the pressure from gravity (e.g. Norman & Bryan, 1999a). This affects the mass estimate derived

from hydrostatic equilibrium, see Eq. 1.5. Cosmic rays are believed to be (re)-accelerated by turbulence, which would be an explanation for the origin of radio halos (see Sec. 1.2.3). A proposed acceleration mechanism is Fermi-II acceleration (see Brunetti & Lazarian, 2016; Eckert et al., 2017, and references therein). In addition, mixing of the hot gas and turbulent transport might counterbalance gas cooling in cool core clusters (e.g. Zhuravleva et al., 2014a). X-ray and SZ-observations of galaxy clusters reveal patchy structures in density, temperature and pressure on scales of a few tens to hundreds of $\sim$ kpc (e.g. Shibata et al., 2001; Gu et al., 2009; Hofmann et al., 2016; Churazov et al., 2012; Khatri & Gaspari, 2016; Werner et al., 2016). At the same time numerical simulations reveal that both compressive (curl-free) and solenoidal (divergence-free) turbulence, with Reynolds numbers of $Re \geq 10^3$, are driven in galaxy clusters across different scales (e.g. Gaspari et al., 2014; Miniati & Beresnyak, 2015; Porter et al., 2015; Beresnyak & Miniati, 2016; Vazza et al., 2006, 2009b, 2011a, 2017b, and references therein). On galactic scales, $\sim$ 10 kpc, the main drivers of turbulence are the lobes and jets from AGN as well as buoyancy and magneto-thermal instabilities in the ICM (e.g. Heinz et al., 2006; Parrish & Stone, 2007; Brüggen & Scannapieco, 2009). The main drivers of turbulence acting on cluster scales, $\sim$ few Mpc, where gravitational energy is converted into kinetic energy, are mergers and accretion. The latter generates turbulence through baroclinic motions, fluid instabilities and tangential flows. Cluster mergers stir the ICM and generate turbulence by core sloshing, shearing instabilities and complex shock patterns. Once turbulence is developed, the turbulent cascade can channel energy into different components of the ICM. Turbulent energy is both dissipated into heat and is converted into magnetic energy by dynamos. Furthermore turbulence may (re)-accelerate of cosmic rays via the non-linear interaction between particles and turbulent waves.

The turbulence observed in simulations is Kolmogorov-like, $E(k) \propto k^{-5/3}$, across many scales and has an effective kinematic viscosity $\nu \leq 10^{29}$ cm^{2}s^{-1} (Vazza et al., 2012b). Simulations have shown that the compressive component only accounts for a few percent of the turbulence in clusters. Yet, this contingent can rise up to 15 % in cluster core and up to 30 % in cluster outskirts during major mergers (Vazza et al., 2017b).

Current X-ray telescopes investigate turbulence via pseudo-pressure maps (e.g. Zhuravleva et al., 2014b). They classify the origin of the observed perturbations by combining density and temperature fluctuations using an effective equation of state (e.g. Zhuravleva et al., 2017). Future X-ray telescopes such as Athena (see Sec. 1.2.2) are expected to observe the actual driving scales of turbulence (e.g. ZuHone et al., 2016). In Chap. 6 we will show how vorticity is injected and evolves in our simulations of galaxy clusters.

1.3.3 Magnetic Fields

Synchrotron radiation and Faraday rotation of background sources provide evidence for the existence of large-scale magnetic fields (see Ferrari et al., 2008; Feretti et al., 2012, and references therein). Furthermore, Faraday rotation measurements of the polarization angle of synchrotron radiation reveal that the magnetic field is tangled across a wide range of scales (e.g. Vacca et al., 2010, and references therein). While synchrotron emission is only visible in clusters that host cosmic-ray electrons, Faraday rotation should be observed in the majority of galaxy clusters as magnetic fields are believed to exist in most of them (Dolag et al., 1999; Brüggen et al., 2005; Subramanian et al., 2006). Magnetic fields are also expected to exist in the voids and filaments of the cosmic web, yet they have not been detected as they are expected to be much weaker, $B < 1$ nG (e.g. Planck Collaboration et al., 2016a; Pshirkov et al., 2016). The origin of the magnetic fields is still an unanswered question. Yet, there are two major, not necessarily competing, theories.

In the first theory, magnetic fields are of cosmological origin. In this case, they have been created during inflation, by the Biermann battery or by some other physical process in the early Universe (see Biermann, 1950; Widrow et al., 2012). Independent of the origin, these seed fields are amplified by the turbulent dynamo, tangential flows or galactic dynamos (Schleicher et al., 2013; Dolag et al., 1999; Hanasz et al., 2004). In the outskirts of galaxy clusters, magnetic fields can be amplified also via magneto-thermal or cosmic-ray driven instabilities (Parrish et al., 2008; Drury & Downes, 2012; Brüggen, 2013).

The other possibility for the origin of the magnetic fields are astrophysical seed fields. These are magnetic fields that form within AGN or (proto)galaxies and that are then ejected into the ICM (e.g. Pudritz & Silk, 1989; Daly & Loeb, 1990; Völk & Atoyan, 2000; Beck et al., 2013). Once the magnetic fields have been released into the ICM, they are both amplified and dispersed. As a consequence of their local injection, astrophysical seed fields tend to be in the vicinity of galaxy formation regions. It has been shown by Cho (2014) that spreading these seed fields can be very ineffective and different spatial distributions of sources have to be taken into account to explain the observations.

The small-scale dynamo that is expected to amplify magnetic fields, in both seeding scenarios, is induced by turbulent motions in the ICM and acts in a two-stage process (Subramanian et al., 2006). An initial exponential growth phase is followed by a non-linear growth phase that acts until saturation (Ryu et al., 2008; Porter et al., 2015; Beresnyak & Miniati, 2016). At high redshifts the small-scale dynamo can induced by supernovae in star forming regions. Miniati & Beresnyak (2015) showed that the efficiency of converting turbulent energy into magnetic energy is within a fixed range of a few percent.

So far, none of the above theories has been ruled out or is preferred over the other. Both of them have been studied in great detail and numerical simulations have been able to reproduce magnetic fields in galaxies and clusters. For example, Brüggen et al. (2005) used

a primordial magnetic field while other works have managed the same using astrophysical seeding. Xu et al. (2009) used AGN as a source, while Beck et al. (2013) seeded magnetic fields by star formation and Donnert et al. (2009) injected them via galactic winds. Donnert et al. (2009) argued that the astrophysical seeding of magnetic fields and their subsequent evolution might be enough to explain the magnetic fields in galaxy clusters. Furthermore, if primordial magnetic fields exists, they should be found in the low density regions that have not been conquered by magnetic fields of astrophysical origin. In particular, one expects to detect primordial magnetic fields in the filaments of the cosmic web (e.g. Vazza et al., 2015c, and references therein). Yet, studying the small-scale dynamo in filaments is still a numerical challenge as the needed resolution cannot be easily achieved by any adaptive Lagrangian or Eulerian simulation (e.g. Vazza et al., 2014b).
In Chap. 6 we will quantify with our simulations the level of dissipation of turbulent energy into the amplification of magnetic fields in the ICM.

1.4 Numerical Simulations

The main components that have to be included in cosmological simulations are the dark matter and the baryonic matter. The collisionless dark matter component can be described by N particles that possess mass, position and velocity, and compute the forces acting on each particle. The gravitational potential is computed by solving the Poisson equation:

$$\nabla^2 \Phi \left(\mathbf{x}, t \right) = 4\pi \mathrm{G} \rho \left(\mathbf{x}, \mathbf{v}, t \right) . \tag{1.28}$$

The above equations can be solved using a brute force approach that computes the gravitational potential and acceleration for each particle directly. Even though this approach is very robust and accurate, it is computationally expensive as it scales with N^2 and other methods have to be invented to reduce the computational costs.
The Particle-Mesh method has been introduced (e.g. Hockney & Eastwood, 1988) to reduce the computational cost and hence to improve the performance. In Particle-Mesh method, at each timestep the particles are assigned to a grid, one which the Poisson equation is solved in Fourier space. This approach reduces the computational costs to $N \log(N)$. Yet, this approach has an uniform spatial resolution, while the Universe evolves local structures that would be desired to be further resolved. The combination of the direct particle method and the Particle-Mesh method (Hockney et al., 1973) can overcome this problem. The basic idea is that the gravitational potential is decomposed into long-range and short-range interactions. The long-range interactions are solved using the Particle-Mesh approach, while the short range interactions are computed using the direct N-body approach.
The baryonic matter component in the cosmic gas obeys the Euler-equations of an ideal

fluid:

$$\frac{\partial \rho}{\partial t} + \nabla \cdot \rho \mathbf{v} = 0 \tag{1.29}$$

$$\frac{\partial \rho \mathbf{v}}{\partial t} + \nabla \cdot (\rho \mathbf{v} \times \mathbf{v}) + \frac{\partial P}{\partial x} = \rho \mathbf{F} \tag{1.30}$$

$$\frac{\partial E}{\partial t} + \nabla \cdot \mathbf{v} \, (E + P) = \rho \mathbf{v} \cdot \mathbf{F} \tag{1.31}$$

In the equations above, following variables have been used: ρ the gas density, $\mathbf{v}$ the gas velocity, E the total fluid energy, P the fluid pressure and and the forces acting on the fluid $\mathbf{F}$. The collisional gas can be represented by a macroscopic velocity field. For cosmological applications, additional expansion terms, related to the scale factor a, are introduced in order to solve such equations in the comoving reference frame.

The Euler-equations, Eq. 1.29-1.31, can be solved using various numerical approaches. One can either use Eulerian methods (e.g. Bryan et al., 2014) that sample the velocity field on a grid or Lagrangian methods (e.g. Springel, 2005), such as *Smoothed Particle Hydrodynamics*, that use particles for the approximation of the fluid field. Recently, moving-mesh methods (e.g. Springel, 2011; Hopkins, 2015), a hybrid between Lagrangian and Eulerian methods, have been introduced.

In *Smoothed Particle Hydrodynamics* (SPH), each particle represents a smooth Lagrangian cloud that carries the information of the fluid (for a recent review see Price, 2012). The continuous fluid is build from the discrete set of tracer particles by using a kernel to interpolate the different quantities. The smoothing length of the kernel determines the spatial resolution and the number of neighbours that contribute to a point. The advantages of SPH codes are that a high resolution is obtained in denser regions, simply because of the larger amount of particles in these regions. Furthermore the entropy formalism ensures conservation of linear and angular momentum, total energy and entropy. Yet, this is also the weakness of SPH codes as the conservation of entropy prohibits the formation of shocks and fluid instabilities. However, the formation of those is important for the study of the non-thermal components in galaxy clusters. To overcome this, discrepancy artificial viscosities have been introduced. For more reviews on SPH methods see for example: Monaghan (2005); Rosswog (2009).

In grid codes, the fluid is sampled on top of a grid. The Euler-equations are solved in each distinct grid cell and numerical fluxes are used to connect the different cells. *Adaptive Mesh Refinement* (AMR) can be used to locally refine the grid in order to obtain more accurate results but minimizing the computational cost. Various Eulerian methods and schemes have been introduced to solve hydrodynamical equations. The relevant methods for this work are the *Piecewise Linear Method* (PLM) and *Piecewise Parabolic Method* (PPM) that are both implemented in the `ENZO` code (see Sec. 2.1). The PLM uses linear functions while the PPM uses parabolic functions to fit the solution in each grid cell (see Colella & Woodward, 1984; Colella & Glaz, 1985, respectively). One advantage of grid methods is their ability of allowing

the formation numerical discontinuities that are necessary to simulate shocks. Unfortunately, numerical schemes tend to oscillate and break down around these discontinuities and methods have to be used to prevent this. When using the PLM method, one can apply slope limiters that reduce the oscillations (Harten, 1983). In the case of using the PPM method, so-called essentially non-oscillatory methods can be used (Harten et al., 1987). These schemes compute an additional smoothness indicator to indicate, whether the order of the reconstruction has to be reduced to avoid oscillations around a discontinuity. This method can be extended by introducing weighted reconstructions that depend on a smoothness operator. For further details, we point to the literature such Levy et al. (1999) or Dolag et al. (2008a), who provide reviews for shock capturing methods in SPH and grid simulations.
Various projects (e.g. Agertz et al., 2007; Tasker et al., 2008; Vazza, 2011; Vazza et al., 2011b; Sembolini et al., 2016) have been dedicated to study the numerical differences between SPH and grid codes and their effects on the underlying physics. For example, a major difference is that SPH codes can only refine on density, which makes the modelling of instabilities or thermal properties in underdensed regions difficult. Recently a lot of effort has been made to overcome these differences and to produce consistent results. For further reading on this important topic, which is beyond the scope of this work, we refer to the above stated references.
If one wants to include magnetic fields into the simulations, on has to solve the equations of *magneto-hydrodynamics* (MHD) instead of the Euler-equations:

$$\frac{\partial \rho}{\partial t} + \nabla \cdot (\rho \mathbf{v}) = 0 \tag{1.32}$$

$$\rho \frac{\partial \mathbf{v}}{\partial t} + \rho \mathbf{v} \cdot \nabla \mathbf{v} + \nabla p - \rho \mathbf{g} - \frac{1}{\mu_0} (\nabla \times \mathbf{B}) \times \mathbf{B} = 0 \tag{1.33}$$

$$\frac{\partial p}{\partial t} + \mathbf{v} \cdot \nabla p + \gamma p \nabla \cdot \mathbf{v} = 0 \tag{1.34}$$

$$\frac{\partial \mathbf{B}}{\partial t} - \nabla \times (\mathbf{v} \times \mathbf{B}) = 0. \tag{1.35}$$

In general, the MHD-equations are discretized as the Euler-equations on a grid. However, the magnetic divergence constraint, $\nabla \cdot \mathbf{B} = 0$, is violated by numerical errors leading to stability problems in the simulations. Therefore, numerical schemes have to be invented to overcome this problem. In *constrained transport*-schemes (e.g. Evans & Hawley, 1988), an initial zero divergence is conserved by a specific finite difference discretization on top of a staggered grid. The other widely used scheme is *divergence cleaning*, in which the magnetic field is projected into the space of divergence-free vector fields, where any non-zero divergence is eliminated, i.e. cleaned. In this work, we will use the method introduced by Dedner et al. (2002). This method introduces an arbitrary function, Ψ, that is included in the magnetic induction equation, Eq. 1.35, and in the divergence constraint. This function couples the divergence constraint to the hyperbolic system of equations and projects the magnetic field

into the desired space of divergence-free vector fields. Elliptical, parabolic and hyperbolic corrections can be chosen for Ψ. In this work, we use the hyperbolic operator as introduced by Dedner et al. (2002):

$$\mathcal{D}(\Psi) := \frac{1}{c_h^2}\frac{\partial \Psi}{\partial t}, \qquad c_h \in (0, \infty)\,. \tag{1.36}$$

The last ingredients of a cosmological code is to couple the methods described above with the expansion of the Universe, see Sec. 1.2.1. This is done by transforming the Euler- (Eq. 1.29 - 1.30) or the MHD-equations (Eq. 1.32 - 1.35) into comoving coordinates and additionally solving the expansion equation during each time step.

2 Methods and Algorithms

2.1 ENZO

The cosmological simulations in this dissertation have been carried out using the ENZO-code. ENZO is an open-source code that has been developed by Greg Bryan and Michael Norman (e.g. Bryan & Norman, 1997; Norman & Bryan, 1999b; Bryan et al., 2001; Norman et al., 2007). Nowadays it is developed by the ENZO-community (see Bryan et al., 2014) and released by the University of California under the Berkley Software Distribution license[1]. ENZO supports the an accurate treatment of the dynamics of supersonic flows and shock waves which is crucial for our work.
It combines a Particle-Mesh solver with the PLM and PPM methods, described in Sec. 1.4, (e.g. Berger & Colella, 1989) to solve for the equations described in Sec. 1.4 on top of a block-structured adaptive mesh refinement grid. Furthermore, ENZO is parallelized using Message Passing Interface (MPI) that spreads equal portions of the simulation across the different processors. ENZO has been used on some of the largest supercomputers such as JUQUEEN[2] and JURECA[3] in Jülich, Piz-Daint at CSCS[4] and many more. Recently, my collaborators produced cosmological magneto-hydrodynamical simulations with ENZO on 2400 computing nodes of Piz-Daint, for runs using up to 4.5 million GPU hours Vazza et al. (2017a). For additional information on ENZO and its properties, we refer to Bryan et al. (2014) and the latest documentation[5].

2.2 CRaTer: A Versatile Lagrangian Analysis Tool

ENZO does not give any Lagrangian information on the gas dynamics, i.e. information on the trajectory of single particles. However, for the problems central to my thesis, from the acceleration of cosmic rays to the evolution of turbulent eddies, it is convenient to obtain

[1] http://enzo-project.org/doc/EnzoLicense.html
[2] http://www.fz-juelich.de/ias/jsc/EN/Expertise/Supercomputers/JUQUEEN/JUQUEEN_node.html
[3] http://www.fz-juelich.de/ias/jsc/EN/Expertise/Supercomputers/JURECA/JURECA_node.html
[4] http://www.cscs.ch/computers/piz_daint_piz_dora/
[5] https://enzo.readthedocs.io/en/enzo-2.5/

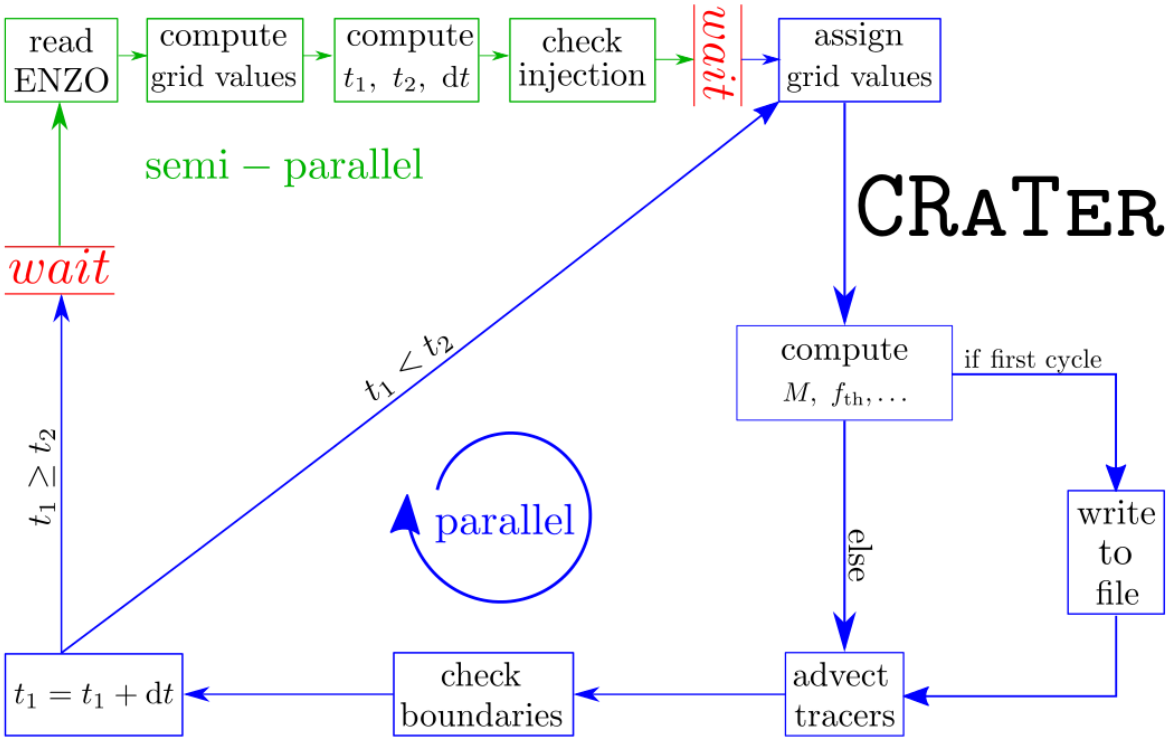

Figure 2.1: Work cycle of the tracer particles between two adjacent snapshots in `CRaTer`. The green region shows the part of the code that runs in semi-parallel and the blue region is the part of the code that is fully parallelized. The `openMP` threads are synchronized at the red *waits*.

a complementary Lagrangian description of the fluid. Therefore, I have developed the Lagrangian analysis tool `Cosmic-Ray Tracers` (`CRaTer`). `CRaTer` is written in C++ and is parallelized using `Open Multi Processing` (`openMP`). It injects tracer particles, or tracers, on top of the `hdf5` outputs of `ENZO`. Its use is not restricted to `ENZO` only but it can easily be exported to any other grid code, as for example `Flash`[6]. The underlying grid data is assigned to the tracer particles by opportunely interpolating the field values to the tracer locations, and they are advected passively with the fluid over time.

In Fig. 2.1, we show the duty cycle of `CRaTer` between two adjacent `ENZO` rootgrid snapshots. At first the `ENZO` data is read and derived quantities, e.g. $\nabla \cdot \mathbf{v}$, $\nabla \times \mathbf{v}$, etc., are computed. Then, the simulation time of the current and next `ENZO` snapshot, $t1$ and $t2$, and the corresponding numerical timesteps dt are computed (see Sec. 2.2.2). Next, following the injection scheme described in Sec. 2.2.1, additional tracers are injected from the boundaries and the grid values are assigned to the tracers using either the *nearest-grid-point* method or the *cloud-in-a-cell* method (see Sec. 2.2.2). These values are then used by the tracers

[6] `http://flash.uchicago.edu/site/flashcode/`

to compute other quantities such as Mach number, obliquity etc. Finally, the tracers are advected using a timestep smaller than the ENZO timestep (see Sec. 2.2.2). Everytime the tracers have been advected, it is checked, if any of the tracers exited the computational domain and proper boundary conditions are applied. The cycle of assigning the grid data until the boundary check is repeated until the sum of local timesteps matches the ENZO timestep (see Sec. 2.2.2). During the first iteration the tracer data is written to file. Once the processes is done, the next ENZO snapshot is read and the whole processes is repeated until the end of the simulation. In the following, we will describe the different features of CRaTer in greater detail.

2.2.1 Particle Injection

Although the particles injected by CRaTer are mass-less tracers of the fluid, in many applications it is convenient to identify approximately the mass they are tracking, e.g. when computing the total cosmic-ray energy associated to each of them. For this purpose, I have devised a procedure to discretise the mass sampling of tracers, defining $m_{\rm tracer}$ as the uniform mass assigned to each of them. In each grid cell, the mass on the grid, $m_{\rm grid}$, is compared to the tracer mass and the corresponding number of tracers, i.e. $N_{\rm tracer} = \lfloor m_{\rm grid}/m_{\rm tracer} \rfloor$, is injected at random positions across the grid cell. The same requirement is used to inject additional tracer particles from the boundary cells of the area sampled by the tracers to ensure that also the infalling matter is simulated properly. This step can be crucial as in some simulations up to $50-60$ % of the cluster mass can enter the sampled region after $z = 1$. The tracer mass is chosen for each cluster separately because it has to be small enough to resolve the cluster structure accurately, but at the same time it still has to be large enough to be computationally managable. The exact mass resolution depends on the specific application. On average, the tracer masses are in the range of $m_{\rm tracer} \approx 10^6 - 10^8\ M_\odot$. In most galaxy clusters analysed in this thesis, this corresponds to a total of $\sim 10^7 - 10^8$ tracers to follow the dynamics of the ICM.

The injection method described above only injects tracers into grid cells that match the requirement $m_{\rm grid} \geq m_{\rm tracer}$. This can lead to a distinct drop in the tracer density, especially in the cluster outskirts, and produce artificial edges in the distribution of tracers. To prevent this effect, I introduced a random-based injection of tracers in the case of $m_{\rm grid} < m_{\rm tracer}$: if a random number drawn within [0-1] is smaller than $m_{\rm grid}/m_{\rm tracer}$, a single tracer particle is injected into that cell. This way, our tracers can also statistically sample the inflow of the rarefied gas which enters the cluster through smooth accretion flows. While this phase is basically irrelevant for the mass accretion of the cluster, smooth gas inflows are characterized by strong accretion shocks, and can be relevant for the injection of cosmic rays (e.g. Ryu et al., 2003).

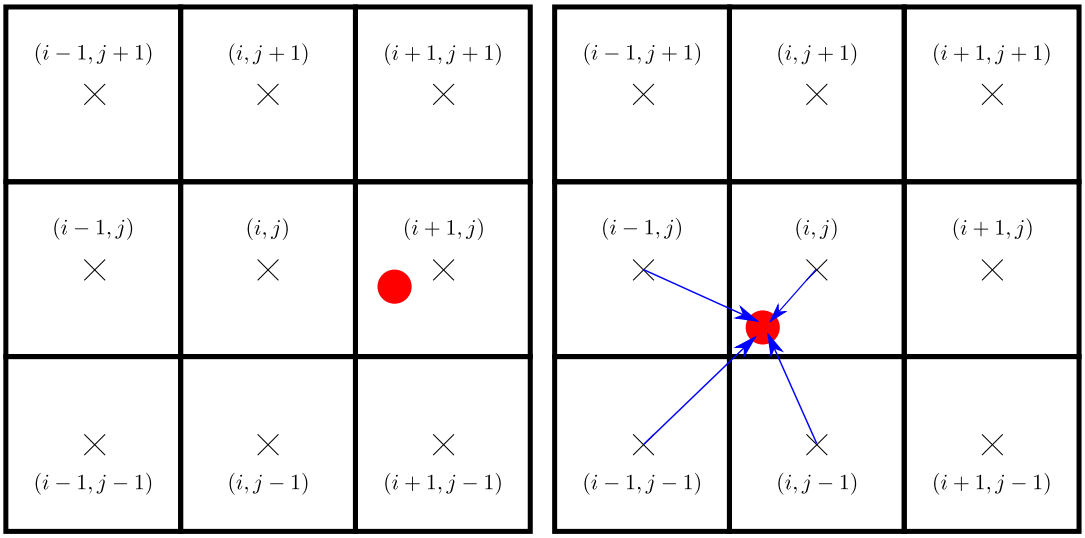

Figure 2.2: Schematic sketches of the velocity interpolation methods in two dimensions. (a) Nearest-grid-point: The particle (red dot) reads the velocity from the nearest grid cell, in this case $(i+1, j)$. (b) Cloud-in-a-cell: The velocities from the four (eight in three dimensions) nearest grid cells are interpolated to the tracers position.

2.2.2 Particle Advection

After the particles have been injected onto the grid, they are advected passively with the fluid. Therefore, they need to compute the local velocity from the underlying grid data. The two most common interpolation schemes are the *nearest-grid-point* method (*NGP*) and the *cloud-in-a-cell* method (*CIC*). In Fig. 2.2, I give schematic sketches on how the two methods work in two dimensions. In *NGP*, see Fig. 2.2(a), the tracer particle reads the velocity of the nearest grid cell. In *CIC*, see Fig. 2.2(b), the velocity is interpolated from the eight nearest neighbours using volume weighting. The velocity using the *CIC* method is computed as

$$v_{\mathrm{CIC}} = \sum_{i=0}^{1}\sum_{j=0}^{1}\sum_{k=0}^{1} v_{i,j,k} w_{i,j,k} \tag{2.1}$$

$$w_{i,j,k} = \frac{|x_p - x_{1-i}|\,|y_p - y_{1-j}|\,|z_p - z_{1-k}|}{\delta x \delta y \delta z}. \tag{2.2}$$

In the equations above, $v_{i,j,k}$ is the grid velocity in cell (i, j, k) and $w_{i,j,k}$ is the corresponding weight. While we routinely interpolate `ENZO` data to the highest available AMR level and evolve the tracer using these data, the `ENZO` output is not saved with the timespacing relative to the highest AMR level, as this would produce disk space that is too large to store the output of entire simulation. Therefore, the tracers have to be advected between the timesteps of saved outputs using sub-cycling. The timestep used to advect the tracers is derived from

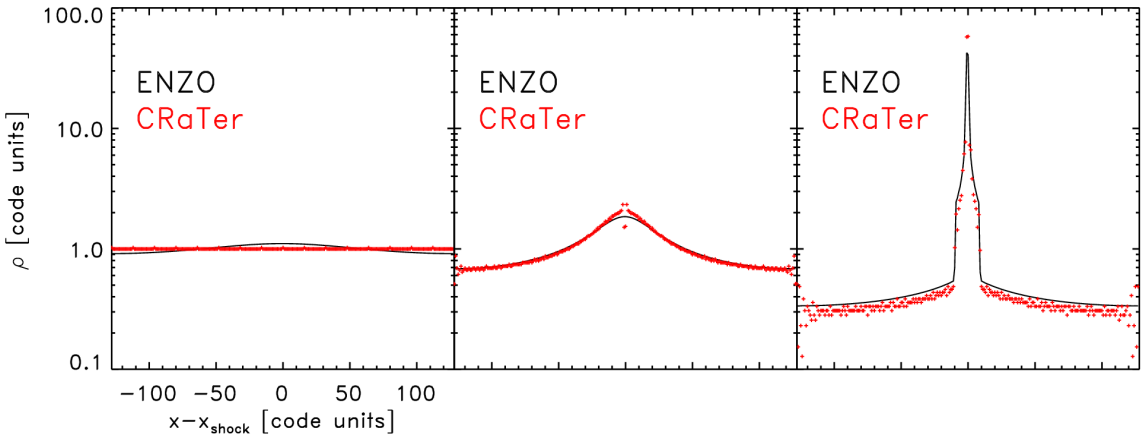

Figure 2.3: The density profile of the Zeldovich Pancake at three different timesteps. The black lines shows the profile of the `ENZO` data and the red crosses show the profile computed using the `CRaTer` data.

the fastest grid velocity $v_{\max}$, the cell size $\mathrm{d}x$, the `ENZO` timestep $\mathrm{d}T_{\mathrm{root}}$ and Courant-Friedrich-Levi number, cfl, of the `ENZO` simulation:

$$\Delta t' = \frac{cfl \cdot \mathrm{d}x}{v_{\max}} \tag{2.3}$$

$$N_t = \left\lceil \frac{\mathrm{d}t_{\mathrm{root}}}{\Delta t'} \right\rceil \tag{2.4}$$

$$\Delta t = \frac{\mathrm{d}t_{\mathrm{root}}}{N_t}. \tag{2.5}$$

We used the *1D-Zeldovich Pancake* (Zel'dovich, 1970) to test if it is sufficient enough to use either the saved timestep or a smaller timestep for the advection of the tracers. In this test case, the tracers follow the flow of the *1D-Zeldovich Pancake* using a 1D-*CIC*-method. In Fig. 2.3, we show `ENZO` and `CRaTer` data at three different times of the simulation. We use timesteps of different sizes to advect the tracer particles. In Fig. 2.4, we show the advection of six different tracers using the different timesteps. In Fig. 2.4(a), we use the simulation timestep between two snapshots. The advection shown in Fig. 2.4(b) resolves the timestep between two snapshots further. Hence, the tracers are advected using a smaller timestep and sub-cycling between two snapshots. In Fig. 2.4(c), we do not advect the tracers between two adjecent timesteps but we skip every other snapshot. This produces a timestep larger than allowed by the cfl-condition. In Fig. 2.4(d), we skip every other snapshot but this time we are using a smaller timesteps, e.g. sub-cycling, to advect the tracers.
In the first two cases, the tracers are following the flow in a proper manner and they do not cross the shock. If the timestep is too large, the advection becomes inaccurate and in this case, the tracers cross the shock front and their trajectories show a bigger scatter. Yet, using sub-cycling on a bigger timestep stabilizes the advection again. Hence, it is possible to advect

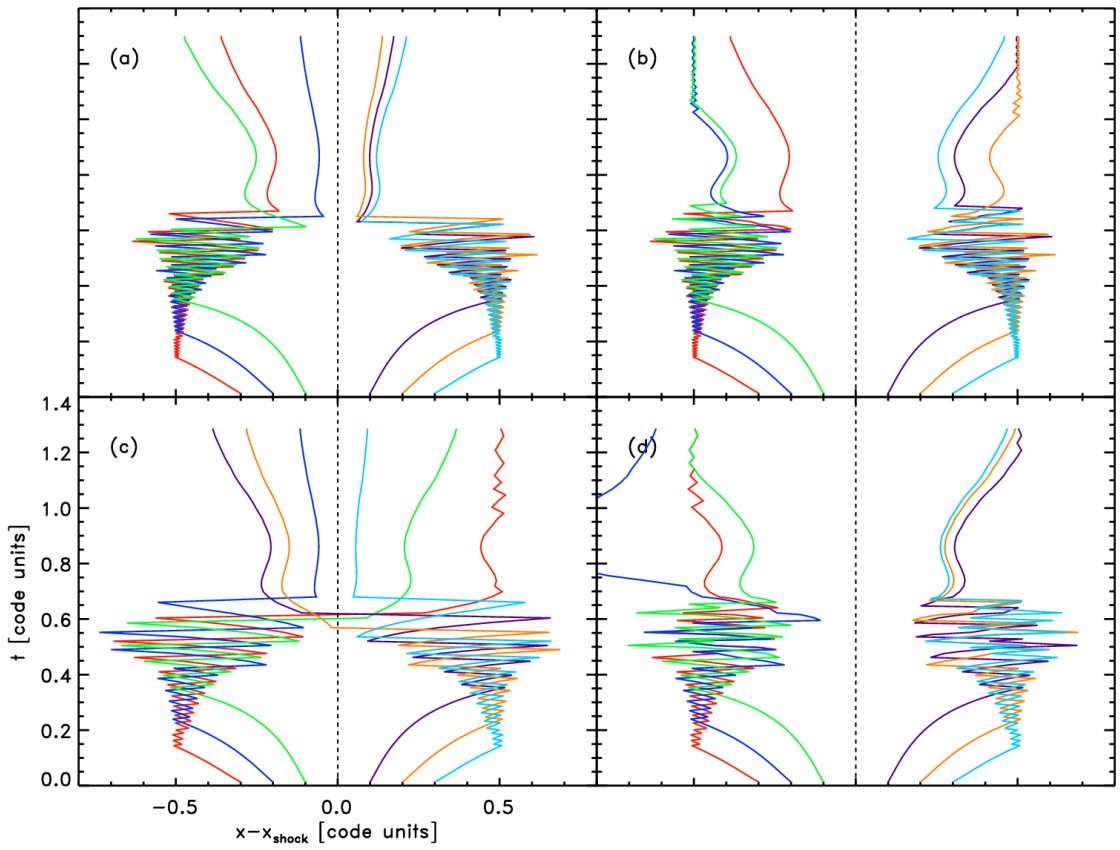

Figure 2.4: Advection of six different tracers using different time-stepping schemes. In panel (a) and (b) the tracers are advected between two adjecent snapshots of `ENZO`. They are using (a) the saved timestep or (b) smaller timesteps for their advection. In panel (c) and (d) the tracers are advected between every other snapshot of `ENZO` and either they are using (c) the saved timestep or (d) smaller timesteps. This test shows that the time-stepping schemes used in panel (a) and (b) are sufficient enough to evolve the tracers. While if the timestep is too large the tracer advection is error-prone as in panel (c) and one should use smaller timesteps as in panel (d).

the tracers between two adjacent snapshots in a proper way by using the `ENZO` timestep, if allowed by the cfl-condition, or a finer timestep and sub-cycling.

To update the trajectory of particles over time, both explicit and implicit time-stepping methods exist (e.g. Springel, 2005). It has been shown that implicit time-stepping is less diffusive. On the other hand, it requires more working storage as the data of two snapshots have to be read into memory at once. In the following, we test if it is sufficient to use explicit time-stepping or if implicit time-stepping is needed. In order to find the most accurate scheme, we injected $\sim 11 \cdot 10^6$ tracers into a cosmological simulation, see Fig. 2.5, and advected them using both the *NGP*- and *CIC*-method in combination with explicit and implicit time-stepping. At $z \approx 0$ we searched for nine massive halos in the cosmological volume (see yellow squares in Fig. 2.5). In order to compare how good the tracers followed the fluid flow, we

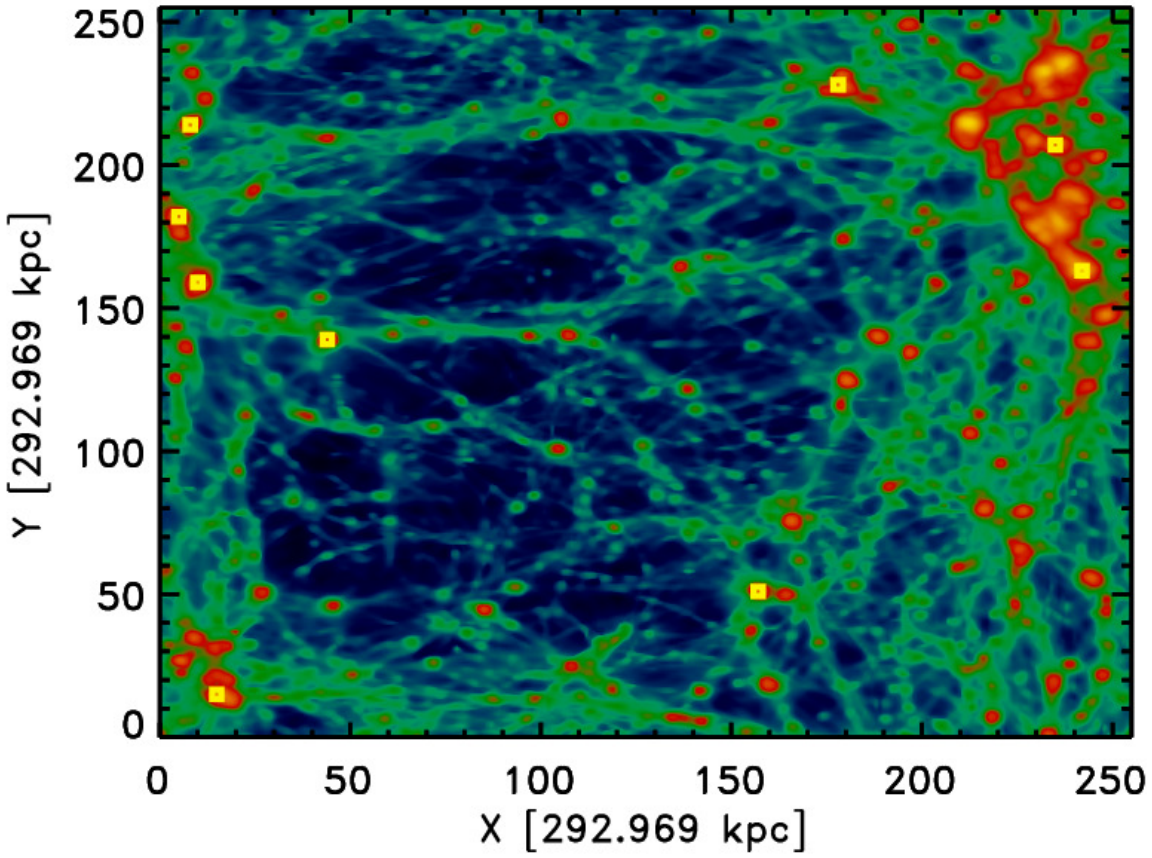

Figure 2.5: Density projection of the cosmological simulation. The yellow squares mark the position of the nine massive halos used for the velocity testing.

compare the density profiles of the selected halos computed with the `ENZO` and `CRaTer` data. In Fig. 2.6, we show the profiles of the nine halos computed using the grid data (black) and using the different combinations of time-stepping and velocity interpolation methods (red and blue lines). For all halos both time-stepping methods resemble the same profile independent of the used interpolation scheme. Hence, it will be sufficient to use explicit time-stepping on the tracers to keep the local memory low and have the code execute as fast as possible.
Tracer particles, that are simply advected using a *NGP*- or *CIC*-method, might not recover the correct mass flow in situations such as turbulent or converging flows, due to the incapability of correctly following the long-term diffusion of mass elements which is naturally captured in the Eulerian view. Stochastic methods (e.g. Genel et al., 2013) have been proposed to overcome this problem. Yet, this is no suitable solution for tracing cosmic rays because their acceleration strongly depends on the shock jump conditions and in such methods it cannot be distinguished between hydrodynamical shocks or artificial shocks due to possible stochastic jumps caused by the method. In this thesis, I have explored possibilities to overcome the problem of recovering the correct mass flow by introducing velocity correction terms meant

to reproduce the slow effect of mass diffusion in a turbulent flow.
The first possible correction term is computed as the average velocity of the surrounding cells. Hence, this correction term for a tracer in cell (i', j', k') is computed as:

$$\delta v_{\mathrm{w\_27}} = \frac{1}{27} \sum_{i=i'-1}^{i'+1} \sum_{j=j'-1}^{j'+1} \sum_{k=k'-1}^{k'+1} v_{i,j,k}. \tag{2.6}$$

Here, $v_{i,j,k}$ is the velocity on the grid. Another possible correction term is:

$$\delta v_{\mathrm{gradP}} = \frac{\nabla P \cdot \mathrm{d}t}{\rho}, \tag{2.7}$$

which is meant to capture slow outwards motion of gas particles away from pressure gradients ∇P. In the equation above, ρ is the density on the grid and $\mathrm{d}t$ is the used timestep. In the following, velocity schemes using Eq. 2.6 and 2.7 will be called *w_27* and *gradP*, respectively.

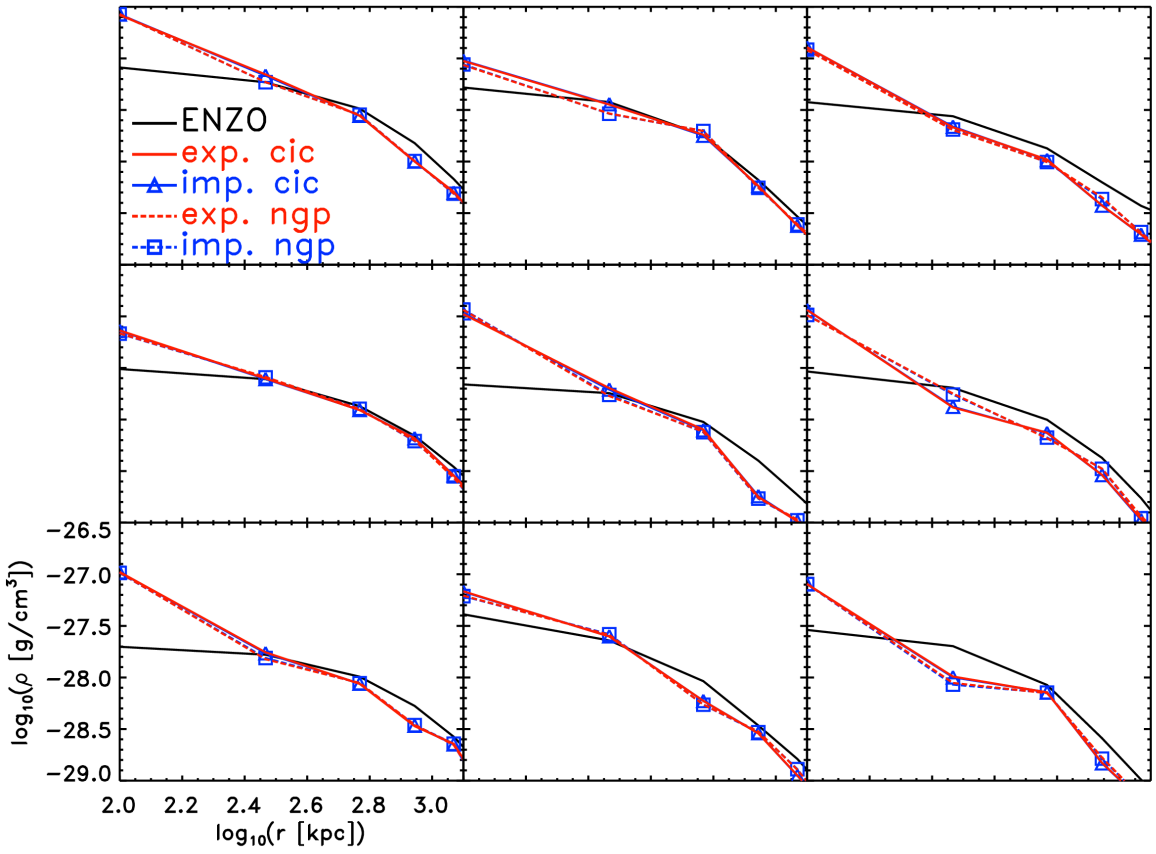

Figure 2.6: Density profiles of the nine clusters found the in the cosmological simulation. The black line shows the profile computed with the ENZO-data and the solid lines show the *CIC* runs and the dashed lines show the *NGP* runs. The red lines were computed using explicit time-stepping and the blue lines were computed using implicit time-stepping.

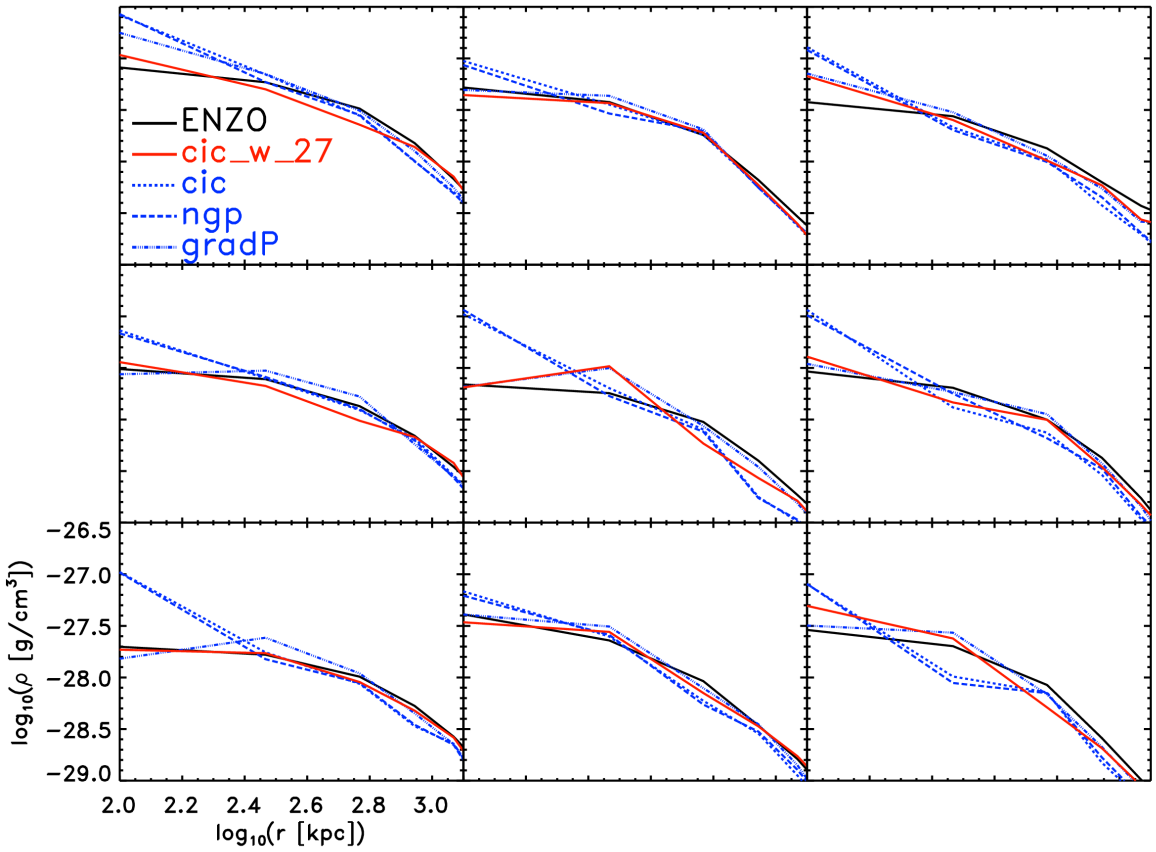

Figure 2.7: Density profiles of the nine clusters found the in the cosmological simulation. The black line shows the profile computed with the `ENZO`-data and the red line shows the *CIC + w_27* run computed with `CRaTer`. The blue lines show the `CRaTer`-runs using: *NGP* (long dashed), *CIC* (short dashed) and *CIC + gradP* (dotted dashed).

The combination of the above stated velocity interpolation schemes and correction terms gives six possible ways to compute the velocity of the tracers. In order to estimate the most accurate method, we advected the tracers on top of the same cosmological simulation as above using the different combinations. In order to compare how good the tracers followed the fluid flow, we again computed the density profiles of the selected halos using the grid data and using the tracer data.

In Fig. 2.7, we show the profiles on the grid (black curve) and of four interpolation schemes: *CIC* (blue dashed), *NGP* (blue long dashed), *CIC + gradP* (blue dashed dotted) and *CIC + w_27* (red). We do not display the results for combining the *NGP* method with either of the correction methods as their performances are clearly inferior to *CIC* methods.

Both the *CIC* and *NGP* method without any additional correction term tend to overestimate the central halo density by a factor of a few in all cases. The profiles computed with the tracers match the profile computed on the grid better, if additional correction terms are used. In Fig.

2.8, we show the absolute and relative difference between the ENZO-profile and the profiles computed with *CIC + gradP* and *CIC + w_27*. The error of the *CIC + w_27* run is on average lower than of the *CIC + gradP* run. Especially in the denser regions, e.g. the cluster centres, it matches the ENZO-profile in a more accurate way. To present the full capabilities of the *CIC + w_27* method, we plot the radial density profiles of all the high-resolution cluster used in this thesis in Fig. 2.9.

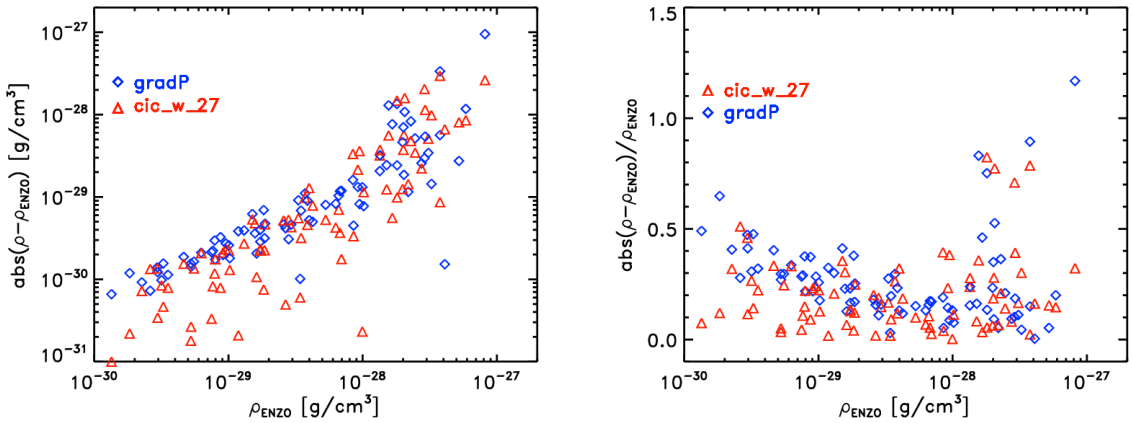

Figure 2.8: Panel (a) shows the absolute difference between the ENZO-profiles and the CRaTer-profiles in the cosmological simulation computed with the *CIC + w_27*- (red) and *cic + gradP*-method (blue). Panel (b) shows the absolute differences normalized to the ENZO-profiles.

2.2.3 Following Cosmic Rays

In this thesis, we used the tracers as a tool to follow the injection of cosmic rays by shocks and their advection. Following the physics described in Sec. 1.3.1, the tracers have to be able to detect shocks. The shock detector of the tracers is similar to the temperature jump method described in Ryu et al. (2003). Contrary to shock detectors on top of grids, the tracer particles in our procedure can only access the field values of the cells they inhabit at a given timestep and not of the cells around them. We therefore devised a recipe to detect shocks through the evolution of the field values at the tracers location. They are shocked if between two consecutive timesteps, see Fig. 2.10, the following requirements for the temperature T, entropy S and velocity v are matched:

- $T_{\rm old} > 100$ K
- $\frac{T_{\rm new}}{T_{\rm old}} > 1.00001$
- $\frac{S_{\rm new}}{S_{\rm old}} > 0$
- $\nabla \cdot \boldsymbol{v}_{\rm new} < 0$.

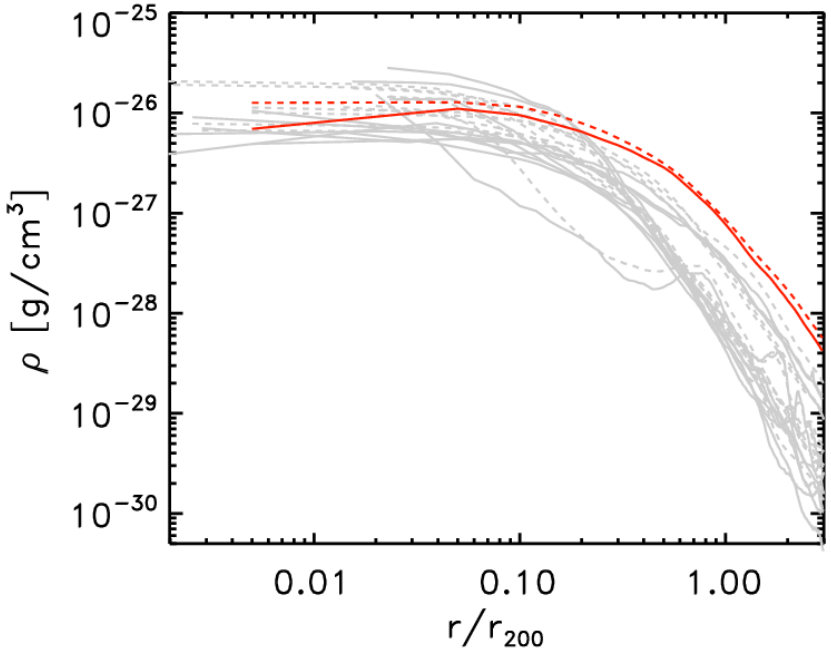

Figure 2.9: Radial density profiles of all the clusters used in the chapters below at $z \approx 0$. The solid lines show the results of the Eulerian, unweighted grid average and the dashed lines show the Lagrangian tracer particle-weighted average. The red lines give the average over all clusters.

If a shock is detected, the Rankine-Hugoniot relations are used to compute the Mach number, assuming $\gamma = 5/3$, as

$$M = \sqrt{\frac{4}{5}\frac{T_{\rm new}}{T_{\rm old}}\frac{\rho_{\rm new}}{\rho_{\rm old}} + 1}. \tag{2.8}$$

The kinetic energy flux across each shock is computed using the pre-shock density $\rho_{\rm pre}$ and shock velocity $v_{\rm sh} = M \cdot \sqrt{\gamma \cdot T_{\rm post} \cdot k_B/(\mu \cdot m_{\rm p})}$ as

$$F_\Psi = 0.5 \cdot \rho_{\rm pre} v_{\rm sh}^3. \tag{2.9}$$

In the equation above, the shock velocity is computed using the Mach number M, the adiabatic index γ, the post-shock temperature $T_{\rm post}$, the Boltzmann-constant k_B, the mean molecular weight μ and the proton mass $m_{\rm p}$. Part of this flux will heat the surrounding gas or inject cosmic rays. The thermal and cosmic-ray energy fluxes are computed using the acceleration efficiencies $\delta\,(M)$ and $\eta\,(M)$:

$$F_{\rm th} = \delta(M) F_\psi \tag{2.10}$$

$$F_{\rm CR} = \eta(M) F_\psi. \tag{2.11}$$

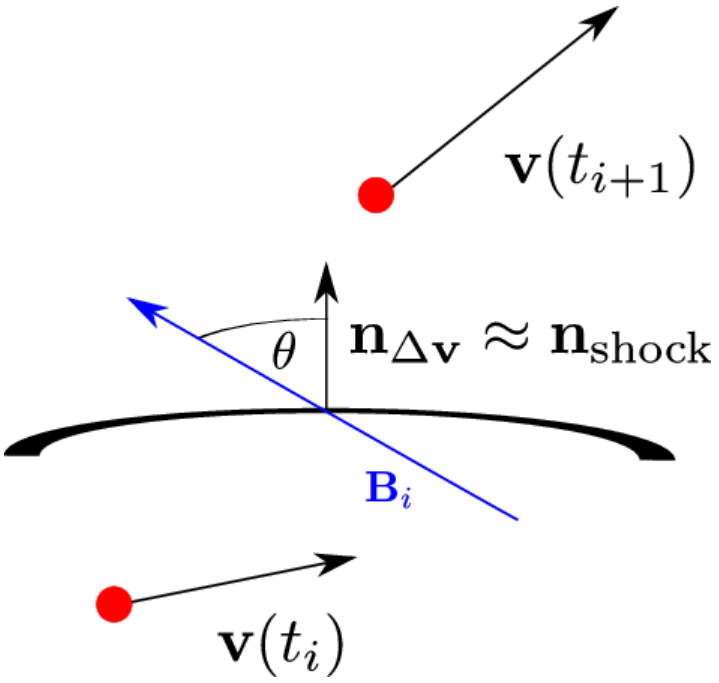

Figure 2.10: Schematic sketch of a tracer being shock in time and how the corresponding shock obliquity is computed.

The acceleration efficiency $\eta\,(M)$ also includes the effect of re-acceleration, in case the shock runs over a region which was previously enriched by cosmic rays. Following Vazza et al. (2014b), we compute the effective acceleration efficiency by interpolating the acceleration efficiencies of the single injection $\eta_{\mathrm{acc}}(M)$ and of the re-acceleration $\eta_{\mathrm{re}}(M)$ case:

$$\eta(M) = \frac{(0.05 - E_{\mathrm{CR}}/E_{\mathrm{gas}}) \cdot \eta_{\mathrm{acc}}(M) + E_{\mathrm{CR}}/E_{\mathrm{gas}} \cdot \eta_{\mathrm{re}}(M)}{0.05}. \tag{2.12}$$

If not stated otherwise, the acceleration efficiencies $\delta(M)$, $\eta_{\mathrm{acc}}(M)$, $\eta_{\mathrm{re}}(M)$ used in this work have been taken from Kang & Ryu (2013), see Fig. 2.11. They are increasing functions of M that saturate for large values of $M \sim 10$. $\eta_{\mathrm{acc}}(M)$ and $\eta_{\mathrm{re}}(M)$ have maximum values of ~ 0.2, while $\delta(M)$ saturates to $\sim 0.4 - 0.5$. The total cosmic-ray energy gained by one tracer is obtained by integrating the cosmic-ray energy flux over time:

$$E_{\mathrm{CR,i}} = \int_{z=1}^{z=0} F_{\mathrm{CR}} \Delta t \mathrm{d}z. \tag{2.13}$$

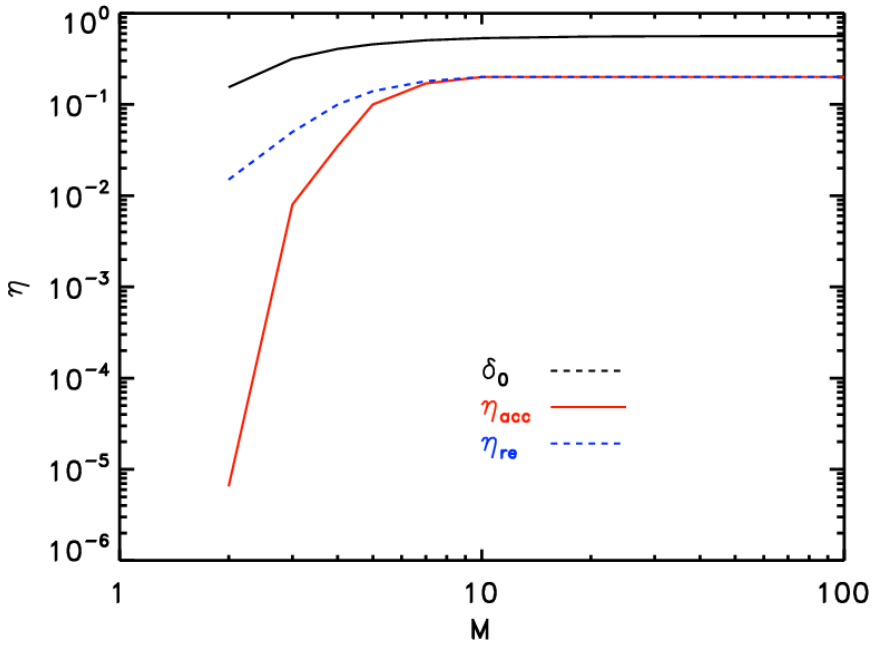

Figure 2.11: The efficiencies for gas heating (black, solid) and the acceleration (red, solid) and re-acceleration (blue, dashed) of cosmic rays depending on the Mach number extracted from Kang & Ryu (2013).

2.2.4 Parallelization with `openMP`

The large number of tracers being processed by `CRaTer` makes a serial advection computationally expensive. At a first step we used `openMP` for the parallelization because the `MPI` implementation is not straightforward due to the inhomogeneous distribution of tracers on the grid.

`openMP` splits the different tasks among a given number of threads that execute the tasks in parallel. For the tracer application, we spread the number of tracers evenly among the different threads. New tracers, that are injected at runtime, are also divided among the different threads equally.

The colours in Fig. 2.1 show the parts of the code that are fully and semi-parallelized. The green region is semi-parallelized meaning that the different tasks such as reading the different `ENZO` fields or computing the grid quantities are executed by one thread only. The first thread to reach this task is the thread to execute it. The blue region is fully parallelized. Here the each thread is computing the advection and quantities on top of the tracers that have been assigned to it. At the barriers, marked by the red *waits*, the threads have to wait for the other threads to finish their tasks. This assures that the grid data of the current timestep is used by all threads.

In order to test the obtained speed-up, we advected $\sim 1.3 \cdot 10^6$ tracers in the central 64^3

region of a high resolution cluster using different number of threads: 1, 2, 4, 8, 16, 32, 48. The tests have been performed on the Intel Xeon E5-2680 v3 Haswell CPUs on the JURECA supercomputer in Jülich. In Fig. 2.12(a), we plot the computing times needed by each part of the code. The single thread run (red line) needs for most parts of the simulations the most amount of time, whereas the 48 thread run is mostly the fastest. Yet, the parallelization reaches convergence with 32 threads already, as the I/O requires more time when 48 threads are used. The absolute speed-up obtained compared the single thread run is plotted in Fig. 2.12(b). A maximum speed up of $\times 12 - 13$ is reached using 32 threads. `CRaTer` has also been successfully exported to other supercomputers all around the world such as Hummel in Hamburg[7], HLRN in Berlin and Göttingen[8] as well as ITASCA in Minneapolis[9].

[7] `https://www.rrz.uni-hamburg.de/services/hpc/hummel-2015.html`
[8] `https://www.hlrn.de/home/view`
[9] `https://www.msi.umn.edu/`

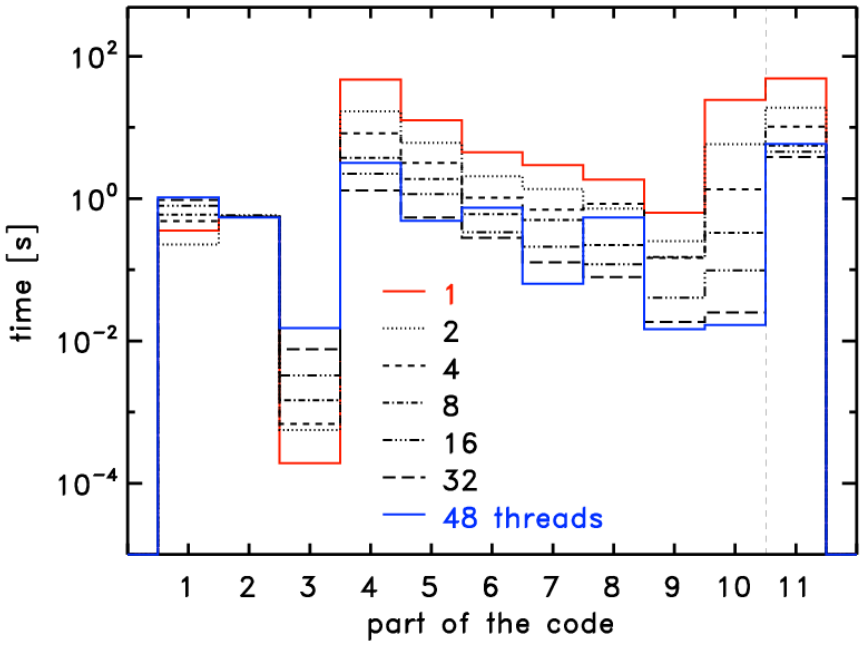

(a)

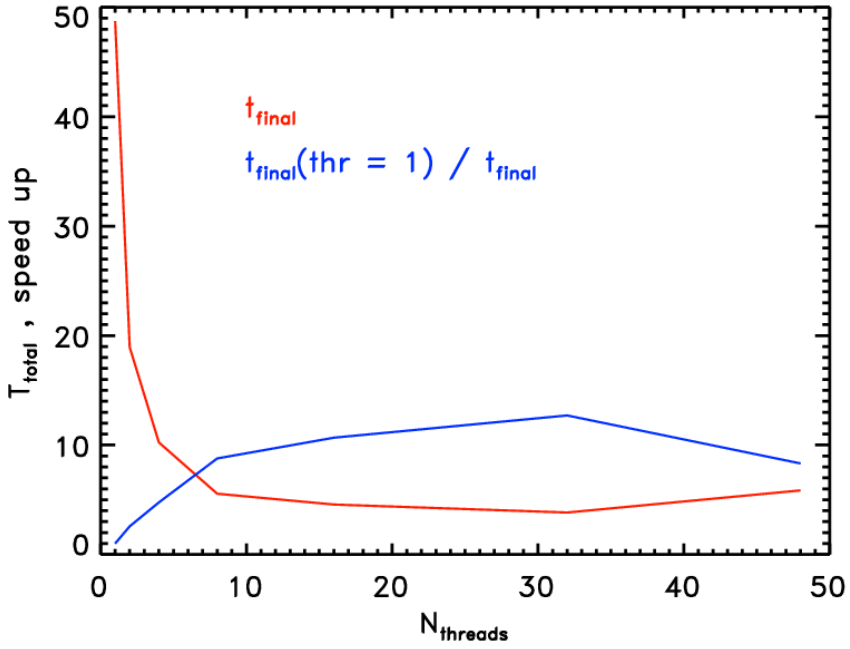

(b)

Figure 2.12: Panel (a) shows the computing times for the different parts of the code: (1) initialization of the run, (2) checking the boundaries for additional tracers, (3) computing the timestep, (4) total time of advecting the tracers in the loop, (5) assigning density and temperature to the tracers, (6) writing the tracer properties to file, (7) assigning the velocities to the tracers, (8) writing the tracers position to file, (9) advecting the tracers, (10) removing tracers that went out of bounce and (11) total time of the simulation. The blue line shows the run using 1 thread and the red line show the run using 48 threads. The dashed lines show the intermediate number of threads runs. Panel (b) shows the total time in arbitrary units needed by each run (red) and the corresponding speed-up compared to the single thread run (blue).

3 The Role of Shock Obliquity in the Acceleration of Cosmic Rays.

The following chapter presents work as it is published in Wittor, Vazza, & Brüggen in MNRAS 2017b, Sec. 3.1, and Wittor, Vazza, & Brüggen in Galaxies 2016, Sec. 3.2. In Sec. 3.3, we present additional material to complete the chapter. While the both works focus on the role of shock obliquity on the cosmic-ray acceleration in galaxy clusters, the first work presents a broader overview. The second work focuses specifically on obliquity properties for different Mach number, which was not explored in the first work. This contribution followed from a talk given by the the first author at the *European Week of Astronomy and Space Science* 2016 in the session *S6: Exploring the outskirts of galaxy clusters.*

3.1 Testing Cosmic-Ray Acceleration with Radio Relics: a High-Resolution Study using MHD and Tracers

3.1.1 Introduction

Galaxy clusters grow through the continuous accretion of matter and by merging with other clusters. In the process, shock waves and turbulent motions in the intracluster medium (ICM) can (re)accelerate cosmic rays (see Brunetti & Jones, 2014, and references therein). Radio emission, observed as diffuse radio halos in the centre of clusters and as highly polarized radio relics at the cluster periphery, confirms the existence of cosmic-ray electrons (e.g. Ferrari et al., 2008). However, cosmic-ray protons that would produce γ-rays or secondary electrons as a product of inelastic collisions with thermal protons, appear to be accelerated less efficiently than expected (for example see Vazza & Brüggen, 2014; Vazza et al., 2015b). The *Large Area Telescope* on board of the *Fermi*-satellite (from here on *Fermi*-LAT, see Atwood et al., 2009, for a detailed description) has thoroughly searched for these γ-rays, yielding upper limits for the γ-ray flux above 500 MeV is in the range of $0.5 - 22.2 \cdot 10^{-10}$ ph cm^{-2} s^{-1} (Ackermann et al., 2014). Huber et al. (2013b) have analysed a collection of stacked *Fermi*-LAT count maps and derived a flux upper limit of the order of a few 10^{-10} ph cm^{-2} s^{-1}. Extended searches for γ-ray emission from the Coma cluster (see Ackermann et al., 2016) and the Virgo

cluster (see Ackermann et al., 2015) have been performed. The limits for the γ-ray flux above 100 MeV have been estimated to be $5.2{\cdot}10^{-9}$ ph cm^{-2} s^{-1} for Coma and $1.2{\cdot}10^{-8}$ ph cm^{-2} s^{-1} for Virgo. Overall, these observations constrain the ratio of cosmic-ray to thermal pressure within the virial radius to be below a few percent.

Recently, Particle-in-Cell (PIC) simulations have quantified how the acceleration efficiency varies with the Mach number and the obliquity, θ, i.e. the angle between shock normal and upstream magnetic field vector (Caprioli & Spitkovsky 2014a; Guo et al. 2014a,b). These studies have shown that cosmic-ray electrons have a higher acceleration efficiency in perpendicular shocks, while the acceleration of cosmic-ray protons is more efficient in parallel shocks (i.e $\theta < 50$, see Fig 3. in Caprioli & Spitkovsky 2014a). Protons are efficiently accelerated by diffusive shock acceleration (DSA) by crossing the shock multiple times where they are scattered off magneto-hydrodynamic waves in the up- and downstream region. Thermal electrons cannot be injected into DSA because their gyro-radius is too small compared to the thickness of the shock front, which is controlled by the gyro-radius of the protons. Therefore, electrons need to be pre-accelerated before they can be injected into the DSA cycle. Recent PIC simulations have shown that even in the case of the weak shocks typically found in galaxy clusters ($M < 5$, where M is the Mach number), electrons can be efficiently pre-accelerated by shock drift acceleration (SDA). In SDA electrons gain energy while drifting along magnetic field lines down the shock front (Guo et al. 2014a,b).

In this paper, we investigate how linking the obliquity of shocks to the acceleration efficiency of cosmic rays may affect the radio and γ-ray emission in galaxy clusters. To this end, we developed a Lagrangian tracer code to track the injection and advection of cosmic rays in the cosmological simulations produced using the `ENZO` code.

This paper is structured as follows. In Sec. 3.1.2 we describe our computational setup in `ENZO`. In Sec. 3.1.2 we introduce our Lagrangian tracer code. Our main results are presented in Sec. 3.1.3. First, we discuss the basic properties of our Lagrangian tracers in Sec. 3.1.3. General results on the distribution of shock obliquities are presented in Sec. 3.1.3. In Sec. 3.1.3 and 3.1.3 we show how the radio and the γ-ray emission are changed by the modified acceleration efficiencies. A more detailed analysis of the simulated relics is presented in Sec. 3.1.3. Finally, we summarize and discuss our results in Sec. 3.1.4. Additional tests on our tracers and on a lower mass cluster are given in the Appendix.

3.1.2 Simulation Setup

ENZO

We simulated the formation of galaxy clusters with the cosmological magneto-hydrodynamical (MHD) code `ENZO` (Bryan et al., 2014). `ENZO` uses a N-body particle-mesh solver to simulate the dark matter (Hockney & Eastwood, 1988), and an adaptive mesh method to follow the baryonic matter (Berger & Colella, 1989).
In our simulations we used a piecewise linear method (Colella & Glaz, 1985) with hyperbolic Dedner cleaning (Dedner et al., 2002) to solve the MHD equations (see Sec. 2.1 in Bryan et al., 2014).
We focus on the re-simulation of a single galaxy cluster extracted from a cosmological volume. This cluster has a final mass of $M_{200} \approx 9.745 \cdot 10^{14}\ M_{\odot}$ at $z = 0$ and it has been chosen for this study because it shows a major merger event at $z \approx 0.27$, leading to detectable radio relics (see Sec. 3.1.3).
The simulation starts from a root grid of volume $\approx (250\ \mathrm{Mpc})^3$ (comoving) sampled with 256^3 cells and 256^3 dark matter particles. The comoving volume of $\approx (25\ \mathrm{Mpc})^3$ centred around the most massive cluster in the box has been further refined 2^5 times using 5 levels of AMR (up to a maximum resolution of 31.7 kpc). In order to resolve the turbulent evolution of the intracluster magnetic field, we adopted the aggressive AMR criterion of refining all cells that are $\geq 10\%$ denser than their surrounding, beginning at the start of the simulation. From $z = 1$, we additionally refined all cells with a 1-dimensional velocity jump $\Delta v/v \geq 1.5$, where Δv is the velocity jump along any coordinate axis and v is the local velocity. This procedure ensures that typically $\sim 80\%$ of the cluster volume is refined up to the highest resolution, and that the virial volume is sampled with $\geq 200^3$ cells. For the post-processing with our tracer algorithm (see Sec. 3.1.2) we saved all snapshots of the root grid timestep, for a total of 250 snapshots. As in our previous work in Vazza et al. (2010a), we chose the cosmological parameters as: $H_0 = 72.0$ km s^{-1} Mpc^{-1}, $\Omega_{\mathrm{M}} = 0.258$, $\Omega_{\Lambda} = 0.742$ and $\sigma_8 = 0.8$. We seeded the large-scale magnetic field with a uniform primordial seed field at $z = 30$, with a comoving value of $B_0 = 10^{-10}$ G along each coordinate axis.

Lagrangian Tracer

We tracked the evolution of cosmic rays using Lagrangian tracer particles. These allow us, both, to accurately follow the advection of baryonic matter and to monitor the enrichment of shock-injected cosmic rays over time. The tracers are generated in post-processing, using the `ENZO` data at the highest spatial resolution (in the case in which the cell value is only available at lower resolution due to the AMR structure, they are linearly interpolated to the maximum resolution).

In the simplest case, the tracers are advected using the velocities at their location, $\boldsymbol{v} = \tilde{\boldsymbol{v}}$, which are interpolated between the neighbouring cells (e.g. Vazza et al., 2010b). However, in the case of complex flows this procedure might underestimate the amount of mixing due to fluid motions, and stochastic correction terms have been proposed to solve this problem (Genel et al., 2013). To cure for this effect we introduced a small correction term, which takes into account the small-scale velocity contribution from the neighbouring 27 cells, $\delta\boldsymbol{v}_{i,j,k}$:

$$\delta\boldsymbol{v}_{i,j,k} = \boldsymbol{v}_{i,j,k} - \frac{\sum_{i=0}^{2}\sum_{j=0}^{2}\sum_{k=0}^{2}\boldsymbol{v}_{i-1,j-1,k-1}}{27}. \tag{3.1}$$

This term is added to the interpolated velocity, $\boldsymbol{v} = \tilde{\boldsymbol{v}} + \delta\boldsymbol{v}$. This procedure (unlike stochastic approaches) ensures that the thermodynamical jumps recorded by the tracers are due to gas dynamics. Our tests showed that the final distribution of tracers is not very sensitive to small variations (e.g. different interpolation schemes) in the advection procedure. After computing their velocity, the tracers are advected linearly in time. During the advection, the local values of the gas on the `ENZO` grid are assigned to each tracer, and other properties (e.g. Mach number, obliquity etc.) are computed on the fly. The solenoidal and compressive modes of the velocity components for a tracer are computed using numerical stencils $\mathrm{d}v_{(x,y,z)}$ as

$$v_{\mathrm{sol}} = \frac{\sqrt{(\mathrm{d}v_z - \mathrm{d}v_y)^2 + (\mathrm{d}v_x - \mathrm{d}v_z)^2 + (\mathrm{d}v_y - \mathrm{d}v_x)^2}}{2}, \tag{3.2}$$

$$v_{\mathrm{comp}} = \frac{\mathrm{d}v_x}{2} + \frac{\mathrm{d}v_y}{2} + \frac{\mathrm{d}v_z}{2}. \tag{3.3}$$

Subsequently, we apply a shock finding method based on temperature jumps as described in Ryu et al. (2003). However, instead of using the shock finder between two neighbouring grid cells, we applied it to the positions of a tracer at two consecutive timesteps. A tracer is considered to be shocked if the following requirements are matched:

- $T_{\mathrm{old}} > 100$ K
- $\frac{T_{\mathrm{new}}}{T_{\mathrm{old}}} > 1.00001$
- $\frac{S_{\mathrm{new}}}{S_{\mathrm{old}}} > 0$
- $\nabla \cdot \boldsymbol{v} < 0$.

The Mach number is computed from the Rankine-Hugoniot relations, assuming $\gamma = 5/3$, as

$$M = \sqrt{\frac{4}{5}\frac{T_{\mathrm{new}}}{T_{\mathrm{old}}}\frac{\rho_{\mathrm{new}}}{\rho_{\mathrm{old}}} + 1}. \tag{3.4}$$

Every time a shock is recorded, the obliquity is computed as the angle between the velocity jump $\Delta \boldsymbol{v} = \boldsymbol{v}_{\rm post} - \boldsymbol{v}_{\rm pre}$ and the pre-/post-shock magnetic field $\boldsymbol{B}_i$:

$$\theta_i = \arccos\left(\frac{\Delta \boldsymbol{v} \cdot \boldsymbol{B_i}}{|\Delta \boldsymbol{v}||\boldsymbol{B_i}|}\right). \tag{3.5}$$

The index, i, refers to either the pre- or post-shock quantity.
The kinetic energy flux across shocks is $F_\Psi = 0.5 \cdot \rho_{\rm pre} v_{\rm sh}^3$, where $\rho_{\rm pre}$ is the pre-shock density and $v_{\rm sh}$ is the shock velocity. Using the acceleration efficiencies $\delta\,(M)$ and $\eta\,(M)$ given in Kang & Ryu (2013), the thermal energy flux is $F_{\rm th} = \delta(M) F_\psi$ and the cosmic-ray energy flux is $F_{\rm CR} = \eta(M) F_\psi$. The acceleration efficiency $\eta\,(M)$ also includes the effect of re-acceleration, in case the shock runs over a region which was previously enriched of cosmic rays. Following Vazza et al. (2014b), we compute the effective acceleration efficiency by interpolating the acceleration efficiencies of the single injection $\eta_{\rm acc}(M)$ and of the re-acceleration $\eta_{\rm re}(M)$ case (given in Kang & Ryu 2013):

$$\eta(M) = \frac{(0.05 - \chi) \cdot \eta_{\rm acc}(M) + \chi \cdot \eta_{\rm re}(M)}{0.05}, \tag{3.6}$$

using the ratio of cosmic-ray to gas energy $\chi = E_{\rm CR}/E_{\rm gas}$.
In order to maximise the number of tracers within the cluster, we injected tracers only in a 256^3 sub-box of the ENZO-simulation, centred on the mass centre of our galaxy cluster at $z \approx 0$. The bulk of the cosmic-ray energy is expected to be generated by shocks at low redshifts (e.g. Vazza et al., 2016a), and therefore we start generating the tracers at $z \approx 1$.
In detail, the tracers were first initialised based on the gas mass distribution on the grid at $z \approx 1$. We assigned a fixed mass to each tracer and we set the number of tracers per cell according to:

$$n_{\rm tracers} = \left\lfloor \frac{m_{\rm cell}}{m_{\rm tracers}} \right\rfloor, \tag{3.7}$$

where $m_{\rm cell}$ is the comoving gas mass within each high-resolution cell. The mass resolution of the tracers has to be high enough to ensure that the structure of the cluster is resolved accurately while it can still be handled computationally. In our case the trade-off is represented by a mass resolution of $m_{\rm tracer}(z = 1) \approx 10^8\ M_\odot$.
Moreover, at each snapshot additional tracers were injected at the boundaries according to Eq. (3.7). In total, we used 240 snapshots from $z = 1$ to $z = 0$ and our procedure generated $N_p \approx 1.33 \cdot 10^7$ tracers during run-time. The final spatial distribution of tracers at $z \approx 0$ and their radial profile (compared to the gas profile directly simulated by ENZO) are shown in Appendix 3.1.A.
In order to speed up the computations and follow the largest possible number of tracers, we parallelized our advection routines using *openMP*. Both, the tracers injected at $z = 1$ and

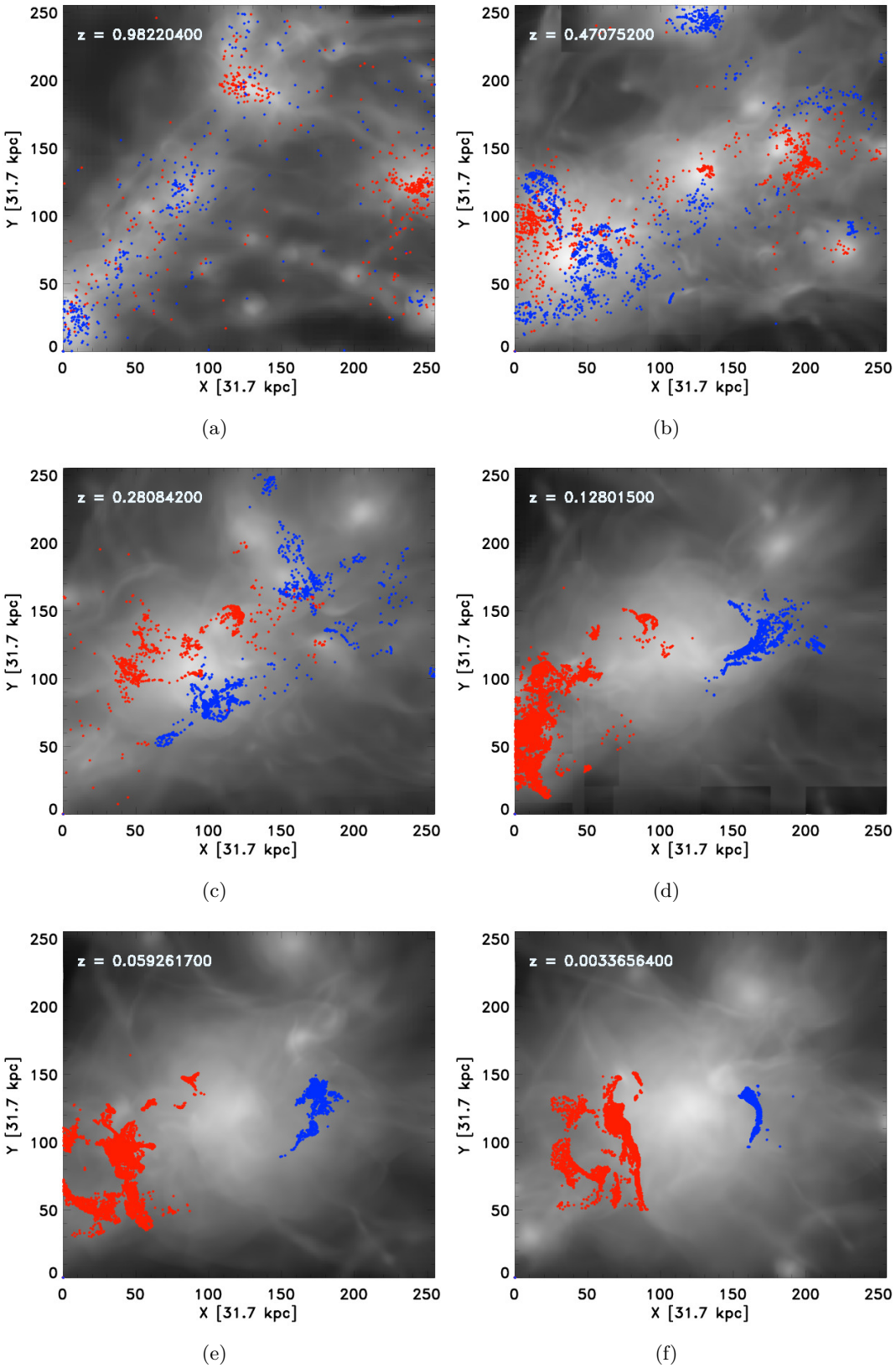

(a) (b)

(c) (d)

(e) (f)

Figure 3.1: Evolution of the projected baryonic matter density (in grey) overlayed with the projected positions of the tracers. Only the tracers ending up in the two relics (see Sec. 3.1.3) are shown and are divided into two colours based on their final position.

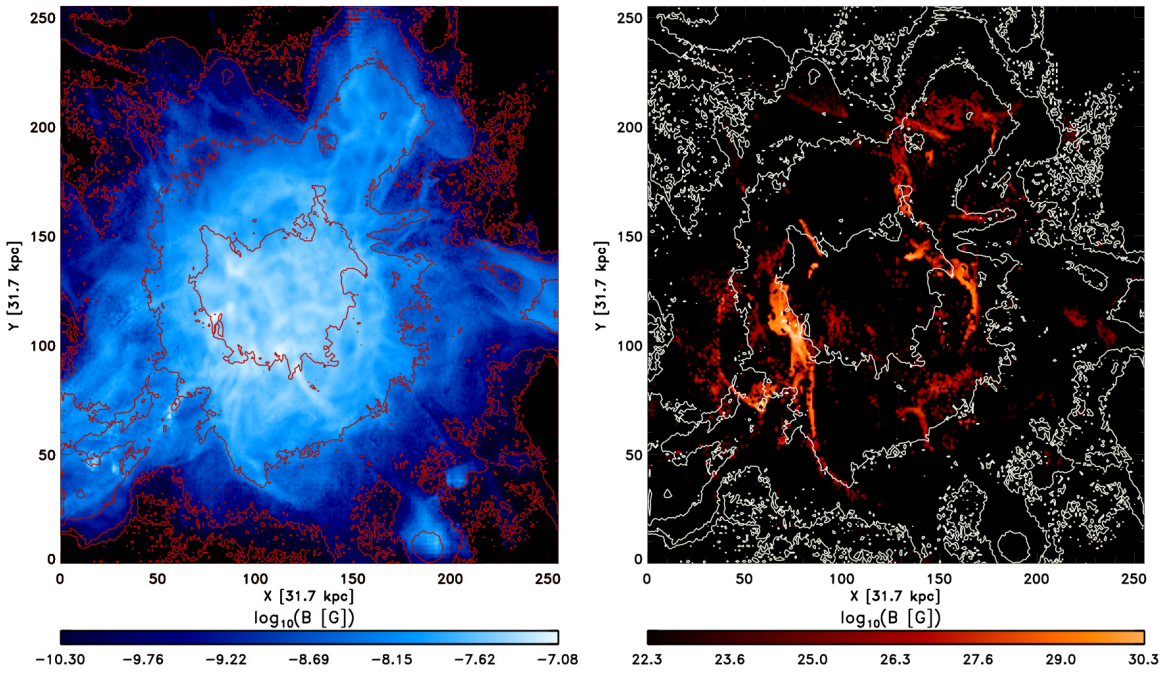

Figure 3.2: Panel (a) shows the projected mass weighted magnetic field strength (colour) overlayed with the corresponding density contours (red contours) at $z \approx 0$. Panel (b) shows the projected radio emission (colour) and the corresponding density contours (white contours) at $z \approx 0$. Both plots have been produced from the tracer data. The outer regions are noisy owing to the lack of tracers in those areas (see also Appendix 3.1.A).

those generated at run-time are evenly spread among the threads, thus balancing the workload.

This simulation used 48 threads minimizing the computational time to 6 hours for the Lagrangian tracer run[1], running on the Intel Xeon E5-2680 v3 Haswell CPUs on the JURECA supercomputer in Jülich.

3.1.3 Results

Thermal and Magnetic Properties

As an example for the application of our tracer-based approach, we show in Fig. 3.1 the trajectories of tracers found in the proximity of the two powerful radio relics (see Sec. 3.1.3). The tracers ending up in the two relics at $z \approx 0$ are, both, coming from the first injection at $z = 1$, as well from the injections at lower redshift. They follow the gas, mostly coming from

[1]Compared to ~ 60 hours in the serial version. We obtain a non-perfect scaling of the speed-up because the bottle neck is the output of the tracer data. Further speed-up could be obtained using parallel I/O.

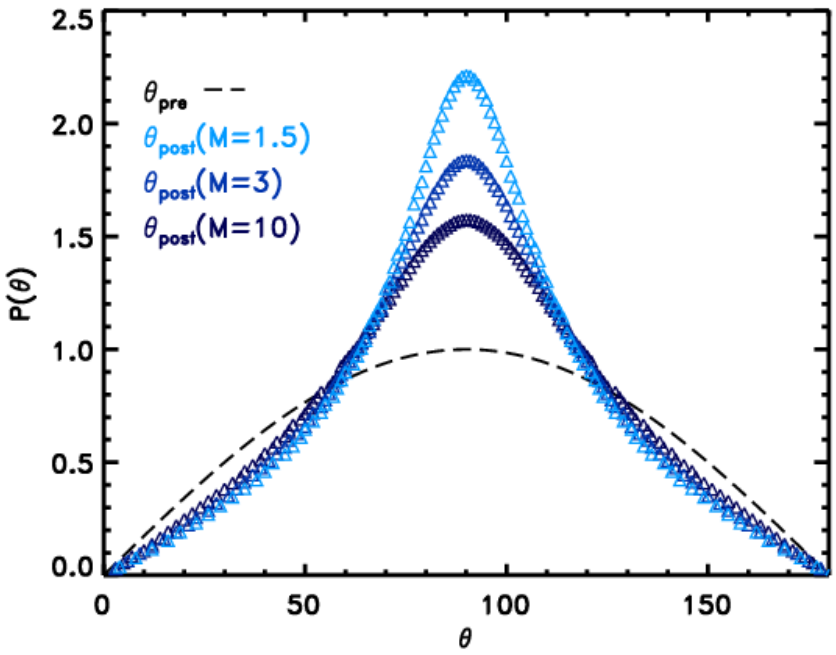

Figure 3.3: Expected distribution of random angles in a three-dimensional space (dashed black line). If a shock of a given Mach number M crosses this distribution of angles the distribution is more concentrated towards $\theta = 90°$ according to Eq. (3.15). The blue curves show these post-shock distributions for $M = 1.5$, $M = 3$ and $M = 10$.

filamentary and clumpy accretion that is heated by shock waves moving outwards after the major merger at $z \approx 0.27$.

In Fig. 3.2(a), we show the projected magnetic fields (mass-weighted along the line of sight) and the contours of the projected gas density probed by the tracers. The magnetic field strengths range from $\sim 1.2 \cdot 10^{-7}$ G in the cluster centre to $\sim 1.9 \cdot 10^{-10}$ G in the cluster outskirts. While the average magnetic field strength within the virial volume is of the order of what is confirmed by observations $\sim 0.1 - 0.2$ μG, the innermost field is significantly lower (e.g. compared to the central 4.7 μG value inferred for the Coma cluster by Bonafede et al., 2010). This is presumed to be caused by insufficient resolution to reproduce the small-scale dynamo, a common problem in MHD simulations (e.g. Vazza et al., 2014a). However, the magnetic field values at the relic locations, of the order of ~ 0.1 μG, are plausible values for peripheral relics (e.g. Hoeft & Brüggen, 2007).

Shock Obliquity

Before assessing the effect of shock obliquity on the acceleration of cosmic rays, we first study the distribution of shock obliquity across the simulated cluster volume. To interpret the re-

sults, it is useful to start by deriving an analytical relation between the shock Mach number and the change in the obliquity across shocks.

As long as the upstream magnetic fields are isotropic, the expected distribution of angles between the shock normal and the upstream magnetic fields follows the geometrical distribution of angles between two random vectors in a 3D space, that is $\propto \sin(\theta)$, as shown by the black dashed line in Fig. 3.3 (see Kaplan, 2009).

Following Fitzpatrick (2014), it is convenient to define a shock frame, where the shock lies in the z-plane and the shock normal is perpendicular to the x-direction and parallel to the y-direction and we transform into the de Hoffmann-Teller frame ($|\boldsymbol{v}_{\rm pre} \times \boldsymbol{B}_{\rm pre}| = 0$). This leads to the general MHD-jump conditions in the form

$$\frac{\rho_2}{\rho_1} = r \tag{3.8}$$

$$\frac{B_{x,\rm post}}{B_{x,\rm pre}} = 1 \tag{3.9}$$

$$\frac{B_{y,\rm post}}{B_{y,\rm pre}} = r\left(\frac{v_{x,\rm pre}^2 - \cos^2\theta_{\rm pre} v_{A,\rm pre}^2}{v_{x,\rm pre}^2 - r\cos^2\theta_{\rm pre} v_{A,\rm pre}^2}\right) \tag{3.10}$$

$$\frac{v_{x,\rm post}}{v_{x,\rm pre}} = r^{-1} \tag{3.11}$$

$$\frac{v_{y,\rm post}}{v_{y,\rm pre}} = \frac{v_{x,\rm pre}^2 - \cos^2\theta_{\rm pre} v_{A,\rm pre}^2}{v_{x,\rm pre}^2 - r\cos^2\theta_{\rm pre} v_{A,\rm pre}^2}. \tag{3.12}$$

The above equations can be further simplified in our case because the pre-shock Alfvén velocity, $v_{A,\rm pre}$, can be safely neglected in comparison to the upstream gas velocity $v_{\rm gas}$. Indeed, we verified that for the entire cluster volume the distribution of $v_{A,\rm pre}/v_{\rm gas}$ is well described by a log-normal distribution centred on $v_{A,\rm pre}/v_{\rm gas} \approx 0.01$, and extending to beyond 1 only in $\sim 10^{-5}$ of cases. Therefore, owing to the low magnetisation of the ICM we can treat our shocks in the (simpler) hydrodynamical regime, in which case the above Eq. 3.10 and 3.12 reduce to $\frac{B_{y2}}{B_{y1}} = r$ and $\frac{v_{y2}}{v_{y1}} = 1$. Using these jump conditions, we derive $\theta(M)$ from

$$\cos\left(\theta_{\rm post}\right) = \frac{\Delta\boldsymbol{v}\cdot\boldsymbol{B}}{|\Delta\boldsymbol{v}|\,|\boldsymbol{B}|} \tag{3.13}$$

as

$$\theta_{\rm post}\left(M\right) = \arccos\left[\frac{B_{x1}}{\sqrt{B_{x1}^2 + r^2 B_{y1}^2}}\right]. \tag{3.14}$$

In Eq. (3.14), $\theta_{\rm post}(M)$ only depends on the pre-shock values. B_{x1} and B_{y1} are connected via $\theta_{\rm pre}$ as $B_{y1} = B_{x1}\cdot\tan\left(\theta_{\rm pre}\right)$. Therefore, the change of a pre-shock obliquity only depends on

the angle itself and the compression ration r as

$$\theta_{\rm post}\left(M\right) = \arccos\left[\frac{1}{\sqrt{1 + r^2 \tan\left(\theta_{\rm pre}\right)^2}}\right]. \tag{3.15}$$

For any Mach number the distribution is compressed towards 90°, and the compression is stronger for stronger shocks. In Fig. 3.3, we show how the distribution of obliquity changes, once it is passed by a shock. Overall the distribution of pre- and post-shock obliquities in the cluster is strongly linked to the dynamical history of the cluster itself as the pre-shock distribution at later timesteps is a result of the post-shock distribution at earlier timesteps.
We computed the distribution of the pre- and post-shock obliquities in our simulation at $z \approx 0.12$ (see red and blue line Fig. 3.4(a)). Overall their shapes match the distribution of random angles in 3D well (black line in Fig. 3.4(a)). The differences to the distribution of random angles is plotted in Fig. 3.4(b). We chose $\theta = 50°$ as the threshold angle to mark the division between quasi-parallel and quasi-perpendicular shocks. This choice is based on Fig. 3 of Caprioli & Spitkovsky (2014a) as the acceleration efficiency of protons drops significantly beyond this for $M \leq 10$ shocks. In both distributions we observe more quasi-perpendicular shocks and less quasi-parallel shocks than expected. For the post-shock distribution this is expected according to Eq. (3.15). We find that also the pre-shock distribution shows a departure from isotropy, caused by shock compression at the previous epochs. Although turbulent motions in the ICM are expected to distribute angles randomly, the rather continuous crossing by shocks tends to concentrate the angles toward quasi-perpendicular geometry. This makes the pre-shock distribution at all epochs already slightly more concentrated towards perpendicular angles, than expected from isotropy.
This is confirmed by the distribution of pre-shock angles at different redshifts: in Fig. 3.4(c) we show their differences to the isotropic distribution. Independent of redshift, we observe more quasi-perpendicular shocks than quasi-parallel shocks. Moreover, the distribution tends to concentrate slowly towards $\sim 90°$ as a function of time but the effect is very small and by and large the angles are distributed isotropically.
Finally, at $z = 0$ we we divided the box into five spherical, concentric, equidistant shells and computed the pre-shock distributions for each shell separately. The differences to the predicted distribution is shown in Fig. 3.4(d). All shells show patterns that are compatible with a random distribution of angles. The central region (blue line in Fig. 3.4(d)) is most turbulent and the magnetic fields are most isotropic. The distribution shows a larger excess of quasi-perpendicular shocks at larger radii (from light blue to red lines in Fig. 3.4(d)). Indeed, in cluster outskirts shocks are more frequent and stronger causing a stronger alignment of magnetic fields. In the following subsections we will show how this behaviour might have important consequences in the acceleration of cosmic rays by cluster shocks.

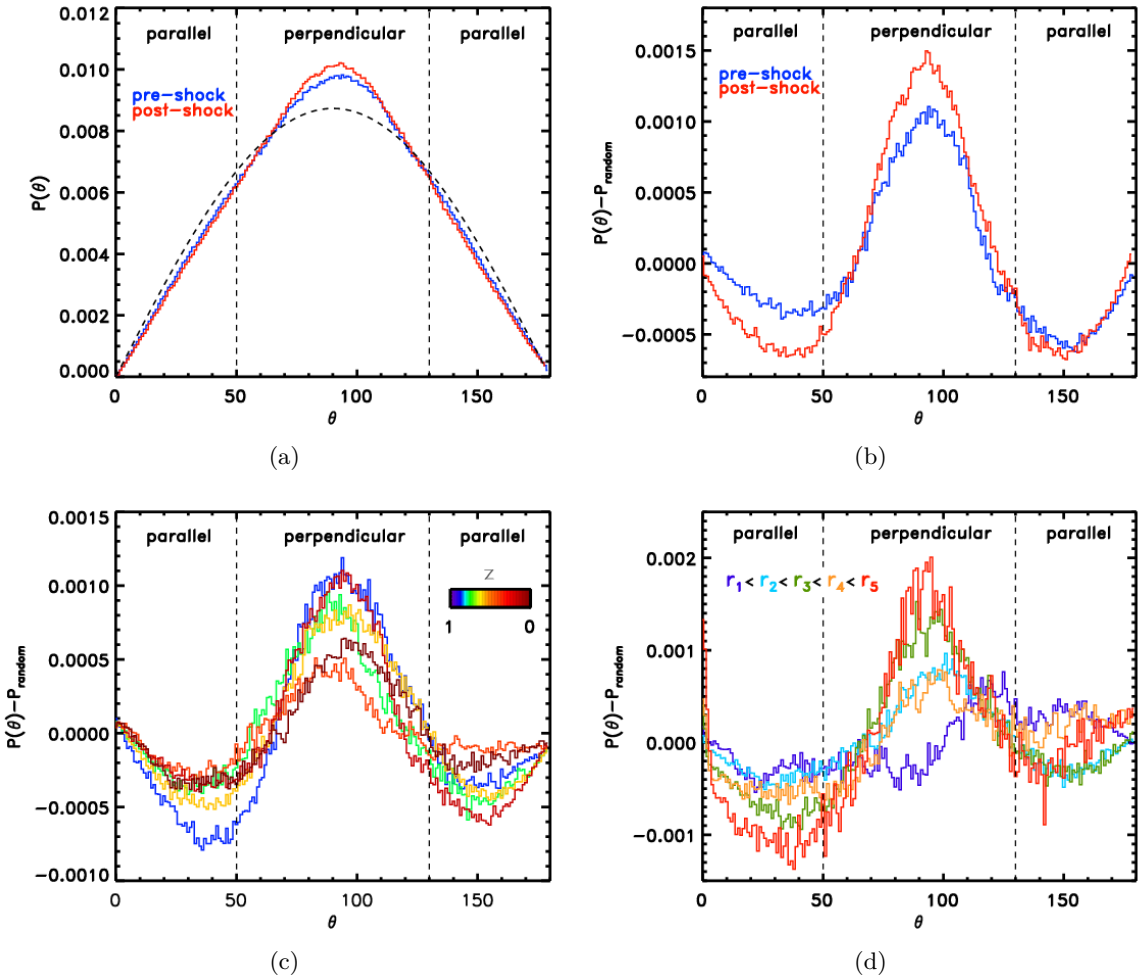

Figure 3.4: Distribution of pre- (blue) and post-shock (red) obliquities at redshift $z \approx 0.12$ are shown in panel (a). The dashed line shows the expected distribution of angles for a random distribution. Panel (b) shows the differences of the computed distributions from the expected distribution. It is observed that the post-shock distribution (red line) is more peaked towards $\theta = 90°$ than the pre-shock distribution (blue line). Panel (c) shows the differences between the distribution of pre-shock obliquities at different redshifts and the expected distribution. Panel (d) shows the differences between pre-shock obliquities for different radial selections at $z \approx 0$ and the expected distribution. The radius of each region is $\frac{1}{5}$-th of the simulation box size.

Cosmic-Ray Electrons & Radio Emission

The cluster studied in this paper has been chosen because it shows two prominent radio relics at $z \approx 0$. These radio relics are produced by shock waves launched by a major merger of three gas clumps and propagate along the horizontal direction in Fig. 3.1 and 3.2. We compute the radio emission on shocked tracers using the formula (from Hoeft & Brüggen, 2007)

$$\frac{\mathrm{d}P_{\mathrm{radio}}\left(\nu_{\mathrm{obs}}\right)}{\mathrm{d}\nu} = \frac{6.4 \cdot 10^{34}\ \mathrm{erg}}{\mathrm{s} \cdot \mathrm{Hz}} \frac{A}{\mathrm{Mpc}^2} \frac{n_e}{10^{-4}\ \mathrm{cm}^{-3}} \frac{\xi_e}{0.05} \left(\frac{T_d}{7\ \mathrm{keV}}\right)^{\frac{3}{2}} \times \left(\frac{\nu_{\mathrm{obs}}}{1.4\ \mathrm{GHz}}\right)^{-\frac{s}{2}} \frac{\left(\frac{B}{\mu\mathrm{G}}\right)^{1+\frac{s}{2}}}{\left(\frac{B_{\mathrm{CMB}}}{\mu\mathrm{G}}\right)^2 + \left(\frac{B}{\mu\mathrm{G}}\right)^2} \cdot \eta\left(M\right) \quad . \tag{3.16}$$

The quantities in the formula that either have been recorded from the grid or computed with the recorded values, are: A the surface area of a tracer[2], n_e the number density of electrons, T_d the downstream temperature, B the magnetic field strength and the acceleration efficiency $\eta\left(M\right)$ depending on the Mach number M. We used the acceleration efficiencies $\eta\left(M\right)$ derived in Kang & Ryu (2013). The other quantities are the electron-to-proton ratio, $\xi_e = 0.01$, the equivalent magnetic field of the cosmic microwave background, $B_{\mathrm{CMB}} = 3.2 \cdot (1+z)^2\ \mu$G and the observed frequency band, $\nu_{\mathrm{obs}} = 1.4$ GHz .

In Fig. 3.2(b), we show the observed radio emission at $z \approx 0$, overlayed with the corresponding density contours, which features two prominent radio relics at opposite sides of the cluster core. The alignment and morphologies of the two relics indicate that they have been produced by the major merger at $z \approx 0.27$, which happened along the horizontal axis in the image. We measure a Mach number $M \approx 3.5$ for the relic located west of the cluster centre (hereafter relic 1), and $M \approx 2.7$ for the relic located at the opposite side (hereafter relic 2). The total radio emission from the cluster is $P_{\mathrm{radio}} \approx 3.12 \cdot 10^{31}$ erg s^{-1} Hz^{-1}, while the emission from relic 1 is $P_{\mathrm{radio}} \approx 2.61 \cdot 10^{31}$ erg s^{-1} Hz^{-1} and from the relic 2 is $P_{\mathrm{radio}} \approx 2.27 \cdot 10^{30}$ erg s^{-1} Hz^{-1} (see Fig. 3.5). If the cluster is located at the luminosity distance of 100 Mpc, relic 1 is bright enough to be detectable at 1.4 GHz by both the JVLA (assuming the 0.45 mJy/beam sensitivity of the NVSS survey, Condon et al. 1998b) and by ASKAP (assuming a sensitivity of 0.01 mJy/beam as in the EMU survey, Norris et al. 2011). At the distance of 100 Mpc, relic 2 would be too faint for the JVLA, while it would be instead at the edge of detection with ASKAP.

Next, we used the obliquity θ to limit the injection of cosmic-ray electrons and study its observable effect on the relic emission. In the following we compare the radio emission including all shocked particles to the one produced by particles that have only crossed a quasi-

[2]The surface area is computed from the volume occupied by a tracer in a gridcell as: $A = \left(V_{\mathrm{cell}} \cdot \frac{m_{\mathrm{cell}}}{m_{\mathrm{tracer}}}\right)^{\frac{2}{3}}$. Here V_{cell} is the volume of the cell and m_{cell} is the total mass in that cell. m_{tracer} is the tracer mass.

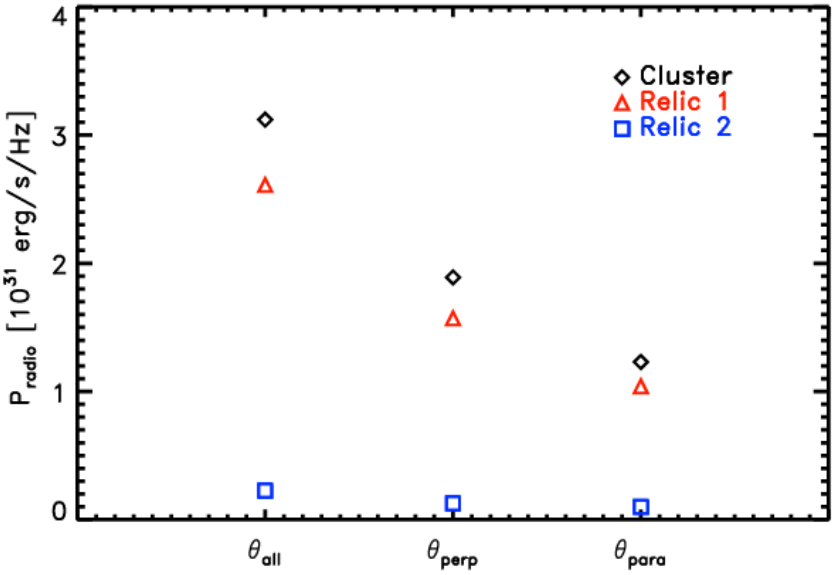

Figure 3.5: Total radio emission from our simulated cluster at $z \approx 0$, considering the total emission from the cluster (diamond) or the emission from relic one (triangle) or relic two (square), for different selections of the obliquity angle, θ.

perpendicular[3] or quasi-parallel[4] shock. In the following, the subscripts all, perp and para correspond to the cuts mentioned above.

From the total emission shown in Fig. 3.5, we can see that relic 1 is still observable even if only quasi-perpendicular shocks are allowed to accelerate the cosmic-ray electron, while relic 2 would remain undetectable. We give a close-up view onto the relic regions in Fig. 3.6, where we show the projected temperatures and the radio contours, with additional vectors of projected magnetic fields. The range of magnetic vectors is too large to allow a clear visualisation, and therefore all vectors have been renormalised to the same unit length while the magnetic intensity is shown through the color coding (with intensity increasing from light to dark blue). The radio emission produced by $\theta_{\rm all}$ (left column), $\theta_{\rm perp}$ (middle column) and $\theta_{\rm para}$ (right column) is given for relic 1 on the upper row, and fore relic 2 in the lower row. The emission does not dramatically decrease across most of the relic surface when either of the two obliquity cuts is performed. This is because in these regions the angles are distributed close to the random distribution (see Sec.3.1.3), and therefore the radio emitting volume in both scenarios is still of the same order of magnitude as in the case without obliquity selection. Based on this test, we conclude that it is possible that observed radio relics are indeed tracing cosmic-ray electrons only accelerated by quasi-perpendicular shocks (and hence, from the combination of SDA and DSA, Guo et al. 2014a). We performed the same analysis for a $2.8 \cdot 10^{14}$ $M_\odot$ cluster (see Appendix 3.1.B) and we found similar results.

[3] $\theta \in [50°, 130°]$
[4] $\theta \in [0°, 50°]$ or $\theta \in [130°, 180°]$

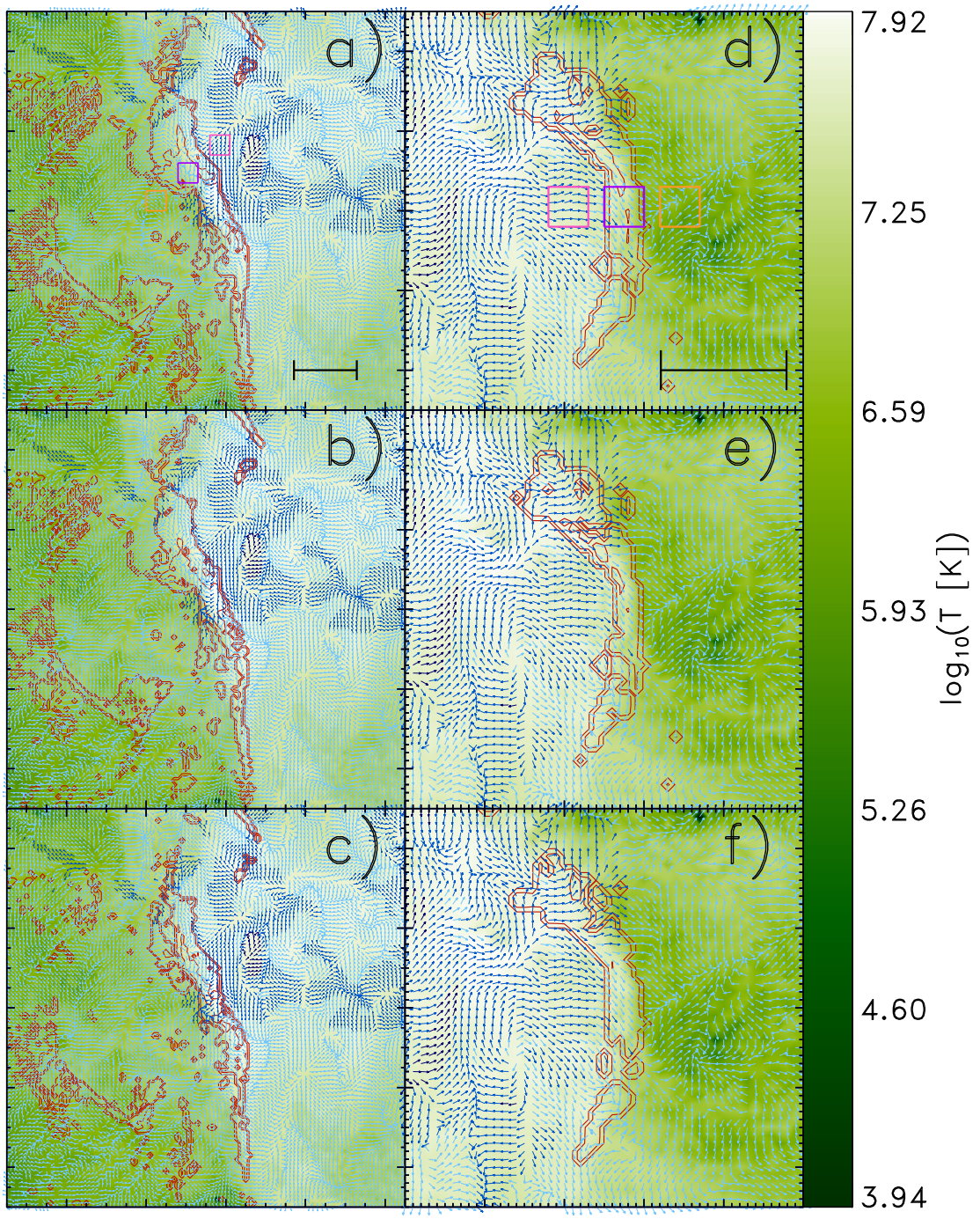

Figure 3.6: Zoomed versions of our simulated radio relics. The left column (Fig. (a), (b) and (c)) displays relic 1, while relic 2 is shown in the right column ((d), (e) and (f)). The green colours show the temperature of the ICM. The direction of the arrows indicates the direction of the magnetic field and their colour gives their magnetic field strength, with a logarithmical stretching, while the red contours show the radio emission. The top row shows $\theta_{\rm all}$. The middle row shows $\theta_{\rm perp}$ and the bottom row shows $\theta_{\rm para}$. The axis are in dx = 31.7 kpc units. The squares in Fig. (a) and (d) mark the regions of the tracers selected in Sec. 3.1.3. The colours orange, purple and pink mark the regions in front of, on top of and behind the relic respectively. The bars in Fig. (a) and (d) show the length of 500 kpc. We notice that the format of the plot has been changed from its original version (Wittor et al., 2017b) to match the layout of this thesis.

Cosmic-Ray Protons & γ-Rays

Next we test the time-integrated effects of imposing the same selection as above (see Sec. 3.1.3) in the obliquity of shocks accelerating cosmic-ray protons, following the results of Caprioli & Spitkovsky (2014a), who found an efficient acceleration of cosmic-ray protons only for quasi-parallel shocks. The total energy budget in cosmic ray protons as a function of redshift is obtained by integrating

$$E_{\rm CR} = \int_{z=1}^{0} \sum_{i=1}^{N_p} F_{k,i} \Delta t(z_1, z_2) \xi\left(\theta_i\right) \mathrm{d}z. \tag{3.17}$$

over all timesteps. In Eq. 3.17, $F_{k,i}$ is the kinetic or cosmic-ray energy flux, $k \in$ [CR, gas] and $i \in$ [all, para, perp]. For simplicity, we neglect energy losses (which is reasonable in the case of this perturbed cluster, which is not characterised by $\geq 10^{-2}$ part/cm^3 gas densities), and therefore our values represent an upper limit on the cosmic-ray energy at all time steps. In the equations above, $\xi\left(\theta_i\right)$ is a Heaviside function which allows us to compute only the energy content for specific obliquities. Therefore we applied $\xi\left(\theta_{\rm all}\right)$ to let cosmic-rays to be accelerated in all shocked tracers, $\xi\left(\theta_{\rm para}\right)$ for only parallel shocks and $\xi\left(\theta_{\rm perp}\right)$ that only accounts perpendicular shocks. In the following the subscripts all, perp and para will correspond to the above selections. The acceleration efficiencies (see Eq. 3.6) have been further reduced by a factor of 2 in the case of quasi-parallel shocks, following the recent results by Caprioli & Spitkovsky (2014a).

Finally, we note that it in the complex flows in galaxy clusters the identification of weak shocks, e.g. $M \leq 1.5$, is made uncertain by numerics, while the injection of cosmic rays is expect to be dominated by $M \gg 2$ in DSA (e.g. Ryu et al., 2003). For these reasons, we only include shocks with $M > 2$ in the following analysis.

The evolution of the cosmic-ray energy across all tracers is shown in Fig. 3.7. At $z \approx 0$ the cosmic-ray energy for $\theta_{\rm all}$ is $\sim 8.9\%$ of the thermal energy of the gas. The cosmic-ray energy of $\theta_{\rm perp}$ is about $\sim 6.2\%$ of the gas energy and for $\theta_{\rm para}$ the cosmic-ray energy is about $\sim 2.6\%$ of the thermal gas energy. Most of the cosmic-ray energy is stored in the particles that have crossed a quasi-perpendicular shock, about $\sim 71\%$. The ratio of $E_{\rm CR}\left(\theta_{\rm perp}\right)$ to $E_{\rm CR}\left(\theta_{\rm para}\right)$ is ~ 2.5. This ratio stays constant over time. At early redshifts $z > 0.4$ a higher kinetic energy flux is injected by $\theta_{\rm perp}$ due to more cosmic-ray injection by quasi-perpendicular shocks. Between $z \sim 0.6$ and $z \sim 0.25$ the injected energy is about the same for $\theta_{\rm perp}$ and $\theta_{\rm para}$. At $z \sim 0.2$ the kinetic energy is higher for $\theta_{\rm perp}$. After $z \sim 0.2$ the injected energy is about the same again for $\theta_{\rm perp}$ and $\theta_{\rm para}$. The ratio of cosmic-ray energy injected by $\theta_{\rm perp}$ and $\theta_{\rm para}$ is, except for a few exceptions, in the range of $\sim 1 - 5$. We computed the γ-ray emission following the standard approach described, e.g., in Donnert et al. (2010), Huber et al. (2013b) and Vazza et al. (2015b) (see also the Appendix 3.1.C). For every shocked tracer we compute the

spectral index of the momentum distribution of accelerated cosmic rays as $s = -2 \cdot \frac{M^2+1}{M^2-1}$. At each timestep we compare the injection spectrum to the spectrum of the existing distribution of cosmic-rays (in case the tracers have been previously shocked already) and the current spectral index is set to the flatter among the two. Averaged over the tracer population, we observe a continuous decrease in the average spectral index until $z \approx 0.25$, indicating that the shocked population of tracers is progressively dominated by weaker and energetic shocks. However, the spectral index experiences a new steep increase caused by a strong shock event, corresponding to the time of the major merger in our simulation. Overall the spectral index varies only modestly, $s_{\max} - s_{\min} \approx 0.15$, across the investigated cluster evolution from $z = 1$. To compare in detail with the limits set by *Fermi*-LAT, we selected four clusters (A1795, A2065, A2256 and ZwCl1742) of similar masses given in Ackermann et al. (2014), and the Coma cluster (Ackermann et al., 2016), all located in the redshift range $z \in [0.02, 0.08]$. We used all upper limits at the low energy range of 500 MeV[5]. Table 3.1 shows the main properties of those galaxy clusters.
Our simulated γ-ray emission (for the energy range of $E \in [0.5, 200]$ GeV) and the observed upper limits derived are given in the first panel of Fig. 3.10. The γ-ray emission of our cluster for $\theta_{\rm all}$ is $\approx 0.64 \cdot 10^{45} \frac{\rm ph}{\rm s}$ and is above the upper limit for the Coma cluster. If we only use the energy of the cosmic rays gained by crossing parallel shocks (see Eq. 3.17), the γ-ray emission is lowered by a factor of ~ 3.4. However, even in this case the γ-ray emission for $\theta_{\rm para}$ exceeds the observed limits for the Coma cluster.

In the framework of the DSA theory, it is uncertain whether a specific minimum value of upstream magnetization is necessary to scatter the particles enough to enter the DSA acceleration loop. On the one hand, the extrapolation of DSA from the highly magnetized regime of supernova remnants ($\sim 1-100\ \mu$G) to the cosmic web is very uncertain. On the other hand, several papers have suggested that collisionless shocks can significantly amplify the upstream magnetic field independently of the initial conditions (e.g. Drury & Downes 2012, Brüggen 2013, Caprioli & Spitkovsky 2014b). As an explorative study, we investigated the effect of a minimum magnetisation level to allow for DSA, by limiting the acceleration of cosmic-ray protons to upstream fields $B_{\rm up} > B_{\rm min}$. Here we tested the cases of $B_{\rm min} \geq 0.1\ \mu$G and $B_{\rm min} \geq 0.5\ \mu$G. The results are shown in 3.10(a). In both cases the hadronic γ-ray emission is lowered towards the observed upper limits of the Coma cluster. The emission is significantly lowered towards the upper limit of Coma, if additionally only quasi-parallel shocks with an

[5] In the case of Coma, the limits given by Ackermann et al. (2016) are given for the lower energy limit of 100 MeV. Therefore, we rescaled this value to the higher low-energy range of 500 MeV used in our comparison, as $F(E > 500\ \text{MeV}) = F(E > 100\ \text{MeV}) \frac{\int_{E_1}^{E_3} A \cdot E^{-\Gamma} \mathrm{d}E}{\int_{E_2}^{E_3} A \cdot E^{-\Gamma} \mathrm{d}E}$ assuming a photon index $\Gamma = 2$, $E_1 =$ 500 MeV, $E_2 = 100$ MeV and $E_3 = 1$ TeV.

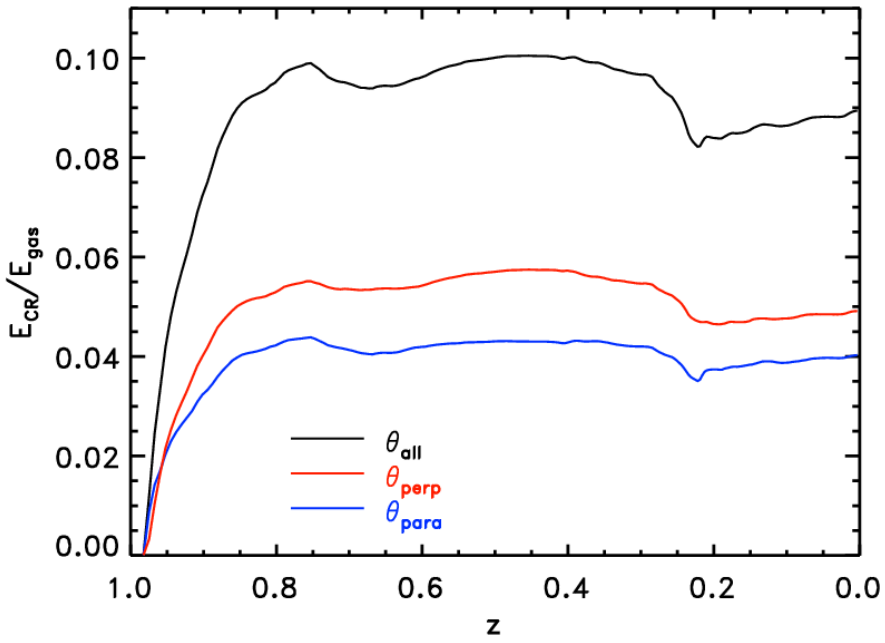

Figure 3.7: Evolution of the ratio of cosmic-ray to thermal gas energy for $\theta_{\rm all}$ (black), $\theta_{\rm perp}$ (red) and $\theta_{\rm para}$ (blue) across all tracers.

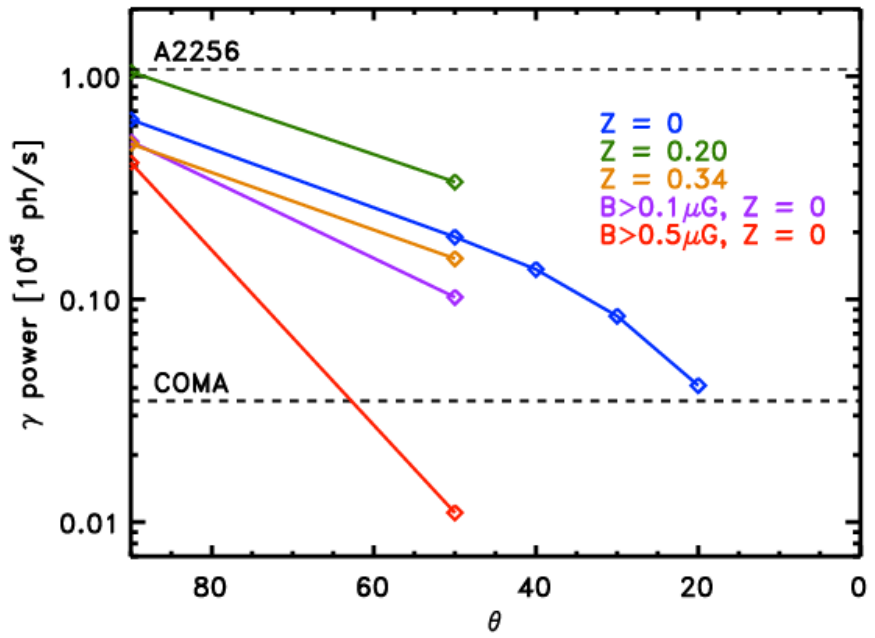

Figure 3.8: Total integrated γ-ray emission of our different models (color). The dashed lines show the *Fermi*-limits of A2256 and the Coma cluster taken from Ackermann et al. (2014) and Ackermann et al. (2016).

Name	z	M_{200} $[10^{15}\ M_\odot]$	$F_\gamma^{\rm UL}(E > 500$ MeV) $\left[10^{45}\frac{\rm ph}{\rm s}\right]$
$\theta_{\rm all}$	0.00	0.97	0.640
$\theta_{\rm para}$	0.00	0.97	0.190
$\theta_{\rm all}$, $B > 0.1\mu$G	0.00	0.97	0.512
$\theta_{\rm para}$, $B > 0.1\mu$G	0.00	0.97	0.102
$\theta_{\rm all}$, $B > 0.5\mu$G	0.00	0.97	0.411
$\theta_{\rm para}$, $B > 0.5\mu$G	**0.00**	**0.97**	**0.011**
$\theta_{\rm all}$,	0.20	0.66	1.047
$\theta_{\rm para}$	0.20	0.66	0.336
$\theta_{\rm all}$,	0.34	0.12	0.498
$\theta_{\rm para}$	0.34	0.12	0.152
θ_{40},	0.00	0.97	0.136
θ_{30}	0.00	0.97	0.084
θ_{20},	0.00	0.97	0.041
A1795	0.06	0.95	6.068
A2065	0.07	1.09	5.256
A2256	0.06	1.18	1.075
Coma	0.02	0.96	0.035
ZwCl1742	0.08	0.98	2.560

Table 3.1: Comparison of the total integrated γ-ray emission of our different models and a number of observed clusters at the bottom. For each cluster we give the name, redshift z, mass M_{200} and upper γ-flux $F_\gamma^{\rm UL}$. The last five rows show the reference clusters taken from Ackermann et al. (2014). The first two rows show our simulations for $\theta_{\rm all}$ and $\theta_{\rm para}$. The following rows show the results for the different simulations depending on $B_{\rm min}$, z and different selections of θ. Our cluster simulation compatible with the *Fermi*-limits for the Coma cluster is highlighted in boldface.

upstream magnetic field larger than 0.5 μG inject cosmic rays. In this case, the γ-ray emission drops significantly below the observed upper limit of the Coma cluster by a factor of ~ 117. The γ-ray properties discussed above are also present 0.5 Gyr before and after the major merger (see second panel of Fig. 3.10). The role played by shock obliquity on the injection of cosmic rays is found to be as strong as at $z = 0$: in both cases the γ-ray emission drops by a factor of $\sim 3.1 - 3.3$. But in neither of the cases the hadronic γ-ray emission is below the upper limit of the Coma cluster.
The γ-ray emission depends on the value chosen for θ_i in Eq. 3.17. We conducted the same experiment using different ranges for $\theta_{\rm para}$:

- θ_{50}: $\theta \in [0°, 50°]$ and $\theta \in [130°, 180°]$
- θ_{40}: $\theta \in [0°, 40°]$ and $\theta \in [140°, 180°]$
- θ_{30}: $\theta \in [0°, 30°]$ and $\theta \in [150°, 180°]$
- θ_{20}: $\theta \in [0°, 20°]$ and $\theta \in [160°, 180°]$

The γ-ray emission is reduced every time we restrict the shocks to a smaller range of obliquities (see third panel of Fig. 3.10). Only in the case of θ_{20} the γ-ray emission is close to the limit of the Coma cluster. Therefore, the hadronic γ-ray emission is not very sensitive to the selection of $\theta_{\rm para}$.
In summary, with our tracer-based method we tested two possible scenarios to reconcile the hadronic γ-ray emission from protons accelerated by cluster shocks with the observed upper limits for galaxy clusters (Ackermann et al., 2014, 2016). First, we tested how an obliquity switch affects the γ-ray emission. Second, we studied the effect of a minimum magnetic field strength on the acceleration of cosmic-ray protons and on their hadronic emission. In both cases the γ-ray emission was reduced, yet the fluxes were not reduced below the limits established by the *Fermi*-LAT observation of the COMA cluster (see Ackermann et al., 2016). A combination of both might be a possible explanation for the missing γ-ray emission as it reduces the fluxes below the *Fermi*-limits. The results of our different simulations are summarized in Table 3.1 and plotted in Fig. 3.8.

Close-up View of the Relic Regions

Finally, we take a closer look at the thermodynamical and magnetic properties of particles in the relic regions. We selected three sets of particles in front of (i.e. upstream), on top of and behind (i.e. downstream) the relics seen in figure 3.6(a) and 3.6(b). The selected regions are of the size of $158.8 \cdot 1268 \cdot 1268$ kpc^3 for both relics. The number of particles per selection are about $1 - 9 \cdot 10^3$.

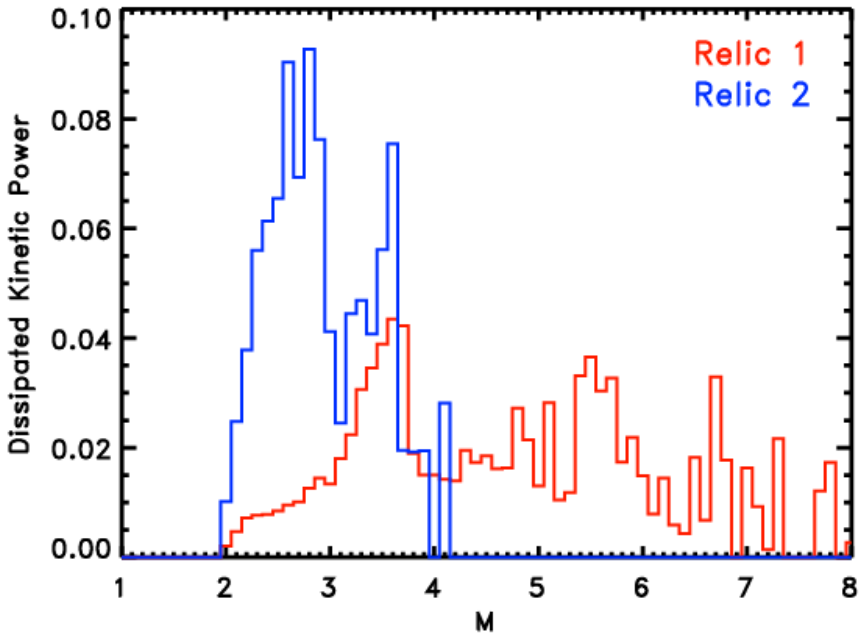

Figure 3.9: Dissipated kinetic power weighted distribution of the Mach numbers across the two relics.

In Fig. 3.11, we show the evolution of temperature, magnetic field strength and ratio of compressive to solenoidal energy (using Eq. 3.3 and Eq. 3.2) across the last two Gyr. The evolution of the temperature and magnetic field strength in all sets of particles is similar at early times. Later on, the tracers selected to be in the post-shock region at $z \approx 0$ show a significant jump in temperature and magnetic field strength, owing to the compression by the shocks they experienced. The Mach numbers producing the radio emission cover a big range in both relics (consistent with the findings of Skillman et al., 2010), yet the bulk of radio emission comes from the $M \sim 3.5$ (relic 1) and $M \sim 2.7$ (relic 2) shock (see Fig. 3.9). However, the magnetic field varies more than the temperature because of the chaotic evolution downstream of the two shocks. On average, the amplification of the downstream magnetic fields is $\sim 2-3$ at most. This is in line with recent results based on tailored MHD simulations of shocks by Ji et al. (2016), who reported a similar amplification downstream of magnetic fields, mostly due to compressive turbulent motions of $M = 4$ shocks. In the lower panel of Fig. 3.11 we show the modal decomposition of small-scale turbulence measured by the tracers: for most of their evolution, the solenoidal velocity is found to be predominant, $\sim 3-10$ times larger than the compressive component. However, relic 1 shows more compressive turbulence from $z \approx 0.15$. Based on Fig. 3.1, this is likely due to the fact that a large fraction of the gas ending up in relic 1 has crossed the central cluster region, where shocks launched by the major merger have increased the compressive energy component. The tracers connected to relic 1 also seem to have been subjected to a significant injection of cosmic rays by previous shocks.

In Fig. 3.12(a), we show the evolution of the mean Mach number (weighted for the injected cosmic-ray energy) for the particles ending up behind the relics. We see that up to redshift $z \approx 0.35$ the particles have crossed several weak shocks with values about $\langle M \rangle_{\rm ECR} \approx 2.5$. In the redshift range $z \approx 0.35 - 0.30$ the particles are exposed to stronger shocks, $\langle M \rangle_{\rm ECR} \approx 4$. These events correlate with the time of the major merger observed in our cluster. After $z \approx 0.2$ the tracers ending up in relic 1 have been crossed by several strong shocks, whereas the particles connected to relic 2 have only been crossed by a strong shock close to the major merger, at $z \approx 0.2$[6].

We also study the occurrence of multiple shocks on the particles swept by relics, by computing the average number of times each tracer has been crossed by shocks of a given Mach number shown in Fig. 3.12(b), and the corresponding shocked mass fraction shown in Fig. 3.12(c). For both relics we observe a continuous increase in the average number of particles shocked by $M > 1.5$ shocks and by $z = 0$ basically all particles have been shocked at least once by a $M \geq 1.5$ shock. Less particles are crossed by $M > 2$ or $M > 3$ shocks, especially before the last major merger. By $z \sim 0.1$, $\sim 40 - 60\%$ of particles in both selected regions have been already shocked by $M \geq 2$ shocks, while only $\sim 10 - 20\%$ of the particles have been shocked by $M \geq 3$ shocks. This finding suggests that a large fraction of radio emitting particles present in relics may have been subject to several cycles of DSA (re)acceleration over their lifetime.

Finally, we found no evidence supporting the possibility of significant turbulent re-acceleration Fujita et al. (2015) of radio emitting electrons neither in the upstream nor downstream of relics, owing to the typically long ($\geq 1 - 10$ Gyr) acceleration time on our tracers, which are much larger than the typical radiative cooling time of these particles. However, we defer to future work a more systematic analysis of this scenario, which also requires to carefully model the balance of energy gain and losses of radio emitting electrons in a time-dependent way (e.g. Donnert & Brunetti, 2014).

3.1.4 Discussion & Conclusions

We have studied the Lagrangian properties of gas in a galaxy cluster over the course of its history and tracked the energy evolution of cosmic rays accelerated by shock waves. Thus, we could test a few variations of the DSA picture for the acceleration of cosmic rays at shocks, with the aim of reproducing, both, the observed occurrence of radio emission in radio relics and the lack of γ-ray emission from galaxy clusters. Focusing on the evolution of a massive cluster with a major merger at low redshift, we obtained the following results:

- We measured the distribution of shock obliquities across the cluster, which is very

[6] We notice that the apparent floor of $\langle M \rangle_{\rm ECR} \approx 2$ is a result of restricting only $M > 2$ shocks to inject cosmic rays (see Sec. 3.1.2)

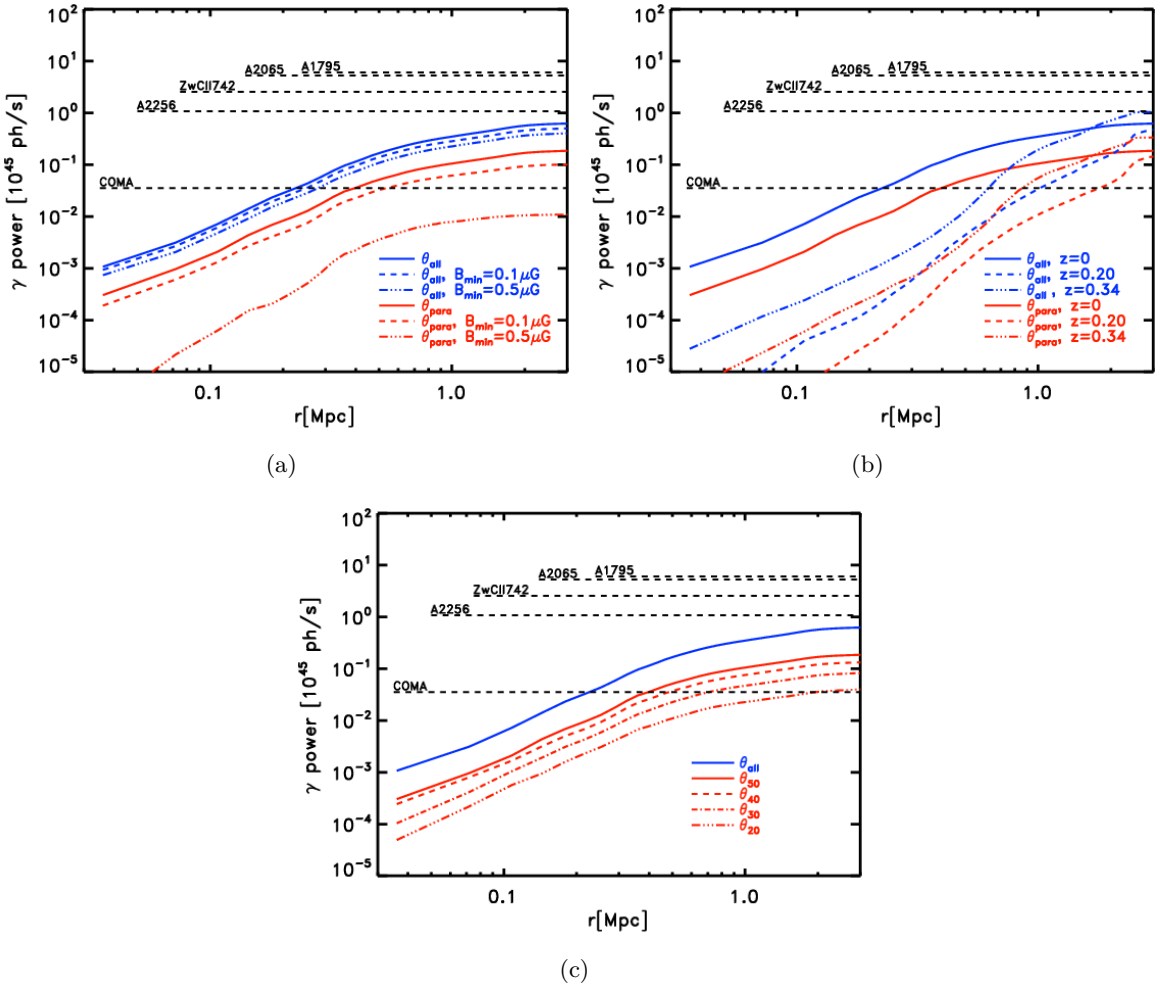

(a) (b)

(c)

Figure 3.10: Integrated γ-ray emission for all tracers (blue, solid line) and for the tracers that only experienced quasi-parallel shocks (red, solid line). The dashed lines in panel (a) show the results for the additional requirement of a minimum magnetic field. Panel (b) gives the results at different redshifts. Panel (c) shows the results for different ranges of θ. In all plots the horizontal dashed black lines give the *Fermi*-limits derived by Ackermann et al. (2014).

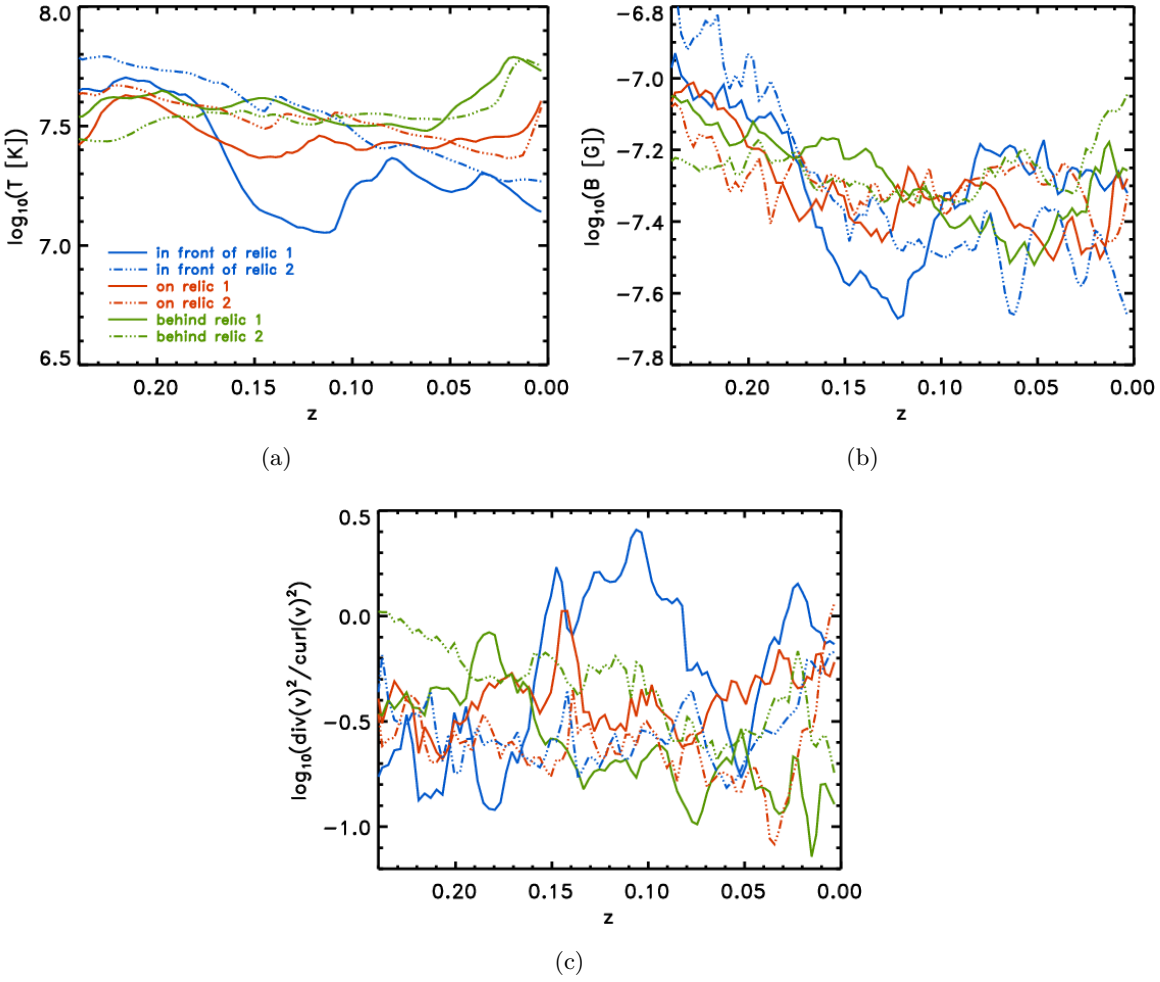

Figure 3.11: Evolution of (a) the temperature, (b) the magnetic field and (c) the ratio of compressive and solenoidal turbulent energy of the selected tracers over the last two Gyr. The solid lines show the selection of relic 1 and the dashed lines show the selection of relic 2. The colours indicate if the selection is upstream of the relic (green), on top of the relic (red) or downstream of the relic (blue).

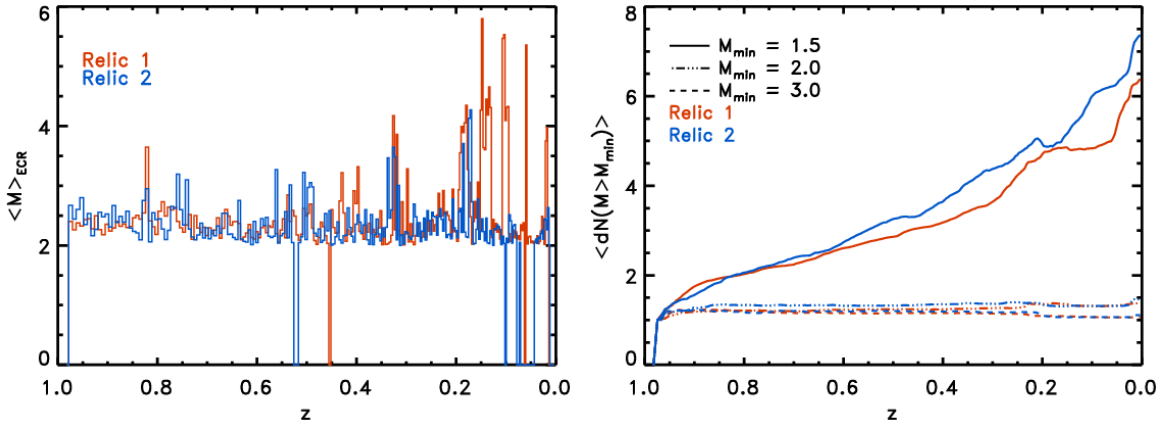

Figure 3.12: Evolution of (a) the cosmic-ray energy weighted Mach number, (b) frequency of $M > M_{\rm min}$ shocks sweeping tracers and (c) mass fraction for the particles ending up behind the relics. The red lines show the first relic and the blue lines show the second relic. In panels (b) and (c) the solids line show $M_{\rm min} = 1.5$, the long dashed lines show $M_{\rm min} = 2.0$ and the short dashed lines show $M_{\rm min} = 3.0$.

nearly consistent with an isotropic field distribution. After shock passage, the pre-shock distribution gets progressively more concentrated towards 90°. (see Sec. 3.1.3)

- We studied how the radio emission changes if only quasi-perpendicular shocks are able to accelerate particles (e.g. Guo et al., 2014a,b). The radio emission is not much affected by any obliquity switch, i.e. it drops by $\sim 40\%$ if only quasi-perpendicular shocks are taken into account, still producing detectable radio relics. (see Sec. 3.1.3)

- We used a similar restriction on obliquity to limit the acceleration of cosmic-ray protons to quasi-parallel shocks (e.g. Caprioli & Spitkovsky, 2014a) and we computed the resulting hadronic γ-ray emission. Over the cluster, the injected cosmic-ray proton energy is on average reduced by ~ 3.6 if DSA is allowed only for quasi-parallel shocks. For the investigated cluster, this is still not enough to decrease the predicted γ-ray flux below the present constrains by *Fermi*-LAT on the Coma cluster. (see Sec. 3.1.3)

- Only by limiting the acceleration of cosmic-ray protons to shocks with $\theta \leq 20°$ the hadronic emission from our cluster is found to be close to the upper limits of the Coma cluster.

- We have tested the reduction in cosmic-ray proton acceleration resulting from imposing a minimum magnetization level. Only for a minimum magnetic field $\geq 0.5\mu G$ the γ-ray emission decreases below the *Fermi*-LAT limits, also for the Coma cluster. Combining the requirement of a minimum magnetic field and only using proton injection by quasi-parallel shocks, the γ-ray emission decreases by a factor of ~ 117 and is below the *Fermi*-limits. In this case, the predicted hadronic γ-ray emission should lie only a factor of a few below the limits by *Fermi*. (see Sec. 3.1.3)

- The gas in the post-shock region of relics has been shocked about $7 - 8$ times more often by a $M = 1.5$ shock than by $M = 3$ shocks. While the observed γ-ray spectrum is dominated by the few strong shocks observed in the past, the cosmic-ray energy is dominated by re-acceleration of weak shocks at lower redshift. (see Sec. 3.1.3 and Sec. 3.1.3)

- We did not find evidence supporting acceleration of electrons via *Fermi*-II re-acceleration, neither upstream nor downstream of relics. (see Sec. 3.1.3)

Our study has shown that if DSA operates very different for different shock obliquities the acceleration of cosmic-rays in the ICM can be modified at a significant level compared to what has been assumed so far. If the acceleration of cosmic-ray protons is limited to *quasi-parallel* shocks (e.g. Caprioli & Spitkovsky, 2014a) the resulting hadronic γ-ray emission decreases towards the upper limits by *Fermi*, alleviating the reported tension with observations (Vazza & Brüggen, 2014; Vazza et al., 2015b). It is not possible to make any conclusive assessment based on our comparison with the Coma cluster, because the Coma cluster is in a different dy-

namical state, minor merger, than our simulated cluster, major merger. Conversely, the radio emission from merger shocks (i.e. radio relics) is changed at a level which is still compatible with observations if only *quasi-perpendicular* shocks can accelerate the cosmic-ray electrons (e.g.Guo et al. 2014a and Guo et al. 2014b). This is because in the regions where radio relics are typically formed, the magnetic field is so tangled that the distribution of angles closely follows the random distribution, which peaks towards 90°.
As a concluding caveat, in this work we did not include any microphysics such as microscopic magnetic field generation in a shock (e.g. Brüggen, 2013) or microscopic plasma instabilities (e.g. Kunz et al., 2014). Therefore, we restricted ourselves to the assumption that the magnetic field obliquity (and strength) observed at the scales resolved in this simulation are preserved down to much smaller scales where cosmic rays are accelerated via DSA and SDA. The validity of this assumption can only be tested in future work, where we plan to combine these results with tailored PIC simulations of cosmic shocks.

Acknowledgements

The cosmological simulations were performed using the ENZO code (http://enzo-project.org) and were partially produced at Piz Daint (ETHZ-CSCS, http://www.cscs.ch) in the Chronos project ID ch2 and s585, and on the JURECA supercomputer at the NIC of the Forschungszentrum Jülich, under allocations no. 7006 and 9016 (FV) and 9059 (MB). DW acknowledges support by the Deutsche Forschungsgemeinschaft (DFG) through grants SFB 676 and BR 2026/17. FV acknowledges personal support from the grant VA 876/3-1 from the DFG. FV and MB also acknowledge partial support from the grant FOR1254 from DFG.
The distances in Sec. 3.1.3 and Appendix 3.1.C have been computed using the Ned Cosmology Calculator (Wright, 2006). We thank our anonymous referee for the useful feedback, that helped improving the final quality of this paper. We also acknowledge fruitful discussions with T. Jones, K. Dolag and C. Gheller.

3.1.A Density Distribution

In order to use Lagrangian tracers for analysing the properties of the ENZO-simulation we need to verify that the tracers accurately follow the mass distribution of the cluster. Fig. 3.1 only gives a visual impression that the tracers are following the mass in a correct way. The density profiles are shown on Fig. 3.13. Especially in the cluster outskirts, where most of the cosmic rays are accelerated, the profile is very well sampled. Only in the cluster centre the tracers have a lower density profile compared to the real gas density, which can be explained

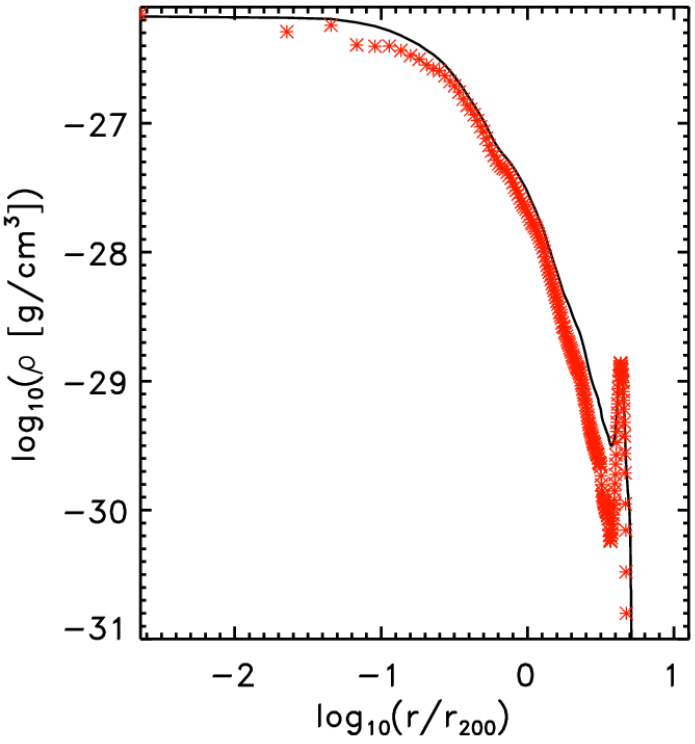

Figure 3.13: Density profile at $z \approx 0$ of the simulated cluster. The solid black line shows the ENZO-profiles and the red asterixs show the profile computed with the tracers.

by numerical diffusion (see 3.1.2) as well as by the finite mass resolution of the tracers. In Fig. 3.14, we compare the projected density of the ENZO-simulation and the tracers at redshift $z \approx 0$. The tracers show more detailed structures than the ENZO-simulation. We also observe that the tracers cannot resolve the masses smaller than their threshold (e.g. empty regions in the right panel).

3.1.B Accretion Shocks and Filaments

We ran the same analysis of the main paper also for a smaller cluster with a mass of $2.8 \cdot 10^{14}\ M_{\odot}$. This cluster is part of an other ENZO-simulation with a root grid consisting of 256^3 cells with a resolution of $\mathrm{d}x = 292$ kpc. The used cosmological parameters are: $H_0 = 70.2$ km s^{-1} Mpc^{-1}, $\Omega_{\mathrm{M}} = 0.272$ and $\Omega_{\Lambda} = 0.728$ and $\sigma_8 = 0.8$. The tracers were evolved on a 128^3 subgrid with resolution $\mathrm{d}x = 36.62$ kpc from $z = 1$ to $z = 0$ for a total of 192 timesteps. The final number of tracers is $N_p(z = 0) \approx 6 \cdot 10^7$.
The smaller size of the cluster allows us to analyse filaments and accretion shocks because the cluster is well contained in the support grid used to evolve tracers. Fig. 3.15 shows the distribution of angles across time. Also in this object and at all epochs, we observe more quasi-perpendicular angles than quasi-parallel angles, in agreement with the results of the

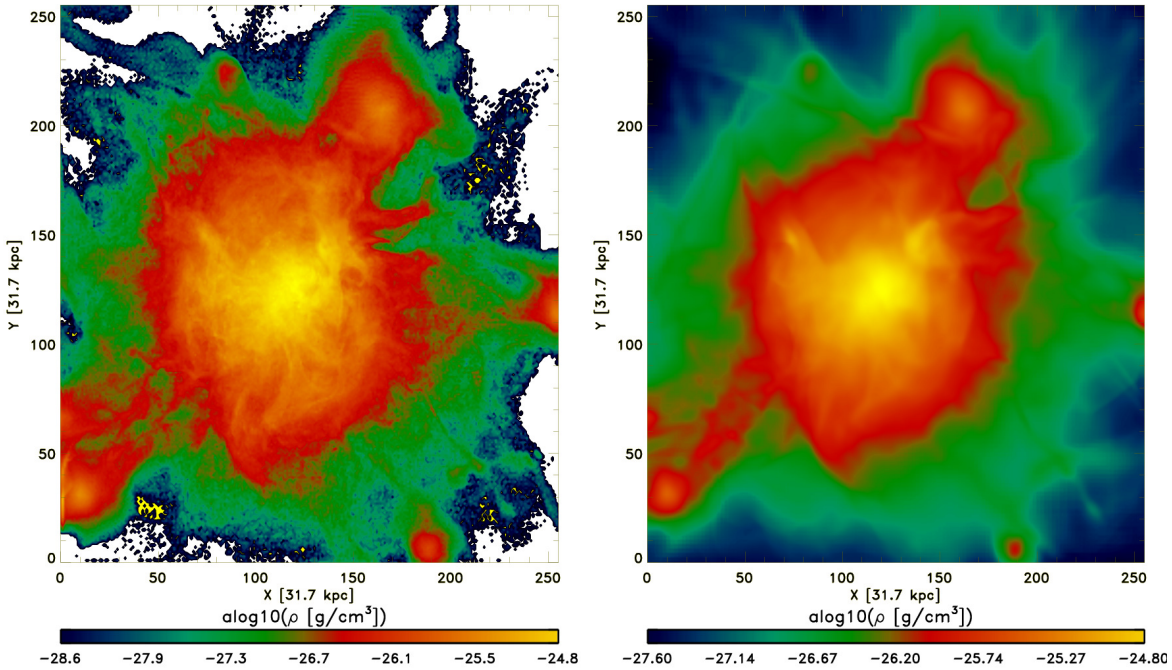

Figure 3.14: Density projections at $z \approx 0$. The left panel shows the projected density computed with tracers, while the right panel shows the projected density directly simulated in the ENZO run.

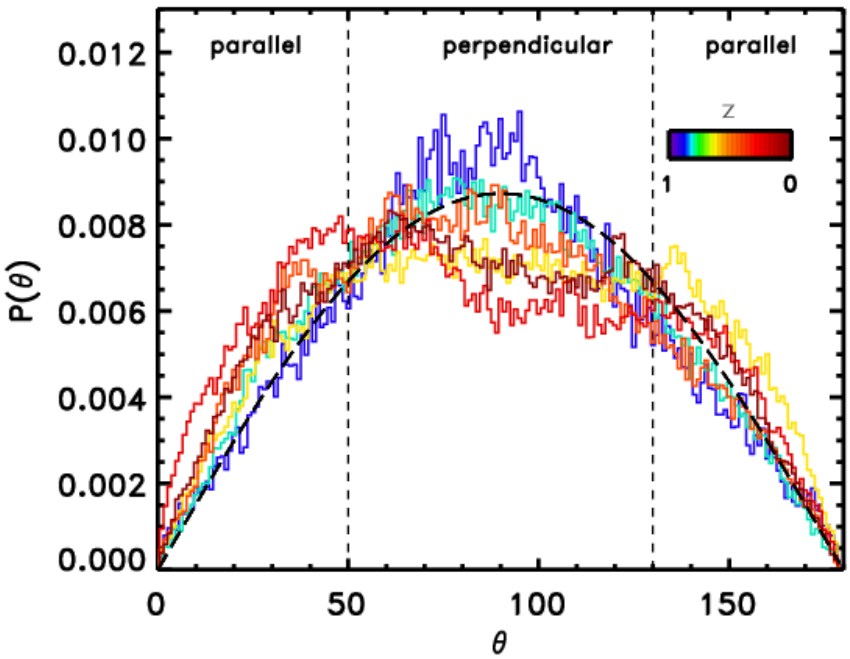

Figure 3.15: Distribution of pre-shock obliquities at different redshifts. The solid lines show the results from our simulation. The redshift is colour-coded going from black $z = 1$ to red $z = 0$. The dashed line shows the expected distribution of angles for a random distribution.

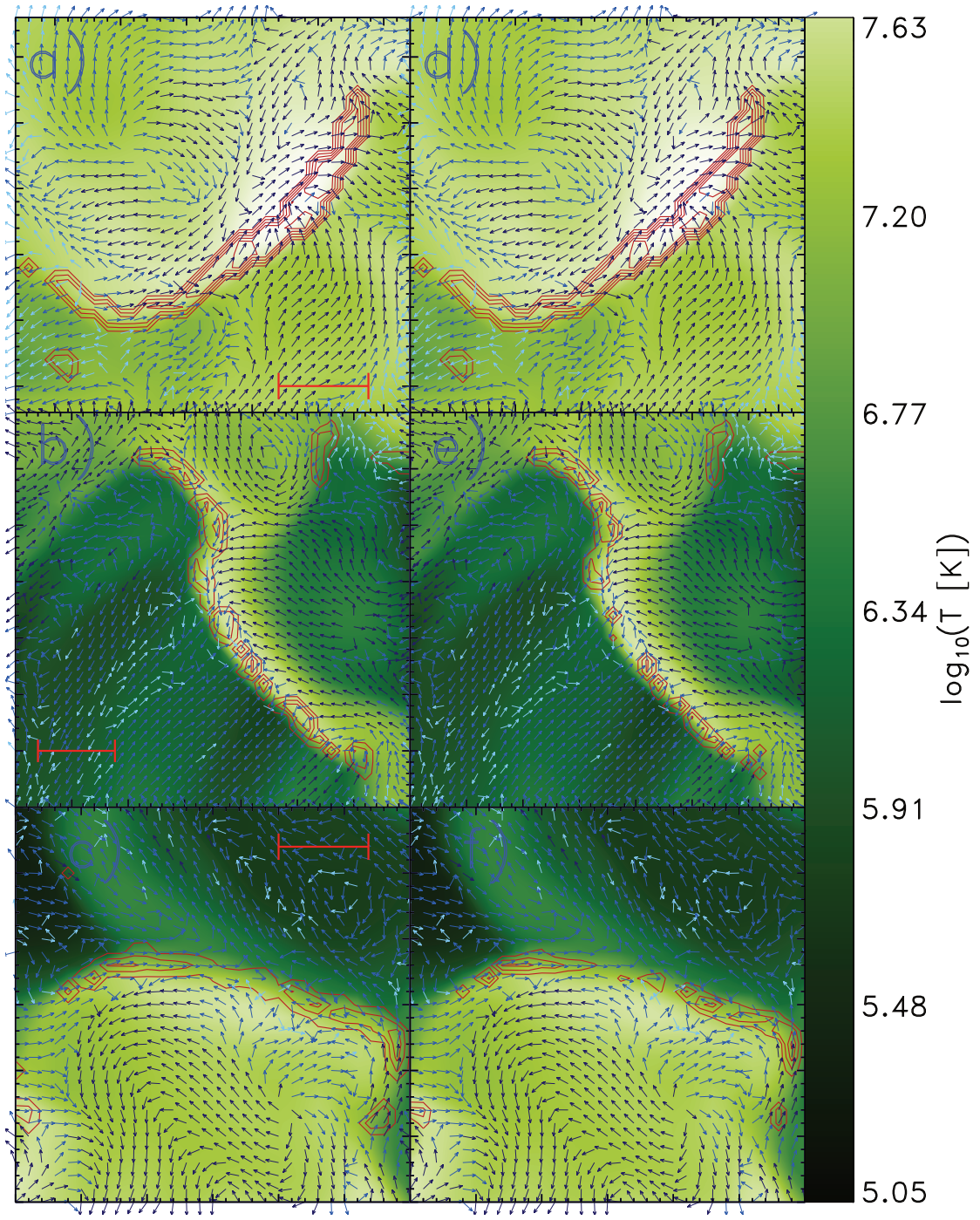

Figure 3.16: Zoomed versions of the three radio emitting regions are shown at $z \approx 0$. The colour shows the temperature of the ICM. The direction of the arrows indicates the direction of the magnetic and their colour gives their magnetic field strength in logarithmical units. The contours show the radio emission. Plots (a) and (d) show the central relic, plots (c) and (f) show the accretion shock and plots (b) and (e) show the filament. The left column ((a), (b) and (c)) shows the radio emission for θ_{all}. The right column ((d), (e) and (f)) shows the radio emission for θ_{perp}. The bars in Fig. (a), (b) and (c) show the length of 250 kpc. We notice that the format of the plot has been changed from its original version (Wittor et al., 2017b) to match the layout of this thesis.

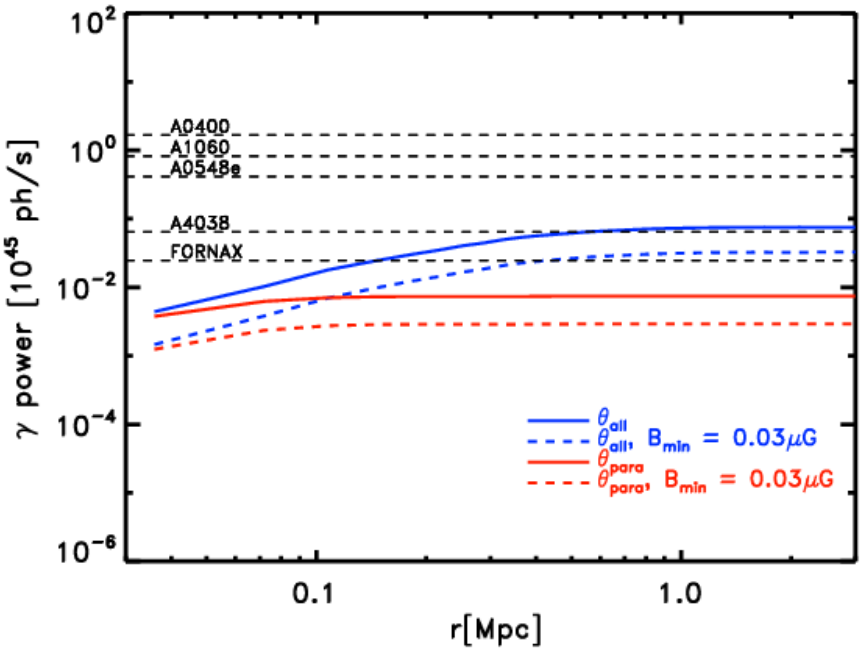

Figure 3.17: The γ-ray emission for all tracers (blue, solid line) and for the tracers that experienced quasi-parallel shocks (red, solid line). The dashed lines show the result for the additional requirement of a minimum magnetic field of $B_{\rm min} = 0.03$ μG to accelerate cosmic rays.

main paper. We also observe small excesses for quasi-parallel shocks. These are the result of a preferred parallel alignment of the magnetic field in filaments.

Following the approach described in Sec. 3.1.3 we investigated three regions of the cluster. We investigated a central relic (see Fig. 3.16(a) and Fig. 3.16(d)), a filament (see Fig. 3.16(b) and Fig. 3.16(e)) and an accretion shock (see Fig. 3.16(c) and Fig. 3.16(f)). As we see in Fig. 3.16 for all three regions the bulk of radio emission caused by quasi-perpendicular shocks.

Similar to Sec. 3.1.3, we computed the γ-ray emission from shock accelerated cosmic-ray protons. We compared the emission to real clusters[7] with similar masses taken from Ackermann et al. (2014). The γ-ray emission coming from $\theta_{\rm all}$ is above the limits of A4038 and FORNAX. The γ-ray emission drops by a factor of 2.3 if only quasi-parallel shocks accelerate the cosmic rays. Finally, we added the requirement in the minimum magnetic field strength. For this object, a limiting magnetic field of $B_{\rm min} = 0.03\mu$G is necessary to reduce the hadronic emission at the level of the *Fermi*-limits. Using this additional switch the γ-ray emission is reduced by a factor of 10.1 for $\theta_{\rm all}$ and by a factor 25.8 for $\theta_{\rm para}$.

We conclude that the distribution of shock obliquities and the resulting effects on particle acceleration are rather similar in groups and galaxy clusters.

[7]These clusters are: A0400, A1060, A0548e, A4038 and FORNAX.

3.1.C Computing the γ-Ray Emission

To compute the γ-ray emission we used the same approach as in Vazza et al. (2015b), Donnert et al. (2010) and Huber et al. (2013b). The total emission is given by the integral

$$I_\gamma = \int_r \lambda_\gamma(r)\, S(r)\, \mathrm{d}r. \tag{3.18}$$

Has to be computed using the emission per unit of volume $\lambda_\gamma(r)$:

$$\begin{aligned}\lambda_\gamma(r) &= \int_E \mathrm{d}E_\gamma q_\gamma(E_\gamma) \\ &= \frac{\sigma_{\mathrm{pp}} m_\pi c^3}{3\alpha_\gamma \delta_\gamma} \frac{n_{th} K_p}{\alpha_\mathrm{p} - 1} \frac{(E_{\min})^{-\alpha_\mathrm{p}}}{2^{\alpha_\gamma - 1}} \frac{E_{\min}}{\mathrm{GeV}} \\ &\quad \times \left(\frac{m_{\pi_0} c^2}{\mathrm{GeV}}\right)^{-\alpha_\gamma} \left[\mathcal{B}_\mathcal{X}\left(\frac{\alpha_\gamma + 1}{2\delta_\gamma},\ \frac{\alpha_\gamma - 1}{2\delta_\gamma}\right)\right]_{x_2}^{x_1}.\end{aligned} \tag{3.19}$$

Here $\mathcal{B}_\mathcal{X}(a, b)$ is the incomplete β-function, n_{th} is the number density of the protons, α_p and α_γ are the spectral index for the protons and the γ-rays, $\delta_\gamma = 0.14\alpha_\gamma^{-1.6} + 0.44$ is the shape parameter, $E_{\min}$ is the proton energy threshold, K_p is the normalization, c is the speed of light, m_π and m_{π_0} are the pion-mass. For the effective cross-subsection σ_{pp} we used Eq. (79) given in Kelner et al. (2006)

$$\begin{aligned}\sigma_{\mathrm{pp}}(E) &= \left(34.3 + 1.88L + 0.25L^2\right)\left[1 - \left(\frac{E_{\mathrm{th}}}{E}\right)^2\right]^4 \mathrm{mb} \\ &\text{with} \qquad L = \ln\left(\frac{E}{1\ \mathrm{TeV}}\right) \\ &\text{and} \qquad E_{th} = m_p + 2m_\pi + \frac{m_\pi^2}{2m_p} \sim 1.22\ \mathrm{GeV}.\end{aligned} \tag{3.20}$$

In the cross-subsection E_{th} is the threshold energy of the production of a π^0-meson. m_p and m_π are the proton and pion masses.

3.2 Studying the Effect of Shock Obliquity on the γ-ray and Diffuse Radio Emission in Galaxy Cluster

3.2.1 Introduction

The existence of peripheral, elongated and often polarised radio emission in galaxy clusters, so-called radio relics, gives evidence of cosmic-ray electrons being accelerated by shock waves in the intracluster medium (see Brunetti & Jones, 2014, and references therein). Cosmic-ray protons should undergo the same acceleration mechanism, but yet no evidence of their presence has been found. The *Large Area Telescope* on-board of the *Fermi*-satellite (Atwood et al., 2009) is searching for signatures of the cosmic-ray protons, which should produce γ-ray emission through collisions with the thermal gas. Yet no detection of these γ-rays has been confirmed and for a variety of clusters the upper flux limits have been estimated to be in the range of $0.5 - 2.2 \cdot 10^{-10}$ ph/s/cm^2 above 500 MeV Ackermann et al. (2014). Extended searches for the γ-ray emission in the Coma cluster Ackermann et al. (2016) and the Virgo cluster Ackermann et al. (2015) have set the flux limits above 100 MeV to $5.2 \cdot 10^{-9}$ ph/s/cm^2 for the former and to $1.2 \cdot 10^{-8}$ ph/s/cm^2 for the latter.
Recent results from particle-in-cell simulations Caprioli & Spitkovsky (2014a); Guo et al. (2014a,b) suggest that the efficiency of shock acceleration does not only depend on the shock strength but also on the shock obliquity, e.g. the angle between the shock normal and the underlying upstream magnetic field. Cosmic-ray protons should be accelerated more efficiently by diffusive shock acceleration (DSA) in parallel shocks Caprioli & Spitkovsky (2014a). In contrast, cosmic-ray electrons should prefer a perpendicular configuration as they are first accelerated by shock drift acceleration before they are injected into the DSA cycle (Guo et al., 2014a,b).
In our recent work, we have tested if in galaxy clusters the additional dependence on the shock obliquity can explain the missing γ-ray emission and still produce detectable radio relics (Wittor et al., 2017b). In this contribution we present the most relevant results from that work and include new results.

3.2.2 Methods

Cosmological MHD Simulations

The cosmological magneto-hydrodynamical (MHD) simulation presented in this work has been carried out with the `ENZO`-code Bryan et al. (2014). In our simulation we solve the MHD equations (see Sec. 2.1 in Bryan et al., 2014) using a piecewise linear method (Colella & Glaz, 1985) in combination with hyperbolic Dedner cleaning (Dedner et al., 2002). We re-simulate

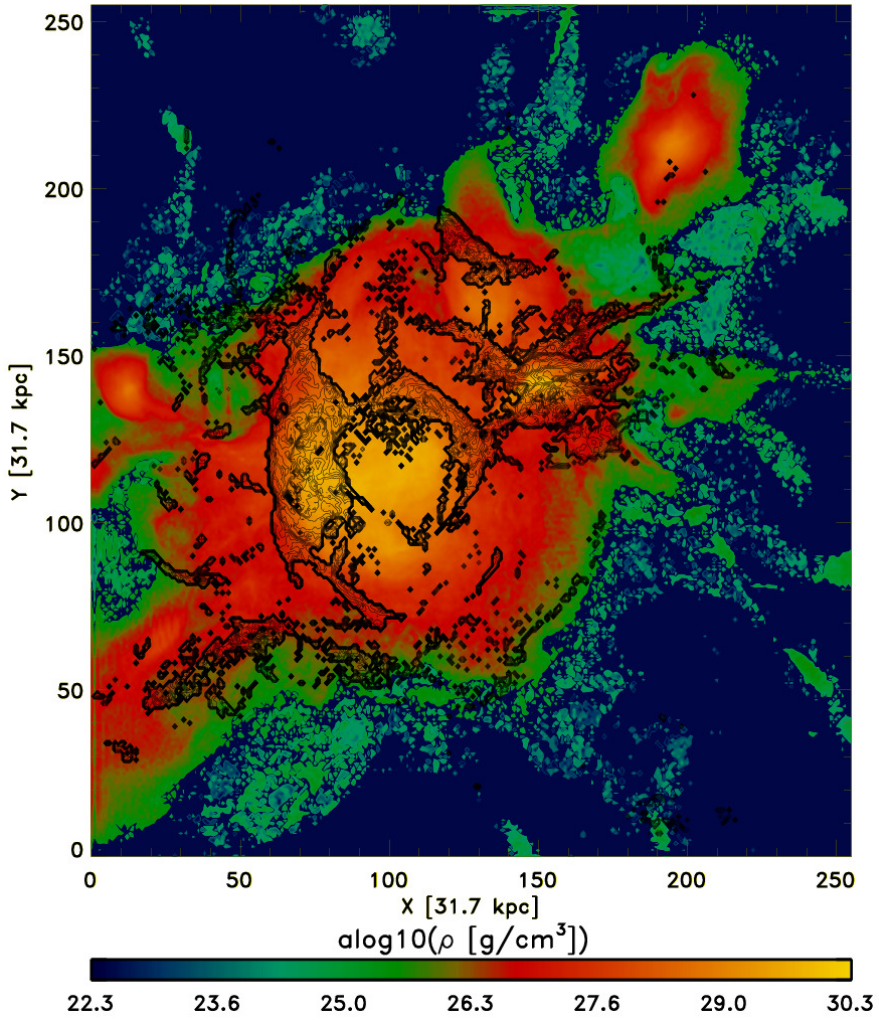

Figure 3.18: Projected gas density (colours) and radio contours at $z \approx 0.2$. Two radio relics can be seen on the right ($P_{\text{radio}} \approx 3.42 \cdot 10^{31}$ erg/s/Hz) and left ($P_{\text{radio}} \approx 2.26 \cdot 10^{32}$ erg/s/Hz) side of the cluster centre.

a single galaxy cluster with a final mass of $M_{200}(z \approx 0) \approx 9.74 \cdot 10^{14}\ M_{\odot}$. The cluster shows a major merger at $z \approx 0.27$, which is strong enough to produce detectable radio relics (see Wittor et al., 2017b, for further information). We simulate a $250^3 \sim \text{Mpc}^3$ comoving volume from $z \approx 30$ to $z \approx 0$, starting from a root grid of 256^3 cells and 256^3 dark matter particles. Furthermore, using 5 levels of AMR we refine 2^5 times a $\approx 25^3$ Mpc^3 region centred around our massive cluster, resulting in a final resolution of 31.7 kpc for a large portion of the cluster volume. For the seeding of the large scale-magnetic fields we use a primordial magnetic seed field with a comoving value of $B_0 = 10^{-10}$ G along each direction.

Lagrangian Analysis

We track the evolution of cosmic rays using Lagrangian tracer particles (see Wittor et al., 2017b, for more details). The tracer particles follow, both, the advection of the baryonic matter and the enrichment of shock-injected cosmic rays in time. In post-processing, the tracers are advected in a sub-box consisting of 256^3 cells of the finest grid of the simulation. The sub-box is centred around the mass centre of our galaxy cluster at $z \approx 0$. The tracers are first injected into the box at $z \approx 1$ following the mass distribution of the gas. During run-time, additional tracers are injected from the boundaries following the mass distribution of the entering gas. In total we generate $N_p \approx 1.33 \cdot 10^7$ tracers with a final mass resolution of $m_{\rm tracer} \approx 10^8\ M_\odot$.
The tracers are advected linearly in time using the velocities at their location: $\boldsymbol{v} = \tilde{\boldsymbol{v}} + \delta\boldsymbol{v}$. Here $\tilde{\boldsymbol{v}}$ is the interpolated velocity between the neighbouring cells and $\delta\boldsymbol{v}$ (see Eq. (1) in Wittor et al., 2017b) is a correction term to cure for a possible underestimate due to mixing in complex flows (see Genel et al., 2013, for more details).
The local gas values are assigned to every tracer and other properties are computed on the fly. Subsequently, we apply a shock-finding method based on the temperature jump between the positions of a tracer at two consecutive timesteps, similar to the method described in Ryu et al. (2003). Every time a shock is recorded, the Mach number and the corresponding shock obliquity are computed. The latter is calculated using the velocity jump $\Delta\boldsymbol{v} = \boldsymbol{v}_{\rm post} - \boldsymbol{v}_{\rm pre}$ between the pre- and post-shock velocity of the tracer:

$$\theta_i = \arccos\left(\frac{\Delta\boldsymbol{v}\cdot\boldsymbol{B_i}}{|\boldsymbol{v}||\boldsymbol{B_i}|}\right). \tag{3.21}$$

In the equation above, the index i refers to either the pre- or post-shock values. Across each shock, we compute the kinetic energy flux as $F_\Psi = 0.5 \cdot \rho_{\rm pre} v_{\rm sh}^3$, where $\rho_{\rm pre}$ is the pre-shock density and $v_{\rm sh}$ is the shock velocity. The thermal energy flux, $F_{\rm th} = \delta(M) F_\Psi$, and cosmic-ray energy flux, $F_{\rm CR} = \eta(M) F_\Psi$, are computed using the acceleration efficiencies $\delta(M)$ and $\eta(M)$ given in Kang & Ryu (2013). The efficiency, $\eta(M)$, is taken from Kang & Ryu (2013) and it includes the effects of magnetic field amplification at the shocks and thermal leakage of suprathermal particles. We include (as in Vazza et al., 2014b; Wittor et al., 2017b) the effect of re-acceleration by computing an effectiv $\eta_{\rm eff}(M)$ that is interpolated from the acceleration efficiencies of acceleration and re-acceleration given in Kang & Ryu (2013).
We use the formula given in (Hoeft & Brüggen, 2007) to compute the radio emission from the shocked tracers:

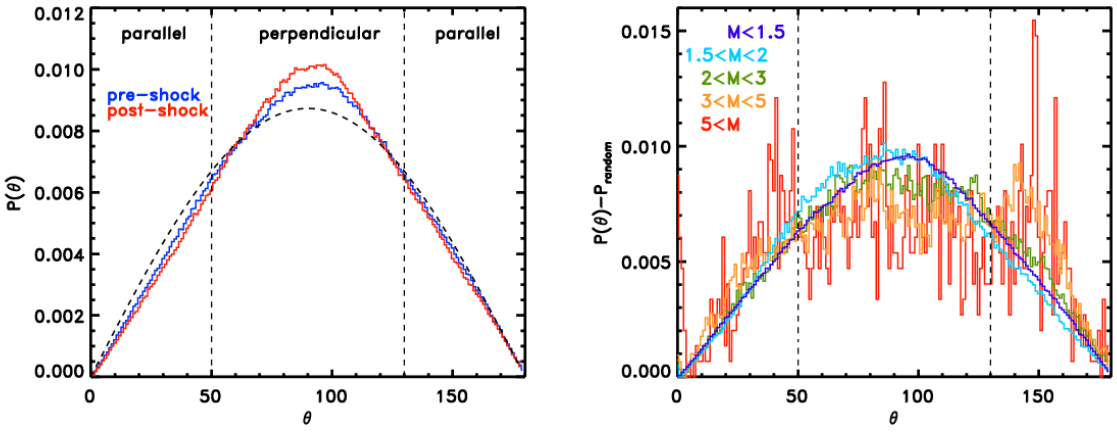

Figure 3.19: Distributions of shock obliquities at $z \approx 0.2$. The left panel shows the pre-shock (blue) and post-shock (red) distribution of obliquities. The black dashed line shows the expected $\propto sin(\alpha)$ distribution of angles based on pure geometry. The right panel shows the distribution of pre-shock obliquities for different ranges of Mach numbers: $M < 1.5$ (dark blue), $1.5 < M < 2$ (light blue), $2 < M < 3$ (green), $3 < M < 5$ (orange) and $M > 5$ (red).

$$\frac{\mathrm{d}P_{\mathrm{radio}}\left(\nu_{\mathrm{obs}}\right)}{\mathrm{d}\nu} = \frac{6.4 \cdot 10^{34}\ \mathrm{erg}}{\mathrm{s} \cdot \mathrm{Hz}} \frac{A}{\mathrm{Mpc}^2} \frac{n_e}{10^{-4}\ \mathrm{cm}^{-3}} \frac{\xi_e}{0.05} \left(\frac{T_d}{7\ \mathrm{keV}}\right)^{\frac{3}{2}} \times \left(\frac{\nu_{\mathrm{obs}}}{1.4\ \mathrm{GHz}}\right)^{-\frac{s}{2}} \frac{\left(\frac{B}{\mu\mathrm{G}}\right)^{1+\frac{s}{2}}}{\left(\frac{B_{\mathrm{CMB}}}{\mu\mathrm{G}}\right)^2 + \left(\frac{B}{\mu\mathrm{G}}\right)^2} \cdot \eta\left(M\right) \quad . \tag{3.22}$$

The quantities that are taken from the grid are: A the surface area of a tracer, n_e the number density of electrons, T_d the downstream temperature, B the magnetic field strength and the acceleration efficiency $\eta\left(M\right)$ depending on the Mach number M taken from Kang & Ryu (2013)[8]. The other quantities are the electron-to-proton ratio[9], $\xi_e = 0.01$, the observed frequency band, $\nu_{\mathrm{obs}} = 1.4$ GHz and the equivalent magnetic field of the cosmic microwave background, $B_{\mathrm{CMB}} = 3.2 \cdot (1+z)^2\ \mu$G. We use the same approach as in Vazza et al. (2015b), Donnert et al. (2010) and Huber et al. (2013b) to compute the γ-ray emission. We refer to Appendix C of our previous publication Wittor et al. (2017b) for a summary of the method.

[8]We notice that the application of $\eta(M)$ to Eq. 3.22 is limited to spectra flatter than $s \approx -3$, because Eq. 3.22 has been derived in energy space while $\eta(M)$ has been derived in momentum space. However, our modelling is accurate enough for the radio frequency we are investigating here (produced by electrons with Lorentz factor of $\gamma > 10^3$) (see Hoeft & Brüggen, 2007).

[9]Following Hoeft & Brüggen (2007) we assume that the minimum electron energy is 10 times the thermal gas energy, while the minimum proton energy is fixed to 780 MeV.

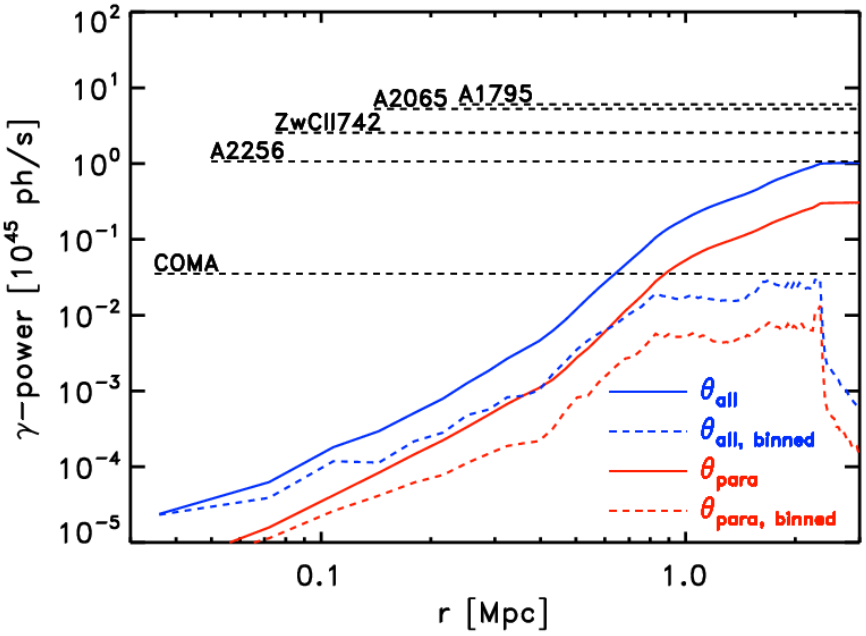

Figure 3.20: Profiles of the γ-ray emission. The solid lines show the total integrated emission profiles and the coloured dashed lines show the radial emission profiles. The γ-ray emission produced by cosmic-ray protons accelerated in all shock is given by the blue lines. The red line shows the case of only quasi-parallel shocks being able to accelerate cosmic rays. The black dashed lines show the upper *Fermi*-limits for galaxy clusters that have a comparable mass to our simulated cluster.

3.2.3 Results

In Wittor et al. (2017b) we studied how linking the shock acceleration efficiency to the shock obliquity can affect the acceleration of cosmic rays by predicting the amount of radio and γ-ray emission produced by either quasi-perpendicular or quasi-parallel shocks[10]. We define a shock to be quasi-perpendicular, if $\theta_{\rm pre} \in [50°, 130°]$, and to be quasi-parallel, if $\theta_{\rm pre} \in [0°, 50°]$ or $\theta_{\rm pre} \in [130°, 180°]$.

We found that the distribution of shock obliquities in a galaxy cluster roughly follows the distribution of random angles in three-dimensional space, $\propto \sin(\alpha)$. Just based on this, one can expect to observe more quasi-perpendicular shocks than quasi-parallel shocks. Hence, the acceleration of cosmic-ray electrons should be more favoured than the acceleration of cosmic-ray protons. For the results on how this affects the radio and γ-ray emission we point to our previous publication Wittor et al. (2017b) as they are similar to the ones presented below.

In this contribution, we present a closer analysis of the same cluster at the epoch of the peak of the total radio emission. We show the projection of the gas density overlayed with the

[10]Following Fig. 3 of Caprioli & Spitkovsky (2014a) we define quasi-perpendicular shocks as $\theta \in [50°, 130°]$ and quasi-parallel shocks as $\theta \in [0°, 50°]$ & $[130°, 180°]$. However, a more detailed analysis in Wittor et al. (2017b) showed that the effects on the acceleration of cosmic rays are not very sensitive to the selection of θ.

radio contours in Fig. 3.18. The cluster is still in a very active phase after it experienced a major merger at $z \approx 0.27$, and several smaller gas clumps are still falling onto the cluster.
First, we measure the distribution of pre- and post-shock obliquities at $z \approx 0.2$. The left panel of Fig. 3.19 shows the measured distributions consistent with isotropy. The right panel of Fig. 3.19 shows the distribution of pre-shock obliquities for different selections in the shock Mach numbers. While the obliquity distributions of $M < 3$ shocks roughly follow the distribution of random angles, stronger (and rarer) shocks are found to cluster at specific obliquity values, related to single large-scale magnetic structures in the cluster volume.
In the following we perform a similar analysis as in our previous work Wittor et al. (2017b) to investigate how coupling the shock acceleration efficiencies to the shock obliquity affects the γ-ray emission 3.2.3 and the radio emission 3.2.3.

γ-Ray Emission

In Fig. 3.20, we show the total integrated γ-ray emission and radial γ-ray emission profiles produced in the cluster at this epoch. The total γ-ray emission received from inside r_{200} is $\sim 1.03 \cdot 10^5$ ph/s, which is above the corresponding *Fermi*-limits[11] of the Coma ($0.035 \cdot 10^{45}$ ph/s) cluster and just below the limits of A2256 ($1.075 \cdot 10^{45}$ ph/s). The γ-ray emission resulting from cosmic-ray protons that have been accelerated only by quasi-parallel shocks is $\sim 0.31 \cdot 10^{45}$ ph/s. This is still above the lowest upper limit of the Coma cluster. The observed drop in γ-ray emission is consistent with the fact that at low Mach numbers only $\sim 1/3$ of all shocks are quasi-parallel (see Fig. 3.19).
Consistent with our findings from Wittor et al. (2017b), we conclude that the missing γ-ray emission cannot be entirely reproduced by limiting the acceleration of cosmic-ray protons to quasi-parallel shocks.

Radio Emission

We observe two radio relics on the left (hereafter relic one) and right (hereafter relic two) side of the cluster core (see Fig. 3.18). Both relics are in the range detectability by modern radio observations. Fig. 3.21 shows the complex geometry of the magnetic field lines in the relic regions. We observe that the morphologies of the relics do not change significantly, if only either quasi-perpendicular (middle panel) or quasi-parallel (right panel) shocks are able to accelerate cosmic-ray electrons.
In the first relic, only $\sim 46\%$ of the radio emission is produced by cosmic-ray electrons that have been accelerated by quasi-perpendicular shocks. This is consistent with the distribution of obliquities (see Fig. 3.19), as relic one is mostly produced by higher Mach number shocks

[11] See Wittor et al. (2017b) for the exact computations.

with $M \sim 3-5$ (see Fig. 3.22), that do not follow the distribution of random angles in a three dimensional space (see Fig. 3.19). On the other hand, $\sim 59\%$ of the shocks producing relic two are quasi-perpendicular, as it is produced by weaker shocks with $M \sim 2-3$ (see Fig. 3.22).
However, consistent with Wittor et al. (2017b), we find that both simulated relics remain visible if the acceleration of electrons is limited to quasi-perpendicular shocks.

3.2.4 Discussion

Combining MHD-simulations and Lagrangian tracers we continued our study on how restricting the shock acceleration efficiencies to the obliquity affects cosmic rays in galaxy clusters. At the epoch of the highest radio emission, we examined how cosmic rays, that have been accelerated by either quasi-parallel or quasi-perpendicular shocks, contribute to the resulting γ-ray and radio emission. We chose this epoch for our investigation as the two radio relics are the most prominent.
Our findings agree with our results from Wittor et al. (2017b): The distribution of shock obliquities follows the distribution of random angles in a three dimensional space. Furthermore, we discovered that this only holds for low Mach numbers $M \leq 3$. The distribution of shock obliquities for the few high Mach numbers $M \geq 3$ does not show this trend, as they tend to cluster around single magnetic field structures.
Consistent with our findings from Wittor et al. (2017b), the γ-ray emission drops by a factor of ~ 3 if only quasi-parallel shocks are able to accelerate the cosmic rays. Yet, this drop is not large enough the explain the low upper limits set by the *Fermi*-satellite Ackermann et al. (2014), especially in the case of the Coma cluster Ackermann et al. (2016).
On the other hand, the radio emission remains observable if only quasi-perpendicular shocks are able to accelerate cosmic rays. This also holds if the majority of the radio emission is produced by a strong quasi-parallel shock. This supports our conclusion from Wittor et al. (2017b) that it is possible that the cosmic-ray electrons in observed radio relics have only been accelerated by quasi-perpendicular shocks.
We mention that we do not include any other additional mechanisms such as cosmic-ray reacceleration by cluster weather or turbulence (e.g. Brunetti & Lazarian, 2011) which would produce further cosmic-ray protons. On the other hand we do not allow any spatial diffusion of the cosmic-rays, that would reduce the γ-ray flux through proton accumulation in the cluster outskirts (e.g. Wiener et al., 2013; Lazarian, 2016).

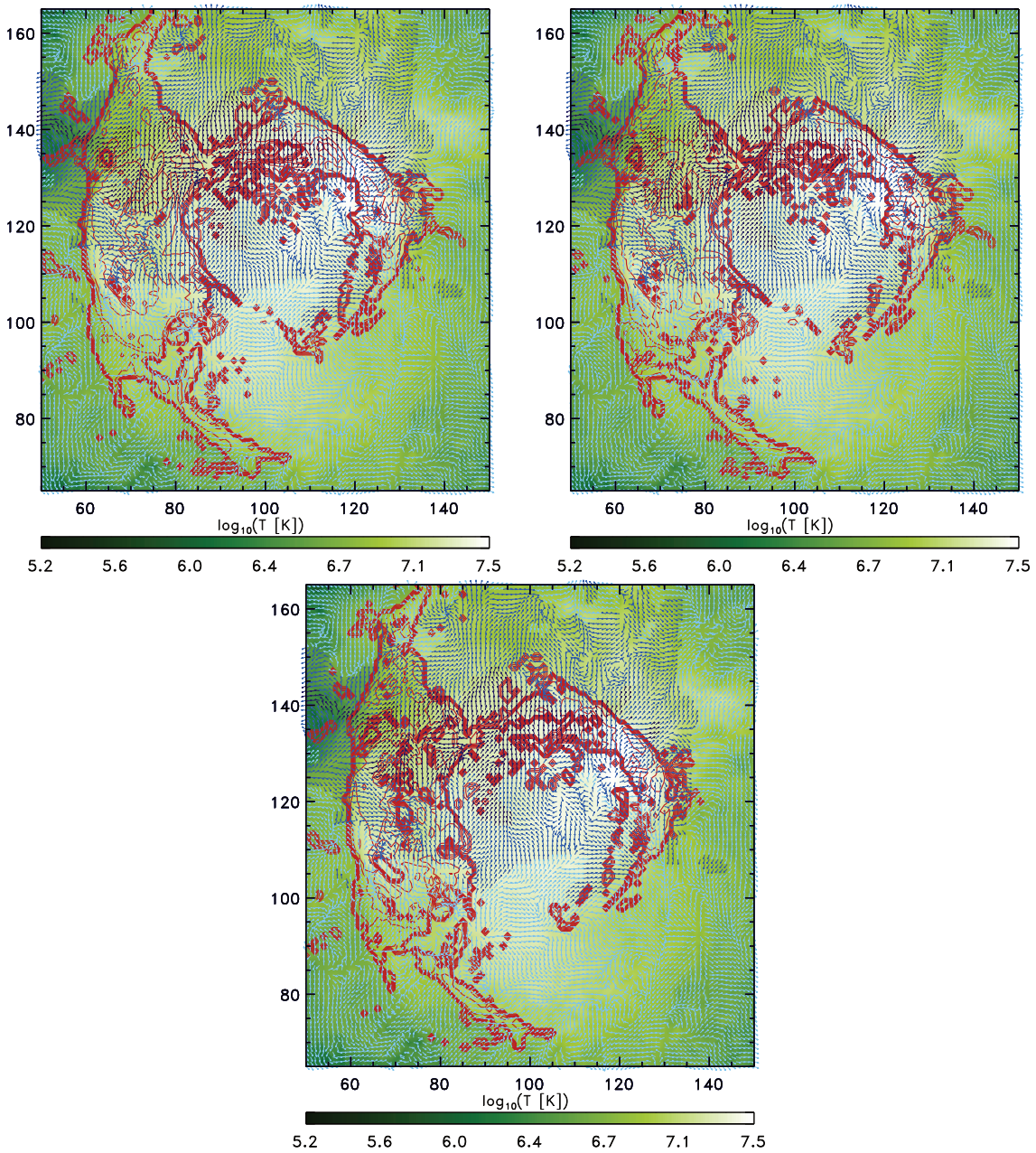

Figure 3.21: Isolated zoomed versions of our simulated radio relics. The green colours show the gas temperature. The blue arrows show the magnetic field. Their direction indicates the magnetic field direction and the colours give their magnetic field strength using a logarithmical stretching (as brighter the blue as stronger the magnetic field). The red contours show the radio emission. The left panel shows the relics produced by all cosmic-ray electrons. The middle panel shows the relics produced by electrons that have been accelerated by quasi-perpendicular shocks only. The right panel shows the relics produced by electrons that have been accelerated by quasi-parallel shocks only. The axes are in dx = 31.7 kpc units.

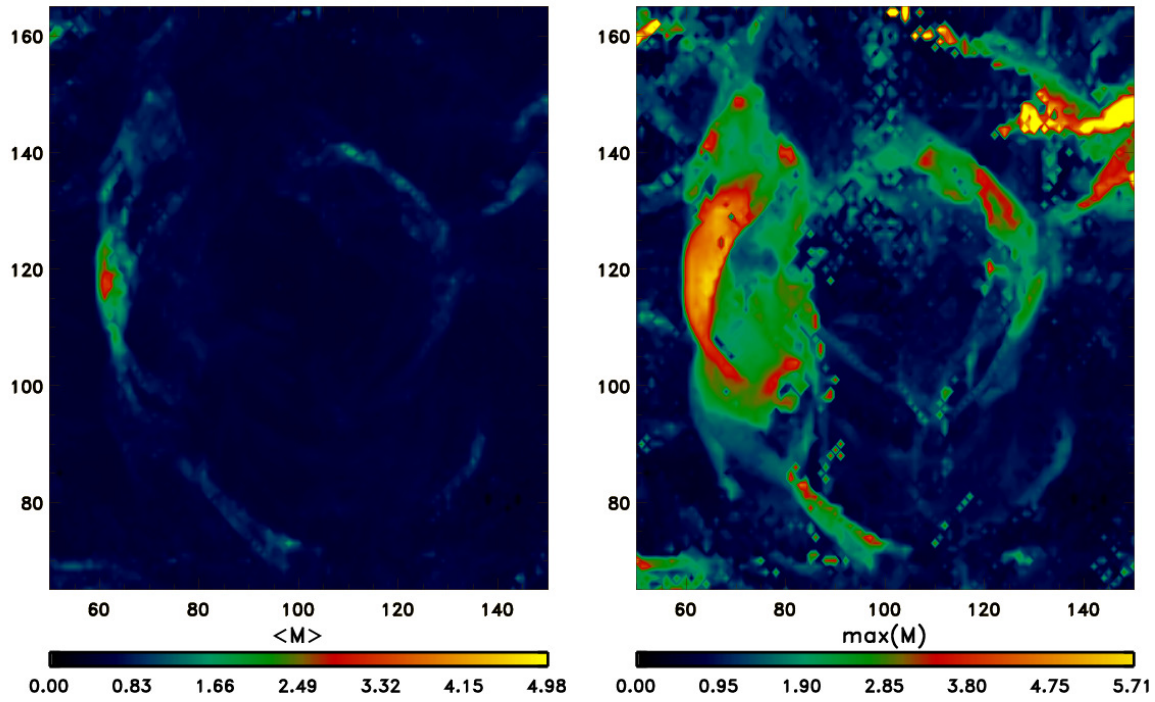

Figure 3.22: Maps of the mean (left panel) and maximum (right panel) Mach numbers of the shocks that are producing the radio relics. The axes are in dx = 31.7 kpc units.

Acknowledgements

The cosmological simulations accomplished in this work were performed using the ENZO code (http://enzo-project.org), and were partially produced at Piz Daint (ETHZ-CSCS, http://www.cscs.ch) in the Chronos project ID ch2 and s585, and on the JURECA supercomputer at the NIC of the Forschungszentrum Jülich, under allocations no. 7006 and 9016 (FV) and 9059 (MB). DW acknowledges support by the Deutsche Forschungsgemeinschaft (DFG) through grants SFB 676 and BR 2026/17. FV acknowledges personal support from the grant VA 876/3-1 from the DFG. FV and MB also acknowledge partial support from the grant FOR1254 from DFG.
We computed all cosmological distances using the Ned Cosmology Calculator (Wright, 2006). We acknowledge fruitful discussions with T. Jones, K. Dolag and C. Gheller.

3.3 Additional Material Relation θ_{pre} and θ_{post}

In this project, we derived a relation between the pre-shock and post-shock obliquity, namely:

$$\theta_{\mathrm{post}}(M) = \arccos\left[\frac{1}{\sqrt{1 + r^2 \tan(\theta_{\mathrm{pre}})^2}}\right]. \tag{3.23}$$

This relation was derived following Fitzpatrick (2014) and in this section we will give a more detailed view on its derivation.
At first we define a shock frame, in which the shock is in the z-plane and the shock normal is perpendicular to the x-direction and parallel to the y-direction. This is transformed into the de Hoffmann-Teller frame, where $|\boldsymbol{v}_{\mathrm{pre}} \times \boldsymbol{B}_{\mathrm{pre}}| = 0$, leading to the MHD-jump conditions in the form:

$$\frac{\rho_2}{\rho_1} = r \tag{3.24}$$

$$\frac{B_{x,\mathrm{post}}}{B_{x,\mathrm{pre}}} = 1 \tag{3.25}$$

$$\frac{B_{y,\mathrm{post}}}{B_{y,\mathrm{pre}}} = r\left(\frac{v_{x,\mathrm{pre}}^2 - \cos^2\theta_{\mathrm{pre}} v_{A,\mathrm{pre}}^2}{v_{x,\mathrm{pre}}^2 - r\cos^2\theta_{\mathrm{pre}} v_{A,\mathrm{pre}}^2}\right) \tag{3.26}$$

$$\frac{v_{x,\mathrm{post}}}{v_{x,\mathrm{pre}}} = r^{-1} \tag{3.27}$$

$$\frac{v_{y,\mathrm{post}}}{v_{y,\mathrm{pre}}} = \frac{v_{x,\mathrm{pre}}^2 - \cos^2\theta_{\mathrm{pre}} v_{A,\mathrm{pre}}^2}{v_{x,\mathrm{pre}}^2 - r\cos^2\theta_{\mathrm{pre}} v_{A,\mathrm{pre}}^2}. \tag{3.28}$$

The above equations can be simplified by neglecting the Alfvènic velocity $v_{A,\mathrm{pre}}$. In fact, the gas velocity v_{gas} is dominant over the Alfvèn velocity $v_{A,\mathrm{pre}}$ throughout the whole simulation. The ratio of the two is well described by a log-normal distribution centred on $v_{A,\mathrm{pre}}/v_{\mathrm{gas}} \approx 0.01$, and extending to beyond 1 only in $\sim 10^{-3}\%$ of the grid cells. In Fig. 3.23, we plot the profile and normalized grid distribution of $v_{A,\mathrm{pre}}/v_{\mathrm{gas}}$. Therefore $v_{A,\mathrm{pre}}$ is neglected due to the low magnetisation of the ICM and shocks can be treated hydrodynamical. This way the above Eq. 3.26 and 3.28 reduce to $B_{y2}/B_{y1} = r$ and $v_{y2}/v_{y1} = 1$. Using these jump conditions, we derive $\theta_{\mathrm{post}}(M)$ from

$$\cos(\theta_{\mathrm{post}}) = \frac{\Delta\boldsymbol{v} \cdot \boldsymbol{B}}{|\Delta\boldsymbol{v}|\,|\boldsymbol{B}|} \tag{3.29}$$

$$= \frac{\begin{pmatrix} v_{x,\mathrm{pre}}(r^{-1} - 1) \\ 0 \end{pmatrix} \cdot \begin{pmatrix} B_{x,\mathrm{pre}} \\ B_{y,\mathrm{post}} r \end{pmatrix}}{v_{x,\mathrm{pre}}(r^{-1} - 1) \cdot \sqrt{B_{x,\mathrm{pre}}^2 + B_{y,\mathrm{post}}^2 r^2}} \tag{3.30}$$

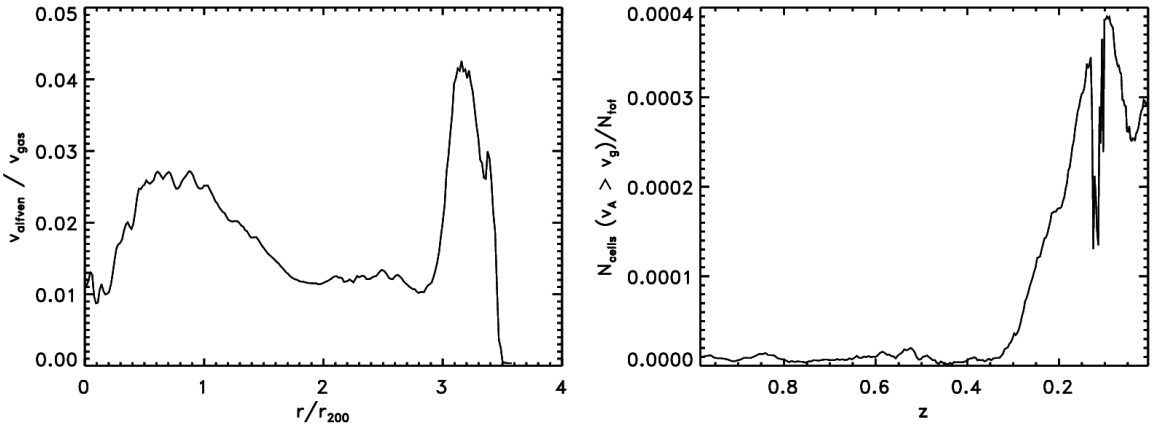

(a) (b)

Figure 3.23: Panel (a) shows the profile of the ratio of the Alfvènic and gas velocity. Panel (b) shows the evolution of the normalized number of grid cells that have a larger Alfvènic velocity than gas velocity.

a form of $\theta_{\rm post}(M)$ that only depends on the pre-shock values

$$\theta_{\rm post}\left(M\right) = \arccos\left[\frac{B_{x,\rm pre}}{\sqrt{B_{x,\rm pre}^2 + r^2 B_{y,\rm pre}^2}}\right]. \tag{3.31}$$

Using $\theta_{\rm pre}$ as $B_{y1} = B_{x1} \cdot \tan\left(\theta_{\rm pre}\right)$, one can show that the change of a pre-shock obliquity only depends on the obliquity itself and the compression ration r as

$$\theta_{\rm post}\left(M\right) = \arccos\left[\frac{1}{\sqrt{1 + r^2 \tan\left(\theta_{\rm pre}\right)^2}}\right]. \tag{3.32}$$

In the equations above, B is the magnetic field and the subscripts pre and post refer to the pre- and post-shock values.

4 Constraining the Efficiency of Cosmic-Ray Acceleration by Cluster Shocks

The following chapter presents work as it is published by Vazza, Brüggen, Wittor, Gheller, Eckert, & Stubbe in MNRAS 2016a, coauthored by me. I provided the Lagrangian re-simulation of the AMR region described in Sec. 4.3.4. The data obtained by this analysis is displayed in Fig. 4.11 and contributes to Fig. 4.12. This analysis was fundamental to the discussion in Sec. 4.4.

4.1 Introduction

The growth of cosmic structures naturally leads to the formation of powerful shock waves into the intergalactic and the intralcluster medium (IGM and ICM, respectively) (e.g. Sunyaev & Zeldovich, 1972a; Cavaliere & Lapi, 2013). The Mach number of shocks within galaxy clusters at late epochs must be low because the mergers are between virialized halos (Gabici & Blasi, 2003). On the contrary, stronger accretion shocks must be located at all epochs in the outer parts of large-scale structures, as they mark the transition from infalling matter to the onset of the virialisation process (Miniati et al., 2000; Ryu et al., 2003). Cosmological simulations show that the bulk of kinetic energy dissipation in the cosmological volume proceeds via shocks with Mach numbers $2 \leq M \leq 3$ (e.g. Vazza et al., 2011b).
Radio relics are steep-spectrum radio sources that are usually detected in the outer parts of galaxy clusters, $\sim 0.5-3$ Mpc from their centres and often found in clusters with a perturbed dynamical state (e.g. Ensslin et al., 1998; Hoeft & Brüggen, 2007). However, radio observations of radio relics (Ferrari et al., 2008; Feretti et al., 2012) are biased towards merger shocks with $2 \leq M \leq 5$, due to the larger weighting of radio-emitting electrons with a flatter spectral index (Skillman et al., 2013a; Hong et al., 2014). Diffusive shock acceleration (DSA, e.g. Caprioli, 2012; Kang & Ryu, 2013; Caprioli & Spitkovsky, 2014a) has been singled out as the most likely mechanism to accelerate relativistic particles at cosmic collisionless shocks. However, the relative efficiency of this process for electrons and protons, and its dependence on the shock and plasma parameters are poorly constrained. Recently, hybrid simulations have shown that the diffusive shock acceleration of relativistic protons and the CR-driven

amplification of magnetic fields in $5 \leq M \leq 50$ shocks are efficient only for quasi-parallel configurations, $\theta \leq 45^{\circ}$ (Caprioli & Spitkovsky, 2014a).
While the power-law emission spectra of radio-emitting electrons in radio relics are naturally explained by DSA (e.g. Hoeft & Brüggen, 2007; van Weeren et al., 2010), recent modelling suggests that at least in some cases the measured acceleration of electrons is too large, and at odds with DSA (e.g. Kang et al., 2012; Pinzke et al., 2013). The inclusion of re-accelerated particles can alleviate the tension in some cases, yet in order for the cosmic ray protons to be equally reaccelerated and become detectable in γ-rays, their injection efficiency must be much below the predictions from DSA (Vazza & Brüggen, 2014; Vazza et al., 2015a; Brunetti & Jones, 2014).
Our findings suggest that additional acceleration mechanisms might be responsible for channeling energy into the acceleration of radio-emitting electrons, while keeping the acceleration efficiency of protons rather low. Promising results in this direction have been recently obtained with Particle-In-Cell simulations (Guo et al., 2014a,b).
The release of relativistic protons into the ICM by cosmological shock waves, and the fact that they can be stored there for longer than the Hubble time has been investigated in many works (Dennison, 1980; Berezinsky et al., 1997; Blasi & Colafrancesco, 1999; Pfrommer et al., 2007). Interactions with the thermal ions of the ICM lead to diffuse hadronic γ-ray emission, in the range of what can already be tested by γ-ray observations (Aharonian et al., 2009; Aleksić et al., 2010; Ackermann et al., 2010; Arlen et al., 2012; Aleksić et al., 2012; The Fermi-LAT Collaboration et al., 2013; Zandanel & Ando, 2014). To date, no diffuse γ-ray emission from the ICM has been detected by FERMI (Ackermann et al., 2010; The Fermi-LAT Collaboration et al., 2013). With this information, one can set upper limits on the amount of CR-protons in the ICM, of the order of a few percent for the virial volume of clusters provided that the radial distributions are similar to that of thermal baryons (Ackermann et al., 2010; Huber et al., 2013b; Zandanel & Ando, 2014; Griffin et al., 2014). In this work, we analyze a large sample of simulated galaxy clusters and compare the expected level of hadronic γ-ray emission as a function of the assumed acceleration scenario to constraints from observations.

4.2 Methods

Our simulations are produced using original modifications for cosmic ray physics on top of the `ENZO` code (Bryan et al., 2014), as presented in previous work (Vazza et al., 2012a, 2013, 2014b). We assume the WMAP 7-year cosmology (Komatsu et al., 2011) with $\Omega_0 = 1.0$, $\Omega_{\rm BM} = 0.0455$, $\Omega_{\rm DM} = 0.2265$, $\Omega_{\Lambda} = 0.728$, Hubble parameter $h = 0.702$, a normalisation for the primordial density power spectrum $\sigma_8 = 0.81$ and a spectral index of $n_s = 0.961$ for the primordial spectrum of initial matter fluctuations, starting the runs at $z_{\rm in} = 30$.
Compared to the suite of simulations presented in Vazza et al. (2014b) here we only analyse

boxes of 300^3 Mpc^3 and 150^3 Mpc^3 simulated with 2048^3 and 1024^3 cells/DM particles, respectively. In the second case, several resimulations compare the effects of CRs and gas physics on the hadronic emission. The use of large grids with constant resolution yields a large sample of clusters with appropriate detail in describing the outer cluster regions, where most shocks occur (Vazza et al., 2011b). A study of resolution effects is provided in the Appendix. Table 1 gives a schematic view of the runs used in this work. All halos with $\geq 10^{13}$ $M_{\odot}$ are sampled by at least $\sim 10^4$ DM particles, ensuring a robust modelling of the innermost cluster dynamics. At $z = 0$ the CUR1 box contains ≈ 170 halos with masses $M_{\rm v} \geq 10^{13}$ $M_{\odot}$ and ≈ 400 with masses $M_{\rm v} \geq 10^{14}$ $M_{\odot}$ while the CUR2 boxes contains about ~ 8 fewer objects due to their smaller volume. Although our goal of properly resolving the injection of CRs in a large sample of galaxy cluster can only be presently achieved with large unigrid runs, in Sec. 4.3.4 we also discuss higher resolution simulations of a galaxy cluster where we used adaptive mesh refinement, in order to better compare with small-scales X-ray and radio features of an observed galaxy cluster.

4.2.1 Cosmic-Ray Physics

The injection of CRs and their dynamical feedback on the evolution of baryons is incorporated into the PPM hydrodynamical method of `ENZO`, using a two-fluid approach (Vazza et al., 2012a, 2014b). The efficiency of conversion between the shock kinetic energy flux and the CR-energy flux is set by the Mach number measured on-the-fly. The models of DSA tested in these simulations follow from modelling of shock acceleration with 1-D diffusion-convection methods (e.g. Kang & Jones, 2007; Kang & Ryu, 2013). Following these results, we assume that a fraction η of the kinetic energy flux across the shocks surface ($\Phi_{\rm kin}$) is converted into CR-energy: $\Phi_{\rm CR} = \eta(M)\Phi_{\rm kin}$, where $\eta = \eta(M)$. Simulated shocks can both inject CRs and re-accelerate pre-existing CRs, and we model both processes at run-time by appropriately rescaling the efficiency function as a function of the energy ratio between CR and gas upstream of each shock (Vazza et al., 2014b). Away from shocks, the CR-fluid is advected using the fluxes from the PPM solver, assuming that CRs are frozen into the gas component by magnetic fields, which is realistic given the large timescale for CRs diffusing out of our ≥ 100 kpc cells. The dynamical impact of CRs follows from the effective equation of state of each cell, which comes from the energy-weighted ratio of the gas and CRs ultrarelativistic index, $4/3 \leq \Gamma_{\rm eff} \leq 5/3$. We also include Coulomb and hadronic losses for CRs based on (Guo & Oh, 2008).

In this work, we tested the acceleration efficiency by Kang & Jones (2007), the (less efficient) acceleration scenario by Kang & Ryu (2013) and a more simplistic scenario with a fixed acceleration efficiency of $\eta = 10^{-3}$ independent of the Mach number. We have also tested the more recent studies of DSA with hybrid-simulations by Caprioli & Spitkovsky (2014a).

In the absence of an analytical or interpolated prescription for the acceleration efficiency as a function of Mach number and shock obliquity (which would require an expensive exploration of parameters), we can roughly model the net DSA acceleration efficiency of this model by rescaling the efficiencies of the Kang & Ryu (2013) model for an appropriate constant. The acceleration efficiency measured by Caprioli & Spitkovsky (2014a) for $M \sim 5 - 10$ quasi-parallel shocks is ≈ 0.5 of the efficiency in Kang & Ryu (2013) for the same Mach number range. If we assume the probability distribution of shock obliquities to be purely random ($P(\theta) \propto \sin(\theta)$), only ≈ 0.3 of shocks have $\theta \leq 45°$. Hence, by combining these two factors we can roughly mimic the effect of DSA in the model by Caprioli & Spitkovsky (2014a) by rescaling the Kang & Ryu (2013) acceleration model by $f_{\rm CS} = 0.15$. Obviously, this is a very crude assumption and we defer to future magneto-hydrodynamical simulations to study how the shock obliquity affects the injection of CRs (Wittor et al., in prep).

4.2.2 Gas Physics

In runs including radiative cooling of gas, we assume a constant composition of a fully ionized H-He plasma with a uniform metallicity of $Z = 0.3\ Z_{\odot}$. The APEC emission model (e.g. Smith et al., 2001) has been adopted to compute the cooling function of each cell at run-time as a function of temperature and gas density (Bryan et al., 2014). For the cold gas in the simulated volume, with temperatures $T \leq 10^4$ K, we use the cooling curve of Smith et al. (2011), which is derived from a complete set of of metals (up to an atomic number 30), obtained with the chemical network of the photo-ionization software *Cloudy* (Ferland et al., 1998). The thermal effect of the UV re-ionization background (Haardt & Madau, 1996) is approximately modelled with a gas temperature floor within $4 \leq z \leq 7$ (Vazza et al., 2010a). The implementation of feedback from AGN has been presented in Vazza et al. (2013) and Vazza et al. (2014b). The code releases bipolar thermal jets at high gas density peaks in the simulation, identified within all massive halos. Our feedback scheme starts at $z = 4$ ("AGN" model) or at a lower redshift, $z = 1$ ("AGN-low" model) and deposits $E_{\rm AGN} = 10^{59}$ erg of thermal energy in the two cells on opposite sides of the gas density peaks (tagged as $n \geq n_{\rm AGN} = 10^{-2}$ cm^{-3} comoving), with a random direction along the coordinate axes of the grid. This method for AGN feedback is admittedly simplistic as it by-passes, both, the problem of monitoring the mass accretion rate onto the central black hole within each galaxy, and the complex small-scale physical processes which couple the energy from the black hole to the surrounding gas (see discussion in Vazza et al., 2014b). However, the tests presented in this work (Sec. 4.3.1) show it can produce realistic profiles of clusters on ≥ 100 kpc scales.

$L_{\rm box}$	$N_{\rm grid}$	Δx	details	DSA-efficiency
216 Mpc/h	2048^3	105 kpc/h	CUR1 non-rad.	KR13
108 Mpc/h	1024^3	105 kpc/h	CUR2 non-rad.	KR13
108 Mpc/h	1024^3	105 kpc/h	CUR2 non-rad.	KJ07
108 Mpc/h	1024^3	105 kpc/h	CUR2 cool.+AGN(high)	KR13
108 Mpc/h	1024^3	105 kpc/h	CUR2 cool.+AGN(low)	KR13
108 Mpc/h	1024^3	105 kpc/h	CUR2 non-rad.	10^{-3}
108 Mpc/h	1024^3	105 kpc/h	CUR2 cool.+AGN(low)	10^{-3}
108 Mpc/h	1024^3	105 kpc/h	CUR2 non-rad.	CS14

Table 4.1: List of the simulations used in this work. Column 1: size of the simulated volume. Column 2: number of grid cells. Column 3: spatial resolution. Column 4: physical implementations and run name. Column 5: diffusive shock acceleration efficieny of cosmic rays (KJ07=Kang & Jones (2007), KR13=Kang & Ryu (2013), 10^{-3}=constant efficiency, CS14=Caprioli & Spitkovsky (2014a)).

4.2.3 Adaptive Mesh Refinement Resimulations of MACSJ1752.0+0440

We have performed an additional adaptive mesh refinement (AMR) resimulation of one massive galaxy cluster that shows a good X-ray and radio morphological similarity with the cluster MACSJ1752.0+0440, that we already studied in Bonafede et al. (2012). Similar to other clusters with double relics, this object represents an important testbed for particle acceleration in the ICM, because the location of relics allows us to precisely constrain the timing and the parameters of the merger (Vazza & Brüggen, 2014; Vazza et al., 2015a). This cluster has a total virial mass of $\approx 1.37 \cdot 10^{15}\ M_{\odot}$ at $z = 0$, while this is $\approx 0.65 \cdot 10^{15}\ M_{\odot}$ at the epoch of a major merger at $z = 0.3$, similar to what is inferred from the X-ray data of MACSJ1752.0+0440 at $z = 0.366$. We produced multiple resimulations of this object by varying the modelling of CR injection and use the FERMI data to constrain the CR-acceleration scenario. The initial conditions for this object are taken from set of nested grids sampling a volume of 264^3 Mpc^3, centred on the formation region of the cluster. AMR based on the local gas/DM overdensity and on velocity jumps is used to increase the resolution in the cluster region additional 2^3 times, down to a maximum resolution of ≈ 25 kpc/h for a ~ 80 % fraction of the ICM volume. For a more details on the simulation procedure we refer the reader to Vazza et al. (2010a).

4.2.4 γ-Ray Observation of MACSJ1752.0+0440

For this project we derived upper limits for the γ-ray emission from the region of MACSJ1752.0+0440 at $z = 0.366$, analyzing the FERMI catalog.
We analyzed the data of the Large Area Telescope on board FERMI at the position of MACS J1752 to set constraints on the π^0 emission arising from the interaction of cosmic-ray protons with the ambient intra-cluster medium. We follow the method presented in Vazza et al. (2015a) to analyze the FERMI-LAT data. Namely, we use the `ScienceTools` v9r32p5 soft-

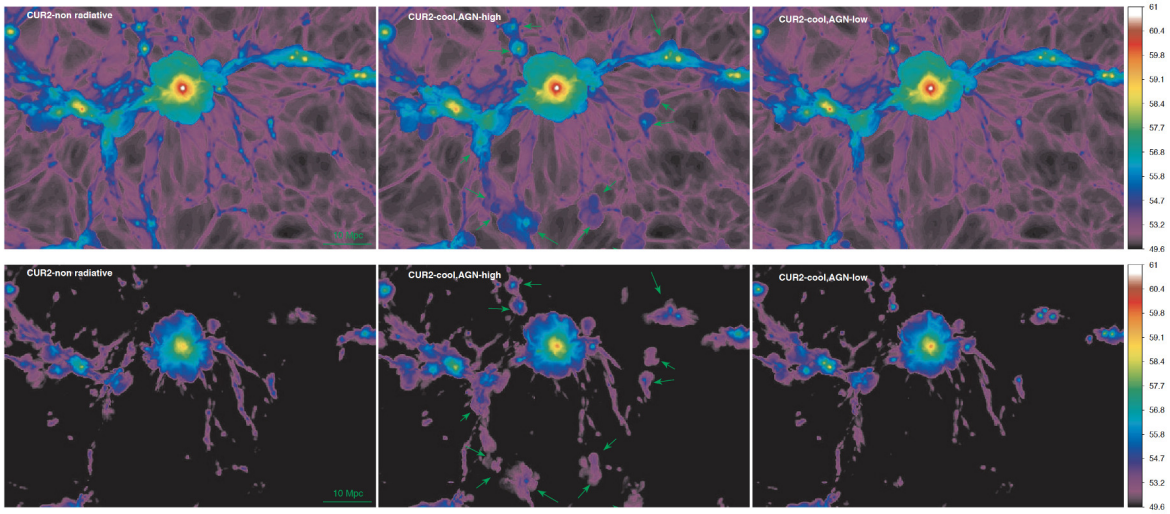

Figure 4.1: 2-dimensional slice (with thickness 3 Mpc) of the gas energy (top panels) and CR-energy (bottom panels) for a subvolume of the CUR2 volume at $z = 0$, where we compare the non-radiative and the cooling plus AGN feedback runs. The color bar gives the energy per cell in units of $\log_{10}$ [erg]. To guide the eye, we indicate with green arrows the regions where the effect of AGN feedback is more prominent.

ware package and the P7SOURCE_V6 instrument response files. We construct a model for the expected γ-ray spectrum arising from π^0 decay by convolving the simulated cosmic-ray spectrum in the [0.2-300] GeV band with the proton-proton interaction cross section from Kelner et al. (2006). The observed spectrum is then fit with the model template and the significance of the signal over the background is estimated by computing the likelihood ratio between the best-fit model and the null hypothesis (i.e. no additional source), usually referred to as the test statistic (TS). This analysis yields a very mild improvement in the likelihood (TS=0.04), which indicates that no significant signal is detected at the position of MACS J1752. The 95 % upper limit to the source flux is 1.2×10^{-9} ph/cm^2/s in the [0.2-300] GeV band. For more details on the data analysis procedure, we refer to Huber et al. (2012) and Huber et al. (2013b).

4.3 Results

4.3.1 Cluster Properties

The panels in Fig. 4.1 show the thermal and CR energy distribution in a subvolume of the CUR2 run with different prescriptions for gas physics and containing clusters of different masses. The impact of gas cooling and feedback is not very significant on the scale of the two massive objects in this image ($\sim 2 \times 10^{14}$ $M_\odot$ and $\sim 4 \times 10^{14}$ $M_\odot$, respectively), while it is

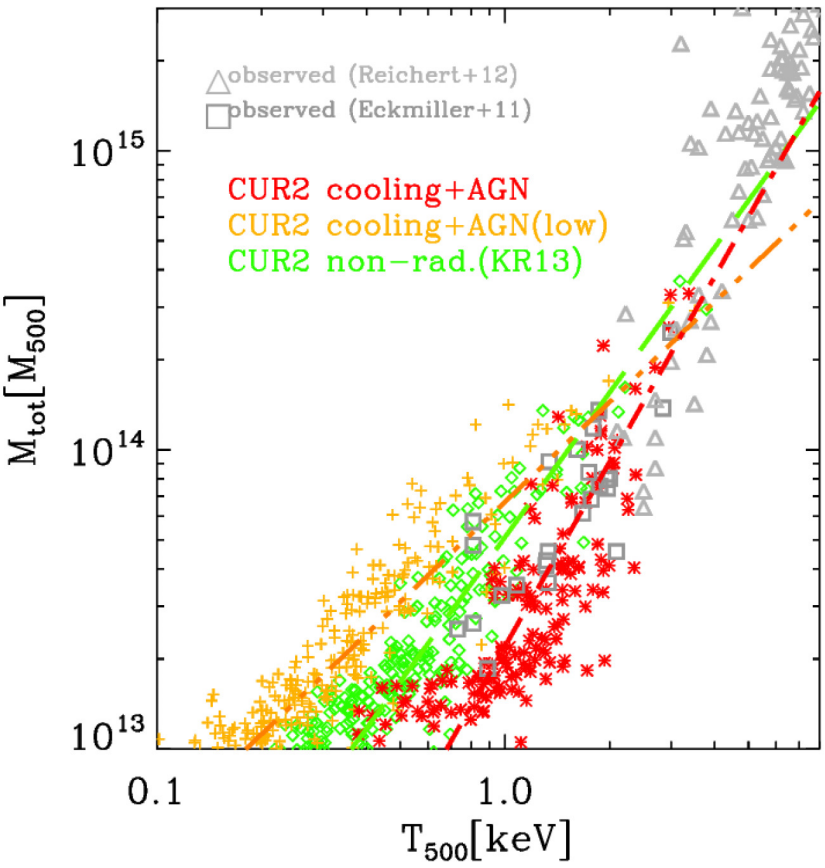

Figure 4.2: Mass-temperature scaling relation for the halos in the radiative and non-radiative runs of the CUR2 volume (150^3 Mpc^3), computed inside R_{500} for each object at $z = 0$. The additional lines show the best fit of the simulated data, while the two set of gray symbols are for real cluster observations using CHANDRA by Eckmiller et al. (2011) and Reichert et al. (2011). To better compare with the simulated cluster and minimise the effect of cosmic evolution, we only consider observed cluster in the $0 \leq z \leq 0.2$ redshift range.

more evident at the scale of galaxy groups, where AGN feedback promoted the expulsion of entropy and CR enriched gas outside of halos, as an effect of past powerful bursts. Compared to the non-radiative case, the core of clusters/groups is always richer of CRs, due to additional injection following the shocks released by the thermal AGN feedback. The CR energy is everywhere smaller than the gas energy, with a ratio that goes from a few percent to a few tens of percent going from the centre to the outskirts of clusters. In the lower redshift AGN feedback case, the outer atmosphere of clusters is less extended in the other cases, due to the unbalanced compression by cooling.

In order to assess how realistic the thermal gas distribution in our clusters is, we compute the mass-temperature relation for all identified halos in the volume, inside the reference overdensity of $\Delta = 500$, and compare it to the X-ray observed scaling relations by Reichert et al. (2011) and Eckmiller et al. (2011), see Fig. 4.2.

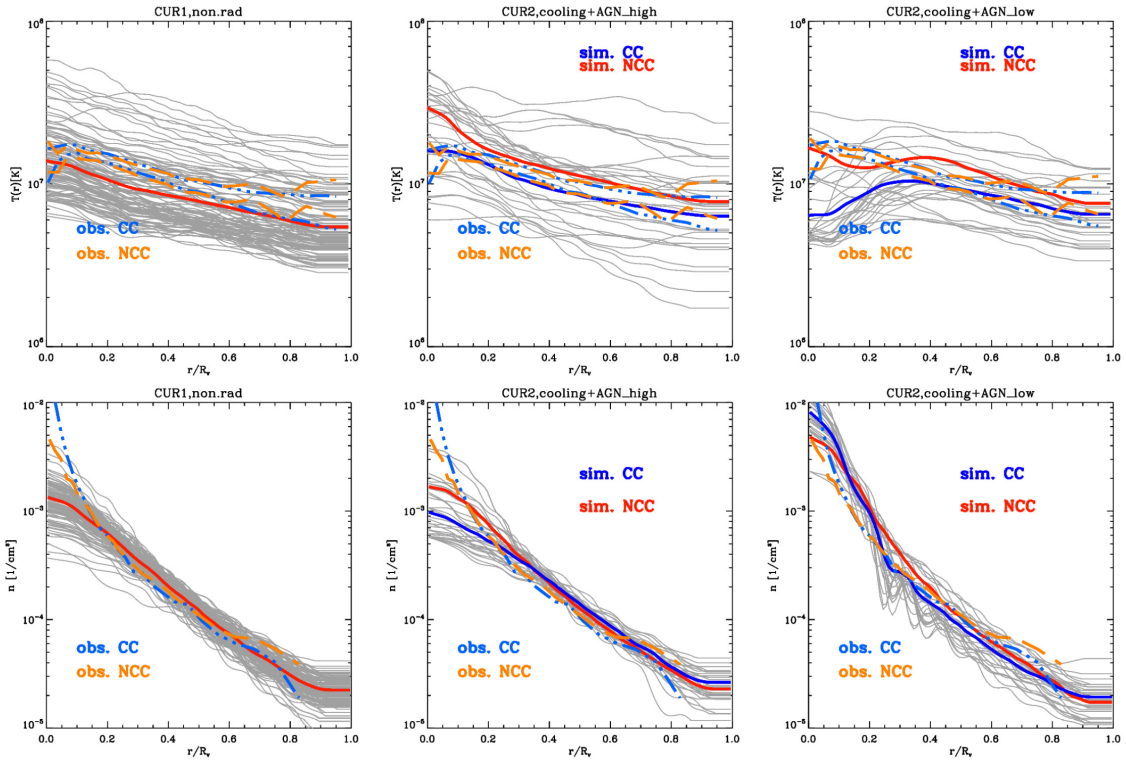

Figure 4.3: Radial profile of gas temperature and density for all simulated clusters with $M_{\rm vir} \geq 10^{14}\ M_{\odot}$ in the 300^3 Mpc^3 volume of the CUR1 run (non-radiative) and in the 150^3 Mpc^3 volume of the CUR2 run (with cooling and two AGN feedback modes). The profiles of individual objects are shown in gray, while the $\pm\sigma$ around the mean profile of the sample are drawn with continuous lines (red lines for the NCC-like, blue line for the CC-like or the non-radiative clusters). The additional lines shows the $\pm\sigma$ around the mean profile of CC (dashed light blue) or the NCC (dot-dashed orange) from observations (Eckert et al., 2012; Planck Collaboration et al., 2013).

As expected, clusters in non-radiative runs closely follow the self-similar scaling, $M \propto T^{3/2}$, while the cooling+AGN runs show significant departures from self-similarity. The run with lower redshift AGN feedback produces significant overcooling in small-size halos, which produces a *flattening* of the (T, M) relation. In these runs the AGN feedback is just sufficient to quench the cooling flow, but most clusters below $M_{500} \leq 10^{14}\ M_{\odot}$ are too cold compared to observations. On the other hand, the run with early AGN feedback produce a scaling relation which is in better agreement with observations, with hints of a steepening for $M_{500} \leq 10^{14}\ M_{\odot}$. No objects with a central temperature below ~ 0.5 keV are formed in this case. The scatter in temperature is also increased due to the intermittent AGN activity.

We conclude that our fiducial AGN model is suitable to produce clusters with a realistic mass-temperature (and hence gas energy) relation, and can therefore represent a robust baseline model to test the outcome of different CR-acceleration models against FERMI data. However, the lack of spatial resolution and physics at the scale of galaxies in these runs makes

it impossible to model star formation and star feedback (both energetic and chemical), and to properly compare the outcome of this against observed relations (e.g. Planelles & Quilis, 2013; Rasia et al., 2015; Hahn et al., 2015, for recent reviews). In the Appendix (Sec. 4.B), we also show that the impact of CRs on the X-ray scaling relations is negligible in both tested acceleration models.

In Fig. 4.3, we show the average radial profiles of gas temperature and density for our clusters, for the CUR1 and the CUR2 run with cooling and high redshift AGN feedback. The results are compared to the observed mean profiles of gas density and temperature (Eckert et al., 2012) and pressure (Planck Collaboration et al., 2013) derived from X-ray and SZ observations of nearby clusters (Eckert et al., 2012; Planck Collaboration et al., 2013). Observations reported the consistent detection of a bimodal gas distribution in clusters having a cool-core (CC) or a without it (NCC), which shows up prominently as a difference of the innermost density, temperature and entropy profiles (e.g. De Grandi & Molendi, 2001; Cavagnolo et al., 2009; Hudson et al., 2010) as well as a smaller large-scale radius difference in density (Eckert et al., 2012).

We therefore split our cluster samples into CC and NCC classes based on the central temperature gradient observed in each object at $z = 0$. This is one of the several possible working definitions proposed in the literature (e.g. Hudson et al., 2010), which work well for the coarse resolution we have for the central regions of the the lowest mass systems in the sample. The gradient is defined as $\Delta T = T(r + \Delta r) - T(r)$ based on the spherical mass-weighted temperature profile, $T(r)$, and we consider a cluster CC-like if $\Delta T \geq 0$ in the first radial bin, or NCC-like otherwise.

All objects with $M_{\rm vir} \geq 5 \cdot 10^{13}\ M_{\odot}$ of the non-radiative CUR1 dataset are considered as NCC according to this criterion. In the CUR2 sample with cooling and low redshift feedback case, we find a NCC/CC ratio close to 0.5, yet all our objects are characterized by a too large central density, similar to or exceeding the one of CC systems. On the other hand, with the adoption of cooling and efficient feedback the ratio becomes NCC/CC ~ 0.32, i.e. quite close to observations (i.e. ≈ 0.39, Hudson et al., 2010).

While the gas density profiles of clusters with different masses can be averaged, in averaging the temperature profiles we normalized each profile at R_{500}, based on the self-similar $T_{500} \propto M_{500}^3/2$ relation (e.g. Eckert et al., 2013). The large-scale trends of thermodynamical quantities are reproduced reasonably well by our runs. The cluster population in the CUR1 non-radiative run present an overall good match of the observed profiles in the range $0.1 \leq R/R_{\rm vir} \leq 0.9$, but cannot reproduce the CC/NCC bimodality. The cluster population of the CUR2 run with cooling and early feedback does a similarly good job and shows hints of the CC/NCC bimodality. However, in this case the innermost density/pressure profile is underestimated compared to observations, due to the fact that the average cluster mass in this smaller volume is smaller and an increasing ratio of clusters has a core which is relatively

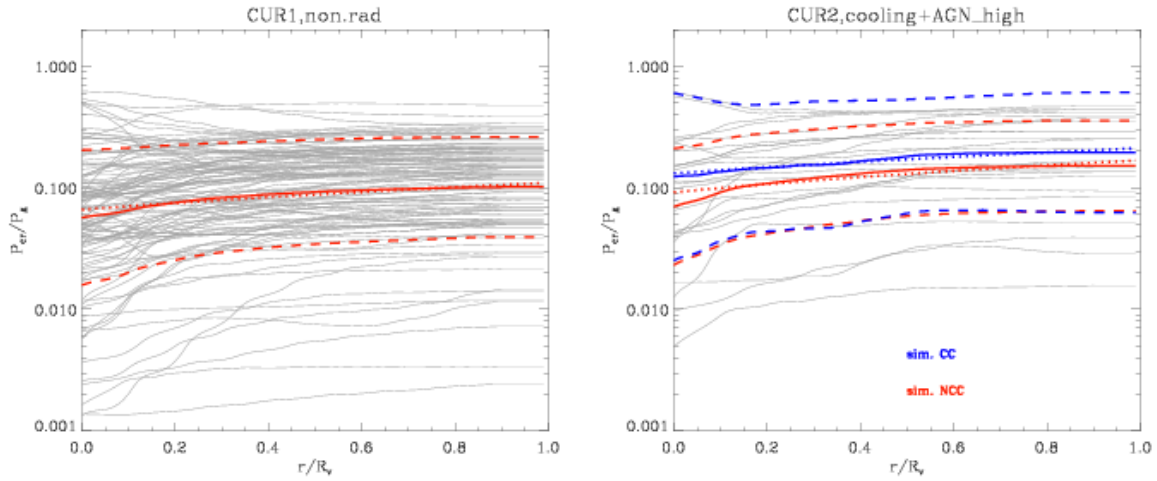

(a) (b)

Figure 4.4: Average radial profile of the CR to gas pressure ratio for all simulated clusters in the CUR1 and CUR2 run with cooling and feedback, in all cases for the Kang & Ryu (2013) model of CR acceleration. The gray lines give the profiles of individual clusters while the coloured lines give the mean and the $\pm\sigma$ dispersion. The additional thin coloured line dotted lines give the best fit for the average profiles, with parameters given in Tab. 4.2.

poorly resolved compared to the CUR1 run, where many larger clusters are formed. We stress that while this effect may cause an underestimate of the hadronic γ-ray emission from the innermost regions (as this scales as $\propto n^2$) the effect is overall not large because typically only ≤ 10 % of the γ-emission is produced within $\leq 0.1\ R_{\rm vir}$ (see Sec. 4.B). On the other hand, the cluster population in the CUR2 run with low redshift feedback produces typically too cold and dense CC clusters compared to observations, as an effect of overcooling.
In summary, the comparison with observations suggests that the clusters in the non-radiative CUR1 run as well as in the cooling+AGN CUR2 run can be further used to study cosmic ray acceleration. These cluster populations are representative enough of the global ICM properties for a wide range of masses/temperature to allow a comparison with FERMI observations in a similar range of masses. In particular, while clusters in the CUR1 can best represent the high-mass end of the observed distribution ($\geq 5 \cdot 10^{14}\ M_\odot$), the clusters in the CUR2 run can be used to better study the CC and NCC populations in the lower mass end.

4.3.2 Cosmic-Ray Properties

We extracted the spatial distribution of CR-energy for each simulated cluster at $z = 0$, and estimate the relative pressure ratio of CRs compared to the thermal gas pressure. This is computed by integrating the total pressure of CRs within increasing radii, and dividing this by the total gas pressure within the same radius, $X(R) = P_{\rm cr}(< R)/P_{\rm g}(< R)$. The pressure of

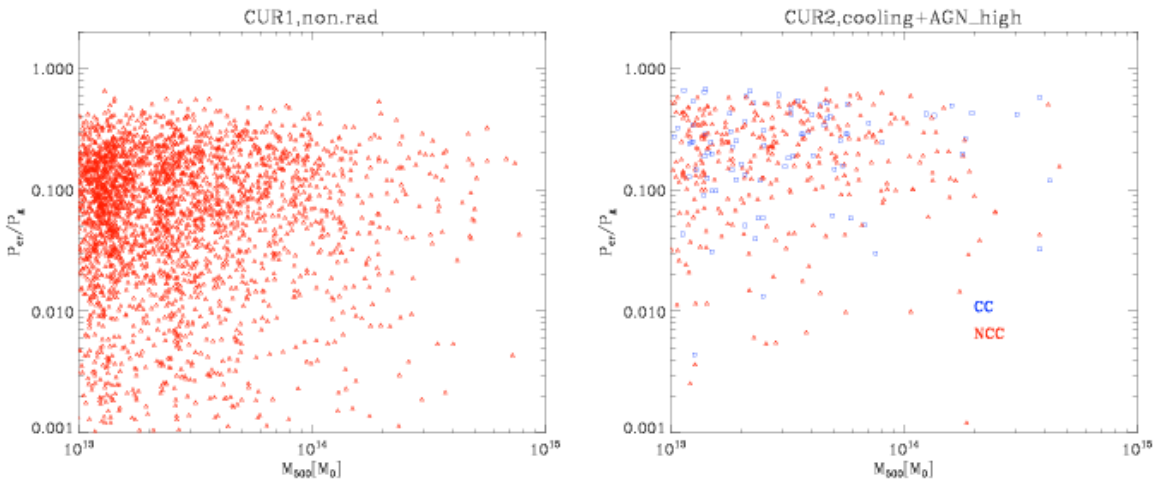

(a) (b)

Figure 4.5: Average enclosed pressure ratio of CR and gas for simulated clusters at $z = 0$. The top panel shows the distribution for the CUR1 run, the bottom panel shows the distribution for the CC- and NCC-like clusters in the CUR2 run with cooling and high redshift AGN feedback.

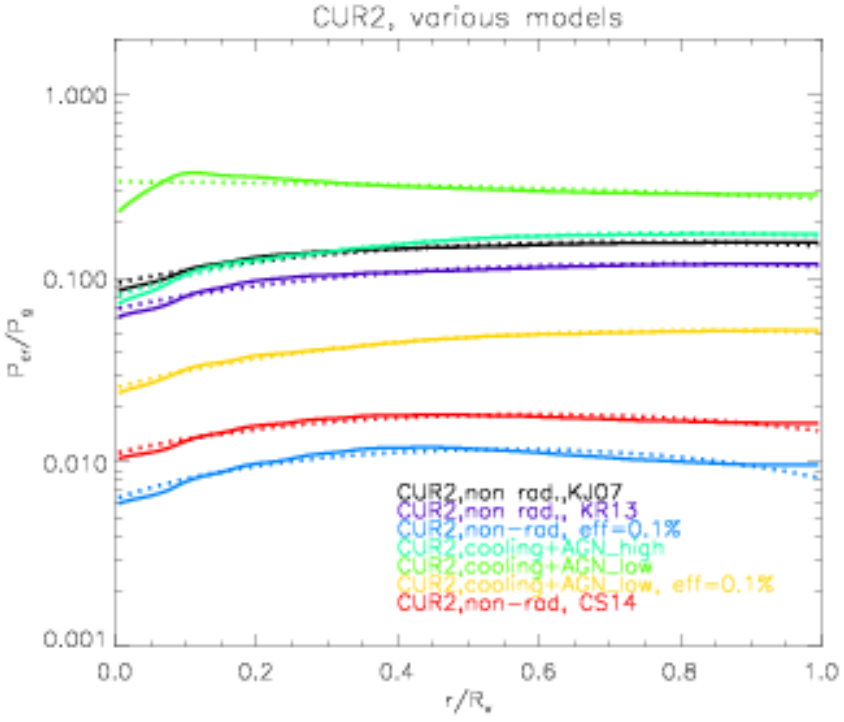

Figure 4.6: Average profile of $X(R)$ for all $M \geq 10^{14}$ $M_\odot$ clusters in the CUR2 run, comparing different physical prescriptions for CRs and baryons. The dotted lines give the best fit relation for each model, with parameters given in Tab.2, whereas the dashed lines give the $\pm 1\sigma$ standard deviations on the average profiles.

CRs is $P_{\rm CR} = (\Gamma_{\rm CR}-1)E_{\rm CR}$, where $E_{\rm CR}$ is the primitive variable simulated with our two-fluid method (Sec. 4.2.1). We consider the ultra-relativistic equation of state for CRs, $\Gamma_{\rm CR} = 4/3$, and therefore the pressure ratio can be written as $X = P_{\rm CR}/P_{\rm g} = [(\Gamma_{\rm CR}-1)/(\Gamma-1)]E_{\rm CR}/E_{\rm g} = 0.5E_{\rm CR}/E_{\rm g}$.

The panels of Fig. 4.4 give the profiles of $X(R)$ of the simulated clusters at $z = 0$, Here we limit to the CUR1 run and to the CUR2 radiative run with high redshift AGN feedback, where we further split the sample into CC-like and NCC-like objects. The average profiles are always very flat up to the virial radius, and are well fitted by a 2nd order polynomial,

$$X(R) = X_0 + \alpha_1 \frac{R}{R_{\rm vir}} + \alpha_2 (\frac{R}{R_{\rm vir}})^2, \tag{4.1}$$

with best fit parameters given in Table 2 for all runs.

On average, the pressure ratio in the core of NCC-like clusters is $\sim 5-7$ %, while this is ~ 10 % in CC-like clusters, while in all cases this ratio settles to $\sim 10-15$ % at $R_{\rm vir}$. However, the scatter in the cluster samples is rather large, as shown in Fig. 4.5 where we show the relation between the cluster mass within R_{500} and the total enclosed CR-to-gas pressure. The data does not show a tight correlation of X with cluster mass or cluster average temperature (not shown), and for every mass bin variations of the ratio in the range $X \sim 10^{-3} - 0.3$ can be found. This is at variance with the earlier results by (Pinzke & Pfrommer, 2010), based on a different numerical methods, where a tight decreasing correlation of X with the host cluster mass is found. The extreme flatness of our profiles is also not in agreement with earlier SPH results (Pfrommer et al., 2007), while it is much more similar to more recent SPH simulations (Pinzke & Pfrommer, 2010), indicating that numerical details play a significant role in the spatial distribution of CRs. We give our interpretation for this comparison in Sec. 4.4.

Fig. 4.6 shows the average profile of CR-to-gas pressure ratio for all $M \geq 10^{14}\ M_{\odot}$ clusters at $z = 0$, where we compare the outcome of the different models for gas and CR physics. The best-fit parameters in this case are given in the lower half of Table 4.2. Basically all models predict the same flat shape, with a minimum of $X(R)$ in the cluster core. In this set of models we also show the case of a *fixed* (re)acceleration efficiency of $\eta = 10^{-3}$ and of the approximated acceleration model we derive from Caprioli & Spitkovsky (2014a). In the $\eta = 10^{-3}$ model, both radiative and non-radiative runs also predict a very flat profile outside of clusters core, with a minimum of $X \approx 0.6$ % in the non-radiative run and $X \approx 2$ % in the cooling and AGN case. The fact that the same fixed acceleration efficiency gives a ~ 5 times increased CR-to-gas pressure ratio stresses how much baryon physics can affect the modelling of CRs in the intracluster medium, and the quantitative interpretation of γ-ray data (see Sec. 4.3.3). The profiles obtained with the Caprioli & Spitkovsky (2014a) model have a similar shape, with a ~ 2 higher normalisation.

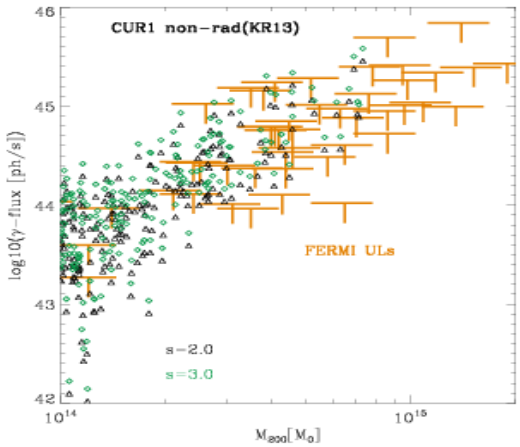

(a)

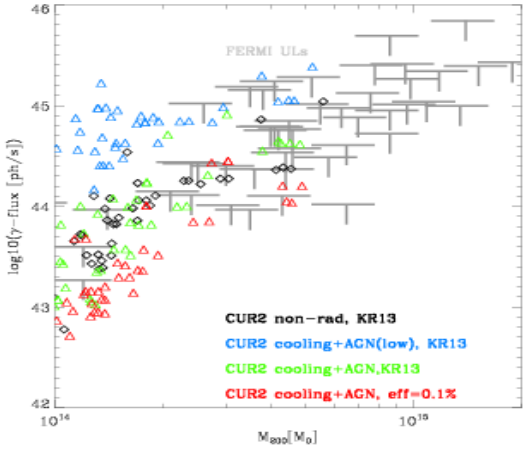

(b)

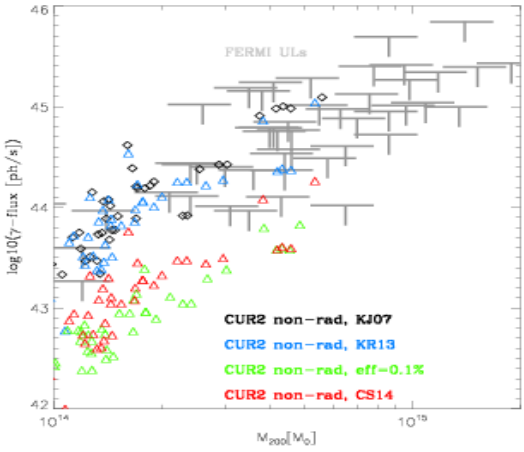

(c)

Figure 4.7: Hadronic emission for our simulated clusters at $z = 0$, in the 0.2-200 GeV energy range. Top panel: γ-emission for clusters in the CUR1 box, assuming CR-spectra of $s = 2.0$ or $s = 3.0$. Centre: γ-ray emission from clusters in the CUR2 runs, for different models of gas physics. Bottom: γ-ray emission from clusters in our non-radiative CUR2 run, for runs with different acceleration efficiency of CRs. The gray symbols are the upper limits from the FERMI catalog in the same energy range.

run	X_0	α_1	α_2
CUR1	0.056	0.099	-0.055
CUR2, cool+AGN high (CC)	0.117	0.162	-0.082
CUR2, cool+AGN high (NCC)	0.072	0.198	-0.116
CUR2, cool+AGN low (CC)	0.497	-0.373	-0.192
CUR2, cool+AGN low (NCC)	0.367	-0.030	-0.044
CUR2, non-rad, KJ07	0.094	0.170	-0.113
CUR2, non-rad, KR13	0.068	0.132	-0.084
CUR2, non-rad, 10^{-3}	0.006	0.019	-0.017
CUR2, non-rad, CS14	0.011	0.023	-0.020
CUR2, cool+AGN high, KR13	0.079	0.244	-0.155
CUR2, cool+AGN low, KR13	0.334	-0.012	-0.052
CUR2, cool+AGN high, 10^{-3}	0.025	0.067	-0.038

Table 4.2: Best fit parameters for the X, R relation for clusters in the CUR1 and CUR2 run, assuming $X(R) = X_0 + \alpha_1(R/R_{\rm vir}) + \alpha_2(R/R_{\rm vir})^2$. In the upper half of the table, we give the best fit for the CC and NCC-like clusters separately, in radiative runs. The lower half of the table gives the best fit parameters limited to all $M \geq 10^{14}\ M_\odot$ clusters in the CUR2 runs.

4.3.3 Hadronic γ-Ray Emission from Simulated Cluster Samples

The hadronic emission from the CRs population of each simulated cluster is computed following the standard formalism of Pfrommer & Enßlin (2004); Donnert et al. (2010, and), with the only difference that for the hadronic cross-section we use the parametrisation of the proton-proton cross section given by Kelner et al. (2006), as in Huber et al. (2013b). A recent review of the method is given in Vazza et al. (2015a). Our 2-fluid formalism cannot follow particle spectra and therefore we have to guess a fixed spectral energy distribution of CRs in the simulated volumes. We consider here the large $0.2 - 200$ GeV energy range to be less sensitive to the exact spectral energy distribution of CRs, which is not directly simulated in our method. The first panel of Fig. 4.7 shows the distribution of the predicted emission as a function of the cluster mass for the non-radiative clusters of the CUR1 run, where we computed the hadronic emission from each cluster for the cases of a fixed $s = 2.0$ (corresponding to a γ-ray spectrum of $s_\gamma \approx 2.5$ at high energy[1]) and $s = 3.0$ ($s_\gamma \approx 3.33$). We notice that here we assume slightly steeper spectra compared to Pinzke & Pfrommer (2010), who found nearly universal energy spectra compatible with $s \approx 2.3$ for most of the CR-energy range. In our case, these estimates follows from the distribution of CR-energy injected by merger shocks seen in these simulations (Vazza et al., 2009a, 2010a, 2011b), and are also confirmed by our tracer-based modelling of the following Section (Sec. 4.3.4). In all cases, considering the large energy range used here to compare with FERMI data, the effect of the spectral shape is not big in our predictions and the total photon flux is only varied by a ~ 50 % going from $s = 2.0$ to $s = 3.0$, not a big effect. Our predictions are compared to the observed upper

[1] s_γ is the spectrum of the γ-ray emission and is given by $s_\gamma = 4(s - 1/2)/3$ (e.g. Pfrommer & Enßlin, 2004).

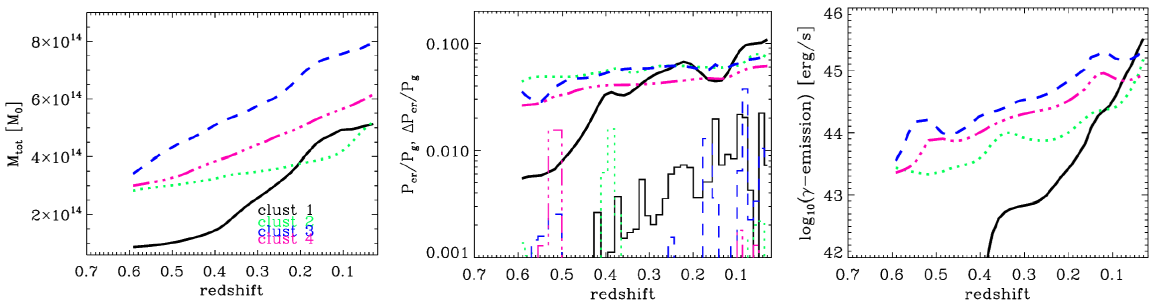

Figure 4.8: Evolution of four clusters with a final mass $\geq 5 \cdot 10^{15}\ M_{\odot}$ in the CUR1 volume. From left to right the image shows: the enclosed total mass with fixed 6^3 Mpc^3 comoving volumes; the total CR to gas pressure ratio (thick lines) and the relative CR pressure increment snapshot by snapshot (think lines);c the total hadronic γ-ray emission from the same volumes.

limits from the FERMI satellite, within the same energy range, obtaining by converting each limits on the received photon flux into a limit on the absolute luminosity at the distance of each object. For ~ 50 % of simulated clusters the predicted emission is at the level or above the upper limits from FERMI observations.

The effect of different prescriptions for gas physics or CR physics is shown in the lower panels of Fig. 4.7. Radiative feedback worsens the comparison with observations, by producing typically denser gas cores (CUR2 run with low redshift feedback) or by increasing the number of shocks connected to AGN feedback (CUR2 run with high redshift feedback). The use of the (higher) acceleration efficiency assumed in Kang & Jones (2007) obviously produces an even higher hadronic flux. The approximated version of the Caprioli & Spitkovsky (2014a) acceleration model significantly reduces the number of objects above FERMI limits, but does not to entirely solve the problem as still $\sim 10 - 20$ % of simulated objects are above FERMI limits. We found that only by limiting the overall acceleration efficiency of shocks to $\eta = 10^{-3}$ for all Mach numbers, the predicted hadronic emission goes below the FERMI limits in the non-radiative case, while the fraction of clusters that is inconsistent with FERMI limits is now limited to ≤ 10 % in the cooling+AGN feedback case. In the latter case, these high γ-ray emitters are the densest CC-like objects in the volume.

All models vary with mass in that the hadronic emission scales as $\epsilon_{\gamma} \propto M^{5/3}$, with normalisation varying with the physical model and a $\sim 1 - 2$ dex scatter around the mean relation that increases going to the lowest masses. While the $\propto M^{5/3}$ relation is in line with earlier results by Pfrommer (2008) and Pinzke & Pfrommer (2010)[2], the level of scatter we observe is significantly larger.

To understand the origin of this large scatter we focus on 4 clusters in the largest CUR1 box,

[2]The $\sim 5/3$ exponent can be understood if the average CR to gas energy ratio is a constant, in which case the total γ-emission scales as the thermal gas energy of the cluster, $\epsilon_{\gamma} \propto E_{\rm g} \int_V nX$, and $E_{\rm g} \propto M^{5/3}$ in virialised clusters (e.g. Vazza et al., 2006).

with large final masses ($\geq 5 \cdot 10^{14}\ M_{\odot}$) but different dynamical histories. For each of these objects we analyzed 50 snapshots equally spaced in time from $z = 0.6$ to $z = 0$, and extracted the mean properties of gas and CRs within fixed comoving volumes centred on each object. Fig. 4.8 gives the evolution of the total enclosed mass, of the CR to gas pressure ratio (including the CR pressure ratio generated by the injection of CRs over each single snapshot), and of the enclosed γ-ray emission. The evolutionary tracks of these clusters show that the total cluster mass is not the only variable that sets the γ-ray emission, but also the mass accretion rate induces significant scatter on top of the global $\epsilon_{\gamma} \propto M^{5/3}$ relation. For example, cluster 1 has the final smallest mass in this sample, but the highest hadronic emission at $z = 0$, because it has been rapidly assembled during $z = 0.4 - 0.2$ in a merger event. This led to an increase of the number of shocks, to enhanced injection of CRs and to a nearly $\sim 10^4$ times increased γ-ray emission from $z = 0.4$ to $z = 0$. On the other hand, the hadronic emission of more massive but more relaxed clusters 3 and 4 is only increased by $\sim 10^2$ from $z = 0.6$ to $z = 0$. Cluster 2 experiences a major merger late in its evolution ($z \leq 0.1$), which leads to a ~ 10 times increase of hadronic emission over the last ~ 1.5 Gyr. These different evolutionary paths show that the hadronic emission in our clusters can vary by a few orders of magnitudes during the typical crossing time of clusters, due to the enhanced injection of CRs and due to the gas compression of the ICM during mergers. Cooling and AGN feedback further add a source of scatter to the relation with the host cluster mass. We further elaborate on the variance of our results compared to Pfrommer (2008) and Pinzke & Pfrommer (2010) in Sec. 4.4.

4.3.4 Hadronic γ-Ray Emission from MACSJ1752

We finally focus on the resimulations of a major merger event leading to X-ray and radio morphologies similar to the observed cluster MACSJ1752.0+0440, which we already studied in Bonafede et al. (2012). Fig. 4.9 gives the merger sequence ($0.4 \geq z \geq 0.25$) for the simulated cluster, showing the projected X-ray brightness and the radio emission using the formalism by Hoeft & Brüggen (2007). Since the magnetic field is not included in our simulation, we assume that the energy in the magnetic field is everywhere $1/\beta = 1/100$ of the thermal gas energy within the cell, which gives $\sim \mu$G fields in this case. For the electron acceleration efficiency at shocks, we assumed that this is $10^{-3} \times \eta(M)$, where $\eta(M)$ is the acceleration efficiency by Kang & Ryu (2013).

The total virial mass of the system after the collision is $\approx 0.65 \cdot 10^{15}\ M_{\odot}$, while the mass ratio of the merger is $M_1/M_2 \sim 1.6$. At $z \sim 0.3$ the shock propagating downstream of the main cluster progenitor has $M \approx 4.5$ and produces a total radio emission of $P_{\rm radio} \sim 10^{26}$ erg/s/Hz at 325 MHz over an extent of ~ 1.5 Mpc, similar to observations. Downstream of the smaller cluster progenitor, also a second radio relic ~ 700 kpc wide and with a total power $P_{\rm radio} \sim$

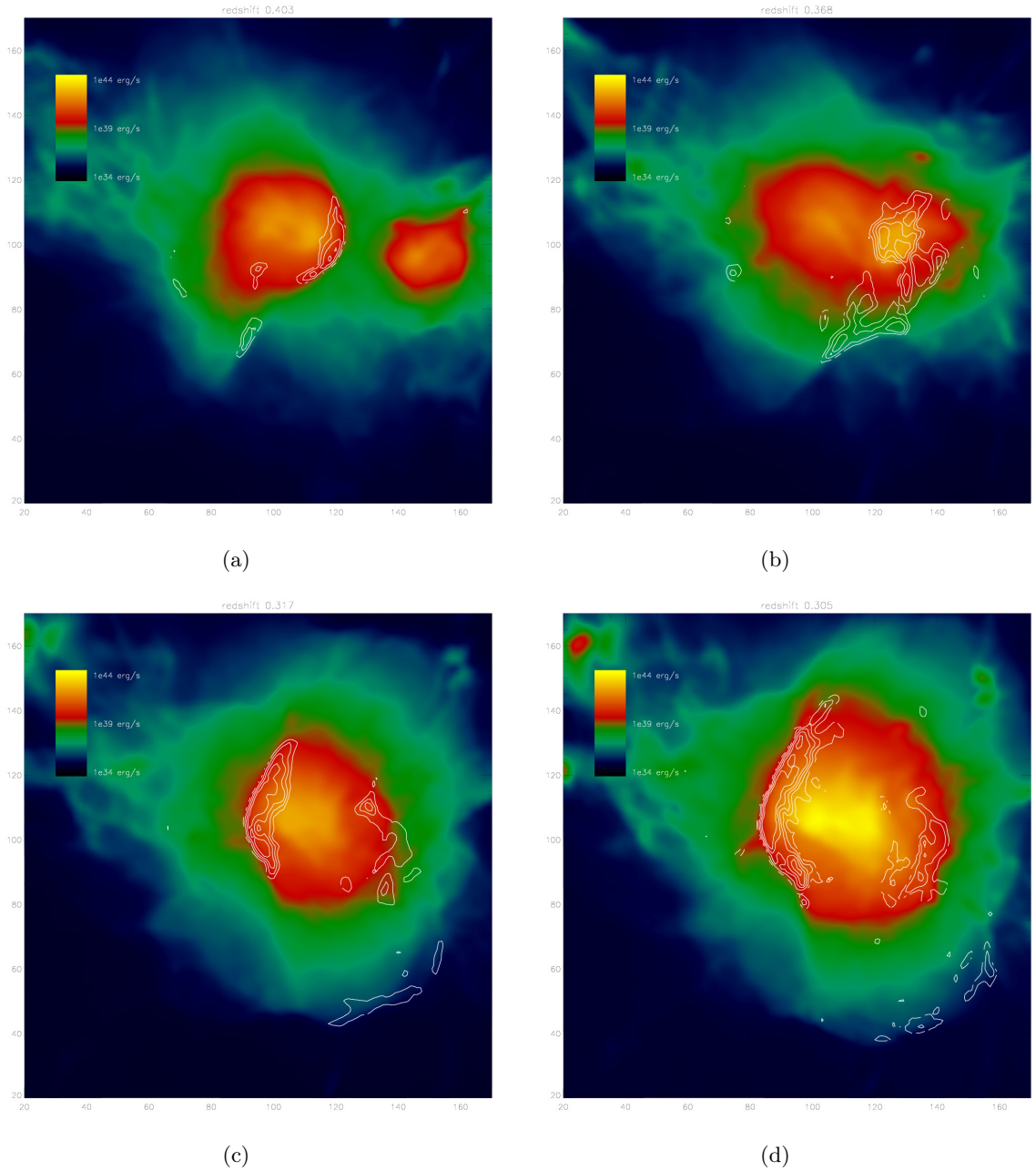

(a) (b)

(c) (d)

Figure 4.9: Simulated merger sequence for a $\sim 10^{15}$ $M_\odot$ cluster using AMR, with X-ray emission in colours and radio emission in white contours. The approximate epoch of the observed merger in MACSJ1752.0+0440 is $z \approx 0.3$. Each image is 5×5 Mpc^2 (comoving) across. The contours are equally spaced with $\sqrt{2}$ multiples of the radio emission, starting from $\approx 10^{23}$ erg/s/Hz per pixel.

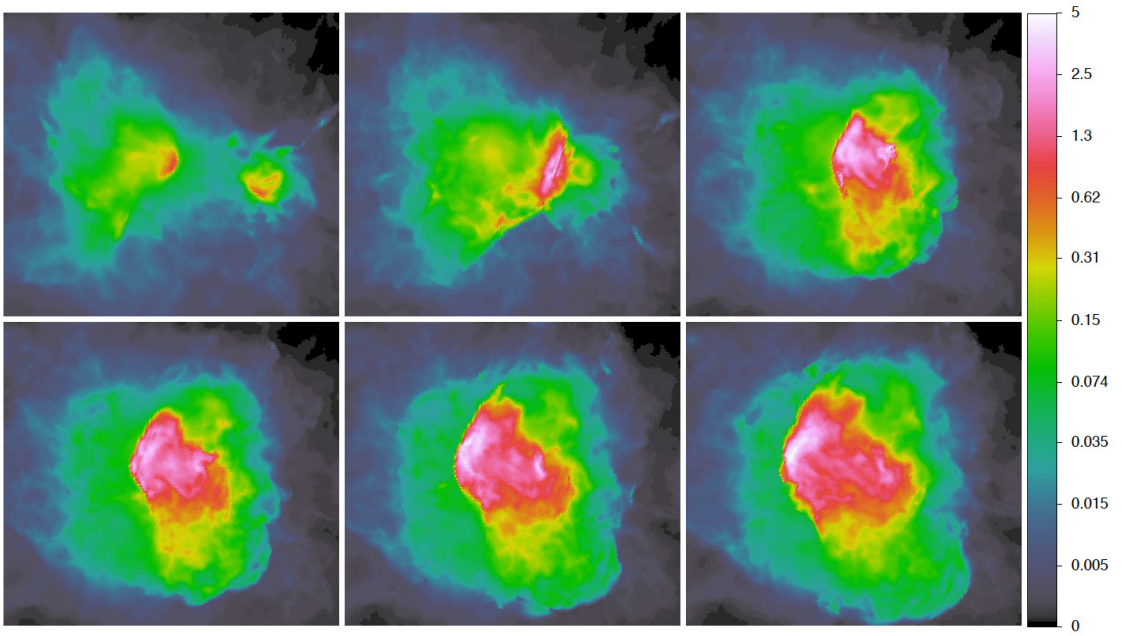

Figure 4.10: Merger sequence for our simulated versions of the cluster MACSJ1752.0+0440 using AMR for the same area of Fig. 4.9 and for the epochs of $z = 0.403$, 0.368, 0.317, 0.305, 0.294 and 0.281. The colours show the total projected CR-energy in code units.

$3 \cdot 10^{25}$ erg/s/Hz is formed. The double relic configuration observed in MACSJ1752.0+0440 at $z \approx 0.3$ should be produced ~ 0.8 Gyr after the central collision of the cores, and we use this epoch also to constrain the acceleration scenario of CRs based on the lack of γ-ray emission. The evolution of the projected CR-proton energy simulated with our two-fluid method in `ENZO` is given in Fig. 4.10, for the Kang & Ryu (2013) injection model. The late energy budget of CRs in the innermost cluster regions is clearly dominated by the injection through the $M \sim 4$ shock launched by the major merger at $z \approx 0.3$. However, on larger scales the CR-energy mostly results from the cumulative activity of previous formation shocks and can be considered as a background CR-energy distribution present regardless of the last major merger. We notice that, compared to our first study in Bonafede et al. (2012), the effect of the additional CR-pressure in this set of simulations results into a less satisfactory match of the simulated X-ray and radio emission compared to the observation. However, several significant features as the elongated a disrupted inner X-ray structure, the emergence of the double relic and the off-set of the least powerful relic respect to the merger axis are well reproduced. Given that the masses and the relative distances between the gas cores and the relics allow a reasonable reconstruction of the merger scenario, we consider this system an interesting case to test CR acceleration models against the FERMI limits for this system (Sec. 4.2.4).
While our two-fluid formalism only allows us to monitor the total CR-energy in each cell, with the complementary use of passive tracer particles we can better follow the spatial evolution

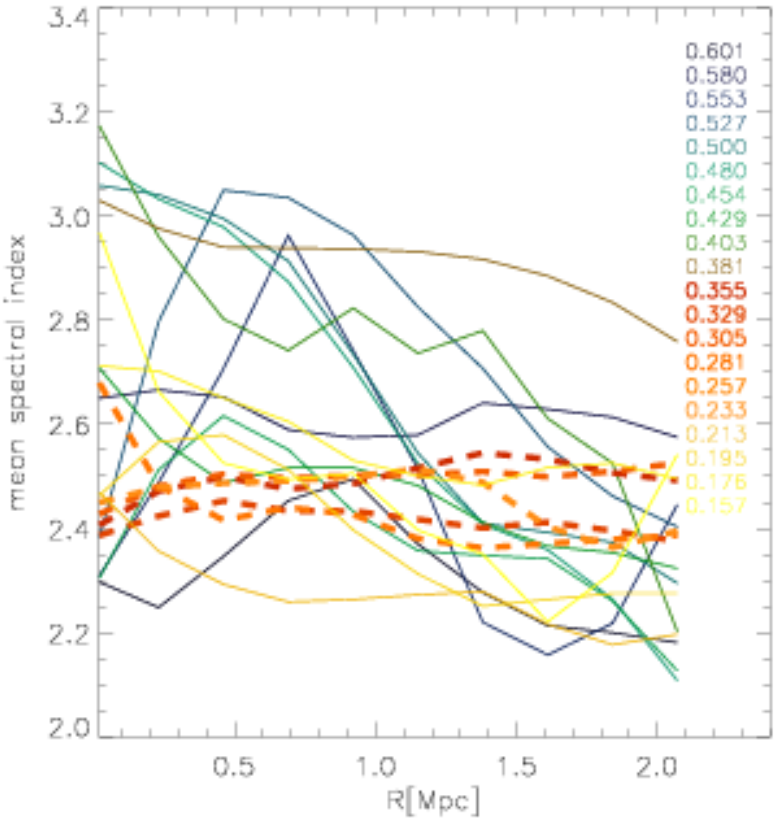

Figure 4.11: γ-ray emission weighted radial distribution of the spectral index of CR-energy in the AMR resimulation of MACSJ1752 for different redshifts (marked in different colours). The thick dashed lines marked the epochs closer to the observed radio emission.

of CRs in the ICM (e.g. Vazza, 2011). To this end, for one AMR run we saved ~ 50 equally time-spaced snapshots from $z = 1$ to $z = 0$ and we evolved the trajectory of passive tracers using the output 3-dimensional velocity field. The underlying assumption is that CRs can be treated as frozen into the gas as their spatial diffusion in negligible on these scales (~ 34 kpc). We injected in total $\approx 6 \cdot 10^6$ tracers at $z = 1$, with initial distribution proportional to the gas density in the `ENZO` run. Their positions were updated at every time step with explicit time integration and using the same Courant condition of the `ENZO` simulation. The tracer velocity was computed from the grid values at the tracer position using a CIC interpolation that includes a turbulent correction term to better model the mass flux. For each tracer we recorded the CR energy read from the grid, and evolved the spectral index of the CR-energy of each tracer integrating over all injected populations of CRs, assuming an injection spectrum of $s = 2(M^2 + 1)/(M^2 - 1)$. In the case of multiple shocks hitting a tracer, the final CR-spectrum kept the smallest slope given by the time sequence of shocks (e.g. Kang & Ryu, 2010), while the normalisation was updated based on the CR-energy, computed from the grid.

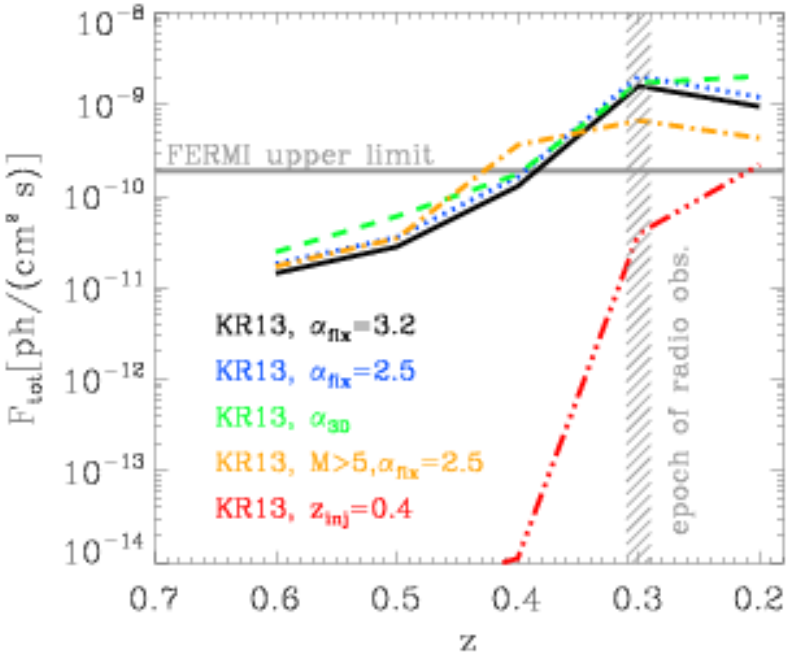

Figure 4.12: Evolution of the total hadronic γ-ray emission in the $0.2 - 100$ GeV energy range for the various resimulations of cluster MACSJ1752. The vertical hatched region shows the epoch of the observed X-ray/radio configuration, while the horizontal line marks the upper limits from FERMI on the hadronic emission from this cluster.

With this approach we can monitor the spatial evolution of CR spectra in the cluster and have a better modelling of the resulting γ-ray emission. More details on the tracers algorithm will be given in a forthcoming paper, by Wittor et al. (in preparation).

Fig. 4.11 shows the average γ-ray emission weighted profile of CR-spectra for this cluster at different redshifts, with the thick dashed lines marking the epochs around the merger event.The average spectrum of CRs is initially steep in the cluster centre, $s \approx 3$ and flatter in the outskirts, $s \approx 2.2$, mirroring the typical distribution of shocks in clusters, which are weaker in the centre and stronger outwards (e.g. Vazza et al., 2011b). Later on, with the progress of the merger the spectrum flattens everywhere as the $M \sim 4 - 5$ shock sweeps the intracluster volume. At the approximate epoch of the X/radio observation, the average spectrum has a flat distribution around $s \sim 2.4 - 2.5$, with significant fluctuation patches spread over the cluster volume.

As a final result, the evolution of the predicted γ-ray emission for a few scenarios for CRs is given in Fig. 4.12. Here we show the hadronic emission obtained using fixed CR-spectra of $s = 2.5$ or $s = 3.2$, or directly using the 3D spectral information from the tracers. Despite fluctuations of order $\sim 2 - 3$ in the total emission, the FERMI limits derived in Sec. 4.2.4 are in all cases exceeded by a factor ~ 10 at the epoch of the radio observation of

MACSJ1752.0+0440. It is not only the major merger that is responsible for the boost of the γ-emission: in an additional run assuming the Kang & Ryu (2013) model we only allowed the injection/re-acceleration of CRs by $M \geq 5$ shocks. In this case, the hadronic emission is greatly reduced compared to all previous models, yet the FERMI limits are still exceeded by a factor $\sim 2-3$ at $z = 0.3$. Finally, as a simple test we rerun the AMR simulation by imposing that the acceleration of particles only begins at $z = 0.4$, i.e. when the major merger begins. The hadronic emission ramps up during the merger, yet the predicted emission at $z = 0.3$ is below the constraints by FERMI. This confirms that while the injection of CRs during a merger can significantly boost the hadronic emission from the ICM, the problem of simulated models to full fill FERMI constraints more generally stems from the assumed CR-enrichment across the full structure formation process. Our findings here for MACSJ1752.0+0440 are also consistent with the semi-analytical model we presented in Vazza et al. (2015a), where the predicted hadronic emission resulting from the major merger is ~ 10 % of the FERMI limit for this object. However, in the case of a few closer systems with relics such as A3367, ZwCLJ2341, A754 and A2256, the limits by FERMI are challenged even by considering the last merger only (see Vazza & Brüggen, 2014; Vazza et al., 2015a, for more details).

4.4 Discussion

Both our non-radiative and radiative runs produce galaxy clusters with a budget of CRs in tension with the latest FERMI limits (e.g. The Fermi-LAT Collaboration et al., 2013), suggesting the necessity of a revision of the acceleration efficiency from DSA in cosmic shocks. These conclusions are in line with the results of our previous semi-analytical modelling of double relics (Vazza & Brüggen, 2014; Vazza et al., 2015a) and put typically stronger constraints on the acceleration of CRs by cosmic shocks compared to previous works based on simulations (e.g. Ryu et al., 2003; Kang et al., 2007; Pfrommer et al., 2007; Pinzke & Pfrommer, 2010; Vazza et al., 2012a, 2013).

We can briefly discuss possible explanations for this finding. First, the real efficiency from diffusive shock (re)acceleration of protons by weak shocks ($M \leq 5$) is $\sim 10-100$ times below the current estimates from DSA. This is reasonable as the latest results of particle-in-cell and hybrid simulation of cosmic shocks are revising downwards the estimates of CR-protons acceleration efficiency (Caprioli & Spitkovsky, 2014a; Guo et al., 2014a). Our test based on the Caprioli & Spitkovsky (2014a) acceleration model shows that the tension with FERMI is alleviated if the overall DSA acceleration efficiency is revised downwards assuming that only quasi-parallel shocks efficiently accelerate CR-protons, and that the acceleration efficiency is $\sim 1/2$ of what derived in Kang & Ryu (2013). However, in this case the acceleration mechanism in radio relics must be different from DSA, due to the too large electron-to-proton ratio ($K_{\rm e/p} > 10^{-2}$) needed to explain the data (Vazza & Brüggen, 2014; Brunetti & Jones, 2014;

Vazza et al., 2015a). The shock-drift-acceleration mechanism may indeed lead to this result, as shown by Guo et al. (2014a,b). However, due to computational limitations it was impossible to reach the full FERMI I acceleration regime, and therefore the acceleration efficiency of electrons is not yet well constrained in this scenario.
On the other hand, aged relativistic electrons that are reaccelerated by shocks can solve the problem (e.g. Pinzke et al., 2013; Kang & Ryu, 2015), but only if the electrons have been injected by leptonic-dominated jets from radio galaxies (or other leptonic scenarios). If instead the aged electrons are assumed to be the result of previous injection by cosmic shocks, the problem is even exacerbated (Vazza & Brüggen, 2014; Vazza et al., 2015a). In addition, the acceleration efficiency from DSA might be a steep function of the up-stream magnetisation level, i.e. for typical intracluster or intergalactic magnetic fields below some given threshold the acceleration efficiency might drop. This would limit the injection of CRs to some fraction of the intracluster volume, where the magnetic field is amplified, and to the fraction of the cosmic time where cosmic magnetic fields have grown enough (e.g. Brüggen et al., 2005; Dolag et al., 2008b; Widrow et al., 2012; Vazza et al., 2014a). However, assessing the limiting magnetic field needed to produce DSA in these regimes is difficult, also because upstream magnetic fields might be always amplified by a CR-driven dynamo (Drury & Downes, 2012; Brüggen, 2013; Park et al., 2015). While in this work we could only explore the impact of magnetic fields in a very crude way (CS14 model) by assuming they are randomly oriented in space, we defer to future work with MHD simulations (Wittor et al., in prep), that will exactly address this issue.
Finally, we discuss the main limitations of our modelling and the comparison with the literature.

- *Comparison with SPH results.* Our distribution of the CR-to-gas pressure ratio is at variance with SPH (Pinzke & Pfrommer, 2010), who found a much tighter relation between the host cluster mass. We find instead that mergers boost the ratio up to $\sim 1-2$ orders of magnitude. This is mostly due to the steeper acceleration efficiency model we assume here (Kang & Ryu, 2013). For example, our acceleration efficiency goes from $\approx 10^{-5}$ at $M = 2$ to $\approx 10^{-2}$ at $M = 3$. On the other hand, in the model by Enßlin et al. (2007) the acceleration efficiency goes from ≈ 0.01 to ≈ 0.2 in the same range of Mach numbers, i.e. their acceleration efficiency is $\sim 10 - 10^2$ times larger than ours. Therefore, our model for CRs is more sensitive to the rare $M \geq 3$ shocks driven by mergers, while in Pinzke & Pfrommer (2010) the injection of CRs is overall more constant over time because also $M < 3$ shocks inject significant CRs. Additionally, the way in which gas (and the frozen-in CRs) is transported in the central core of clusters simulated with grid and SPH methods is known to be different (e.g. Frenk et al., 1999; Springel, 2010; Vazza, 2011; Vazza et al., 2011b; Sijacki et al., 2012; Schaller et al., 2015) and this can further amplify differences in the budget of CRs in the cluster centre.

- *Comparison with grid results.* Compared to the earlier work by Miniati et al. (2001) and Miniati (2003) we improve on the spatial resolution by $\sim 2-4$ times and the total number of simulated clusters by $\sim 10^2$ times. The hydro scheme we applied is also different, and the CRs have a dynamical impact on the gas evolution, while they are passive in Miniati et al. (2001) and Miniati (2003). Our main findings however, including the cluster to cluster scatter, are basically in line with these previous results.

- *Comparison with semi-analytical results.* The results of this work are overall in agreement with our recent modelling of CRs acceleration in double relics using semi-analytical methods (Vazza & Brüggen, 2014; Vazza et al., 2015a). There we limited our analysis to the (re)acceleration of electrons and protons by the merger shocks which should be responsible for the observed radio emission, and therefore we had to neglect the previous enrichment of CRs during structure formation. Even in this case, we find that overall the acceleration efficiency of protons must be limited to $\leq 10^{-3}$ for the range of Mach numbers inferred by radio spectra, $M \sim 2-5$.

- *Spatial resolution.* Our spatial resolution is the result of a compromise between the necessary detail on shocks and on the need of sampling large volumes. Earlier works (e.g. Ryu et al., 2003; Skillman et al., 2008; Vazza et al., 2009a, 2011b) show that a spatial resolution of $\sim 200-300$ kpc is enough to properly resolve the thermalisation by cosmic shocks. Our analysis of these simulated volumes (Vazza et al., 2014b) also shows that at the resolution of $\sim 100-200$ kpc the global properties of CRs are converged. Additional resolution tests are given in the Appendix.

- *Cooling and AGN feedback.* While we do not find a significant *direct* impact of AGN feedback and CR enrichment for the large scales of interest here, the cumulative effect of the cooling-feedback interplay can change the thermodynamical structure of the ICM and affect the CR-to-gas ratio and the γ-ray emission. Modelling AGNs in cosmological simulations is still challenging (Sijacki & Springel, 2006; Sijacki et al., 2009; Dubois et al., 2010; McCarthy et al., 2010), and so is the complex interplay between AGN injected CRs and the surrounding gas (Aleksić et al., 2012; Pfrommer, 2013; Vazza et al., 2013). However, our simulations show that including cooling and feedback *worsens* the comparison with FERMI limits. Therefore our main findings on the too large acceleration of CRs should be conservative against more complex models for the gas physics.

- *Limitations of CR physics.* Our runs do not include all possible interactions between CRs and gas and we assume that CRs do not diffuse neither stream out of the gas distribution. However, in Vazza et al. (2013) we tested that including CR-losses does not affect the distribution of CRs outside of cluster cores, while most of the γ-emission is mostly produced on larger scales. Additional mechanisms of (re)acceleration of CRs,

such as turbulent reacceleration (e.g. Brunetti & Jones, 2014), reconnection (e.g. Lazarian et al., 2015) and injection by AGN and supernovae (e.g. Völk et al., 1996) can only increase the budget of CRs estimated in our simulations. The spatial diffusion of CRs can modify the distribution simulated by our 2-fluid method (Berezinsky et al., 1997). Yet again, this cannot significantly affect our predicted γ-ray emission, which is spread across $\sim$ Mpc scales, while the diffusion of $\sim 1-10$ GeV protons over Gyrs can only affect $\sim 10-10^2$ kpc scales. Finally, the detailed calculation by Wiener et al. (2013) showed that even in a scenario in which CRs can stream out of the gas distribution faster than the Alfvén speed, the γ-ray emission is not affected in the energy range probed by FERMI, but only at much higher energies ($E = 300-1000$ GeV).

4.5 Conclusions

We simulated the acceleration of CRs by structure formation shocks, and focused on the observable γ-ray outcome of CRs in galaxy clusters. Our suite of simulations has been designed to simulate several realistic scenarios for CRs and gas physics, and to enable the testing for large complete samples of galaxy clusters (Vazza et al., 2014b).

- All tested CRs (re)acceleration models based on DSA predict a level of hadronic emission inconsistent with γ-ray observations. A significant fraction of our simulated clusters ($\sim 25-50$ % depending on the model) produce γ-ray emission above the upper limits reported by FERMI (Ackermann et al., 2010; Huber et al., 2013b; The Fermi-LAT Collaboration et al., 2013; Ackermann et al., 2014; Griffin et al., 2014; Zandanel & Ando, 2014).This result is robust against the variations in the gas physics that we have tested.

- Regardless of the models (with the exception of the unrealistic gas model producing overcooling within halos) we find that the average radial profile of CRs to gas pressure, $X(R)$, is well described by a simple 2nd order polynomial expression (Eq.1). In all models the profiles are very flat for $R \geq 0.2R_{\rm vir}$, and have a central normalisation X_0 depending on the acceleration model. This average profile can be useful for the inversion of FERMI data of clusters (e.g. Ackermann et al., 2014).

- Clusters of similar mass have a total pressure ratio X that varies up to a factor $\sim 10-10^2$ depending on their dynamical state. In non-radiative simulations, the main source of scatter is caused by mergers, which inject new CRs and boost the hadronic emission. In radiative simulations, cooling and feedback can also increase the CR-to-gas pressure ratio by lowering the gas temperature and by triggering stronger shocks from the innermost cluster regions of CC-like clusters.

- The different average CR-to-gas pressure ratio in clusters with similar mass, due to their different dynamical history, suggests that the present FERMI limits are actually constraining the total budget of CRs in the average cluster population to a deeper level than usually assumed. Indeed, the non-detection of hadronic emission mostly puts a constrain on the budget of CRs in the active systems, which must be limited to $X \sim 1$ % to be consistent with FERMI limits (Huber et al., 2013b; The Fermi-LAT Collaboration et al., 2013; Ackermann et al., 2014; Griffin et al., 2014). However, given the range of scatter in X across our simulated clusters, we conclude that in more relaxed systems this ratio must be even lower, $X \sim 0.1$ %, i.e. nearly ten times below the average limit given by the modelling of FERMI stacking (Huber et al., 2013b; The Fermi-LAT Collaboration et al., 2013).

- This result suggests that the (re)acceleration efficiency assumed for CRs must be significantly scaled down compared to all models tested here, which are derived from diffusion-convection simulations of DSA (Kang & Jones, 2007; Kang & Ryu, 2013). Revising the acceleration efficiency by Kang & Ryu (2013) downwards based on the latest results of hybrid simulations by Caprioli & Spitkovsky (2014a) is found to limit the tension with FERMI data to a few objects. A *fixed* proton (re)acceleration efficiency $\eta = 10^{-3}$ at all shocks produces hadronic emission from clusters below the present upper limits from FERMI. In this case, the central CR to gas pressure ratio is ≈ 0.6 % and reaches 1 % within the virial radius. The energetics of CRs in clusters is largely dominated by $M \sim 2 - 5$ shocks, this turns into a requirement for the acceleration efficiency in this Mach number range. However, also the acceleration efficiency by stronger external shocks (usually assumed in the range $\eta \sim 10$ %) must be revised, as our test in Sec. 4.3.4 shows. This result is in agreement with the independent modelling based on semi-analytical mergers discussed in Vazza et al. (2015a), where also a $\sim 10^{-3}$ acceleration efficiency of protons at shocks was found to be necessary to reconcile with the lack of detected hadronic emission from clusters hosting radio relics.

- These results stregthen the problems we pointed out in a related series of semi-analytical paper focusing on double relics (Vazza & Brüggen, 2014; Vazza et al., 2015a), where we reported that in order to reconcile the shock-acceleration model of relics with the absence of γ-ray emission from protons, a electron-to-proton injection ratio ($\gg 10^{-2}$) larger than canonic DSA must be assumed. A promising solution to this problem might come from the latest work on particle acceleration given by particle-in-cell simulations (Guo et al., 2014a,b), which found efficient pre-acceleration of relativistic electrons and very little proton injection by $M \leq 5$ shocks, due to shock-drift-acceleration (SDA). In addition, hybrid (Caprioli & Spitkovsky, 2014a,b) or PIC (Park et al., 2015) simulations of proton acceleration by stronger shocks reported large variations of the injected CR-energy depending on the shock obliquity with the upstream magnetic field.

In conclusion, this study shows that cosmological simulations joined with γ-ray observations can be used as a laboratory to study the acceleration of cosmic rays by weak cosmic shocks, in a regime complementary to supernova remnants and solar wind shocks.

Acknowledgments

This work was strongly supported by computing resources from the Swiss National Supercomputing Centre (CSCS) under projects ID ch2 and s585 in 2014-2015. FV acknowledges personal support from the grant VA 876/3-1 from the Deutsche Forschungsgemeinschaft. FV and MB also acknowledge partial support from the grant FOR1254 from the Deutsche Forschungsgemeinschaft. We acknowledge the use of computing resources under allocations no. 7006 and 9016 (FV) and 9059 (MB) on supercomputers at the NIC of the Forschungszentrum Jülich. We acknowledge the use of the online "Cosmology Calculator" by Wright (2006). We thank K. Dolag for very fruitful discussions at an early stage of this work, and our referee H. Kang for very useful comments on the manuscript.

4.A Effects of Resolution and Additional Physics

We use the smallest simulated volume in our suite of simulation (CUR3, with side 75 Mpc, see Vazza et al., 2014b) to compare the effects of resolutions and different physical prescriptions for baryon physics onto the radial distribution of baryons and CRs. Fig. 4.13 shows the radial profiles of gas density, gas temperature, CR-pressure and γ-ray emission for the most massive halo formed in this box, a cluster with a total mass of $\sim 2 \times 10^{14}$ $M_{\odot}$ in a fairly relaxed dynamical state at $z = 0$. We compare here two sets of data: a) non-radiative runs using the acceleration efficiency of Kang & Ryu (2013) for CRs, and increasing spatial resolution from 210 to 52.5 kpc (i.e. from the number of cells/DM particles in the full volume goes from 256^3 to 1024^3); b) runs including equilibrium gas cooling and high redshift AGN feedback, as the main article (see Vazza et al., 2014b, for details), at the resolution of 52.5 and 105 kpc. The trends which are most relevant for the main findings of our article are the effects of resolution/physics in the spatial distribution of gas and CRs in the innermost cluster regions. The most significant differences connected to resolution and gas physics are limited to the innermost $\leq 0.3R_{500}$ region, where the gas density is increased at most by ~ 10 times when cooling is not contrasted by AGN feedback, which also appears as a drop in the gas temperature in these runs. The outcome in the CR-pressure is also limited to the innermost region, where radiative runs without AGN feedback present a strong peak in the core, which also corresponds to a ~ 10 times larger total γ-ray emission. When AGN feedback is applied, the γ-ray emission is only a factor ~ 2 above the prediction from non-radiative runs at the

same resolution. The last panel of Fig. A1 shows indeed that the hadronic emission is mostly produced at $\geq 0.3 - 0.4R_{500}$, where the differences played by resoluton and gas physics are small. In all cases, the predicted hadronic emission for this cluster is larger than the upper limits set by FERMI (e.g. Huber et al., 2013b). These tests confirm that the problems in explaining the unseen population of CRs in galaxy clusters, outlined in our main article, are robust against variations in resolution and prescriptions for gas physics.

4.B Impact of CR Physics on Cluster Scaling Relations

Fig. 4.14 shows the (M, T) scaling relation within R_{500} for all halos in the non-radiatie CUR1 run (300^3 Mpc^3) and in the non-radiative CUR2 runs (150^3 Mpc^3) volume, where the impact on the different acceleration models (Kang & Jones, 2007; Kang & Ryu, 2013) are compared. For the typical pressure ratio between CRs and gas of these runs ($\leq$ 10 %) the dynamical impact of CRs is not enough to cause any significant departures from the self-similar scaling in the $M \propto T^{3/2}$, nor to affect the mass-function of halos (not shown). In addition, the impact of CRs on the global scaling relation is the same also when more massive clusters (as in the CUR1 run) are included.

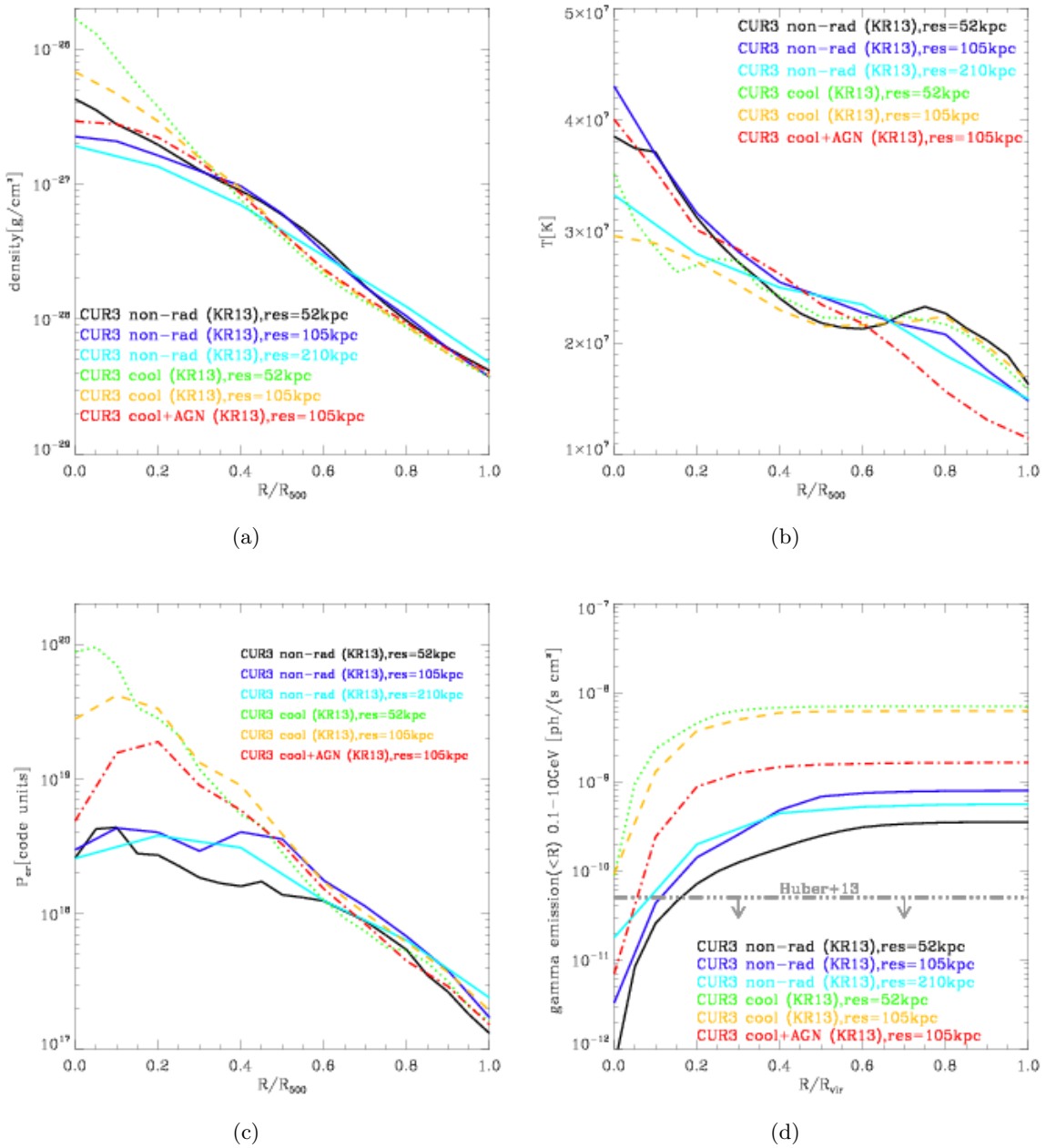

Figure 4.13: Radial profiles of gas density, gas temperature, CR-pressure and γ-ray emission inside the radius for a $\sim 2 \times 10^{14}$ $M_{\odot}$ simulated cluster at $z = 0$, for different resolutions and physical prescriptions for baryons (see text). The additional horizontal line in the last panel marks the upper limit on the γ-ray emission for the stacking of clusters obtained by Huber et al. (2013b).

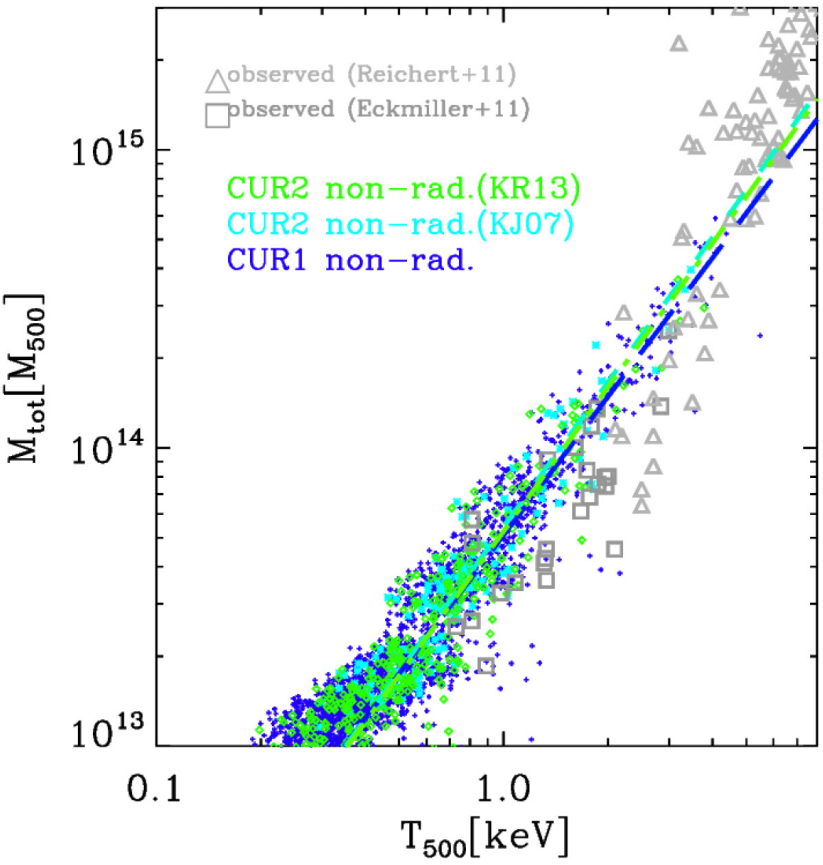

Figure 4.14: Mass-temperature scaling relation for the halos in the CUR1 and CUR2 volumes at $z = 0$, where the effect of the Kang & Jones (2007) and Kang & Ryu (2013) acceleration model for CRs are compared. The additional lines show the best fit of the simulated data, while the two set of gray symbols are for real cluster observations using CHANDRA by Eckmiller et al. (2011) and Reichert et al. (2011). To better compare with the simulated cluster and minimise the effect of cosmic evolution, we only consider observed cluster in the $0 \leq z \leq 0.2$ redshift range.

5 Polarization of Radio Relics: an on-going Study

5.1 Introduction

As described in Chap. 1.2.3, radio relics are highly polarized sources ($\sim 10-50$ %). In principle the high degree of polarization could be caused either a regular large-scale magnetic field or the compression of a tangled small-scale magnetic field (Laing, 1980). Several of observations have been devoted to studying the polarization properties of radio relics (e.g. Bonafede et al., 2009; van Weeren et al., 2010, 2012; Kale et al., 2012; de Gasperin et al., 2015). Skillman et al. (2013b) studied the polarization of radio relics in cosmological magneto-hydrodynamical simulations of galaxy clusters at $\nu_{\rm obs} = 1.4$ GHz. They observed a significant variation both across and along the relic with a peak polarization of ~ 75 %. Furthermore, they showed that the polarization fraction is much larger if the relic is seen "edge-on" instead of "face-on". Yet independent of the viewing angle, polarization never reaches its maximum as a number of physical and instrumental effects lower the degree of polarization. These phenomena are referred to as depolarization.
The most common observed physical depolarization is the so called Faraday depolarization (see Gardner & Whiteoak, 1966; Klein & Fletcher, 2015, for reviews). In this case, Faraday rotation, i.e. the rotation of the electric-field vector of a linearly polarized wave that is propagating through a magnetized plasma, causes depolarization. The Faraday rotation depends on the rotation measure $\Phi \propto n_e B_{\rm para}$ and the wavelength of the observation frequency λ as:

$$\Delta\Psi = \Phi \cdot \lambda^2. \tag{5.1}$$

Therefore, one normally tends to use high frequency observations for the study of polarization, where the effect of Faraday depolarization, is small (e.g. Kierdorf et al., 2017, and references therein). Through the rotation measure, depolarization depends on the magnetic field component parallel to the line-of-sight and the electron number density. Hence, the combination of depolarization studies with X-ray observations, that provide the thermal gas distribution, is a powerful tool for the estimation of the magnetic fields in the ICM. Yet, it is still unclear, whether most of the depolarization happens between the source and the observer or at the

source itself.

Two common instrumental effects can occur that also cause depolarization: beam and bandwidth depolarization (e.g. Hamaker et al., 1996; Sault et al., 1996; Klein & Fletcher, 2015). Beam depolarization happens when different field orientations within the resolution beam produce different polarisation angles, which partly cancel out. For example, linearly polarized emission from two regions suppress each other, if their magnetic-field directions are perpendicular. Bandwidth depolarization reduces the degree of polarization by rotation of the electric-field vector across the bandpass.

In this section, we study the polarization of relics at radio frequencies to determine where depolarization is the strongest. For our analysis, we use the same radio relic that has already been described and studied in Chap. 3. We compute the polarization properties of this relic both at 0.14 GHz and 1.4 GHz combined with and without the effect of depolarization. We notice that we do not include any instrumental depolarization. The work presented in this chapter is still an on-going project and will be submitted as a paper in the near future.

This chapter is organized as follows: at first we will describe how the polarization of a radio relic is computed using `CRaTer`, Sec. 5.2. This is followed by the presentation, Sec. 5.3, and discussion, Sec. 5.4, of our results. For the description of the numerical methods used in `ENZO` and `CRaTer`, we refer the reader to Chap. 3 of this thesis.

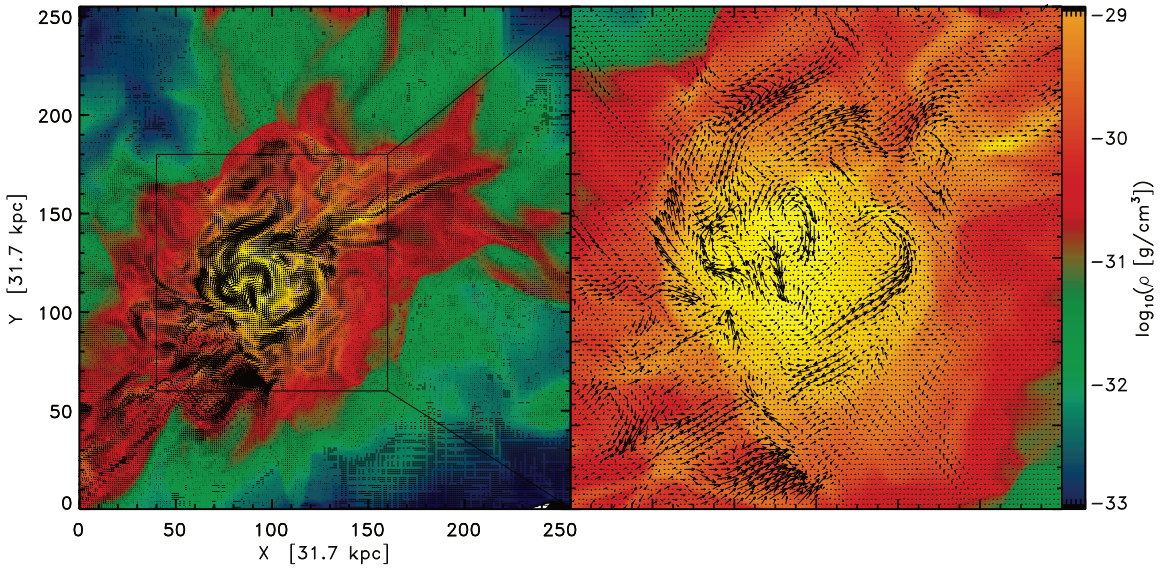

Figure 5.1: Density slice through the cluster centre overlayed with the corresponding magnetic field vectors. This plot has been produced using the `ENZO`-data.

5.2 Polarization in CRaTer

Burn (1966) derived a formalism to compute the observed polarization of the integrated emission:

$$P_{\mathrm{burn}}(\lambda^2) = \frac{\int\limits_{\mathrm{los}} P_{\mathrm{tot}} \Pi \exp\left(2i\left(\beta + \Phi\lambda^2\right)\right) \mathrm{d}s}{\int\limits_{\mathrm{los}} P_{\mathrm{tot}} \mathrm{d}s}. \tag{5.2}$$

Here P_{tot} is the emission per volume, Π is the intrinsic degree of polarization, β is the intrinsic angle of polarization and $\Phi\lambda^2$ is the Faraday rotation that causes depolarization. In this section, we present how Eq. 5.2 is computed using `CRaTer`. To compute the emission per volume we follow the approach of Hoeft & Brüggen (2007) and compute it as the convolution of the electron spectrum $n_E(\tau, t)$ and the function $F\left(\tau^{-2}\right)$ as[1]

$$P_{\mathrm{tot}} = \frac{C_{\mathrm{sync}} m_e c^2}{C_\tau} \int_0^\infty n_E(\tau, t) F\left(\frac{1}{\tau^2}\right) \mathrm{d}\tau. \tag{5.3}$$

In the equation above, we use the electron mass m_e and the speed of light c. The integration variable τ is computed using the Lorenz-factor $\gamma_{\mathrm{L}} = E/m_e c^2 + 1$ and takes the form $\tau = 4.85 \cdot 10^{-5} \left(B/\mu\mathrm{G}\right)^{0.5} \left(1.4\ \mathrm{GHz}/\nu_{\mathrm{obs}}\right)^{0.5} \gamma_{\mathrm{L}}$. C_{sync} and C_τ depend on the underlying magnetic field B, the pitch angle α and the observation frequency ν_{obs} as:

$$C_{\mathrm{sync}} = \frac{\sqrt{3} e^3 B \sin(\alpha)}{m_e c^2} \tag{5.4}$$

$$C_\tau = \sqrt{\frac{3eB}{\nu_{\mathrm{obs}} 16 m_e c}}. \tag{5.5}$$

The electron spectrum, injected at time t_0, evolves in time t as:

$$n_E(E, t) = \begin{cases} n_e C_{\mathrm{spec}} \frac{1}{m_e c^2} \tilde{e}^{-s} \left(1 - \left(\frac{1}{\tilde{e}_{\mathrm{max}}} + C_{\mathrm{cool}} \Delta t\right) \tilde{e}\right)^{s-2} & \text{if } \tilde{e} C_{\mathrm{cool}} \Delta t < 1 - \tilde{e}/\tilde{e}_{\mathrm{max}} \\ 0 & \text{else} \end{cases}. \tag{5.6}$$

Here $\Delta t = t - t_0$, hence for $t = t_0$ the equation computes the injection spectrum. The term $C_{\mathrm{cool}} \Delta t$ accounts for energy looses due to inverse Compton scattering of the CMB photons and synchrotron radiation. In Eq. 5.6, n_e is the number of electrons per tracer and $\tilde{e} = E/m_e c^2$. The spectral index $s = (r+2)/(r-1)$ is computed via the compression ratio $r = \rho_2/\rho_1$. C_{spec} gives the fraction of electrons at $E = m_e c^2$ and accounts for the normalization of the

[1] $F(x)$ is computed using the modified Bessel-Function as $F(x) = x \int_x^\infty K_{5/3}(\xi)\, \mathrm{d}\xi$.

spectrum. It is computed as:

$$C_{\rm spec} = \eta \frac{u_d m_p}{c^2 m_e} \frac{(q-1)}{q I_{\rm spec}}. \tag{5.7}$$

Here η is the fraction of energy injected by a shock of a given Mach number into the acceleration of cosmic-rays. We choose in our later analysis both a fixed value of $\eta = 0.05$ and the Mach number dependent acceleration efficiencies derived by Kang & Ryu (2013). For the detailed computation of $C_{\rm spec}$ and $C_{\rm cool}$ we refer to Sec. 2.2 and 2.3 in Hoeft & Brüggen (2007). We use the same spectrum to compute the radiated power perpendicular, $P_\perp$, and parallel, $P_\parallel$, to the projection of the magnetic field[2]:

$$P_\perp = \frac{C_{\rm sync} m_e c^2}{C_\tau} \int n_E(\tau) \left[F(\tau^{-2}) + G(\tau^{-2}) \right] {\rm d}\tau \tag{5.8}$$

$$P_\parallel = \frac{C_{\rm sync} m_e c^2}{C_\tau} \int n_E(\tau) \left[F(\tau^{-2}) - G(\tau^{-2}) \right] {\rm d}\tau. \tag{5.9}$$

Then the intrinsic degree of polarization is computed as

$$\Pi = \frac{P_\perp - P_\parallel}{P_\perp + P_\parallel}. \tag{5.10}$$

The last ingredients of computing polarization is the estimation of the amount of Faraday depolarization: $\Phi\lambda^2$. Here λ is the wavelength corresponding to the observation frequency and Φ is the rotation measure:

$$\Phi = 812 \int_0^L \frac{n_e}{10^{-3}\ {\rm cm}^{-3}} \frac{B_{\rm para}}{\mu{\rm G}} \frac{{\rm d}l}{\rm kpc} \ \left[\frac{\rm rad}{\rm m^2} \right]. \tag{5.11}$$

Here n_e is the electron density and $B_{\rm para}$ is the magnetic field parallel to the line-of-sight. The equation is integrated along the line-of-sight. In our simulation we compute the rotation measure on the grid and assign it to the tracers using a *NGP*-method.
The emission per volume, Eq. 5.3, and the intrinsic degree of polarization, Eq. 5.10, are both calculated for each tracer individually. The integrals along the line-of-sight in Eq. 5.2 are replaced by the sum over the tracers:

$$P_{\rm burn}(\lambda^2) = \frac{\sum_{i=0}^{N_p} P_{{\rm tot},i} \Pi_i \exp\left(2i\left(\beta_i + \Phi_i \lambda^2\right)\right)}{\sum_{i=0}^{N_p} P_{{\rm tot},i}}. \tag{5.12}$$

[2] $G(x)$ is computed using the modified Bessel-Function as $G(x) = xK_{2/3}(x)$.

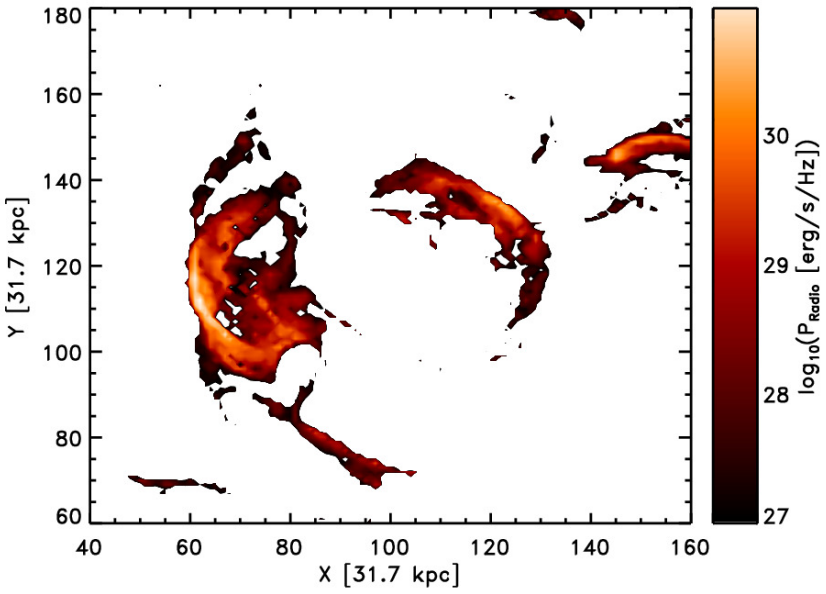

Figure 5.2: Projected radio emission at $z = 0.27$. This plot has been produced using the `CRaTer`-data.

5.3 Results

In this chapter we study the same relics as previously in Chap. 3.2. In Fig. 5.1, we show a density slice through the centre of the cluster overlayed with the corresponding magnetic field vectors at $z \approx 0.27$. As the cluster undergoes a major merger at this epoch, shock waves start sweeping through the ICM and produce two bright radio relics, i.e. $P_{\rm radio} \approx 3.42 \cdot 10^{31}$ erg/s/Hz and $P_{\rm radio} \approx 2.26 \cdot 10^{31}$ erg/s/Hz. In Fig. 5.2, we plot the total emission of the two relics, that has been computed with Eq. 32 from Hoeft & Brüggen (2007) (see Chap. 3 for more details on the computation). In the following discussion, we will focus only on the brighter of the two, located left from the cluster core.

5.3.1 Mach Number and Spectral Index Distributions

First, we use the shock detector described in Chap. 2.2.3 to identify all tracers that have been shocked and estimate the specific Mach number accordingly. Using the corresponding spectral index, we compute the injected electron spectrum $n_E(E,t)$, Eq. 5.6, for each tracer and subsequently estimate the corresponding emission per volume, Eq. 5.3. The distribution of Mach numbers, see black line in Fig. 5.4(a), ranges from a minimum value[3] of $M = 1.3$ to $M > 3$. The average Mach number recorded is ~ 2.3. This is in line with previous works (e.g.

[3]We notice, that this is the smallest Mach number allowed for detection as for lower values it cannot be distinguished, whether the shock is of physical or numerical nature.

Hong et al., 2015; Skillman et al., 2013b, and Chap. 3 of this thesis) that have indeed shown that merger shocks in the ICM are not simply associated with a single-valued Mach number, which stems from the rather patchy structure of the ICM across $\sim$ Mpc scales. Yet, the radio emission weighted distributions of Mach numbers, blue and red line in Fig. 5.4(a), show that most of the emission is produced in the few high Mach number shocks. When using the shock acceleration efficiencies provided by Kang & Ryu (2013) about ~ 98 % of the radio emission is coming from $M > 4$ shocks. Also for a constant acceleration efficiency of $\eta = 0.05$ shocks with $M > 4$ produce about ~ 81 % of the observed radio emission. This trend is also seen in the radio weighted average Mach number that is ~ 4.8 and ~ 4.4, respectively.

This discrepancy in Mach number estimates is also seen in the two dimensional projection of Mach numbers, that rather mirrors the observations in place of the three dimensional distribution. In Fig. 5.3, we plot the projection average and radio weighted Mach numbers across the relic seen along different line-of-sights. We show the corresponding distributions of Mach numbers in Fig. 5.4. We observe that the average projected Mach numbers (black lines in Fig. 5.4(b)-5.4(d) and left column in Fig. 5.3) show a large scatter in the range of $\langle M \rangle \approx 1.7 - 5.0$ with both means and medians in the range of $\sim 3.0 - 3.5$. On the other hand, the radio emission weighted Mach number shows much larger values in the range of $\langle M \rangle_{\rm radio} \approx 3.0 - 5.4$ with both means and medians $\gtrsim 4.0$.

Furthermore the qualitative view on Fig. 5.3 shows that some low average Mach number regions show a high radio weighted Mach number. The difference in Mach number distributions is very significant when looking at the shock in the XY- and XZ-plane, Fig. 5.4(b) and 5.4(c) respectively. The distributions show a larger overlap in the YZ-plane, Fig. 5.4(d), where the relic surface is much broader and hence the average along the line-of-sight is taken over fewer tracers.

As an additional test, we rotated the relic around all three axes independently using an angle increment of $\Delta = 1^\circ$. This way, we generated a total of 1080 maps of the relic under different viewing angles. In Fig. 5.4(e), we show the distribution of average Mach number and the radio weighted Mach number taken over all realizations of the relic. The average Mach number in this case takes a value of ~ 3.1 and the average radio emission weighted Mach number shows a value of ~ 4.8. The qualitative comparison of Fig. 5.4(e) to Fig. 5.4(b)-5.4(d) shows that the individual distribution of Mach numbers significantly depends on the viewing angle. Therefore, while the specific comparison between X-ray and radio based estimates of the Mach number can vary depending on the viewing angle, in the general case the radio emission weighted Mach number is significantly higher than the average Mach number.

In Fig. 5.5, we plot the corresponding the mean spectral index and the radio emission weighted spectral index maps. The distribution of spectral indices across the relics matches the previous findings. For all three viewing angles, the average spectral index is in the range of $\langle s \rangle \approx 2.2 - 5.3$ with means of $\sim 2.7 - 3.0$ and medians of $\sim 2.5 - 2.9$. The radio-weighted

spectral index is significantly flatter and is in the range of $\langle s \rangle_{\rm radio} \approx 2.1 - 2.5$ with both a mean and median values of $\sim 2.2 - 2.3$. In all cases the radio weighted average spectral index shows a much more uniform distribution of the flat indices, while the average spectral is only significantly flat in a few regions of the relic. However, the average spectral index in the YZ-plane shows significantly more flatter values than in the XY- and XZ-plane. This is consistent with our previous findings on the Mach number distribution across the relics.
All of our findings above are consistent with previous findings in the literature (Hong et al., 2015). Therefore, the observed radio emission mostly probes the portion of shock fronts which is associated with the highest Mach number. This bias seems to be more significant, if one looks at the radio relic "edge-on" where the emission of a lot of particles is dominated by a few strong ones. On the other hand, the bias is reduced, when the relic is seen "face-on". While the mismatch between X-ray and radio-based Mach number has been already discussed in a few works (e.g. Hong et al., 2015), the additional role of projection effect and hence the surface of the emitting region in making this bias larger is an original finding of this work, as far as we can tell.

5.3.2 Polarization Properties

As a next step we estimated the polarization of the integrated emission, Eq. 5.12, in each pixel/cell of our simulation using the `CRaTer`-data both at $\nu_{\rm obs} = 0.14$ GHz and $\nu_{\rm obs} = 1.4$ GHz. For both observation frequencies we test three cases of depolarization:

1. $\Phi_{\rm full}$: this model includes the rotation measure from all cells between the source and the observer and therefore gives the true amount of Faraday depolarization.

2. $\Phi_{\rm zero}$: this model excludes the effect of Faraday depolarization completely by setting $\Phi = 0$ in Eq. 5.2.

3. $\Phi_{\rm source}$: this model only includes the Faraday depolarization at the source itself. We compute this by setting $n_e = 0$ in all cells that do not host a tracer when computing Φ, see Eq. 5.11.

In Fig. 5.6, we plot the polarized emission overlayed with the corresponding polarization vectors for the six possible combinations of $\nu_{\rm obs}$ and Φ. Our main findings are:

- In both the $\Phi_{\rm full}$- and $\Phi_{\rm source}$-model, the average polarization per pixel at $\nu_{\rm obs} = 1.4$ GHz is higher than at $\nu_{\rm obs} = 0.14$ GHz. Yet, in the $\Phi_{\rm zero}$-model the average polarization per pixel is similar for both frequencies.

- The average polarization at $\nu_{\rm obs} = 0.14$ GHz differs significantly for the three different models. Here, the $\Phi_{\rm zero}$-model shows the hightest average, while the $\Phi_{\rm full}$-model shows

the lowest average. At $\nu_{\rm obs} = 1.4$ GHz, the average polarization of the $\Phi_{\rm full}$-model is significantly lower than for the other two models, that show a similar average.

- For both frequencies and all models, the range of polarization per pixel stays constant and is always in the range of of a few ~ 0.1 % to ~ 70 %. Hence to explain the above stated average polarizations, the number of low and high polarized pixels changes among the different models.

A more detailed summary of our above described results is provided in Tab. 5.1.
In Fig. 5.7, we plot the distribution of polarization in each pixel for the different observing frequencies and depolarization sources. The detected polarization in radio relics ranges from $\lesssim 15$ % to $\gtrsim 60$ %, depending on the observing frequency and the beam of the adopted radio telescope (e.g. van Weeren et al., 2010; Bonafede et al., 2012; Kierdorf et al., 2017). Although our results give a promising match to these values, additional work is needed to compare these results with observations and different models in more detail. We observe that for $\nu_{\rm obs} = 1.4$ GHz the distributions for $\Phi_{\rm source}$ and $\Phi_{\rm zero}$ look fairly similar, while the distribution in the $\Phi_{\rm full}$ significantly peaks towards the lower values. This quantitative observation matches our results obtained above. At $\nu_{\rm obs} = 0.14$ GHz we already observe significant differences between the distribution that neglects depolarization completely and the one that includes depolarization within the source only. The distribution that includes the full depolarization is clearly dominated by the lower values. With future work, we will also investigate the trend with spatial resolution of the depolarization from the intervening intracluster magnetic field, as a higher resolution can introduce additional tangling of magnetic field lines.

$\nu_{\rm obs}$ [GHz]	Φ_i	mean [%]	median [%]	max [%]	min [%]	≥ 0.6 [%]	≤ 0.2 [%]
1.4	$\Phi_{\rm full}$	28.3	26.2	70.5	0.4	8.4	41.6
1.4	$\Phi_{\rm zero}$	37.6	39.3	71.8	1.3	21.3	27.5
1.4	$\Phi_{\rm source}$	35.4	35.6	71.4	0.2	18.8	31.6
0.14	$\Phi_{\rm full}$	18.4	15.0	70.8	0.1	2.8	63.3
0.14	$\Phi_{\rm zero}$	39.1	40.7	72.6	0.2	22.2	24.5
0.14	$\Phi_{\rm source}$	27.5	24.3	71.8	0.1	7.0	42.1

Table 5.1: Summary of the results for the polarization of the radio relic. The first column gives the observation frequency and the second column gives the depolarization model. The third and fourth column present the mean and median of the polarization. The fifth and sixth column provide the minimum and maximum degree of polarization recorded in on pixel. The last two columns provide the fraction of cells that show a polarization ≥ 60 % and ≤ 20 % respectively.

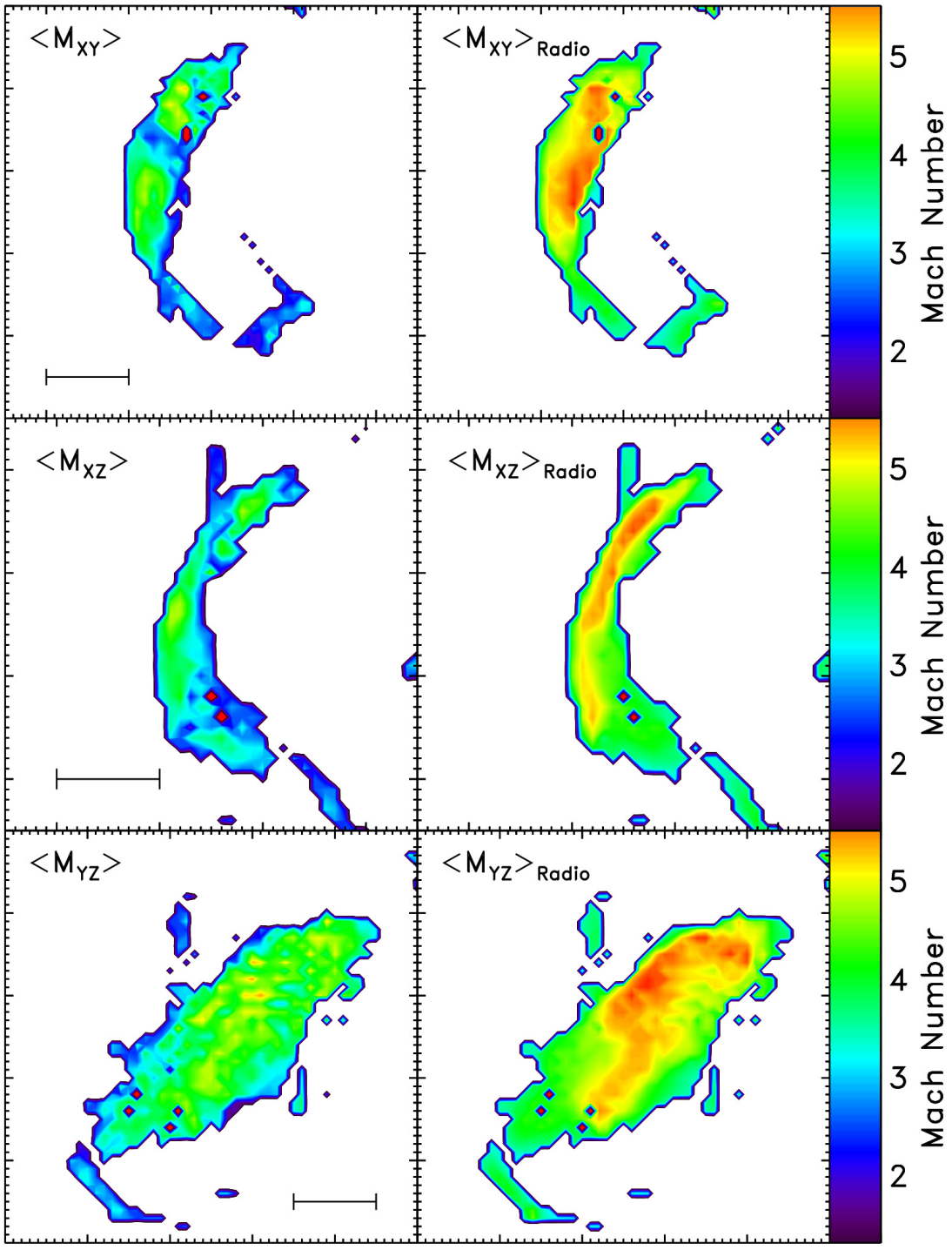

Figure 5.3: Average Mach number maps along the different line-of-sights: XY-plane (top row), XZ-plane (middle row) and YZ-plane (bottom row). Left left column shows the unweighted average and the right column shows the radio emission weighted average using the acceleration efficiencies derived by Kang & Ryu (2013). The black bar shows the length of 300 kpc.

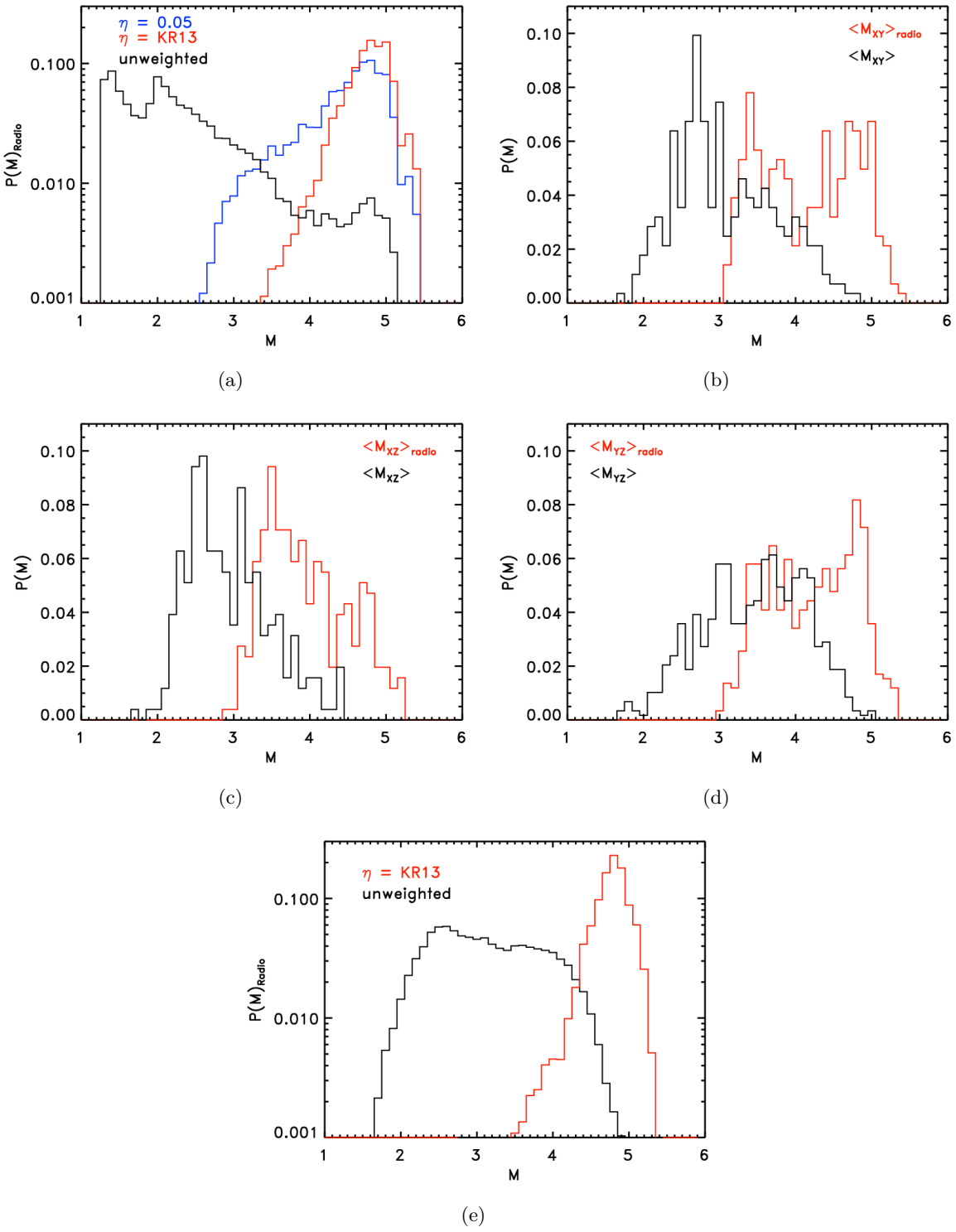

Figure 5.4: Three dimensional distribution of Mach numbers (black) and the corresponding radio emission weighted distribution of the Mach number using the acceleration efficiencies derived by Kang & Ryu (2013) (red) and a fixed acceleration efficiency of $\eta = 0.05$ (blue). Panels (b), (c) and (d) show the projected Mach number in the XY-plane, XZ-plane and YZ-plane. Panel (e) shows the distribution of projected Mach numbers taken along 1080 line-of-sights. The black line show the distribution of average Mach numbers and the red lines show the radio weighted Mach number using the acceleration efficiencies derived by Kang & Ryu (2013).

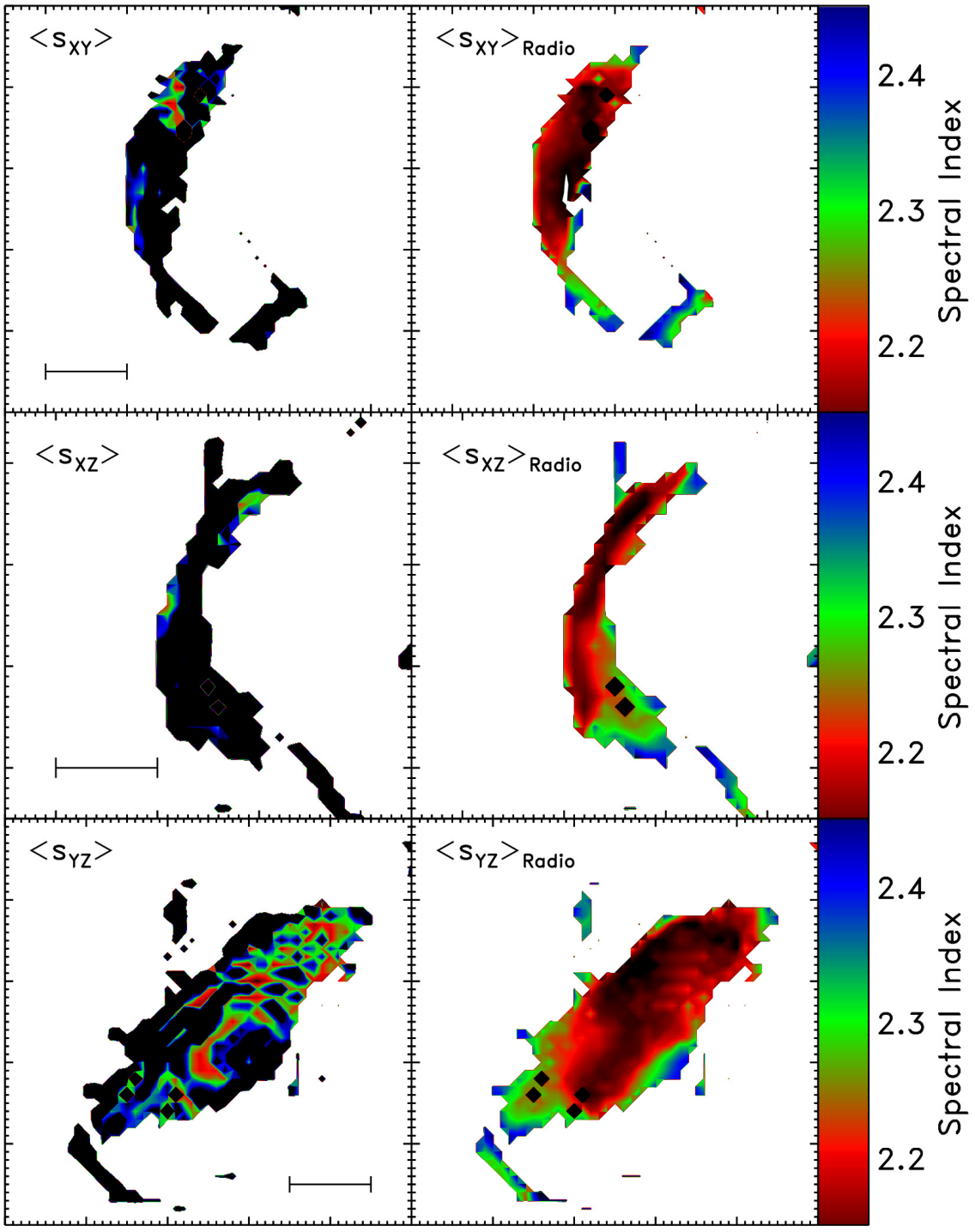

Figure 5.5: Average spectral index maps along the different line-of-sights: XY-plane (top row), XZ-plane (middle row) and YZ-plane (bottom row). Left left column shows the unweighted average and the right column shows the radio emission weighted average using the acceleration efficiencies derived by Kang & Ryu (2013). The black bar shows the length of 300 kpc.

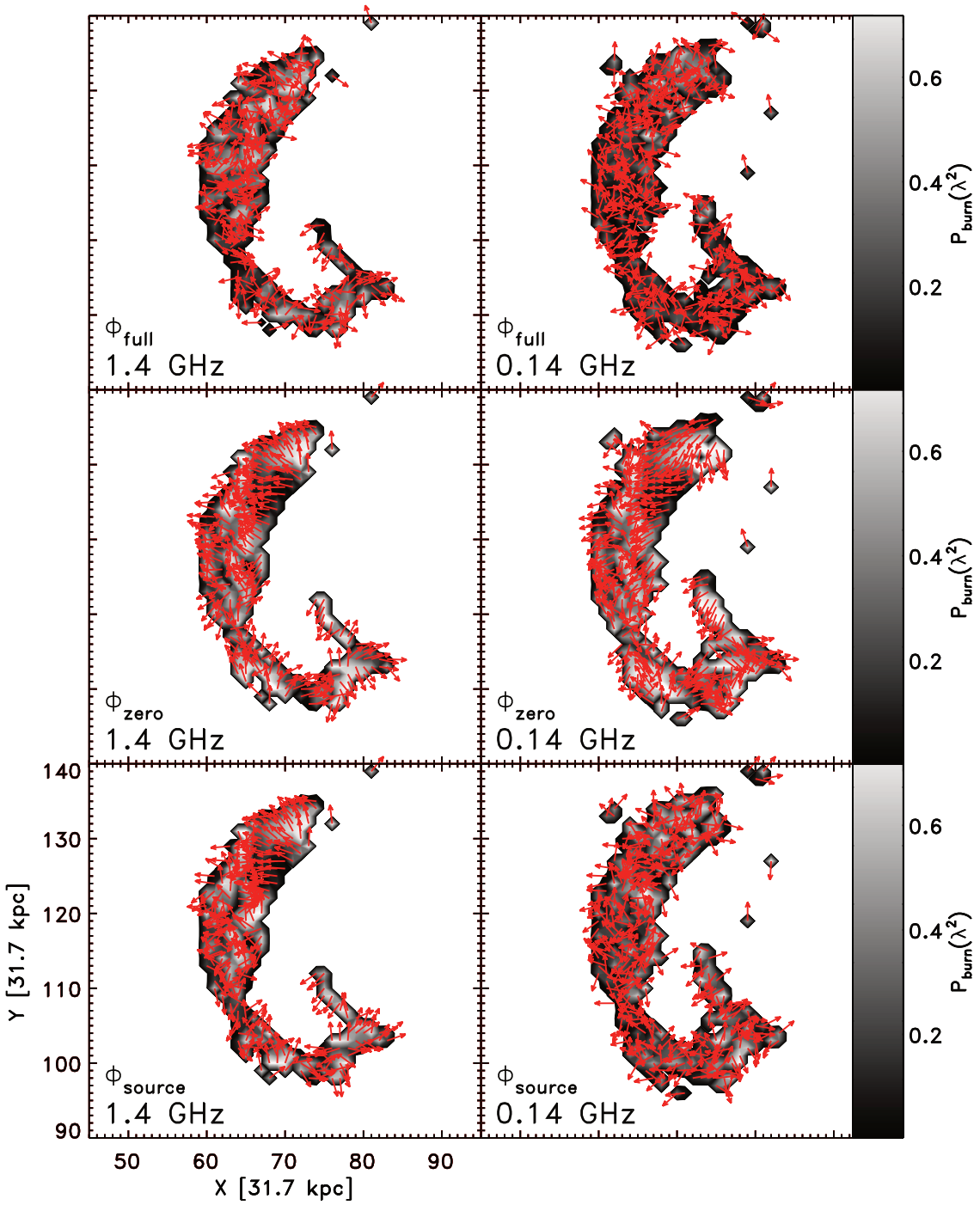

Figure 5.6: Polarization of the integrated radio emission, Eq. 5.12, overlayed with the polarization vectors for our six different combinations of rotation measure and observing frequency. The left column shows $\nu_{\rm obs} = 1.4$ GHz and the right column displays $\nu_{\rm obs} = 0.14$ GHz. The three rows show $\Phi_{\rm full}$, $\Phi_{\rm zero}$ and $\Phi_{\rm source}$ respectively.

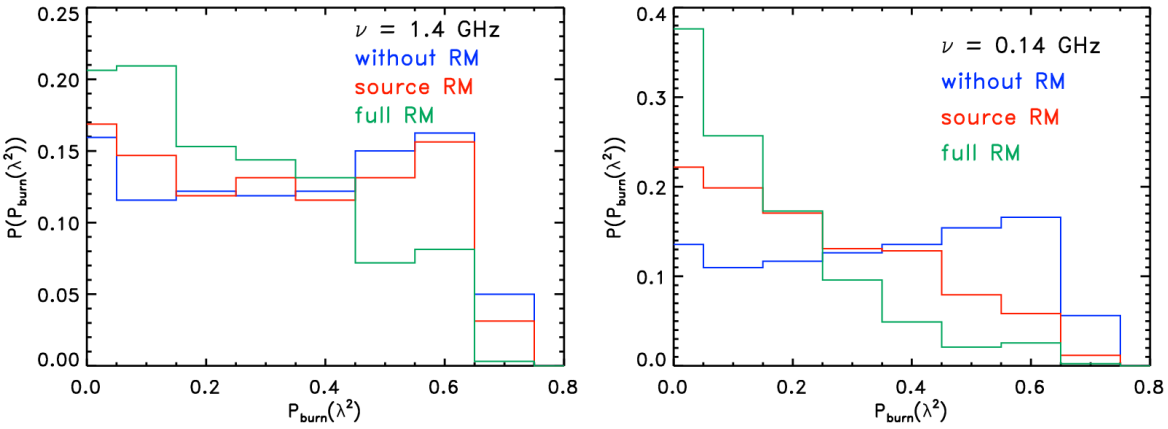

(a) (b)

Figure 5.7: Distribution of the polarized, integrated radio emission, Eq. 5.12, including the effect of depolarization (red) and excluding the effect of depolarization (blue) at (a) $\nu_{\rm obs}$ = 1.4 GHz and (b) $\nu_{\rm obs}$ = 0.14 GHz. The green lines show the distribution, if only the depolarization within the source is included.

5.4 Conclusion

Combining MHD-simulations and Lagrangian tracers we computed the shock-induced cosmic-ray electron spectrum and studied the corresponding spectral and polarization properties of radio relics. Thus, we could test a few possible sources for the depolarization of the observed radio emission. Focusing on the properties of one radio relic, that appears in a massive galaxy cluster after major merger at low redshift, we obtained the following results:

- We calculated the radio weighted distribution of Mach numbers for a fixed acceleration efficiency of $\eta = 0.05$ and the acceleration efficiencies derived by Kang & Ryu (2013). Both of them show their peak in the range of $\sim 4.4 - 4.7$, while the average Mach number itself is significantly lower ~ 2.3. See Fig. 5.4(a).

- We produced projections of the average and radio weighted Mach numbers along three different line-of-sight (XY-, XZ- and YZ-plane), see Fig. 5.3. We observe that the average Mach number in all cases is much lower than the radio weighted Mach number. This trend is more significant, if the observed relic surface is thin (i.e. "edge-on"), hence looking at a higher depth and averaging over more particles. The same trend also applies to the spectral indices (e.g. the radio-weighted one is flatter than the average one).

- Using the equation derived by Burn (1966) we computed the observed polarization of the integrated emission at $\nu_{\rm obs} = 0.14$ GHz and $\nu_{\rm obs} = 1.4$ GHz. While the radio emission

at $\nu_{\rm obs} = 0.14$ GHz is completely depolarized, the radio emission at $\nu_{\rm obs} = 1.4$ GHz is polarized at ~ 28 %, if depolarization from the intervening intracluster magnetic fields is included. By neglecting the effect of depolarization, i.e. setting $\Phi = 0$, at both frequencies we observe a polarization of $\approx 37 - 39$ %.

- We have tested if most of the depolarization is produced in the source itself or in the ICM between source and observer. We did this by only including the depolarization within the source. The polarization at $\nu_{\rm obs} = 0.14$ GHz is already reduced significantly, ~ 24 %, while the polarization at $\nu_{\rm obs} = 1.4$ GHz is only lowered by a few to ~ 36 %.

Our observations also match predictions from Hong et al. (2015), who estimated the Mach numbers derived to be larger than the ones derived from X-rays. Hong et al. (2015) compared two dimensional mock observations of X-ray and radio observations. Yet, they argue that X-ray Mach number underestimates the real Mach number, while our analysis suggests that radio relics tend to pick up strong shocks only and therefore neglecting the weaker ones. However, in both cases the observed discrepancy between Mach numbers derived from X-ray and radio observations (e.g. Ogrean et al., 2014; Itahana et al., 2015; Akamatsu et al., 2017) seems to be due to the fact that radio observations weigh the high Mach numbers, while X-ray observations are more sensitive to the lower Mach numbers.
Furthermore, we noticed that the discrepancy of the distributions computed in two dimensional becomes smaller with an increasing surface of the relic. As the number of tracer particles is conserved in the three maps, this is most likely due to the fact that by construction the averages are taken over more tracer particles in a small surface relic. Hence, one bright particle can outshine all the others, while in large surfaces one averages over less particles. This suggests that discrepancy of Mach number estimates observed in relics seen "edge-on" should be larger than in relics that are observed "face-on".
We observe, as predicted by theory, that without any depolarization the distribution of the measured degrees of polarization per cell looks fairly similar at $\nu_{\rm obs} = 0.14$ GHz and $\nu_{\rm obs} = 1.4$ GHz. On the other hand the effect of depolarization is much more significant at the lower frequency and the two distributions differ a lot. This is in line with modern radio observations (e.g. Kierdorf et al., 2017, and references therein). When only including the depolarization caused within the source itself, the results for the two frequencies are different. At the higher frequency, $\nu_{\rm obs} = 1.4$ GHz, the polarization does not drop significantly compared to the case without polarization and the amount of highly polarized cells, i.e. ≥ 60 %, only drops by a few, ~ 2.5 %. On the other hand, the same test at low frequency, $\nu_{\rm obs} = 0.14$ GHz, caused ~ 15 % of the cells to loose their high degree of polarization. At the same time the amount of unpolarized cells, i.e. ≤ 20 %, increased by about $\sim 17 - 18$ %. This observation indicates that at low frequencies, the depolarization is already significantly reduced within the source. The depolarization at high frequencies on the other hand seems to be happening mostly in the ICM between the source and the observer.

We notice, that we did not include any the effect of beam or bandwidth depolarization (e.g. Hamaker et al., 1996; Sault et al., 1996). Yet, these effects have to be taken into account in the production of more detailed mock observations.

6 Evolution of Vorticity and Enstrophy in the Intracluster Medium

The following chapter presents work as it is published by Wittor, Jones, Vazza, & Brüggen in MNRAS 2017a.

6.1 Introduction

The intracluster medium (ICM) is a hot ($T \sim 10^7 - 10^8$ K), dilute plasma that hosts turbulent motions across all scales. Turbulence is driven on cluster scales, $\sim$ few Mpc, as gravitational energy is converted into kinetic energy during the process of hierarchical structure formation (see Brüggen & Vazza, 2015, and references therein for a recent review). Accretion flows convert their kinetic energy into turbulent motions through tangential flows, fluid instabilities or baroclinic motions. The turbulence then cascades from driving scales to dissipative scales and heats the plasma, (re-)accelerates cosmic-ray particles and amplifies magnetic field (e.g. Brunetti & Lazarian, 2007; Miniati & Beresnyak, 2015; Schmidt et al., 2015). Turbulence can also be driven on galactic scales, $\sim$ 10 kpc, for example by outflows driven by active galactic nuclei (AGN) or ICM-based magneto-thermal instabilities (e.g. Mendygral et al., 2012; ZuHone et al., 2013).
In this work, we are tracking the turbulence associated with substructures that are accreted by clusters at $z < 1$. These are typically groups with typical masses of $\sim 10^{13}$ $M_\odot$, and they are expected to contribute up to $\sim$ 70% to the total mass of massive galaxy clusters (e.g. Berrier et al., 2009).
Current observations measure turbulence through the SZ-effect or pressure fluctuations and line spectroscopy in X-ray (e.g. Khatri & Gaspari, 2016; Pinto et al., 2015; Zhuravleva et al., 2016). Future X-ray observations should be able to detect the driving scale of turbulence directly due to the outstanding spectral resolution of the new generation of telescopes (e.g. `Athena`). The analysis of the turbulent motions is rendered difficult by the need to isolate uncorrelated flows from, both correlated flows on large scales ($\geq 0.1 - 1$ Mpc) and small-scale velocity perturbations produced by shocks. Turbulence is also dependent on the local gas conditions, as the compressive turbulent energy can make up only a few percent or up to

$15 - 30$ per cent of the total turbulent kinetic energy. This is important for example, for the understanding of cosmic-ray acceleration. The compressive turbulent component, e.g. curl-free component, most likely follows a Burgers-like spectrum, which reduces the power for cosmic-ray acceleration[1] (Brunetti & Jones, 2014; Miniati, 2015).
Porter et al. (2015) simulated the properties of MHD turbulence driven by various combinations of solenoidal and compressive processes. Their objective was to understand the physical sources of ICM enstrophy (see Sec. 6.1.1) and the associated turbulent amplification of magnetic fields. Vazza et al. (2017c) extended this work by analysing a major merger cluster, finding that enstrophy is generated by baroclinic and shock-related motions during accretion and merger processes. In the cluster interior, vortex stretching seeded by mergers is enhancing and generating enstrophy.
In this work, we use our post-processing tool `CRaTer` to analyse the Lagrangian evolution of enstrophy in eight different clusters taken from the Itasca Simulated Clusters (ISC). The paper is structured as follows: After summarizing the most important points of enstrophy generation and evolution in Sec. 6.1.1, we will give detailed information on our simulations and numerical tools in Sec. 6.2. In Sec. 6.3.1, we give an overview of the general properties of our cluster sample. Our results on the Lagrangian evolution of enstrophy are presented in 6.3.2. We focus on the evolution of growth and decay times associated with the different source terms that generate enstrophy in Sec. 6.3.3. In Sec. 6.3.4, we give estimates on the turbulent energy dissipation and the corresponding magnetic field amplification. Finally, we summarise our results and conclude in Sec. 6.4. In the Appendix, we further give an analytical derivation of how the dissipation rate of turbulence can be estimated in our simulation.

6.1.1 Evolution of Enstrophy

The kinetic energy of turbulence in the ICM is mostly ($60 - 90$ per cent Miniati & Beresnyak, 2015) of solenoidal nature (divergence-free) and its amount can be measured by the vorticity $\omega = \nabla \times \mathbf{v}$. However, the average vector vorticity tends to zero and other proxies for solenoidal turbulence are needed. The enstrophy $\epsilon = \frac{1}{2}(\nabla \times \mathbf{v})^2$ is such a proxy as it measures the magnitude of vorticity. The equation for the evolution of enstrophy is derived by taking the dot-product of the vorticity and the vorticity equation (for more details see Porter et al., 2015). The evolution of enstrophy in a fixed, Eulerian frame is determined by *advective*, *compressive*, *stretching* and *baroclinic* motions[2] as well as *dissipation*:

$$\left(\frac{\mathrm{d}\epsilon}{\mathrm{d}t}\right)_{\mathrm{euler}} = F_{\mathrm{adv}} + F_{\mathrm{comp}} + F_{\mathrm{stretch}} + F_{\mathrm{baro}} + F_{\mathrm{diss}}. \tag{6.1}$$

[1] In the case the magnetosonic waves, that are responsible for the acceleration of particles, are dissipated at shocks steepening the cascade and reducing the effective energy transfer to the particles (Miniati, 2015).
[2] Notice, Porter et al. (2015) include a *magnetic* term in their equation. This term is neglected here as our simulations only use pure hydrodynamics.

The individual sink and source terms (from here on we will refer to them as source terms) are:

$$F_{\rm adv} = -\nabla \cdot (\mathbf{v}\epsilon) = -(\epsilon \nabla \cdot \mathbf{v} + \mathbf{v} \cdot \nabla \epsilon), \tag{6.2}$$

$$F_{\rm comp} = -\epsilon \nabla \cdot \mathbf{v}, \tag{6.3}$$

$$F_{\rm stretch} = 2\epsilon(\hat{\omega} \cdot \nabla)\mathbf{v} \cdot \hat{\omega}, \tag{6.4}$$

$$F_{\rm baro} = \frac{\vec{\omega}}{\rho^2} \cdot (\nabla\rho \times \nabla P), \tag{6.5}$$

$$F_{\rm diss} = \nu\vec{\omega} \cdot \left(\nabla^2\vec{\omega} + \nabla \times \mathbf{G}\right), \tag{6.6}$$

$$\text{with} \quad \vec{\omega} = \nabla \times \mathbf{v}. \tag{6.7}$$

In the equations above, ρ and P are the gas density and pressure, ν is the kinematic viscosity and $\mathbf{G} = (1/\rho)\nabla\rho \cdot \mathbf{S}$, with the traceless strain tensor $\mathbf{S}$[3] (Mee & Brandenburg, 2006). A hat denotes a unit vector. We notice that all derivatives are computed using a second-order central difference.

Each source term represents a different physical process leading to the generation, amplification and destruction of enstrophy. The *advective*, $F_{\rm adv}$, source term describes conservative advection of enstrophy across the cluster. The *compressive*, $F_{\rm comp}$, source term accounts for both reversible compression and rarefractions as well as enstrophy enhancements due to shock compression. The net influence of shock compression on enstrophy is amplification, although as discussed in (Porter et al., 2015) creation of enstrophy within shocks really comes from the strain term in Eq. 6.6, combined with subsequent compression within the shock. The *stretching* source term, $F_{\rm stretch}$, accounts for the generation of enstrophy by vortex stretching. *Baroclinic*, $F_{\rm baro}$, generation of enstrophy takes place in baroclinic flows, in which the pressure is not a function of density alone; that is, the flow is not barotropic. In our case, where the gas equation of state is adiabatic, that corresponds to flow with non-uniform entropy, which develops behind complex or unsteady shock structures during cluster formation. The *dissipation*, $F_{\rm diss}$, term accounts for viscous dissipation of solenoidal flow. The dominant component of the dissipation term corresponds to the damping of turbulent eddies, although the second component can also act as a source term in shocks. For the moment, we ignore $F_{\rm diss}$ since we have no explicit viscosity, ν, in our simulations. In Sec. 6.3.4 and in Appendix 6.B, we will estimate the effective viscosity by looking at the dissipation of solenoidal turbulent energy. Clearly, the baroclinic and the dissipation term (through its strain tensor contribution) are the only source terms that are able to generate vorticity. The other source terms depend on the enstrophy itself and therefore they cannot generate enstrophy from zero.

Eq. 6.1 describes the Eulerian evolution of enstrophy. For the tracer analysis we need to transform this into a Lagrangian frame, moving with the ICM fluid, as the change of enstro-

[3] $S_{ij} = (1/2)(u_{ij} + u_{ji}) - (1/3)\delta_{ij}\nabla \times \mathbf{u}$

phy recorded by the tracers between two consecutive timesteps corresponds to the Lagrangian time derivative of the enstrophy. It is computed from Eq. 6.1 by adding $\mathbf{v} \cdot \nabla \epsilon$ and neglecting $F_{\rm diss}$, giving

$$\left(\frac{\mathrm{d}\epsilon}{\mathrm{d}t}\right)_{\rm lagrange} = 2 \cdot F_{\rm comp} + F_{\rm stretch} + F_{\rm baro}. \tag{6.8}$$

Enstrophy has the dimensions of inverse time squared, so is intuitively best understood in terms of characteristic "turnover rate, or, alternatively, eddy turn over time" for the turbulence. Similarly, the measurements of each source term in Eq. 6.2-6.6 are most simply understood in terms of the turnover time. As a measurement for the impact of each source term we compute the local, effective and individual source growth/decay times as

$$t_{\rm eff}(t) = \frac{\epsilon(t)}{\Sigma_i F_i(t)} \tag{6.9}$$

$$t_i = \frac{\epsilon(t)}{F_i(t)}. \tag{6.10}$$

In the equations above, the index i refers to the individual source terms.

6.2 Simulation Setup

6.2.1 ENZO

In this work, we study eight galaxy clusters taken from the ISC sample[4]. The sample has been simulated with the `ENZO` code (Bryan et al., 2014) using the the piecewise parabolic method hydro solver (Colella & Woodward, 1984). We applied the WMAP7 ΛCDM cosmology (Komatsu et al., 2011) in our simulations: $\Omega_0 = 1.0$, $\Omega_{\rm B} = 0.0445$, $\Omega_{\rm DM} = 0.2265$, $\Omega_\Lambda = 0.728$, $h = 0.702$, $\sigma_8 = 0.8$ and a primordial index of $n = 0.961$. Each cluster was extracted from an initial cosmological volume, sampled with 400^3 cells and 400^3 dark matter particles, of the size $\approx (63\ \mathrm{Mpc})^3$ (co-moving). The central volume $\approx (6.27\ \mathrm{Mpc})^3$ around each cluster has been refined further for a final resolution of $\mathrm{d}x \approx 20$ kpc. The adaptive mesh refinement (AMR) method used in our simulations is the same as described in Sec. 2 of Vazza et al. (2017c).

All simulations started at a redshift of $z = 30$ and about $\sim 190 - 250$ data dumps from each simulation, $\sim 160-220$ between redshifts $z = 1$ and $z = 0$, were saved for further analysis. Our simulations are non-radiative and do not include any magnetic fields nor non-gravitational heating, except an imposed temperature floor of $T = 3 \cdot 10^4$ K to mimic re-ionization at

[4] http://cosmosimfrazza.myfreesites.net/isc-project

moderate redshifts, e.g. $4 \leq z \leq 7$.

6.2.2 CRaTer

We use our Lagrangian tracer code *C*osmic-*Ra*y *Trac*er (`CRaTer`) (which has already been applied in various works: Wittor et al., 2017b; Vazza et al., 2016a,b; Wittor et al., 2016) to follow the clumpy accretion of gas in post-processing. We use a *Cloud-in-Cell*-method to interpolate the velocity, gas density, temperature, enstrophy and various source terms computed on the `ENZO`-grid to the tracer's position. The tracers are advected linearly in time. Following the mass distribution of the `ENZO`-simulations, the tracers were injected within a volume of 320^3 cells on the finest grid of the `ENZO`-simulation at $z = 1$. Using the same mass threshold we injected additional tracers according to the distribution of the mass entering the simulation box during run time. At $z = 0$ each cluster is consequently populated by $\sim 10^6 - 10^7$ tracers with a mass resolution of $m_{\rm tracer} \approx 3 \cdot 10^6\ M_\odot$. We choose this mass resolution as it is high enough to resolve structures accurately while the corresponding number of tracers can be still handled computationally.

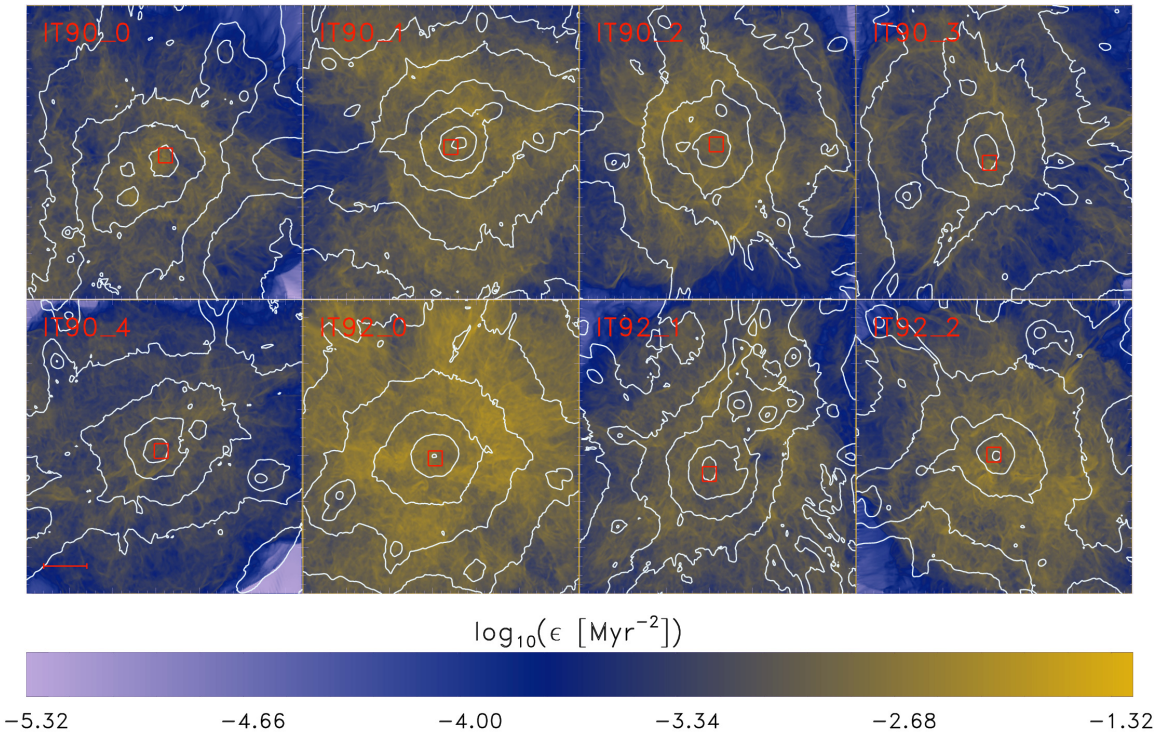

Figure 6.1: Projected enstrophy overlayed with the density contours of the different clusters in the highes AMR region of size $(6.27\ \mathrm{Mpc})^3$ at $z = 0$. The red square in each plot displays the $(320\ \mathrm{kpc})^3$ volume surrounding the peak of enstrophy. The red bar show the length of 1 Mpc. (A coloured version is available in the online article.)

6.3 Results on IT90_3

6.3.1 Cluster Properties

At a redshift of $z = 0$ our eight galaxy clusters cover a mass range of $M_{200} = 0.5-3.3 \cdot 10^{14}\ M_\odot$ (total mass) and a temperature range of $T_{200} \approx 5.1-19.3 \cdot 10^6$ K, which corresponds to a sound speed range of $266 - 516$ km/s. The dynamical and numerical properties of our clusters are summarized in Tab. 6.1, and a closer look at the dynamical histories and X-ray properties of each individual cluster is given in the appendix 6.A. The classification of each system based on the presence of a major merger has been estimated based on the analysis of the mass accretion history of each system.

The projected enstrophy overlayed with density contours at a redshift of $z = 0$ is shown for all eight clusters in Fig. 6.1. The red squares mark the $\sim (320\ \mathrm{kpc})^3$ volume centred around the peak of enstrophy, which has been chosen in three dimensions and is therefore not clearly visible in the projected maps. For our tracers analysis we will focus on the tracers that are located in this region at a redshift of $z = 0$.

Following the methods described in Sec. 6.2.2, we advected tracer particles in post-processing for each cluster between redshifts $z = 1$ and $z = 0$. Most of our discussion will revolve around the merging cluster IT90_3, which has been already studied in great detail in Vazza et al. (2017c). We will point out differences and similarities with the other ISC clusters where it is most instructive.

In Fig. 6.2, we show the projected enstrophy of cluster IT90_3 at redshifts $z = 1$ and $z = 0$. At $z = 1$ the enstrophy already spans a range of $10^{-6} - 10^{-1}$ Myr^{-2} and fine turbulent structures are visible. Even at the earliest output from our simulation $z = 30$, enstrophy is already at the level of about 1 percent of what it is at $z = 1$ or $z = 0$.

ID	M_{200} $[10^{14} \cdot M_\odot]$	r_{200} [kpc]	T_{200} $[10^6 \cdot \mathrm{K}]$	c_s [km/s]	major merger	N_s $(z = 30)$	N_s $(z = 1)$	N_p $(z = 0)$
IT90_0	0.77	881.37	6.88	308	no	187	156	$2.80 \cdot 10^6$
IT90_1	2.45	1292.68	10.55	381	yes	194	164	$7.75 \cdot 10^6$
IT90_2	1.10	998.89	8.29	338	no	196	166	$5.05 \cdot 10^6$
IT90_3	0.72	861.78	6.26	293	yes	193	163	$4.90 \cdot 10^6$
IT90_4	0.54	783.44	5.13	266	no	197	167	$4.07 \cdot 10^6$
IT92_0	3.32	1429.78	19.37	516	yes	244	209	$8.26 \cdot 10^6$
IT92_1	1.00	959.71	7.13	313	no	227	194	$4.82 \cdot 10^6$
IT92_2	1.17	1018.47	8.74	347	no	241	206	$4.73 \cdot 10^6$

Table 6.1: Main characteristics of our eight simulated clusters at z = 0: cluster ID, M_{200}, r_{200}, T_{200}, sound speed, dynamical state of the cluster, number of snapshots available between $z = 30$ and $z = 0$ $N_\mathrm{s}(z = 30)$, number of snapshots available between $z = 1$ and $z = 0$ $N_\mathrm{s}(z = 1)$ and the final number of tracers $N_\mathrm{p}(z = 0)$.

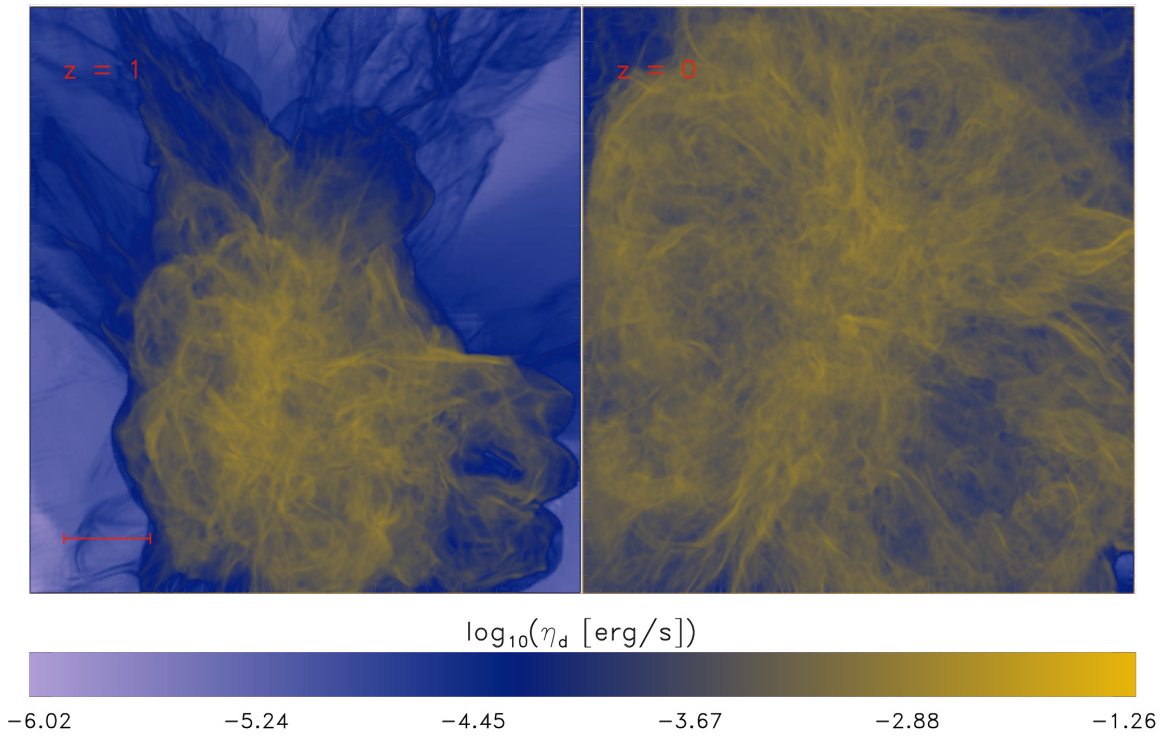

Figure 6.2: Evolution of the projected enstrophy in the highes AMR region of size $(6.27\ \mathrm{Mpc})^3$ of cluster IT90_3 at $z = 1$ (left) and $z = 0$ (right). The red bar show the length of 1 Mpc. (A coloured version is available in the online article.)

6.3.2 Evolution of Enstrophy

In order to investigate the source of enstrophy, we selected all tracers in the $\sim (320\ \mathrm{kpc})^3$ region centred around the peak of enstrophy at $z = 0$ (see the yellow box in the last panel in Fig. 6.3 and red squares in Fig. 6.1). Then we followed the tracer positions back to their positions at $z = 1$. At that point, most of these tracers are located inside of gas clumps or are entering the high resolution box inside of gas clumps at a later time. Only few tracers cannot be associated with any gas clump ($\approx 1-10\%$). At $z = 1$ we further divided the tracers into different families depending on their position (see the different colours in the first panel in Fig. 6.3). We selected eight different families of tracers in each cluster, each associated with a gas clump and containing $\sim 10^3 - 10^4$ tracers plus one additional family that contains all tracers that were injected at the boundaries by mass inflow into the refined volume after $z = 1$.

This procedure mostly selects the gas component at $z = 0$ associated with the densest gas

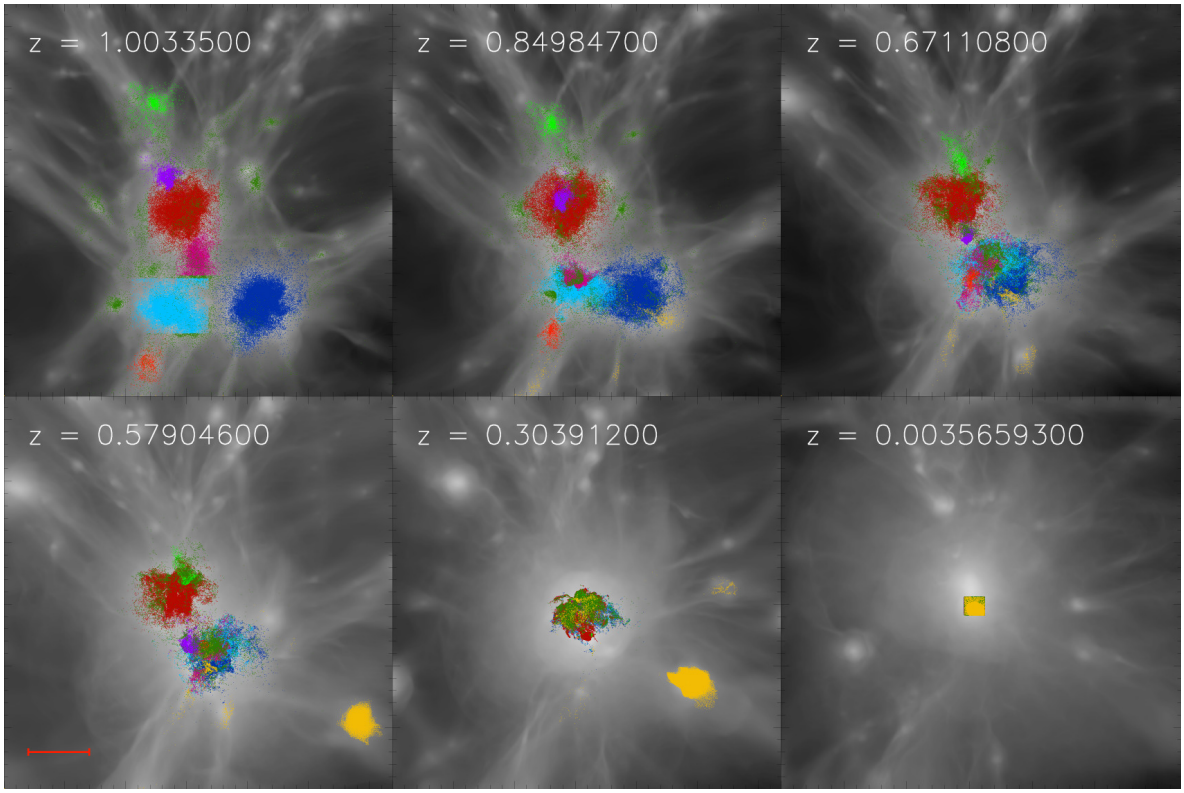

Figure 6.3: Evolution of the projected gas density overlayed with the tracers position of the different selections in cluster IT90_3. The tracers have been separated into groups from different subclumps, indicated by the different colours, at $z = 1$. The boxes are of the size $(6.27 \text{ Mpc})^3$. The red bar show the length of 1 Mpc. (See https://dnswttr.github.io/index.html/it903mov.html for a movie. A coloured version is available in the online article.)

substructures in the ICM, which are mostly associated with single self-gravitating gas clumps[5] that are already formed at $z = 1$ (see Fig. 6.3). The total gas masses of these clumps are typically a few $\sim 10^{12}$ $M_\odot$, corresponding to total masses (gas and dark matter) of a few $\sim 10^{13}$ $M_\odot$ before ram pressure stripping and tidal interactions detach their gas and dark matter components (e.g. Tormen et al., 2004).

In Fig. 6.3, we show the advection of the selected tracers across cluster IT90_3. The enstrophy averaged over each individual family of tracers and over all tracers as a function of time is plotted in Fig. 6.4. The black line shows the results for all tracers, while the colours correspond to the selection from Fig. 6.3. The mean ensemble enstrophy peaks three times: around $t \approx 6.7$, 8.1 and 9.8 Gyr. The times of the first two events correspond to two minor mergers between sub-clumps, while the time of the third event corresponds to the major merger observed in the IT90_3 cluster. Using the tracers we can cleanly isolate the different events. We see that peaks of enstrophy (shown in Fig. 6.4) always occur when two or more

[5] All the clumps have $m_{\text{clump}} > m_{\text{jeans}}$.

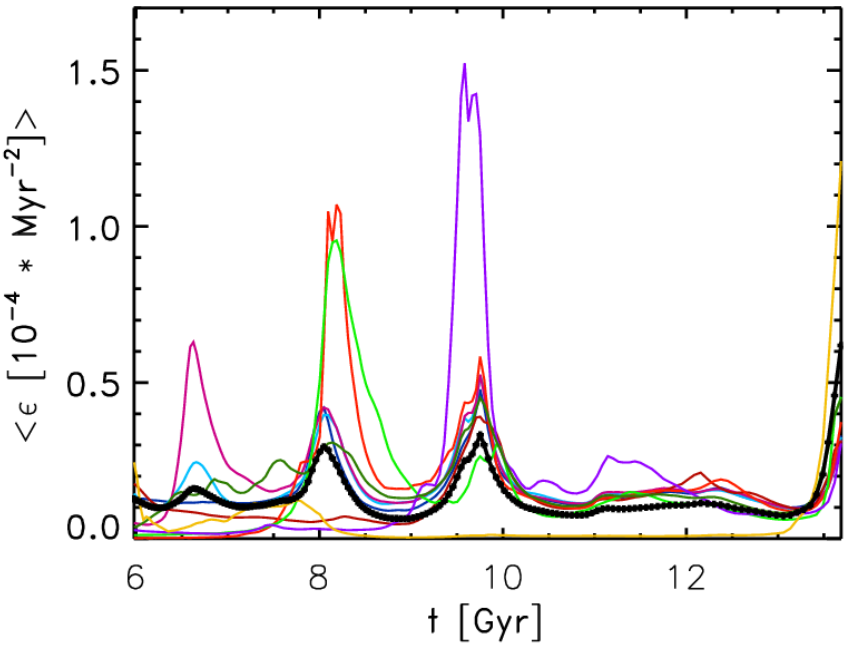

Figure 6.4: Evolution of the enstrophy, averaged over each tracer family selected in IT90_3 (colours). The black solid line displays the evolution of enstrophy, averaged over all tracers in IT90_3. (A coloured version is available in the online article.)

tracer families are colliding. As the tracers are following the gas, these events are connected to the merging of clumps.

In the following, we will focus on the evolution of four tracer families whose collected enstrophy sharply increases at $t \approx 8.1$ Gyr[6]. At $t \approx 6$ Gyr ($z = 1$) the four families are spatially separated. We show the evolution of the group enstrophies in Fig. 6.6(a). The enstrophy of each group always peaks around the time of merging. After the four clumps have merged, they all show the same evolution in enstrophy. The enstrophy peak at $t \approx 9.8$ Gyr happens during another merger involving these now combined clumps

The thermal entropy[7] (see Fig. 6.6(b)) increases significantly when the enstrophy peaks, indicating dissipation either by shocks or by numerical dissipation of turbulence[8] itself. The apparent correlation between enstrophy and entropy then suggests that the dissipation of turbulent energy is the dominant mechanism for gas heating here. The evolution of Mach numbers shows strong Mach numbers at the jumps of entropy and enstrophy. This supports the idea that these events happen during the occurrence of shocks.

We now examine the individual source terms of the enstrophy (see Eq. 6.8) for the tracer

[6]We notice that at the same time the enstrophy of two other families is increased, yet those two families are in a different region at this time and therefore they are related to a different, roughly simultaneous event.

[7]Represented as $S = c\frac{T}{\rho^{2/3}}$, where c is a constant.

[8]For Kolmogorov turbulence it is easy to show from the Navier-Stokes equations that the local turbulent energy dissipation rate scales as $\epsilon^{3/2}$ (see Eq. 6.12) below

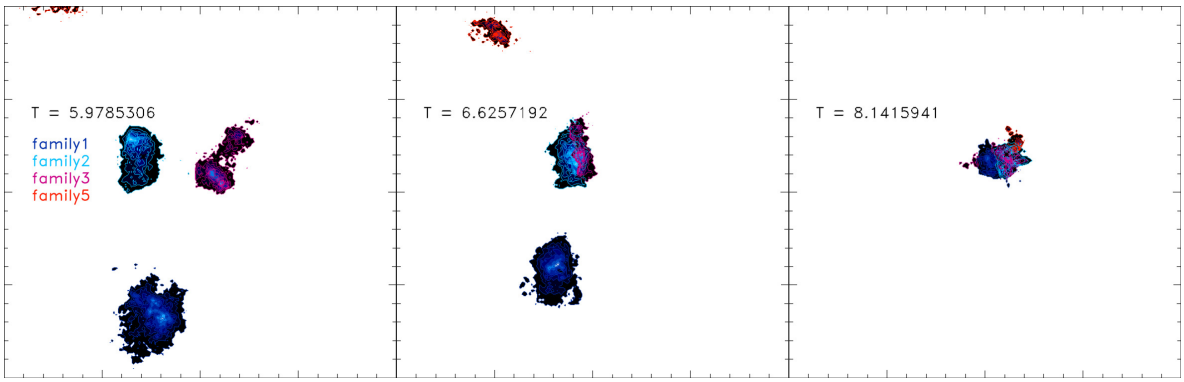

Figure 6.5: Spatial evolution of four tracer families across cluster IT90_3. The enstrophy is amplified at the timesteps displayed here due to the merging of the clumps. The displayed regions are of the size $(400\ \mathrm{Mpc})^2$. (A coloured version is available in the online article.)

family displayed in dark blue (see Fig. 6.7). The enstrophy (top row) shows two maxima at $t \approx 8.1$ Gyr and at $t \approx 9.8$ Gyr, marked by the vertical red lines. The green and purple lines mark the local minima before and after the peak of enstrophy. The compressive and baroclinic source terms (second and third row in Fig. 6.7) are always the strongest before the enstrophy reaches its maximum. On the other hand, the stretching source term (fourth row in Fig. 6.7) peaks after the maximum enstrophy. The other selections of tracers in cluster IT90_3 record the same sequence of events when enstrophy is enhanced (see Fig. 6.8 for all recorded events). The enstrophy and source terms are normalized to a unit time and unit amplitude. We note that the double peaks in some enstrophy lines (e.g., in the 14th column of Fig. 6.8) are numerical artefacts caused by limited time resolution in the ENZO data. In Fig. 6.9, we show the mean values of enstrophy and sources terms for IT90_3 and the other clusters. The same analysis on the other seven clusters gives consistent results: on average the compressive and baroclinic motions are the strongest before the peak of enstrophy, while the stretching source is the strongest after the peak of enstrophy. However, some special cases are pointed out in the following:

IT90_0 shows the biggest delay between the maximum of compressive/baroclinic source terms (red and green lines in Fig. 6.9) and stretching source term (blue line in Fig. 6.9). As it turns out, the other clusters have much more violent and active histories than IT90_0, which is our most relaxed cluster. The other clusters have been exposed to a higher dynamical activity disturbing their ICMs. Consequent stretching motions occur throughout the lives of those clusters. Accordingly, the smaller time offsets between the source terms and the less distinct peaks in F_{stretch} in IT90_2, IT91_1 and IT92_2 compared to IT90_0 are the consequences of cluster-scale evolutionary events rather than events related to local clumps.

In the case of IT90_1, the mean baroclinic source term is significantly stronger than the mean compressive source term. Still the compressive source term peaks before baroclinic source term. This distinction from the other clusters points out that the spatial extent of the

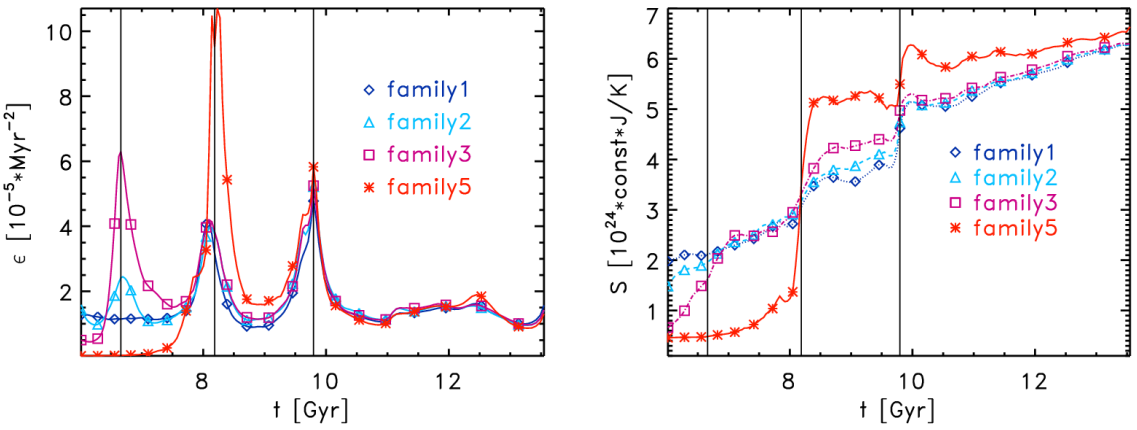

(a) (b)

Figure 6.6: Evolution of enstrophy in panel (a) and entropy in panel (b) recorded by the four tracer families selected in cluster IT90_3 and that are shown in Fig. 6.5. The black vertical lines mark the timesteps of local maximum enstrophy. (A coloured version is available in the online article.)

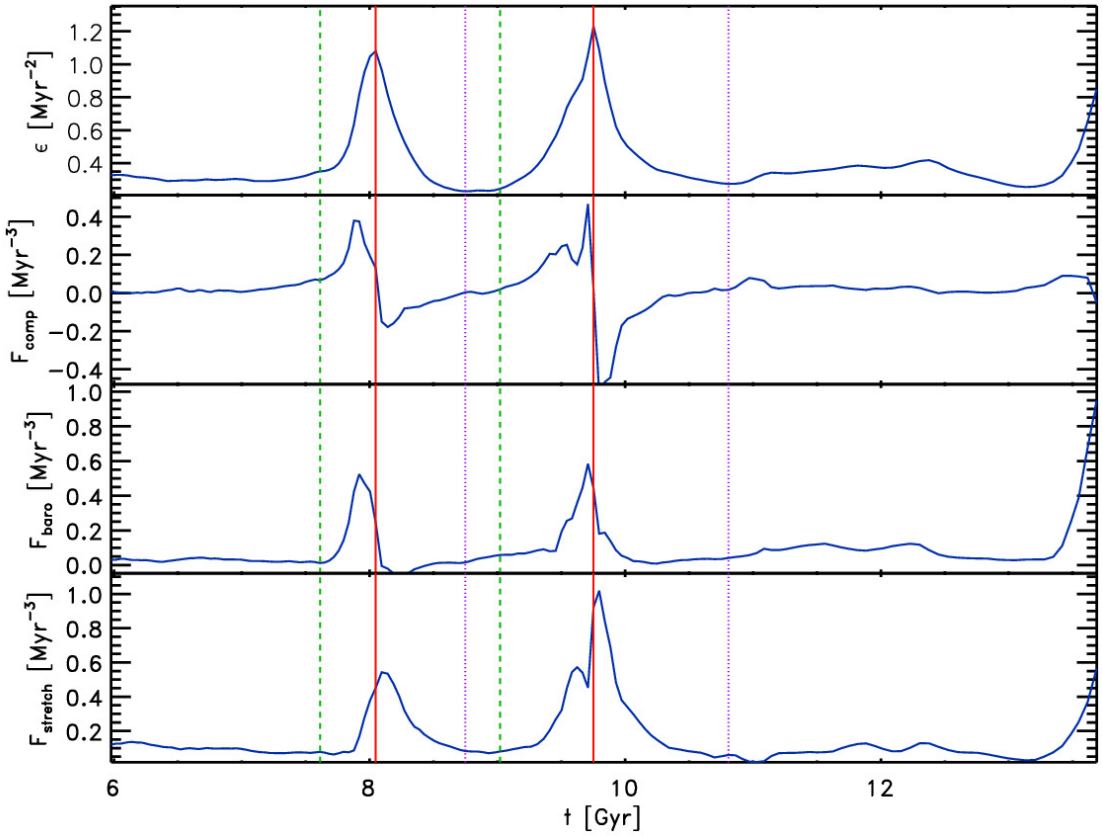

Figure 6.7: Evolution of ϵ, F_{comp}, F_{stretch} and F_{baro} of the first family of tracers in IT90_3 over the last ~ 7 Gyr of the simulation. The red vertical, solid lines mark the local peak of enstrophy, while the green, dashed and purple, dotted lines mark the local minima of enstrophy. (A coloured version is available in the online article.)

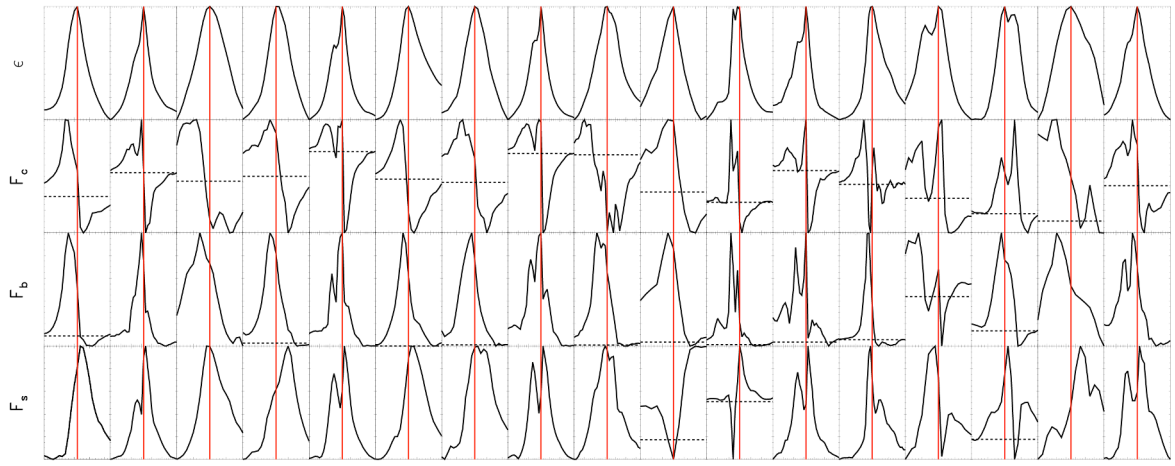

Figure 6.8: Summary of all enstrophy "events" recorded by `CRaTer` in IT90_3. Each column shows a single event recorded by one of the different families. The plots show the evolution of enstrophy (top row), compressive source term (second row), baroclinic source term (third row) and stretching source term (bottom row) around the peaks of enstrophy. The amplitudes (y-axis) of each quantity have been normalized to unity and the time range (width of x-axis) around each each has been normalized to the evolutionary time at the peak of enstrophy. The red line marks the time of the local peak of enstrophy. The black dashed horizontal lines shows the zero level. (A coloured version is available in the online article.)

compressive source term is much more sensitive to specific structures, e.g. shocks, while the baroclinic source can cover a larger volume since it reflects complex consequences of multiple events in the relatively recent history of the cluster.

6.3.3 Growth and Decay Timescales

Following Eq. 6.9 and 6.10, we estimate the enstrophy growth and decay times[9], related to the individual source terms and of the effective change of enstrophy, measured by the tracers. We compute the distributions of the different evolutionary times at the six times marked in Fig. 6.7 (see Fig. 6.10).

At all times the distributions of the effective evolutionary times (left column in Fig. 6.10) show the same shape at all times. Most of the tracers recorded an effective evolutionary time in the range of $t_{\rm eff} \approx 10 - 100$ Myr ($\sim 60\% - 80\%$ of the tracers) or in the range of $t_{\rm eff} \approx 10^2 - 10^3$ Myr ($\sim 20\% - 40\%$ of the tracers). Furthermore we observe that during the events of maximum enstrophy the effective evolutionary times are decreased.

Comparing times for the individual source terms, we notice that $t_{\rm comp}$ is the most variable. At the peak of enstrophy, the compressive time is mostly in the range of $t_{\rm comp} \approx 10 - 100$ Myr while it is in the range of $t_{\rm comp} \approx 10^2 - 10^3$ Myr at other times. The evolutionary times of the

[9] In the following, we will refer to these characteristic growth and decay timescales only as evolutionary times.

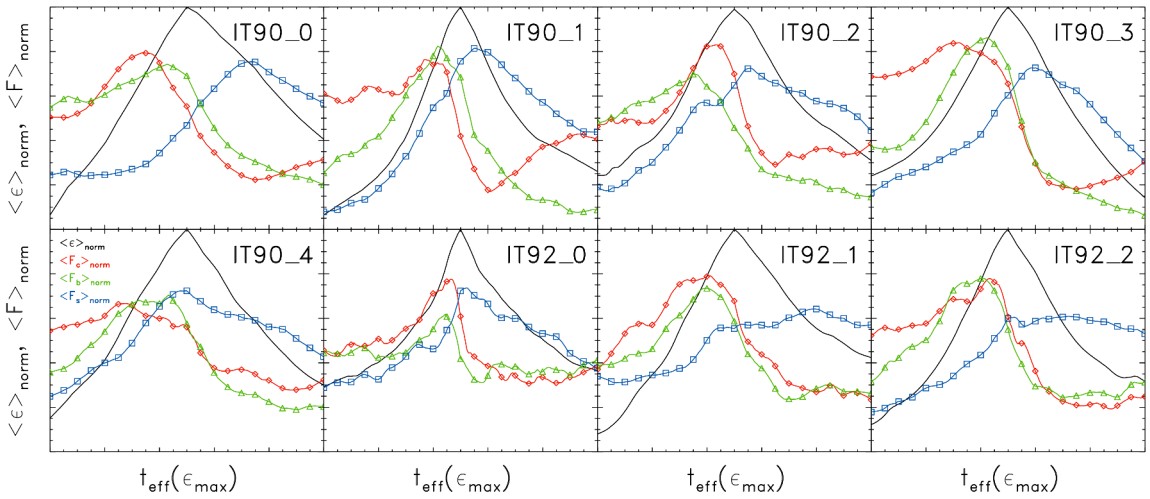

Figure 6.9: Evolution of the means of enstrophy (black), compressive source term (red, diamonds), baroclinic source term (green, triangles) and stretching source term (blue, squares) normalized to an unit amplitude of one and a unit time equivalent to one evolutionary time measured at the peak of enstrophy, e.g. $t_{\rm eff}(\epsilon_{\rm max})$ equals the evolutionary time when the enstrophy is at its maximum. Each panel shows the averages of all events recorded by the tracers in one cluster. It is observed that the compressive and baroclinic source terms are always the strongest before the peak of enstrophy, while the stretching term shows its maximum after the peak of enstrophy. (A coloured version is available in the online article.)

other source terms remain mostly in a certain time range. The stretching time, $t_{\rm stretch}$, falls in the range $\approx 10-100$ Myr and the baroclinic time, $t_{\rm baro}$, falls in the range $\approx 10^2-10^3$ Myr. The analysis of the average evolutionary times (see Fig. 6.11) shows that stretching motions are dynamically most important for the evolution of turbulence within the cluster. The compressive motions are mostly subdominant throughout most of the clusters' lifetime. Yet, they become important during the shock-related amplification of turbulence. The baroclinic source term on the other hand only has a small dynamical impact. While baroclinicity is an essential source of enstrophy, it is mostly a minor contributor to the net growth of enstrophy in comparison to compression and especially to stretching (see Fig. 6.11. At very late times, in this cluster the baroclinic source term becomes competitive with the compressive source term for a short amount of time (see 12 Gyr $< t <$ 13 Gyr in Fig. 6.11), perhaps because baroclinic contributions are more broadly distributed in that era. This is because baroclinic sources are concentrated in shocks, which are relatively weak after the last merger event. On the other hand, the contribution from the baroclinic source term is negligible in dense environments (as it is always smaller than the solenoidal source term). However, in Vazza et al. (2017c) we showed that it gets very important for the enstrophy generation in cluster outskirts, where flows following oblique shocks first inject vorticity in the ICM.

The evolutionary times in the other clusters besides IT90_3 show the same qualitative behaviour. The stretching source term always shows the shortest evolutionary time, in the range

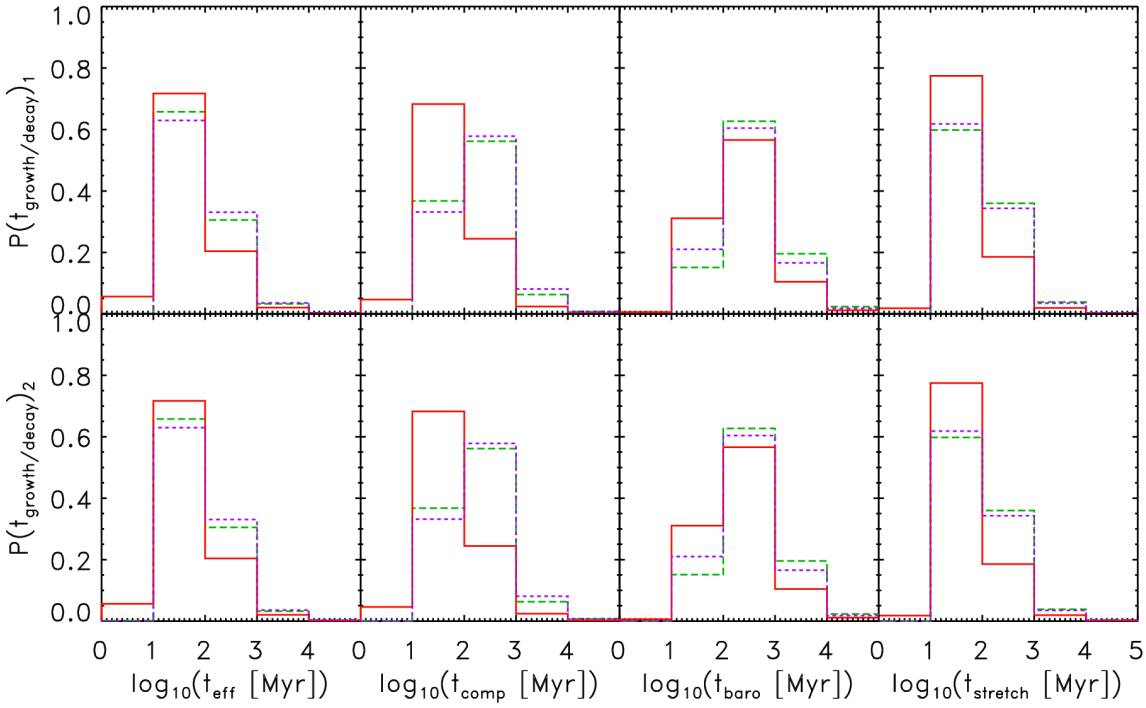

Figure 6.10: Distributions of the evolutionary times computed around the times of maximum enstrophy shown in Fig. 6.7. The top row corresponds to the first peak at $t \approx 8.1$ Gyr and the bottom row corresponds to the second peak at $t \approx 9.8$ Gyr. The colours and linestyles match the time selections shown in Fig. 6.7. (A coloured version is available in the online article.)

of $t_{\rm eff} \approx 10 - 100$, while the other source terms show a comparable evolutionary time around the major events that amplify enstrophy and they show a larger evolutionary time otherwise. We also notice that the more relaxed clusters, e.g. IT90_0, show large evolutionary times of around $t_{\rm eff} \approx 10^2 - 10^3$ Myr.

In summary, our analysis shows that the fastest stage of enstrophy evolution of the densest substructures in the ICM is dominated by compression and shortly followed by stretching of vorticity. The baroclinic generation of vorticity is less important in this density regime, but it produces substantial vorticity at earlier times and across outer accretion shocks.

6.3.4 Dissipation Term and Magnetic Field Amplification

In Eq. 6.8, we neglected the dissipation term since it is not well-defined in an ideal flow. However, the numerical dissipation of turbulent motions is obviously present, as we are not employing sub-grid modelling of turbulence (e.g. Schmidt et al., 2015). Here we try to empirically constrain its amplitude from the offset between the measured enstrophy change and the summed source terms in Eq. 6.8. In Fig. 6.12(a), we plot the evolution of the right (blue line) and left (black line) hand-side of Eq. 6.8 computed with the same tracer family that we have

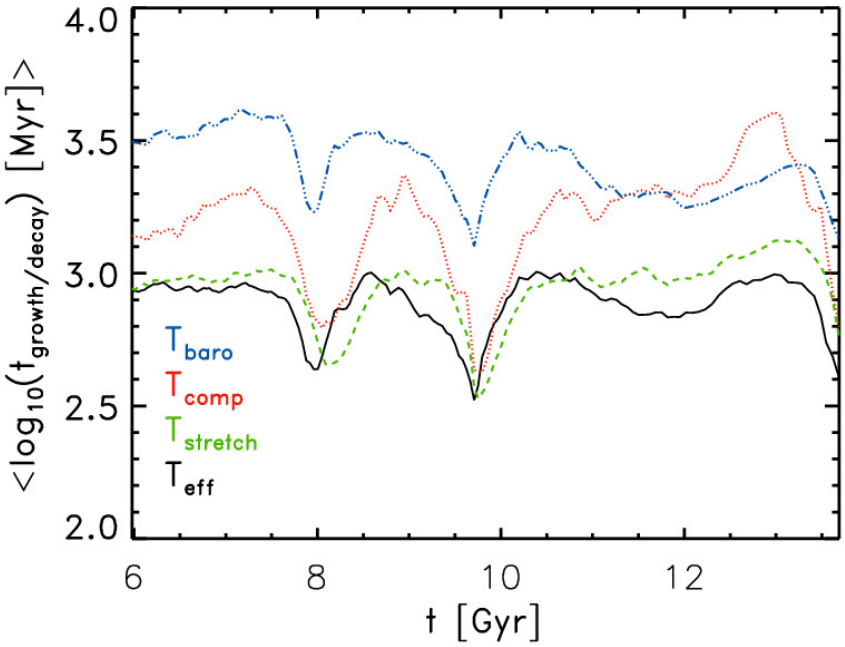

Figure 6.11: Histories of the effective evolutionary times, see Eq. 6.9, (black, solid) and the evolutionary times of the different source terms, see Eq. 6.10, recorded by the same selection of tracers shown in Fig. 6.10: baroclinic (blue, dash-dotted), compressive (red, dotted) and stretching (green, dashed). (A coloured version is available in the online article.)

studied in detail in the previous sections and that is displayed in Fig. 6.7. The two evolutions show a non constant offset, which we plausibly ascribe to the effect of dissipation. Especially at $t \approx 8.2$ Gyr and $t \approx 10$ Gyr the difference is not constant showing that turbulence is dissipated. Hence we compute the dissipation term as:

$$F_{\rm diss} = \frac{\Delta\epsilon}{\Delta t} - (2 \cdot F_{\rm comp} + F_{\rm stretch} + F_{\rm baro}) \,. \tag{6.11}$$

The amount of dissipated enstrophy is the time-integrated absolute value of Eq. 6.11 $\epsilon_{\rm diss} = \int |F_{\rm diss}| \, {\rm d}t$. In the Navier-Stokes formalism (see App. 6.B), the dissipation rate can be computed without any knowledge on the explicit viscosity. In fact, to a first approximation only a minimum turbulent scale is required (which admittedly depends on the existence of an effective viscosity). In our case, this minimum scale is set by the cell size of our grid cells. Hence, we can compare the results of Eq. 6.6 with the net effective dissipation. Following the approach of Vazza et al. (2017c)[10], we compute this as:

$$\bar{\eta}_{\rm i} = 0.014 \cdot \epsilon_i^{\frac{3}{2}} \cdot l_{\rm turb}^2, \tag{6.12}$$

[10]See also App. 6.B.

using a length scale[11] of $l_{\rm turb} = 2 \cdot {\rm d}x$ and the total amount of enstrophy ϵ_i. In Fig. 6.12(b), we compare the mass-integrated values, $\eta_{\rm i}$, of both quantities computed using the tracers. We observe that they are in general agreement (see Fig. 6.12(a)) and assume that $F_{\rm diss}$ in Eq. 6.11 is a reasonable proxy for the dissipation rate of the turbulent cascade in our simulations. If the ICM is magnetised and the gas flow is turbulent enough to produce a small-scale dynamo, a fraction of the turbulent energy in the ICM is transferred to the intracluster magnetic fields (for recent reviews see e.g. Subramanian et al., 2006; Ryu et al., 2008, 2012). In a predominantly sub-sonic, non stationary and solenoidal turbulence the amplification of ICM magnetic fields can substantially differ from what measured in the simulated ISM (e.g. Pan et al., 2016; Kritsuk et al., 2017). Recently, Miniati & Beresnyak (2015) estimated the efficiency of turbulent energy that is transferred to magnetic fields to be in the range of $C_E \approx [4\%, 5\%]$. Following their approach we compute the evolution of the magnetic energy from the history of turbulent dissipation as (see App. 6.B)

$$E_B(t) = \frac{B^2}{8\pi} = C_E \int^t \rho \eta_{\rm i}(t'){\rm d}t'. \tag{6.13}$$

As an example, we estimate the evolution of magnetic energy based on enstrophy evolution by one selection of tracers from IT90_3 in Fig. 6.13(a). At $t \approx 13.1$ Gyr the magnetic energy is of the order of $E_B \approx 0.8 - 1.3 \cdot 10^{-13}$ erg cm^{-3} using $\epsilon_{\rm diss}$ and of $E_B \approx 0.3 - 1.4 \cdot 10^{-13}$ erg cm^{-3} using $\epsilon_{\rm total}$. This translates into magnetic fields ranging around $B \approx 1.4 - 1.8$ μG and $B \approx 0.85 - 1.05$ μG, respectively. The above estimates for the magnetic field strengths were computed using the tracers that reside in the cluster core region at $z = 0$. The values estimated in this way are in good agreement with results from observations (e.g. Govoni et al., 2010). Both, the magnetic field and the magnetic energy are increased stepwise at $t \approx 8$ Gyr and $t \approx 10$ Gyr tracing the evolution of the dissipation term. The timing of these jumps coincide with the times of the merging events in IT90_3. During the mergers, enstrophy is quickly amplified and is then rapidly dissipated again. Part of this energy will be transferred to the magnetic fields on eddy turnover timescales. The magnetic field growth becomes slower soon after the turbulence subsides. For our estimates on the magnetic field amplification, we neglected magnetic field dissipation that becomes important once the turbulence decays. Therefore, our results are an upper limit.

We observe similar results in the other clusters of our sample. In all clusters, we estimated the mass-integrated values of $\eta_{\rm diss}$ and $\eta_{\rm total}$ to be of the same order, which are both in the range of $10^{38} - 10^{40}$ erg s^{-1}. Application of the above model for transfer of solenoidal turbulent energy into magnetic energy produces magnetic fields, this will produce magnetic fields of the order of a few μG. In all cases we observe the episodic jumps in the magnetic field growth. These jumps are always connected to some kind of merging activity.

[11] This is the width of the stencil used to compute the vorticity and which also represents an approximation to the minimum scale for the cascade.

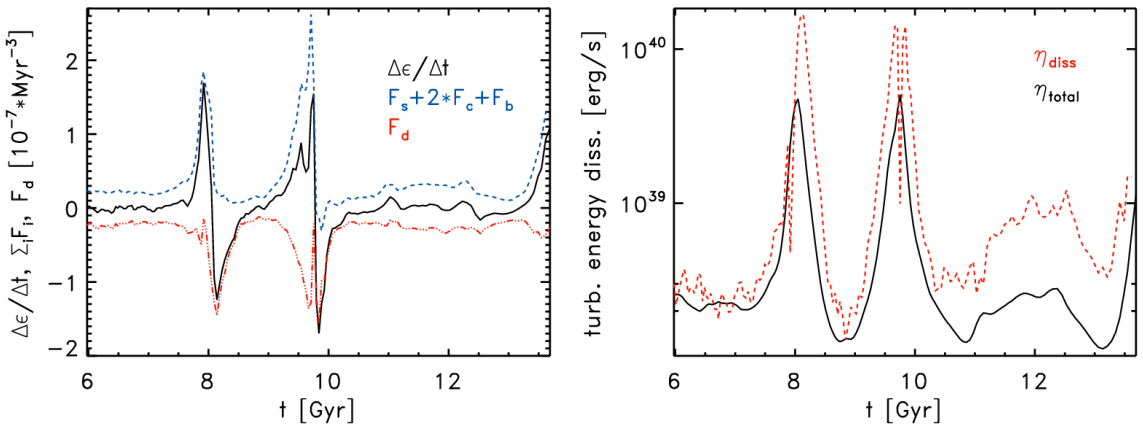

(a) (b)

Figure 6.12: Panel (a): Evolution of the left (black, solid) and right (blue, dashed) handside of Eq. 6.8. The red line shows the difference of the two, which we associate with viscous dissipation, see label $F_{\rm diss}$ (red line, dash-dotted). (b): Comparison of $\eta_{\rm diss}$ (red, dashed), computed with $F_{\rm diss}$ from Eq. 6.11, with the enstrophy dissipation rate computed from Eq. 6.12 (black, solid). (A coloured version is available in the online article.)

6.4 Discussion & Conclusions

We studied the origin and history of enstrophy of the ICM in galaxy clusters formed in Eulerian grid cosmological simulations. We did this using Lagrangian tracer particles that tracked the evolution of the enstrophy in their associated ICM mass along with the associated enstrophy sources and sinks. This way we could analyse the accretion history of turbulence in eight clusters with different formation histories and with different dynamical states at $z = 0$. In the Lagrangian frame, enstrophy sources and sinks can be decomposed into compressive, baroclinic, stretching and dissipative terms derived from the compressible Navier-Stokes equations and as defined in Eq. 6.8. We used the Lagrangian tracer code `CRaTer` to follow these different source terms and the relative timings of cluster formation events at the peaks of enstrophy.

Close examination of the gas flow properties early in our simulations revealed that small small amount of enstrophy, and therefore turbulence in gas clumps, has already been generated at an early age of the cluster, $z \gg 1$. We have not determined the origin of this very early enstrophy, yet we consider that at least some of it may result from baroclinicity in the cosmologically-based simulation initial conditions. Our analysis showed that additional enstrophy is later generated by baroclinic motions resulting from shocks during the cluster evolution. The generated enstrophy is amplified by compressive and stretching motions. En-

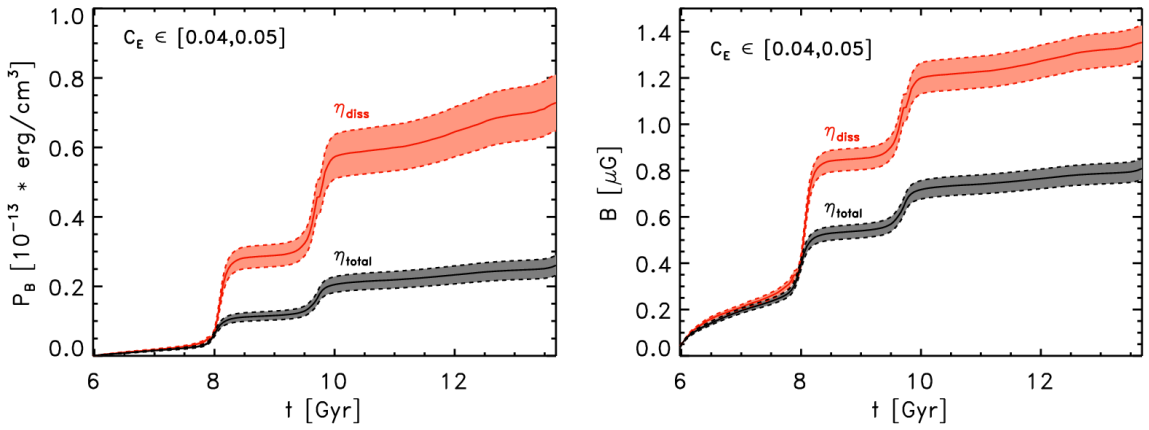

(a) (b)

Figure 6.13: Panel (a): Integrated magnetic field energy fuelled by the dissipation of turbulence. Panel (b): The corresponding magnetic field strength. The dashed lines give the lower and upper limit obtained with efficiencies in the range of $C_E \in [4\%, 5\%]$. (A coloured version is available in the online article.)

strophy, in association with the turbulence, is dissipated on small scales, just as its turbulent kinetic energy. This turbulent energy contribution contributes substantially to heating of the ICM. Our tracer analysis showed that there is a clear sequence of cluster formation events that lead to strong amplification and decay of enstrophy. During merger events we observed first an increase in the compressive source term, indicating that compression that is mostly connected to shocks is amplifying the enstrophy. Around the same time the baroclinic source term is growing as well, supporting the connection to shocks, and additional enstrophy is generated. Following these two developments the enstrophy reaches its maximum and then starts to decay again. From the previous discussion and results in App. B, we see that the enstrophy dissipation rate increases strongly as the enstrophy increases ($F_{\rm diss} \propto \epsilon^{3/2}$), so once $F_{\rm baro}$ and $F_{\rm comp}$, which are the primary solenoidal turbulence drivers, diminish, the dissipation rate overwhelms even a strong $F_{\rm stretch}$ source and ϵ decays along with the solenoidal turbulent energy.

In order to obtain a more quantitative view of the dynamical importance of each source term over time, we computed the effective and individual evolutionary time of the source terms. Throughout the whole cluster history, the stretching source term has on average the shortest evolutionary (the fastest enstrophy amplification) time with $t_{\rm stretch} < 10^3$ Myr and therefore enstrophy amplification is largely controlled by is controlled by stretching. This seems natural as vortex stretching and energy dissipation are independent of the fluid viscosity, e.g. the dissipative anomaly, in incompressible turbulence. On the other hand, the compressive and baroclinic evolutionary times range between $t_{\rm baro,\ comp} > 10^3$ Myr during most of the cluster lifetime making them weak compared to the stretching source term. They only become competitive, when they are $t_{\rm baro,\ comp} < 10^3$ Myr during dynamical events when shocks and

other compressions are strong, such as during mergers. This is consistent with our results that the stretching motions are dynamically most important for the evolution of turbulence in galaxy clusters. Yet, baroclinic motions are needed to initially generate turbulence and compressive motions are, once they are acting, a strong booster for enstrophy. The above results are consistent for all clusters that we examined.
The enstrophy dissipation rate peaks when the enstrophy peaks, as already noted. This situation also corresponds to the most rapid amplification of ICM magnetic field and, quite possibly, the peak rate of turbulent acceleration of cosmic rays (see Brunetti & Jones, 2014, and references therein). In the case of magnetic fields, using magnetic field behaviors from existing MHD turbulence simulations we estimated peak ICM magnetic field strengths $\sim \mu$G in our simulated clusters, consistent with estimates from current radio observations (e.g. Govoni et al., 2010).
As a final remark, we notice that the study of the internal dynamics of gas substructure is very relevant to model high-resolution X-ray observations of groups falling onto larger clusters (e.g. Markevitch et al., 2000; Randall et al., 2008; Eckert et al., 2014; Ichinohe et al., 2015; De Grandi et al., 2016) and their implication to understand plasma processes in these environments. More work is also need to investigate the effects of cooling, feedback (e.g. Dolag et al., 2009) and gas viscosity (e.g. Roediger et al., 2015), which were not included in this work.

Acknowledgements

We thankfully acknowledge G. Brunetti and D. Eckert for fruitful scientific conversations. DW acknowledges support by the Deutsche Forschungsgemeinschaft (DFG) through grants SFB 676 and BR 2026/17. TWJ acknowledges support from the US NSF through grant AST121159. FV acknowledges personal support from the grant VA 876/3-1 from the DFG, and from the European Union's Horizon 2020 research and innovation programme under the Marie-Sklodowska-Curie grant agreement no.664931. FV and MB also acknowledge partial support from the grant FOR1254 from DFG. The `ENZO`-simulations have been carried out in the *ITASCA*-cluster hosted by the University of Minnesota.

6.A Cluster Dynamics

In Fig. 6.14, we compare the radial density profiles computed with the `ENZO` and `CRaTer` data at $z \approx 0$. In light grey we show the profiles for each cluster, while the red lines show the average of the profiles over all eight clusters. On the whole the tracers are able to retain the shape of the `ENZO` profile. In Fig. 6.15, we show the $M - T$ relation of each cluster.

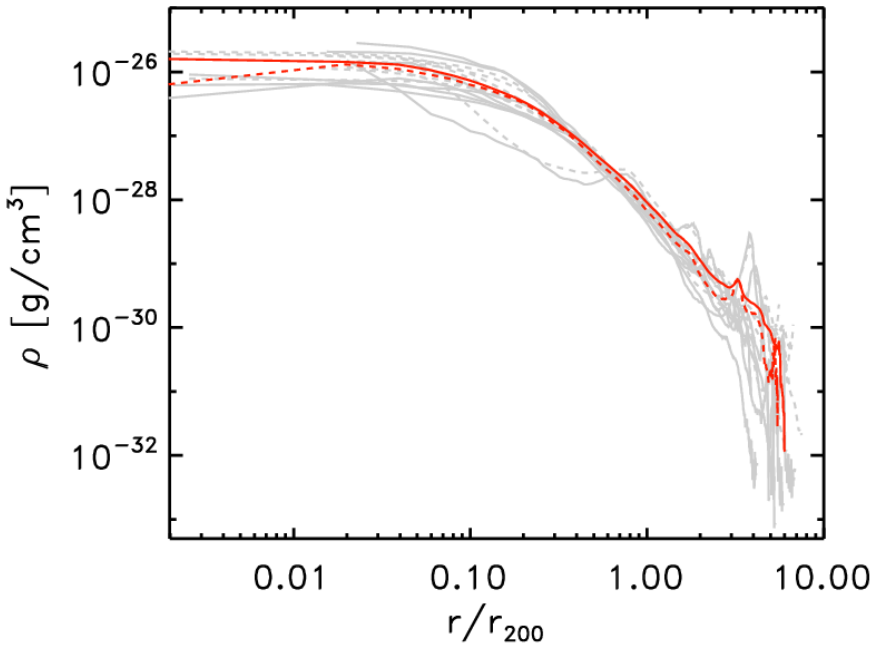

Figure 6.14: Radial density profiles of the clusters at $z \approx 0$. The solid lines give the results of the Eulerian, unweighted grid average and the dashed lines give the Lagrangian tracer particle-weighted average. The red lines show the average over all clusters. (A coloured version is available in the online article.)

The dynamics of the various clusters differ substantially. For example, IT90_3 hosts a major merger at $t \approx 10.2 - 10.3$ Gyr ($z \approx 0.3$), while IT90_0 stays very relaxed until the end of the simulation. Some clusters, e.g. at at the end of the simulation IT90_0 or IT92_1 are on the verge of a major merger, thus accreting a lot of mass, while other clusters, e.g. IT90_1 or IT92_0, are only accreting small clumps.
The X-ray surface brightness maps of each cluster are shown in Fig. 6.16. The cluster centres show a X-ray surface brightness in the range of $L_X = 10^{40} - 10^{42}$ erg s^{-1} (20 kpc)$^{-2}$. We show images of the projected turbulent energy dissipation rate (see Eq. 6.12) of the clusters in Fig. 6.17 at $z = 0$ ($t \approx 13.72$ Gyr) in a (6.4 Mpc)^3 volume.

6.B Simple Models for Turbulent Dissipation Rates

Under the assumption that a turbulent flow with a power law power spectrum can be described as isotropic, solenoidal turbulence, it is possible to express both the kinetic energy dissipation rate, η_d, and the enstrophy dissipation rate, F_{diss}, in forms that do not depend explicitly on the kinematic viscosity, ν. These provide simple and convenient means to estimate the dissipation of turbulence in our simulations, where the viscosity is not well-defined. We start

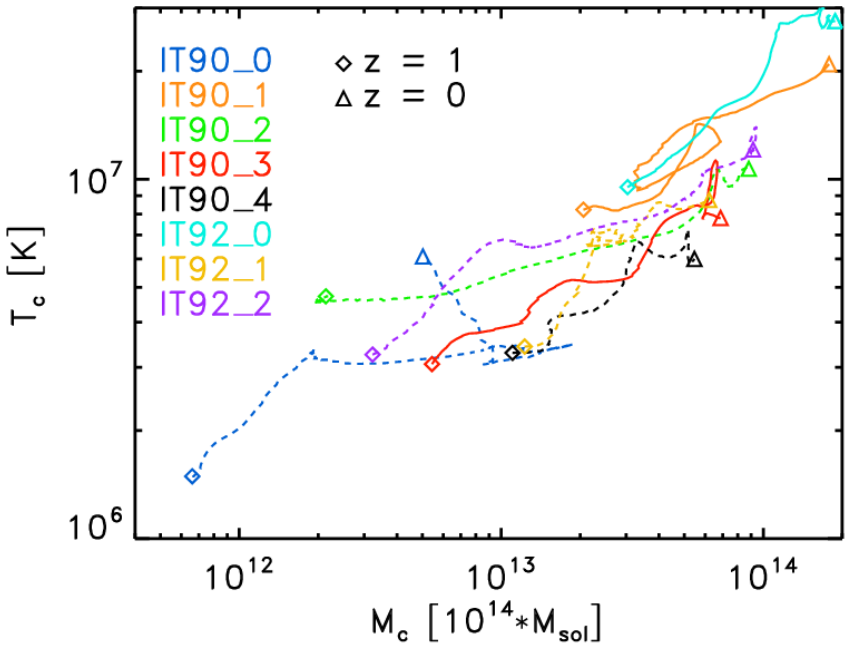

Figure 6.15: Mass-temperature relation measured in the central $(1.44\ \mathrm{Mpc})^3$ of each cluster. The solid lines show the evolution of the major merger clusters and the dashed lines show the evolution of the clusters without a major merger. (A coloured version is available in the online article.)

from equation 6.1, which provides an expression for $d\epsilon/dt_{\mathrm{Euler}} = \partial\epsilon/\partial t$ obtained from the curl of the compressible Navier-Stokes equation (Porter et al., 2015). The various physical contributions to $d\epsilon/dt_{\mathrm{Euler}}$; that is, its source terms, are listed in equations 6.2 - 6.6. We focus here on the dissipative source term,

$$F_{\mathrm{diss}} = \nu\vec{\omega} \cdot \left(\nabla^2\vec{\omega} + \nabla \times \vec{G}\right). \tag{6.14}$$

Ignoring the strain tensor element $\nabla \times \vec{G}$, whose predominant role is inside shocks (Porter et al., 2015), we then look for a simple way to estimate

$$F_{diss} \approx \nu\vec{\omega} \cdot \nabla^2\vec{\omega}. \tag{6.15}$$

To obtain estimates of the right hand side of equation (B2) it is useful to utilize the Fourier representation of the turbulent motions. Assuming for simplicity isotropic, Kologorov turbulence in the range $[\ell_1, \ell_o]$ it has been shown by many authors (e.g., Gotoh et al., 2002; Beresnyak, 2011, and references therein) that the turbulent kinetic energy power spectrum can be be expressed in the Fourier domain as

$$E(k) = C_o\eta_d^{2/3}k^{-5/3} = \frac{1}{2}v_k^2, \tag{6.16}$$

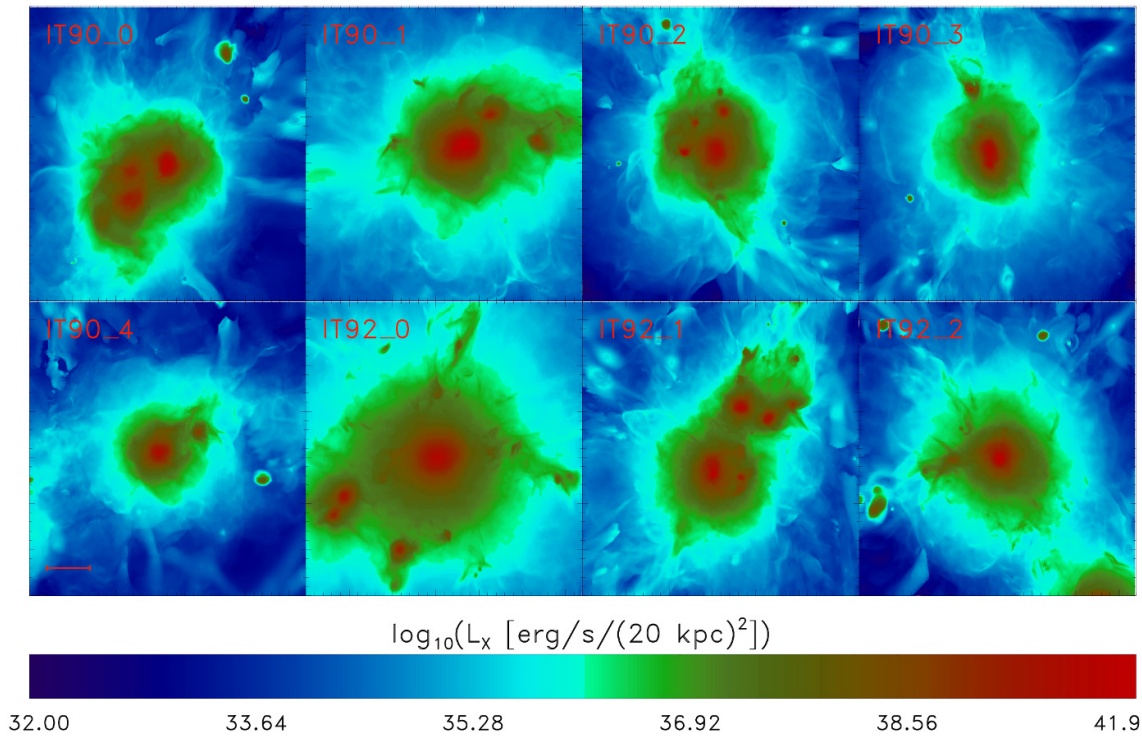

Figure 6.16: Projected X-ray surface brightness along the line of sight of all the clusters of our sample. Each box is of the size $\approx (6.27 \text{ Mpc})^3$ with an resolution of $\mathrm{d}x \approx 20$ kpc. The red line in the panel of IT90_4 show the length of 1 Mpc. The red bar show the length of 1 Mpc. (A coloured version is available in the online article.)

for $k_o = 2\pi/\ell_o \leq k \leq k_1 = 2\pi/\ell_1$, where η_d is the turbulent kinetic energy dissipation rate (per unit mass) and $C_o \sim 1.5$ is the so-called Kolmogorov constant. Given that our intent is primarily to establish simple scaling relations, it is not critical whether or not the inner and outer scales in the turbulence are constant across the cluster. The standard expression for viscous kinetic energy dissipation is (e.g., Landau & Lifshitz, 2013)

$$\eta_{\rm d} = 2\nu \sum_{i \neq j} \left(\frac{\partial v_i}{\partial x_j} \right)^2 . \tag{6.17}$$

In terms of the Fourier power spectrum, we can then write

$$\eta_{\rm d} = 4\nu \int_{k_o}^{k_1} k^2 E(k) dk \tag{6.18}$$

Applying the form for $E(k)$ in equation 6.16 we can then obtain a relation for the viscosity, ν in terms of quantities defining the turbulent power, namely, C_0, η_d and the range of scales

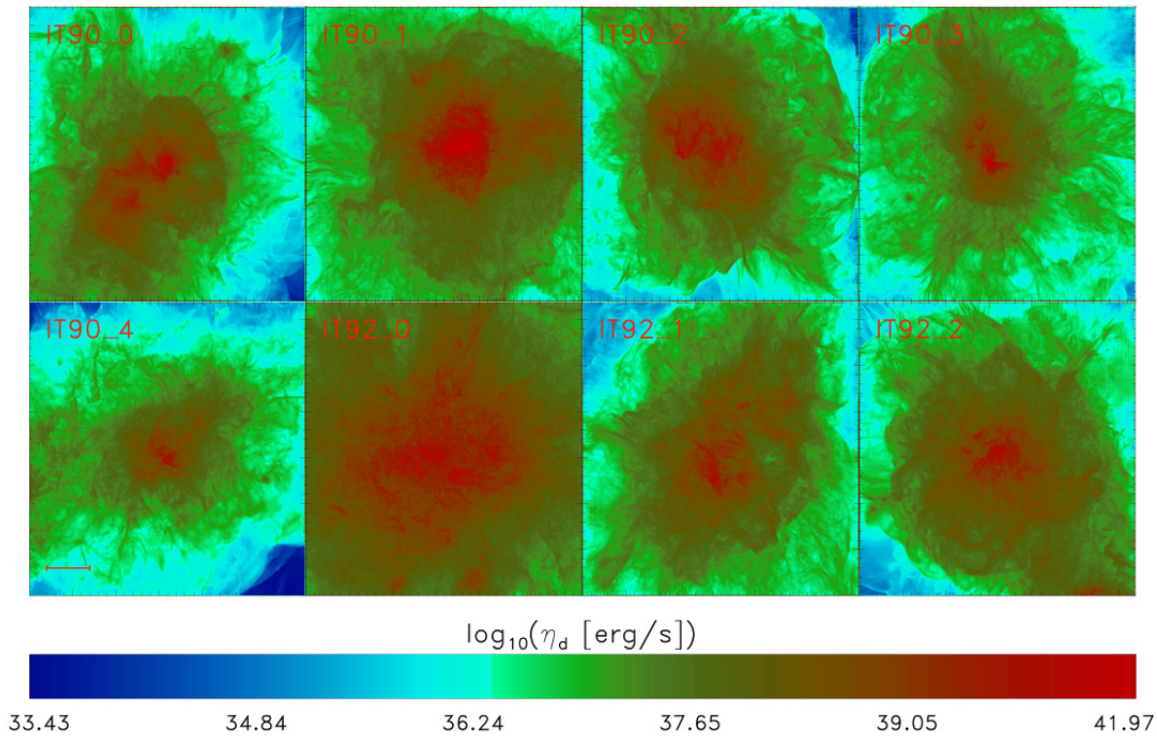

Figure 6.17: Projected turbulent energy dissipation rate along the line of sight of the clusters contained in our sample. Each box is of the size $\approx (6.27 \text{ Mpc})^3$ with an resolution of $\mathrm{d}x \approx 20$ kpc. The red bar show the length of 1 Mpc. (A coloured version is available in the online article.)

characterizing the turbulence,

$$\nu \approx \frac{1}{3C_o} \frac{\eta_{\rm d}^{1/3}}{k_1^{4/3}[1-(\frac{k_o}{k_1})^{4/3}]}. \tag{6.19}$$

Similarly,

$$F_{\rm diss} \approx \nu \int_{k_o}^{k_1} k^2 \omega_k^2 dk \approx \frac{4}{5}\ \nu\ \epsilon k_1^2\ \frac{1-(\frac{k_o}{k_1})^{10/3}}{1-(\frac{k_o}{k_1})^{4/3}}, \tag{6.20}$$

where $\omega_k = \vec{k} \times \vec{v_k}$. Using equation 6.19, equation 6.20 can be written as

$$\begin{aligned} F_{\rm diss} \approx \frac{1}{5}\left(\frac{4}{3C_o}\right)^{3/2}\ \epsilon^{3/2} \frac{1-(\frac{\ell_1}{\ell_o})^{10/3}}{[1-(\frac{\ell_1}{\ell_o})^{4/3}]^{5/2}}\ \ \overrightarrow{\ell_o >> \ell_1} \\ \sim 0.17\epsilon^{3/2}\ [1+(5/2)(\ell_1/\ell_o)^{4/3}]. \end{aligned} \tag{6.21}$$

In the final expression, we assumed $C_o \approx 1.5$. Evidently, the enstrophy dissipation rate is simply $F_{\rm diss} \propto \epsilon^{3/2}$, scaled by a factor that is only moderately sensitive to the ratio of the outer and inner turbulent scales, ℓ_o/ℓ_1. Our empirical estimate for this relation from the

IT90_3 cluster gives $F_{\rm diss} \approx 0.35\epsilon^{3/2}$, corresponding to $\ell_o/\ell_1 \sim 31$. Combining equations 6.17 and 6.19 we can also write the turbulent energy dissipation rate in terms of ϵ without explicit reference to the viscosity, ν; namely,

$$\eta_d = \left(\frac{4}{3C_o}\right)^{3/2} \frac{1}{k_1^2} \frac{\epsilon^{3/2}}{1-(\frac{k_o}{k_1})^{4/3}} \quad \overrightarrow{\ell_o >> \ell_1} \quad \sim 0.02\epsilon^{3/2}\ell_1^2\,[1+(\ell_1/\ell_o)^{4/3}]. \tag{6.22}$$

This is also consistent with our empirical estimate for η_d in the IT90_3 cluster given in equation 6.12. Note, further, according to equations 6.21 and 6.22 that the ratio $\eta_d/F_{\rm diss} \propto \ell_1^2$ with a constant that depends on the ratio of the outer to inner turbulence scales. We note, finally, that even when the turbulence is not truly Kolmogorov, these relations can still provide a useful, if approximate, guide to estimates for the dissipation rates.

7 Conclusion and Perspective

7.1 Summary of Results

In this thesis, we studied the origin, effects and evolution of the non-thermal components in galaxy clusters. For this purpose, we combined Eulerian and Lagrangian simulation techniques to obtain new insights into the physics of the ICM. Thanks to the powerful combination of these techniques, we could study with unprecedented detail the relevance of the relatively small-scale (≤ 100 kpc) properties of the magnetized plasma for the production of non-thermal components of the ICM. In particular, we investigated (for the first time in the literature, to the best of our best knowledge) the interplay between magnetic field topology and the acceleration of cosmic-ray electrons and protons, as well as the observational signatures of radio relics. Furthermore, we examined the evolution of vorticity and enstrophy in the ICM by following its main source terms over time.
This work is divided into four separate project focusing on different aspects on the non-thermal components in galaxy clusters. In a first project, Chap. 3, we studied if using the shock obliquity as an additional parameter for computing the shock acceleration efficiencies solves the problem of the missing γ-rays. For the second project, Chap. 4, we used the non-detection of γ-ray emission to restrict the shock acceleration efficiencies of shock waves in the ICM. The third project, Chap. 5, focused on the effects of depolarization in radio relics and investigated the Mach number discrepancy observed at radio relics. In fourth and final project, Chap. 6, we followed the evolution of enstrophy within the ICM and estimated the amplification of the magnetic field due to turbulent dissipation. Our main findings summarize as follows:

- **Shock obliquities in the ICM are close to random.** The distribution of shock obliquities in the ICM is generally close to random, with more quasi-perpendicular, $\geq 50°$, than quasi-parallel shocks, $\leq 50°$. This trend is amplified by the shocks themselves, which align the magnetic fields in a perpendicular direction. Turbulence, especially in the cluster core, continuously randomizes the distribution. We found that the fraction of quasi-perpendicular shocks is larger in the cluster outskirts than in the cluster core and the distribution of shock obliquities is more randomized for small Mach number shocks than for large Mach numbers.

- **Oblique shocks may reduce the tension with the Fermi-limits**. Based on recent particle-in-cell simulations (i.e. Caprioli & Spitkovsky, 2014b; Guo et al., 2014a,b), we linked the acceleration efficiencies to the shock obliquity. If only quasi-perpendicular shocks are allowed to accelerate cosmic-ray electrons, the total relic radio emission is reduced by a factor of ~ 2, hence remaining observable. The γ-ray emission if reduced by a factor of ~ 3.3, still above the Fermi-limits, if only quasi-parallel shocks are allowed to accelerate cosmic-ray protons. Only if the acceleration of cosmic-ray protons is limited to shocks with an upstream magnetic field larger than ~ 0.1 μG the hadronic γ-ray emission goes below the Fermi-limits.

- **Limits on the acceleration efficiency of cosmic rays.** Our analysis of large cosmological simulations including the dynamical effect of cosmic rays suggests that the budget of cosmic rays allowed by the Fermi-limits is of order of $\sim$ %, and that this limits the acceleration efficiency to $\leq 10^{-3}$ by the typical shocks following structure formation, e.g. $M \leq 5$.

- **On the Mach number bias for shocks observed in radio.** The study of the spectral index properties and Mach number distributions across radio relics, showed that radio observations are typically biased towards the highest Mach number (i.e.flattest spectral component) of the shocked gas leading to relics. Hence, this can be the cause for the discrepancy in the Mach number estimates from radio and X-ray observations. This effect becomes more significant if the relic is observed "edge-on".

- **Depolarization by tangled magnetic fields in the ICM.** The analysis of depolarization in radio relics showed that at high frequencies most of the depolarization happens in the ICM between the source and the observer, due to Faraday Rotation in the magnetised ICM. The depolarization at low frequencies occurs to a same amount at the source and in the intermediate ICM.

- **A complex evolution of vortical motions in the ICM.** The bulk of vorticity in the ICM is generated by baroclinic motions within the ICM. Additional compressive and stretching motions enhance the enstrophy, i.e. vorticity squared, locally. Thanks to our simulations we observed a clear sequence of events leading to the amplification of enstrophy. Following shocks, at first compressive and, to a small amount, baroclinic motions increase. This is followed by the enstrophy reaching its maximum. While the compressive and baroclinic motions start to decay, stretching motions are amplified. Yet, a strong dissipation of enstrophy overwhelms the amplification by stretching, and thus enstrophy decays.

- **Self-similar vorticity evolution of gas substructures.** An analysis of the dynamical timescales of each source term showed, that mainly stretching motions, with

$t_{\rm stretch} < 10^3$ Myr, are responsible for the evolution of enstrophy. The compressive and baroclinic source terms, that have mostly $t_{\rm comp,\ baro} > 10^3$ Myr throughout the cluster lifetime, only become significant around shocks and compressive motions, when their dynamical timescales are reduced to $t_{\rm comp,\ baro} < 10^3$ Myr.

- **Amplification of magnetic fields by turbulence.** The dissipation rate of enstrophy is the strongest when the enstrophy is at its maximum. At this time also the amplification of magnetic fields in the ICM should be the strongest. We estimated that a dissipation of the turbulent kinetic energy flux of a few percent is enough to produce magnetic fields strength of a few $\sim$ μG, that agree with estimates from current radio observations.

7.2 Future Perspectives

The results of this thesis show that with advanced numerical simulations we can investigate the physical link between different non-thermal phenomena observed in galaxy clusters. Furthermore, the unique combination of Eulerian and Lagrangian simulation methods allowed us to extend our theoretical understanding of these processes.
In Chap. 3 and 4, we showed that there is still an unknown parameter space to explore for our understanding of shock acceleration in galaxy clusters. Caprioli & Spitkovsky (2014a) already started to explore the space of acceleration efficiencies for cosmic-ray protons depending on Mach number and shock obliquities using PIC simulations. They studied Mach numbers in the ranges of $M \sim 5 - 50$. However, the Mach numbers in the ICM that are responsible for radio relics are believed to be smaller, $M < 5$. Therefore, it would be desirable to probe this low Mach number space further.
The radio emission computed in Chap. 3 only included freshly injected cosmic-ray electrons, which is reasonable as the simulation timesteps are larger than the assumed cooling time of cosmic-ray electrons. For a proper understanding of the electron spectrum, it is necessary to follow the energy gains and losses of the electrons properly. This can be achieved by using a Fokker-Planck solver, as it has been done for example by Donnert & Brunetti (2014). It would be useful to implement such a module into `CRaTer`. In this case, a Fokker-Planck solver would be attached to each tracer to follow the evolution of the electron spectrum. This way one includes also the radio emission from aged particles. The theoretical study of older electrons will become more important in the near future as the next generation of radio telescopes, e.g. Lofar and SKA-low, will observe at lower frequencies and are expected to find hundreds of radio relics and halos (e.g. Nuza et al., 2012).
At the same time it will also be important to include local cosmic-ray sources, such as AGN, in the simulations. Modules for the simulation of AGN in cosmological simulations are al-

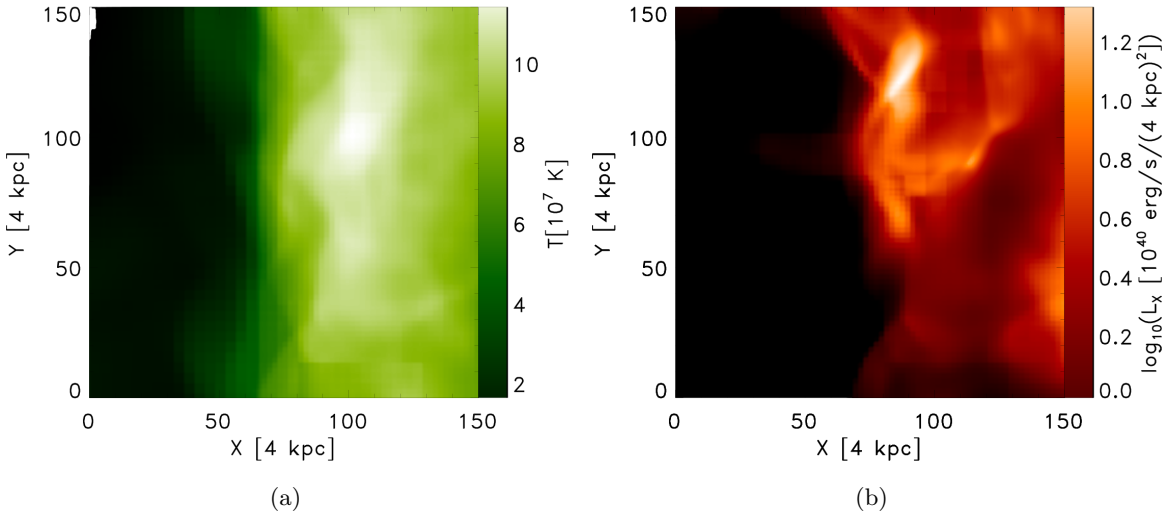

Figure 7.1: Temperature, (a), and X-ray luminosity, (b), projection of the high resolution relic.

ready implemented in `ENZO`. Using `CRaTer` we will also follow the evolution of cosmic-ray electrons injected by different mechanisms. This detailed analysis would provide insights into the cosmic-ray electron content in galaxy clusters coming from global and from local sources. This study would provide further insights on AGN being possible sources for fossil electrons. The study of polarization of radio relics, see Chap. 5, is done using the same simulation as in Chap. 3. Yet, the spatial resolution and time sampling in the simulation are too large to properly resolve the ageing of electrons. Hence, it would be desirable to analyse a high-resolution radio relic with finer timesteps using `CRaTer`. Preliminary analysis of higher resolution simulations of relics (probing a spatial resolution of ~ 4 kpc) have already started, e.g. see Fig. 7.1 and 7.2.

In Chap. 6, we studied the evolution of enstrophy in galaxy clusters at late redshifts. Although the evolution of turbulence is linked to that of the magnetic fields (which can be observed at some extent), it would be crucial to directly relate the simulated turbulence levels to X-ray observations. In association with the next generation of radio telescopes, e.g. Athena and XARM, it would be useful to derive a connection between the observed X-ray emission and the dissipation of enstrophy. Preliminary work connecting dissipative structures in the ICM to projected X-ray luminosity is on-going. In Fig. 7.3, we display the fluctuations of the turbulent kinetic dissipation rate and the X-ray luminosity of the same region in cluster IT90_3, that has been studied in Chap. 6.

As a final conclusions, besides the original results discussed in this thesis, the powerful numerical algorithms developed in the scope of this PhD project will also have the potential to address several of the unsolved questions regarding the non-thermal phenomena observed in the largest cosmic structures.

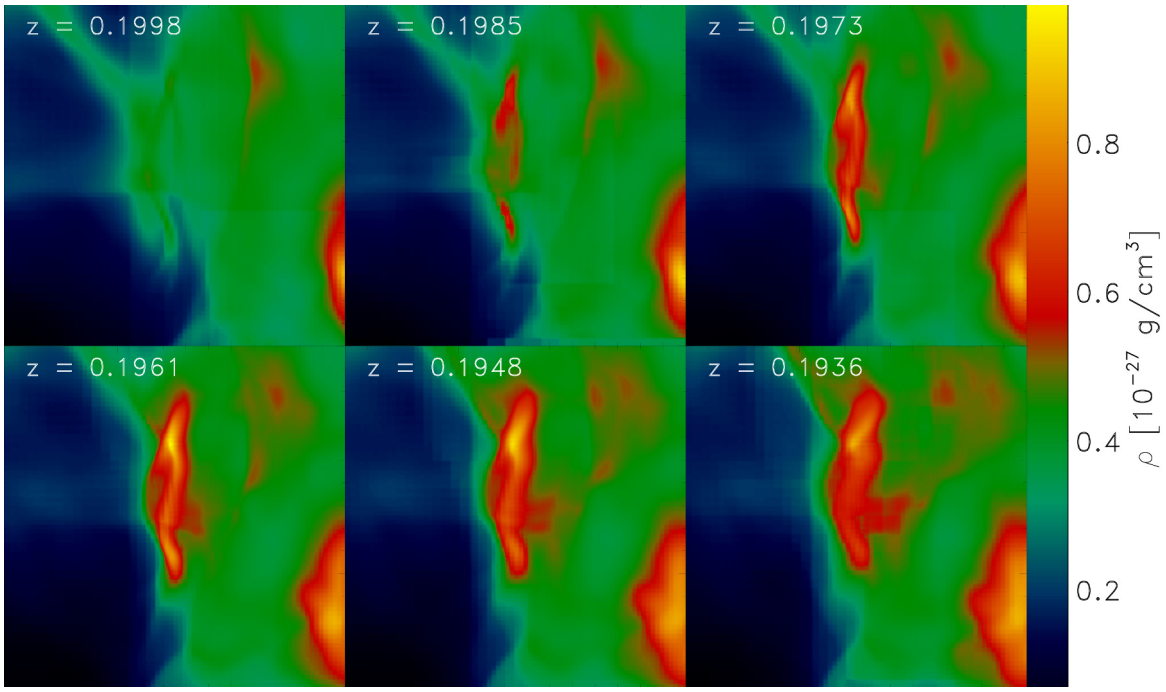

Figure 7.2: High resolution simulation, $\sim$ 4 kpc, of a radio relic. The displayed quantity is the projected gas density along the line-of-sight.

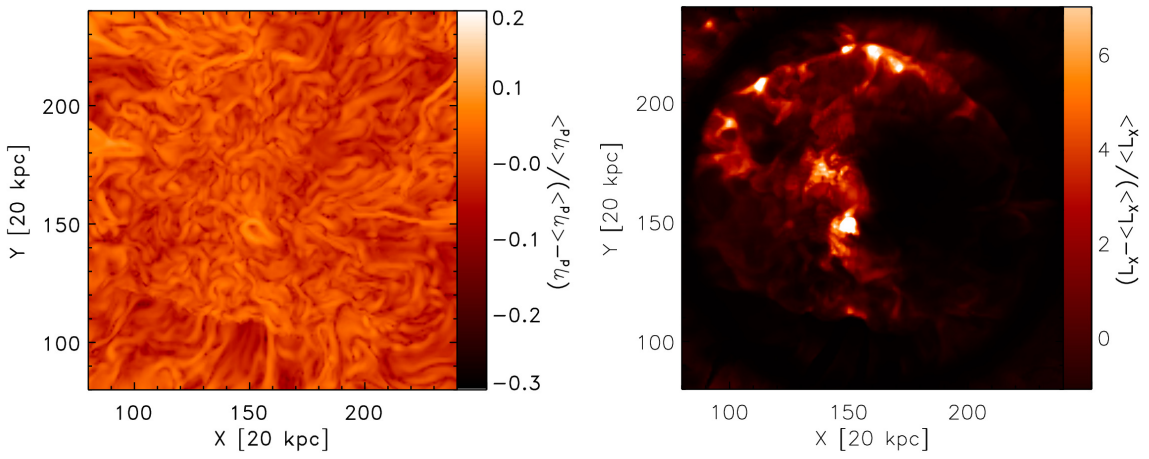

(a) (b)

Figure 7.3: Slices through cluster IT90_3 that has been extensively studied in Chap. 6. (a): fluctuations of the turbulent kinetic dissipation rate (Eq. 6.12). (b): X-ray fluctuations of the same regions.

A Acknowledgements

I would like to take a minute to acknowledge the support of some people without which I would have not been able to write this thesis over the last 3.25 years:

First of all, I would like to thank Dr. Franco Vazza and Prof. Dr. Marcus Brüggen for giving me the opportunity to write this thesis and for providing me with such in interesting topic. Furthermore, I would like to thank them for their patience, especially if it comes to finding my spelling errors, motivation and help! Thank you a lot for sending me on all those fun business trips that have taken me all around the world: form the USA in the west, Sweden in the north, Greece in the South, China in the East and many more.

I would also like to thank my close collaborators Prof. Dr. Thomas Jones and Dr. Matthias Hoeft. I really enjoy(ed) the projects we are/were working on and I hope we can keep these up in the future. Also, thank you very much for the hospitality in Minneapolis and Tautenburg.

Furthermore, I would like to thank Franco, Annalisa and Leo for their hospitality in Bologna. I am really looking forward to more Beatles concerts in the near future.

There are several people at the Observatory of Hamburg that helped me a lot during my thesis: Thanks to Angelika for all the bureaucratic support, for not being annoyed by all my questions concerning traveling funds and for accepting my postal deliveries. Thanks to Anke for always providing cookies in the library, especially in the last few months they have helped me a lot during my night shifts. Thanks to Wolfram, Sören and Rainer for their IT-support. I would like to thank everybody I shared an office with, especially Sarah and Janis for all the short (or long) chats. They really help to refocuse my mind. Yet, I have to apologize for my angry face when I am concentrated, that was nothing personal! A big "Thank You" goes out to all the current and former members of the *Extragalactic Astrophysics and Cosmology* group for all the fun at the lunch breaks. Furthermore I would like to thank Federica and Amanda for the decoration, Johannes for the coffee breaks, Jacques for taking the scuba diving lessons and Dieter for the soccer discussion (still Schalke is cooler than HSV).

I would like to thank ~ 3.73 kg of coffee, that I drank in my office (plus an unknown amount

at conferences, business trips, in Minneapolis, at home, during talks etc.), for always keeping me awake or a least making me believe that I was awake.

In addition to all the people mentioned above, there are several people outside of astronomy without who I would not be where I am right now:

Most important of all, I would like to thank my awesome parents who gave me the opportunity to pursue a career of my choice. Furthermore, I would like to thank them for always supporting me and giving me the freedom to make my own decisions and experiences, even if this results in a trip to Braunschweig in a super-shady car, a visit to the hospital in Barcelona or leaving home to live on the other side of the globe at the age of 16. Thank you very much!

I would also like to thank my wonderful sister for always (re-)setting the bar and having my back everytime and everywhere. I would like to thank my grandparents for all the moral support and the infinite supply of coffee and cookies.

Furthermore, I would like to thank all my friends in the Ruhrpott and in Hamburg for letting me leave my work in the office and providing me a life outside of the University. Here, special thanks go out to Jonas and Merle for infinite number of talks about -you know which topic-.

Last but not least, I would like to thank my skateboard for always being there for me, providing a valve to let of steam and giving me the possibility to clear my mind.

So thanks to all of you, because “The only way on earth to multiply happiness is to divide it.” (Paul Scherrer) also holds for a PhD-thesis!

B List of Figures

1.1 Evolution of a cosmological volume in time from redshift $z \approx 30$ to $z \approx 0$. Small density perturbations (left upper panel) collapse over time and form the Universe as it is know today (bottom right panel): Filaments of matter, the cosmic web, permeate the space. Voids, low density regions, are found between the filaments, while galaxy clusters sit at their intersections. 6

1.2 Combined radio continuum from $1 - 4$ GHz taken with the VLA. The image shows the various radio sources in a galaxy cluster: a radio halo at the cluster centre, a radio relic north west of the halo, a tailed radio galaxy just south of the halo and a foreground AGN in the left corner. These pictures are taken from Pearce et al. (2017). 10

1.3 Chandra X-ray data (blue) and VLA radio data of the MACS.J0416.1-2403 cluster, as shown by NASA, ESA, CXC, NRAO/AUI/NSF, STScI, and G. Ogrean (e.g Ogrean et al., 2016). (b) Spectral index map of 1RXS J0603.3+4214, as displayed in van Weeren et al. (2012). 11

1.4 (a) Radio emission of the double radio relic in PLCKG287.0+32.9 at 323 MHz in blue (GMRT) and the X-ray emission in red (XMM-Newton). This picture is taken from Bonafede et al. (2014). (b) Spectral index map (top) and polarized electric field vectors (bottom) in CIZA 2242.8+5301, as displayed in van Weeren et al. (2010). 12

1.5 1.5(a) Shock dissipation efficiencies for the gas, δ, and the cosmic rays, η, taken from Kang & Ryu (2013). The green and blue line display the cases without adiabatic compression. 1.5(b) Radio power as a function of Mach number at different field strengths taken from Hoeft et al. (2008). 19

2.1 Work cycle of the tracer particles between two adjacent snapshots in `CRaTer`. The green region shows the part of the code that runs in semi-parallel and the blue region is the part of the code that is fully parallelized. The `openMP` threads are synchronized at the red *waits*. 28

2.2 Schematic sketches of the velocity interpolation methods in two dimensions. (a) Nearest-grid-point: The particle (red dot) reads the velocity from the nearest grid cell, in this case $(i+1, j)$. (b) Cloud-in-a-cell: The velocities from the four (eight in three dimensions) nearest grid cells are interpolated to the tracers position. 30

2.3 The density profile of the Zeldovich Pancake at three different timesteps. The black lines shows the profile of the ENZO data and the red crosses show the profile computed using the CRaTer data. 31

2.4 Advection of six different tracers using different time-stepping schemes. In panel (a) and (b) the tracers are advected between two adjecent snapshots of ENZO. They are using (a) the saved timestep or (b) smaller timesteps for their advection. In panel (c) and (d) the tracers are advected between every other snapshot of ENZO and either they are using (c) the saved timestep or (d) smaller timesteps. This test shows that the time-stepping schemes used in panel (a) and (b) are sufficient enough to evolve the tracers. While if the timestep is too large the tracer advection is error-prone as in panel (c) and one should use smaller timesteps as in panel (d). 32

2.5 Density projection of the cosmological simulation. The yellow squares mark the position of the nine massive halos used for the velocity testing. 33

2.6 Density profiles of the nine clusters found the in the cosmological simulation. The black line shows the profile computed with the ENZO-data and the solid lines show the *CIC* runs and the dashed lines show the *NGP* runs. The red lines were computed using explicit time-stepping and the blue lines were computed using implicit time-stepping. 34

2.7 Density profiles of the nine clusters found the in the cosmological simulation. The black line shows the profile computed with the ENZO-data and the red line shows the *CIC + w_27* run computed with CRaTer. The blue lines show the CRaTer-runs using: *NGP* (long dashed), *CIC* (short dashed) and *CIC + gradP* (dotted dashed). 35

2.8 Panel (a) shows the absolute difference between the ENZO-profiles and the CRaTer-profiles in the cosmological simulation computed with the *CIC + w_27*-(red) and *cic + gradP*-method (blue). Panel (b) shows the absolute differences normalized to the ENZO-profiles. 36

2.9 Radial density profiles of all the clusters used in the chapters below at $z \approx 0$. The solid lines show the results of the Eulerian, unweighted grid average and the dashed lines show the Lagrangian tracer particle-weighted average. The red lines give the average over all clusters. 37

2.10 Schematic sketch of a tracer being shock in time and how the corresponding shock obliquity is computed. 38

2.11 The efficiencies for gas heating (black, solid) and the acceleration (red, solid) and re-acceleration (blue, dashed) of cosmic rays depending on the Mach number extracted from Kang & Ryu (2013). 39

2.12 Panel (a) shows the computing times for the different parts of the code: (1) initialization of the run, (2) checking the boundaries for additional tracers, (3) computing the timestep, (4) total time of advecting the tracers in the loop, (5) assigning density and temperature to the tracers, (6) writing the tracer properties to file, (7) assigning the velocities to the tracers, (8) writing the tracers position to file, (9) advecting the tracers, (10) removing tracers that went out of bounce and (11) total time of the simulation. The blue line shows the run using 1 thread and the red line show the run using 48 threads. The dashed lines show the intermediate number of threads runs. Panel (b) shows the total time in arbitrary units needed by each run (red) and the corresponding speed-up compared to the single thread run (blue). 41

3.1 Evolution of the projected baryonic matter density (in grey) overlayed with the projected positions of the tracers. Only the tracers ending up in the two relics (see Sec. 3.1.3) are shown and are divided into two colours based on their final position. 48

3.2 Panel (a) shows the projected mass weighted magnetic field strength (colour) overlayed with the corresponding density contours (red contours) at $z \approx 0$. Panel (b) shows the projected radio emission (colour) and the corresponding density contours (white contours) at $z \approx 0$. Both plots have been produced from the tracer data. The outer regions are noisy owing to the lack of tracers in those areas (see also Appendix 3.1.A). 49

3.3 Expected distribution of random angles in a three-dimensional space (dashed black line). If a shock of a given Mach number M crosses this distribution of angles the distribution is more concentrated towards $\theta = 90°$ according to Eq. (3.15). The blue curves show these post-shock distributions for $M = 1.5$, $M = 3$ and $M = 10$. 50

3.4 Distribution of pre- (blue) and post-shock (red) obliquities at redshift $z \approx 0.12$ are shown in panel (a). The dashed line shows the expected distribution of angles for a random distribution. Panel (b) shows the differences of the computed distributions from the expected distribution. It is observed that the post-shock distribution (red line) is more peaked towards $\theta = 90°$ than the pre-shock distribution (blue line). Panel (c) shows the differences between the distribution of pre-shock obliquities at different redshifts and the expected distribution. Panel (d) shows the differences between pre-shock obliquities for different radial selections at $z \approx 0$ and the expected distribution. The radius of each region is $\frac{1}{5}$-th of the simulation box size. 53

3.5 Total radio emission from our simulated cluster at $z \approx 0$, considering the total emission from the cluster (diamond) or the emission from relic one (triangle) or relic two (square), for different selections of the obliquity angle, θ. 55

3.6 Zoomed versions of our simulated radio relics. The left column (Fig. (a), (b) and (c)) displays relic 1, while relic 2 is shown in the right column ((d), (e) and (f)). The green colours show the temperature of the ICM. The direction of the arrows indicates the direction of the magnetic field and their colour gives their magnetic field strength, with a logarithmical stretching, while the red contours show the radio emission. The top row shows θ_{all}. The middle row shows θ_{perp} and the bottom row shows θ_{para}. The axis are in dx = 31.7 kpc units. The squares in Fig. (a) and (d) mark the regions of the tracers selected in Sec. 3.1.3. The colours orange, purple and pink mark the regions in front of, on top of and behind the relic respectively. The bars in Fig. (a) and (d) show the length of 500 kpc. We notice that the format of the plot has been changed from its original version (Wittor et al., 2017b) to match the layout of this thesis. 56

3.7 Evolution of the ratio of cosmic-ray to thermal gas energy for θ_{all} (black), θ_{perp} (red) and θ_{para} (blue) across all tracers. 59

3.8 Total integrated γ-ray emission of our different models (color). The dashed lines show the *Fermi*-limits of A2256 and the Coma cluster taken from Ackermann et al. (2014) and Ackermann et al. (2016). 59

3.9 Dissipated kinetic power weighted distribution of the Mach numbers across the two relics. 62

3.10 Integrated γ-ray emission for all tracers (blue, solid line) and for the tracers that only experienced quasi-parallel shocks (red, solid line). The dashed lines in panel (a) show the results for the additional requirement of a minimum magnetic field. Panel (b) gives the results at different redshifts. Panel (c) shows the results for different ranges of θ. In all plots the horizontal dashed black lines give the *Fermi*-limits derived by Ackermann et al. (2014). 64

3.11 Evolution of (a) the temperature, (b) the magnetic field and (c) the ratio of compressive and solenoidal turbulent energy of the selected tracers over the last two Gyr. The solid lines show the selection of relic 1 and the dashed lines show the selection of relic 2. The colours indicate if the selection is upstream of the relic (green), on top of the relic (red) or downstream of the relic (blue). 65

3.12 Evolution of (a) the cosmic-ray energy weighted Mach number, (b) frequency of $M > M_{\rm min}$ shocks sweeping tracers and (c) mass fraction for the particles ending up behind the relics. The red lines show the first relic and the blue lines show the second relic. In panels (b) and (c) the solids line show $M_{\rm min} = 1.5$, the long dashed lines show $M_{\rm min} = 2.0$ and the short dashed lines show $M_{\rm min} = 3.0$. 66

3.13 Density profile at $z \approx 0$ of the simulated cluster. The solid black line shows the ENZO-profiles and the red asterixs show the profile computed with the tracers. 69

3.14 Density projections at $z \approx 0$. The left panel shows the projected density computed with tracers, while the right panel shows the projected density directly simulated in the ENZO run. 70

3.15 Distribution of pre-shock obliquities at different redshifts. The solid lines show the results from our simulation. The redshift is colour-coded going from black $z = 1$ to red $z = 0$. The dashed line shows the expected distribution of angles for a random distribution. 70

3.16 Zoomed versions of the three radio emitting regions are shown at $z \approx 0$. The colour shows the temperature of the ICM. The direction of the arrows indicates the direction of the magnetic and their colour gives their magnetic field strength in logarithmical units. The contours show the radio emission. Plots (a) and (d) show the central relic, plots (c) and (f) show the accretion shock and plots (b) and (e) show the filament. The left column ((a), (b) and (c)) shows the radio emission for $\theta_{\rm all}$. The right column ((d), (e) and (f)) shows the radio emission for $\theta_{\rm perp}$. The bars in Fig. (a), (b) and (c) show the length of 250 kpc. We notice that the format of the plot has been changed from its original version (Wittor et al., 2017b) to match the layout of this thesis. 71

3.17 The γ-ray emission for all tracers (blue, solid line) and for the tracers that experienced quasi-parallel shocks (red, solid line). The dashed lines show the result for the additional requirement of a minimum magnetic field of $B_{\rm min} = 0.03\ \mu$G to accelerate cosmic rays. 72

3.18 Projected gas density (colours) and radio contours at $z \approx 0.2$. Two radio relics can be seen on the right ($P_{\rm radio} \approx 3.42 \cdot 10^{31}$ erg/s/Hz) and left ($P_{\rm radio} \approx 2.26 \cdot 10^{32}$ erg/s/Hz) side of the cluster centre. 75

3.19 Distributions of shock obliquities at $z \approx 0.2$. The left panel shows the pre-shock (blue) and post-shock (red) distribution of obliquities. The black dashed line shows the expected $\propto sin(\alpha)$ distribution of angles based on pure geometry. The right panel shows the distribution of pre-shock obliquities for different ranges of Mach numbers: $M < 1.5$ (dark blue), $1.5 < M < 2$ (light blue), $2 < M < 3$ (green), $3 < M < 5$ (orange) and $M > 5$ (red). 77

3.20 Profiles of the γ-ray emission. The solid lines show the total integrated emission profiles and the coloured dashed lines show the radial emission profiles. The γ-ray emission produced by cosmic-ray protons accelerated in all shock is given by the blue lines. The red line shows the case of only quasi-parallel shocks being able to accelerate cosmic rays. The black dashed lines show the upper *Fermi*-limits for galaxy clusters that have a comparable mass to our simulated cluster. 78

3.21 Isolated zoomed versions of our simulated radio relics. The green colours show the gas temperature. The blue arrows show the magnetic field. Their direction indicates the magnetic field direction and the colours give their magnetic field strength using a logarithmical stretching (as brighter the blue as stronger the magnetic field). The red contours show the radio emission. The left panel shows the relics produced by all cosmic-ray electrons. The middle panel shows the relics produced by electrons that have been accelerated by quasi-perpendicular shocks only. The right panel shows the relics produced by electrons that have been accelerated by quasi-parallel shocks only. The axes are in dx = 31.7 kpc units. 81

3.22 Maps of the mean (left panel) and maximum (right panel) Mach numbers of the shocks that are producing the radio relics. The axes are in dx = 31.7 kpc units. 82

3.23 Panel (a) shows the profile of the ratio of the Alfvènic and gas velocity. Panel (b) shows the evolution of the normalized number of grid cells that have a larger Alfvènic velocity than gas velocity. 84

4.1 2-dimensional slice (with thickness 3 Mpc) of the gas energy (top panels) and CR-energy (bottom panels) for a subvolume of the CUR2 volume at $z = 0$, where we compare the non-radiative and the cooling plus AGN feedback runs. The color bar gives the energy per cell in units of $\log_{10}$ [erg]. To guide the eye, we indicate with green arrows the regions where the effect of AGN feedback is more prominent. 90

4.2 Mass-temperature scaling relation for the halos in the radiative and non-radiative runs of the CUR2 volume (150^3 Mpc^3), computed inside R_{500} for each object at $z = 0$. The additional lines show the best fit of the simulated data, while the two set of gray symbols are for real cluster observations using CHANDRA by Eckmiller et al. (2011) and Reichert et al. (2011). To better compare with the simulated cluster and minimise the effect of cosmic evolution, we only consider observed cluster in the $0 \leq z \leq 0.2$ redshift range. 91

4.3 Radial profile of gas temperature and density for all simulated clusters with $M_{\rm vir} \geq 10^{14}\ M_\odot$ in the 300^3 Mpc^3 volume of the CUR1 run (non-radiative) and in the 150^3 Mpc^3 volume of the CUR2 run (with cooling and two AGN feedback modes). The profiles of individual objects are shown in gray, while the $\pm\sigma$ around the mean profile of the sample are drawn with continuous lines (red lines for the NCC-like, blue line for the CC-like or the non-radiative clusters). The additional lines shows the $\pm\sigma$ around the mean profile of CC (dashed light blue) or the NCC (dot-dashed orange) from observations (Eckert et al., 2012; Planck Collaboration et al., 2013). 92

4.4 Average radial profile of the CR to gas pressure ratio for all simulated clusters in the CUR1 and CUR2 run with cooling and feedback, in all cases for the Kang & Ryu (2013) model of CR acceleration. The gray lines give the profiles of individual clusters while the coloured lines give the mean and the $\pm\sigma$ dispersion. The additional thin coloured line dotted lines give the best fit for the average profiles, with parameters given in Tab. 4.2. 94

4.5 Average enclosed pressure ratio of CR and gas for simulated clusters at $z = 0$. The top panel shows the distribution for the CUR1 run, the bottom panel shows the distribution for the CC- and NCC-like clusters in the CUR2 run with cooling and high redshift AGN feedback. 95

4.6 Average profile of $X(R)$ for all $M \geq 10^{14}\ M_\odot$ clusters in the CUR2 run, comparing different physical prescriptions for CRs and baryons. The dotted lines give the best fit relation for each model, with parameters given in Tab.2, whereas the dashed lines give the $\pm 1\sigma$ standard deviations on the average profiles. 95

4.7 Hadronic emission for our simulated clusters at $z = 0$, in the 0.2-200 GeV energy range. Top panel: γ-emission for clusters in the CUR1 box, assuming CR-spectra of $s = 2.0$ or $s = 3.0$. Centre: γ-ray emission from clusters in the CUR2 runs, for different models of gas physics. Bottom: γ-ray emission from clusters in our non-radiative CUR2 run, for runs with different acceleration efficiency of CRs. The gray symbols are the upper limits from the FERMI catalog in the same energy range. 97

4.8 Evolution of four clusters with a final mass $\geq 5 \cdot 10^{15}\ M_{\odot}$ in the CUR1 volume. From left to right the image shows: the enclosed total mass with fixed 6^3 Mpc^3 comoving volumes; the total CR to gas pressure ratio (thick lines) and the relative CR pressure increment snapshot by snapshot (think lines);c the total hadronic γ-ray emission from the same volumes. 99

4.9 Simulated merger sequence for a $\sim 10^{15}\ M_{\odot}$ cluster using AMR, with X-ray emission in colours and radio emission in white contours. The approximate epoch of the observed merger in MACSJ1752.0+0440 is $z \approx 0.3$. Each image is 5×5 Mpc^2 (comoving) across. The contours are equally spaced with $\sqrt{2}$ multiples of the radio emission, starting from $\approx 10^{23}$ erg/s/Hz per pixel. . . . 101

4.10 Merger sequence for our simulated versions of the cluster MACSJ1752.0+0440 using AMR for the same area of Fig. 4.9 and for the epochs of $z = 0.403$, 0.368, 0.317, 0.305, 0.294 and 0.281. The colours show the total projected CR-energy in code units. 102

4.11 γ-ray emission weighted radial distribution of the spectral index of CR-energy in the AMR resimulation of MACSJ1752 for different redshifts (marked in different colours). The thick dashed lines marked the epochs closer to the observed radio emission. 103

4.12 Evolution of the total hadronic γ-ray emission in the $0.2 - 100$ GeV energy range for the various resimulations of cluster MACSJ1752. The vertical hatched region shows the epoch of the observed X-ray/radio configuration, while the horizontal line marks the upper limits from FERMI on the hadronic emission from this cluster. 104

4.13 Radial profiles of gas density, gas temperature, CR-pressure and γ-ray emission inside the radius for a $\sim 2 \times 10^{14}\ M_{\odot}$ simulated cluster at $z = 0$, for different resolutions and physical prescriptions for baryons (see text). The additional horizontal line in the last panel marks the upper limit on the γ-ray emission for the stacking of clusters obtained by Huber et al. (2013b). 112

4.14 Mass-temperature scaling relation for the halos in the CUR1 and CUR2 volumes at $z = 0$, where the effect of the Kang & Jones (2007) and Kang & Ryu (2013) acceleration model for CRs are compared. The additional lines show the best fit of the simulated data, while the two set of gray symbols are for real cluster observations using CHANDRA by Eckmiller et al. (2011) and Reichert et al. (2011). To better compare with the simulated cluster and minimise the effect of cosmic evolution, we only consider observed cluster in the $0 \leq z \leq 0.2$ redshift range. 113

5.1 Density slice through the cluster centre overlayed with the corresponding magnetic field vectors. This plot has been produced using the `ENZO`-data. 116

5.2 Projected radio emission at $z = 0.27$. This plot has been produced using the `CRaTer`-data. 119
5.3 Average Mach number maps along the different line-of-sights: XY-plane (top row), XZ-plane (middle row) and YZ-plane (bottom row). Left left column shows the unweighted average and the right column shows the radio emission weighted average using the acceleration efficiencies derived by Kang & Ryu (2013). The black bar shows the length of 300 kpc. 123
5.4 Three dimensional distribution of Mach numbers (black) and the corresponding radio emission weighted distribution of the Mach number using the acceleration efficiencies derived by Kang & Ryu (2013) (red) and a fixed acceleration efficiency of $\eta = 0.05$ (blue). Panels (b), (c) and (d) show the projected Mach number in the XY-plane, XZ-plane and YZ-plane. Panel (e) shows the distribution of projected Mach numbers taken along 1080 line-of-sights. The black line show the distribution of average Mach numbers and the red lines show the radio weighted Mach number using the acceleration efficiencies derived by Kang & Ryu (2013). 124
5.5 Average spectral index maps along the different line-of-sights: XY-plane (top row), XZ-plane (middle row) and YZ-plane (bottom row). Left left column shows the unweighted average and the right column shows the radio emission weighted average using the acceleration efficiencies derived by Kang & Ryu (2013). The black bar shows the length of 300 kpc. 125
5.6 Polarization of the integrated radio emission, Eq. 5.12, overlayed with the polarization vectors for our six different combinations of rotation measure and observing frequency. The left column shows $\nu_{\rm obs} = 1.4$ GHz and the right column displays $\nu_{\rm obs} = 0.14$ GHz. The three rows show $\Phi_{\rm full}$, $\Phi_{\rm zero}$ and $\Phi_{\rm source}$ respectively. 126
5.7 Distribution of the polarized, integrated radio emission, Eq. 5.12, including the effect of depolarization (red) and excluding the effect of depolarization (blue) at (a) $\nu_{\rm obs} = 1.4$ GHz and (b) $\nu_{\rm obs} = 0.14$ GHz. The green lines show the distribution, if only the depolarization within the source is included. 127

6.1 Projected enstrophy overlayed with the density contours of the different clusters in the highes AMR region of size $(6.27\ {\rm Mpc})^3$ at $z = 0$. The red square in each plot displays the $(320\ {\rm kpc})^3$ volume surrounding the peak of enstrophy. The red bar show the length of 1 Mpc. (A coloured version is available in the online article.) 135
6.2 Evolution of the projected enstrophy in the highes AMR region of size $(6.27\ {\rm Mpc})^3$ of cluster IT90_3 at $z = 1$ (left) and $z = 0$ (right). The red bar show the length of 1 Mpc. (A coloured version is available in the online article.) 137

6.3 Evolution of the projected gas density overlayed with the tracers position of the different selections in cluster IT90_3. The tracers have been separated into groups from different subclumps, indicated by the different colours, at $z = 1$. The boxes are of the size $(6.27\ \mathrm{Mpc})^3$. The red bar show the length of 1 Mpc. (See https://dnswttr.github.io/index.html/it903mov.html for a movie. A coloured version is available in the online article.) 138

6.4 Evolution of the enstrophy, averaged over each tracer family selected in IT90_3 (colours). The black solid line displays the evolution of enstrophy, averaged over all tracers in IT90_3. (A coloured version is available in the online article.) 139

6.5 Spatial evolution of four tracer families across cluster IT90_3. The enstrophy is amplified at the timesteps displayed here due to the merging of the clumps. The displayed regions are of the size $(400\ \mathrm{Mpc})^2$. (A coloured version is available in the online article.) 140

6.6 Evolution of enstrophy in panel (a) and entropy in panel (b) recorded by the four tracer families selected in cluster IT90_3 and that are shown in Fig. 6.5. The black vertical lines mark the timesteps of local maximum enstrophy. (A coloured version is available in the online article.) 141

6.7 Evolution of ϵ, F_{comp}, F_{stretch} and F_{baro} of the first family of tracers in IT90_3 over the last ~ 7 Gyr of the simulation. The red vertical, solid lines mark the local peak of enstrophy, while the green, dashed and purple, dotted lines mark the local minima of enstrophy. (A coloured version is available in the online article.) 141

6.8 Summary of all enstrophy "events" recorded by `CRaTer` in IT90_3. Each column shows a single event recorded by one of the different families. The plots show the evolution of enstrophy (top row), compressive source term (second row), baroclinic source term (third row) and stretching source term (bottom row) around the peaks of enstrophy. The amplitudes (y-axis) of each quantity have been normalized to unity and the time range (width of x-axis) around each each has been normalized to the evolutionary time at the peak of enstrophy. The red line marks the time of the local peak of enstrophy. The black dashed horizontal lines shows the zero level. (A coloured version is available in the online article.) 142

6.9 Evolution of the means of enstrophy (black), compressive source term (red, diamonds), baroclinic source term (green, triangles) and stretching source term (blue, squares) normalized to an unit amplitude of one and a unit time equivalent to one evolutionary time measured at the peak of enstrophy, e.g. $t_{\text{eff}}(\epsilon_{\max})$ equals the evolutionary time when the enstrophy is at its maximum. Each panel shows the averages of all events recorded by the tracers in one cluster. It is observed that the compressive and baroclinic source terms are always the strongest before the peak of enstrophy, while the stretching term shows its maximum after the peak of enstrophy. (A coloured version is available in the online article.) 143

6.10 Distributions of the evolutionary times computed around the times of maximum enstrophy shown in Fig. 6.7. The top row corresponds to the first peak at $t \approx 8.1$ Gyr and the bottom row corresponds to the second peak at $t \approx 9.8$ Gyr. The colours and linestyles match the time selections shown in Fig. 6.7. (A coloured version is available in the online article.) 144

6.11 Histories of the effective evolutionary times, see Eq. 6.9, (black, solid) and the evolutionary times of the different source terms, see Eq. 6.10, recorded by the same selection of tracers shown in Fig. 6.10: baroclinic (blue, dash-dotted), compressive (red, dotted) and stretching (green, dashed). (A coloured version is available in the online article.) 145

6.12 Panel (a): Evolution of the left (black, solid) and right (blue, dashed) handside of Eq. 6.8. The red line shows the difference of the two, which we associate with viscous dissipation, see label F_{diss} (red line, dash-dotted). (b): Comparison of η_{diss} (red, dashed), computed with F_{diss} from Eq. 6.11, with the enstrophy dissipation rate computed from Eq. 6.12 (black, solid). (A coloured version is available in the online article.) 147

6.13 Panel (a): Integrated magnetic field energy fuelled by the dissipation of turbulence. Panel (b): The corresponding magnetic field strength. The dashed lines give the lower and upper limit obtained with efficiencies in the range of $C_E \in [4\%, 5\%]$. (A coloured version is available in the online article.) 148

6.14 Radial density profiles of the clusters at $z \approx 0$. The solid lines give the results of the Eulerian, unweighted grid average and the dashed lines give the Lagrangian tracer particle-weighted average. The red lines show the average over all clusters. (A coloured version is available in the online article.) 150

6.15 Mass-temperature relation measured in the central $(1.44\ \text{Mpc})^3$ of each cluster. The solid lines show the evolution of the major merger clusters and the dashed lines show the evolution of the clusters without a major merger. (A coloured version is available in the online article.) 151

6.16 Projected X-ray surface brightness along the line of sight of all the clusters of our sample. Each box is of the size $\approx (6.27 \text{ Mpc})^3$ with an resolution of $\mathrm{d}x \approx 20$ kpc. The red line in the panel of IT90_4 show the length of 1 Mpc. The red bar show the length of 1 Mpc. (A coloured version is available in the online article.) 152
6.17 Projected turbulent energy dissipation rate along the line of sight of the clusters contained in our sample. Each box is of the size $\approx (6.27 \text{ Mpc})^3$ with an resolution of $\mathrm{d}x \approx 20$ kpc. The red bar show the length of 1 Mpc. (A coloured version is available in the online article.) 153

7.1 Temperature, (a), and X-ray luminosity, (b), projection of the high resolution relic. 158
7.2 High resolution simulation, ~ 4 kpc, of a radio relic. The displayed quantity is the projected gas density along the line-of-sight. 159
7.3 Slices through cluster IT90_3 that has been extensively studied in Chap. 6. (a): fluctuations of the turbulent kinetic dissipation rate (Eq. 6.12). (b): X-ray fluctuations of the same regions. 159

C List of Tables

3.1 Comparison of the total integrated γ-ray emission of our different models and a number of observed clusters at the bottom. For each cluster we give the name, redshift z, mass M_{200} and upper γ-flux $F_\gamma^{\rm UL}$. The last five rows show the reference clusters taken from Ackermann et al. (2014). The first two rows show our simulations for $\theta_{\rm all}$ and $\theta_{\rm para}$. The following rows show the results for the different simulations depending on $B_{\rm min}$, z and different selections of θ. Our cluster simulation compatible with the *Fermi*-limits for the Coma cluster is highlighted in boldface. 60

4.1 List of the simulations used in this work. Column 1: size of the simulated volume. Column 2: number of grid cells. Column 3: spatial resolution. Column 4: physical implementations and run name. Column 5: diffusive shock acceleration efficieny of cosmic rays (KJ07=Kang & Jones (2007), KR13=Kang & Ryu (2013), 10^{-3}=constant efficiency, CS14=Caprioli & Spitkovsky (2014a)). 89

4.2 Best fit parameters for the X, R relation for clusters in the CUR1 and CUR2 run, assuming $X(R) = X_0 + \alpha_1(R/R_{\rm vir}) + \alpha_2(R/R_{\rm vir})^2$. In the upper half of the table, we give the best fit for the CC and NCC-like clusters separately, in radiative runs. The lower half of the table gives the best fit parameters limited to all $M \geq 10^{14}\ M_\odot$ clusters in the CUR2 runs. 98

5.1 Summary of the results for the polarization of the radio relic. The first column gives the observation frequency and the second column gives the depolarization model. The third and fourth column present the mean and median of the polarization. The fifth and sixth column provide the minimum and maximum degree of polarization recorded in on pixel. The last two columns provide the fraction of cells that show a polarization ≥ 60 % and ≤ 20 % respectively. . . 122

6.1 Main characteristics of our eight simulated clusters at z = 0: cluster ID, M_{200}, r_{200}, T_{200}, sound speed, dynamical state of the cluster, number of snapshots available between $z = 30$ and $z = 0$ $N_{\rm s}(z = 30)$, number of snapshots available between $z = 1$ and $z = 0$ $N_{\rm s}(z = 1)$ and the final number of tracers $N_{\rm p}(z = 0)$. 136

D Bibliography

Ackermann M. et al., 2014, ApJ, 787, 18

Ackermann M. et al., 2016, ApJ, 819, 149

Ackermann M. et al., 2015, ApJ, 812, 159

Ackermann M. et al., 2010, ApJ Letters, 717, L71

Agertz O. et al., 2007, MNRAS, 380, 963

Aharonian F. et al., 2009, A&A, 495, 27

Akamatsu H., Kawahara H., 2013, Publications of the Astronomical Society of Japan, 65, 16

Akamatsu H. et al., 2017, A&A, 600, A100

Akamatsu H. et al., 2015, A&A, 582, A87

Aleksić J. et al., 2012, A&A, 541, A99

Aleksić J. et al., 2010, ApJ, 710, 634

Andrade-Santos F., Jones C., Forman W. R., Lovisari L., Chandra-Planck Collaboration, 2017, in American Astronomical Society Meeting Abstracts, Vol. 229, American Astronomical Society Meeting Abstracts, p. 404.04

Arlen T. et al., 2012, ApJ, 757, 123

Atwood W. B. et al., 2009, ApJ, 697, 1071

Ball L., Melrose D. B., 2001, Publications of the Astronomical Society of Australia, 18, 361

Bartlett J. G., 2006, ArXiv Astrophysics e-prints

Basu K., Sommer M., Erler J., Eckert D., Vazza F., Magnelli B., Bertoldi F., Tozzi P., 2016, ApJ Letters, 829, L23

Beck A. M., Dolag K., Lesch H., Kronberg P. P., 2013, MNRAS, 435, 3575

Bell A. R., 1978a, MNRAS, 182, 147

Bell A. R., 1978b, MNRAS, 182, 443

Benson B. A. et al., 2013, ApJ, 763, 147

Beresnyak A., 2011, Physical Review Letters, 106, 075001

Beresnyak A., Miniati F., 2016, ApJ, 817, 127

Berezinsky V. S., Blasi P., Ptuskin V. S., 1997, ApJ, 487, 529

Berger M. J., Colella P., 1989, Journal of Computational Physics, 82, 64

Berrier J. C., Stewart K. R., Bullock J. S., Purcell C. W., Barton E. J., Wechsler R. H., 2009, ApJ, 690, 1292

Biermann L., 1950, Zeitschrift fur Naturforschung, 5, 65

Blandford R., Eichler D., 1987, Physics Reports, 154, 1

Blandford R. D., Ostriker J. P., 1978, ApJ Letters, 221, L29

Blasi P., Colafrancesco S., 1999, Astroparticle Physics, 12, 169

Blasi P., Colafrancesco S., 1999, Astropart. Phys., 122, 169

Bonafede A. et al., 2012, MNRAS, 426, 40

Bonafede A. et al., 2017, MNRAS, 470, 3465

Bonafede A., Feretti L., Murgia M., Govoni F., Giovannini G., Dallacasa D., Dolag K., Taylor G. B., 2010, A&A, 513, A30

Bonafede A., Giovannini G., Feretti L., Govoni F., Murgia M., 2009, A&A, 494, 429

Bonafede A., Intema H. T., Brüggen M., Girardi M., Nonino M., Kantharia N., van Weeren R. J., Röttgering H. J. A., 2014, ApJ, 785, 1

Botteon A., Gastaldello F., Brunetti G., Dallacasa D., 2016, MNRAS, 460, L84

Bravi L., Gitti M., Brunetti G., 2016, MNRAS, 455, L41

Brüggen M., 2013, MNRAS, 436, 294

Brüggen M., Bykov A., Ryu D., Röttgering H., 2012, Science & Space Review, 166, 187

Brüggen M., Kaiser C. R., 2002, Nature, 418, 301

Brüggen M., Ruszkowski M., Simionescu A., Hoeft M., Dalla Vecchia C., 2005, ApJ Letters, 631, L21

Brüggen M., Scannapieco E., 2009, MNRAS, 398, 548

Brüggen M., Vazza F., 2015, in Astrophysics and Space Science Library, Vol. 407, Magnetic Fields in Diffuse Media, Lazarian A., de Gouveia Dal Pino E. M., Melioli C., eds., p. 599

Brunetti G. et al., 2008, Nature, 455, 944

Brunetti G., Jones T. W., 2014, International Journal of Modern Physics D, 23, 1430007

Brunetti G., Lazarian A., 2007, MNRAS, 378, 245

Brunetti G., Lazarian A., 2011, MNRAS, 412, 817

Brunetti G., Lazarian A., 2016, MNRAS, 458, 2584

Brunetti G., Setti G., Feretti L., Giovannini G., 2001, MNRAS, 320, 365

Bryan G. L., Abel T., Norman M. L., 2001, ArXiv Astrophysics e-prints

Bryan G. L., Norman M. L., 1997, in Astronomical Society of the Pacific Conference Series, Vol. 123, Computational Astrophysics; 12th Kingston Meeting on Theoretical Astrophysics, Clarke D. A., West M. J., eds., p. 363

Bryan G. L. et al., 2014, ApJS, 211, 19

Burn B. J., 1966, MNRAS, 133, 67

Bykov A. M., Dolag K., Durret F., 2008, Science & Space Review, 134, 119

Caprioli D., 2012, Journal of Cosmology and Astroparticle Physics, 7, 38

Caprioli D., Spitkovsky A., 2014a, ApJ, 783, 91

Caprioli D., Spitkovsky A., 2014b, ApJ, 794, 46

Cassano R. et al., 2013, ApJ, 777, 141

Cavagnolo K. W., Donahue M., Voit G. M., Sun M., 2009, ApJS, 182, 12

Cavaliere A., Lapi A., 2013, Physics Reports, 533, 69

Cho J., 2014, ApJ, 797, 133

Churazov E. et al., 2012, MNRAS, 421, 1123

Colella P., Glaz H. M., 1985, Journal of Computational Physics, 59, 264

Colella P., Woodward P. R., 1984, Journal of Computational Physics, 54, 174

Condon J. J., Cotton W. D., Greisen E. W., Yin Q. F., Perley R. A., Taylor G. B., Broderick J. J., 1998a, ApJ, 115, 1693

Condon J. J., Cotton W. D., Greisen E. W., Yin Q. F., Perley R. A., Taylor G. B., Broderick J. J., 1998b, ApJ, 115, 1693

Dallacasa D. et al., 2009, ApJ, 699, 1288

Daly R. A., Loeb A., 1990, ApJ, 364, 451

Dasadia S. et al., 2016, ApJ Letters, 820, L20

de Gasperin F., Intema H. T., van Weeren R. J., Dawson W. A., Golovich N., Wittman D., Bonafede A., Brüggen M., 2015, MNRAS, 453, 3483

de Gasperin F., van Weeren R. J., Brüggen M., Vazza F., Bonafede A., Intema H. T., 2014, MNRAS, 444, 3130

De Grandi S. et al., 2016, A&A, 592, A154

De Grandi S., Molendi S., 2001, ApJ, 551, 153

Dedner A., Kemm F., Kröner D., Munz C.-D., Schnitzer T., Wesenberg M., 2002, Journal of Computational Physics, 175, 645

Dennison B., 1980, ApJ Letters, 239, L93

Diaferio A., 1999, MNRAS, 309, 610

Dieckmann M. E., Chapman S. C., McClements K. G., Dendy R. O., Drury L. O., 2000, A&A, 356, 377

Dolag K., Bartelmann M., Lesch H., 1999, A&A, 348, 351

Dolag K., Borgani S., Murante G., Springel V., 2009, MNRAS, 399, 497

Dolag K., Borgani S., Schindler S., Diaferio A., Bykov A. M., 2008a, Science & Space Review, 134, 229

Dolag K., Bykov A. M., Diaferio A., 2008b, Science & Space Review, 134, 311

Donnert J., Brunetti G., 2014, MNRAS, 443, 3564

Donnert J., Dolag K., Cassano R., Brunetti G., 2010, MNRAS, 407, 1565

Donnert J., Dolag K., Lesch H., Müller E., 2009, MNRAS, 392, 1008

Drury L. O., 1983, Reports on Progress in Physics, 46, 973

Drury L. O., Downes T. P., 2012, MNRAS, 427, 2308

Dubois Y., Devriendt J., Slyz A., Teyssier R., 2010, MNRAS, 409, 985

Dyer K. K., Reynolds S. P., Borkowski K. J., Allen G. E., Petre R., 2001, ApJ, 551, 439

Eckert D., Gaspari M., Vazza F., Gastaldello F., Tramacere A., Zimmer S., Ettori S., Paltani S., 2017, ApJ Letters, 843, L29

Eckert D. et al., 2014, A&A, 570, A119

Eckert D., Molendi S., Vazza F., Ettori S., Paltani S., 2013, A&A, 551, A22

Eckert D. et al., 2012, A&A, 541, A57

Eckmiller H. J., Hudson D. S., Reiprich T. H., 2011, A&A, 535, A105

Ensslin T. A., Biermann P. L., Klein U., Kohle S., 1998, A&A, 332, 395

Enßlin T. A., Pfrommer C., Springel V., Jubelgas M., 2007, A&A, 473, 41

Erler J., Basu K., Trasatti M., Klein U., Bertoldi F., 2015, MNRAS, 447, 2497

Evans C. R., Hawley J. F., 1988, ApJ, 332, 659

Feretti L., Giovannini G., Govoni F., Murgia M., 2012, The Astronomy and Astrophysics Review, 20, 54

Ferland G. J., Korista K. T., Verner D. A., Ferguson J. W., Kingdon J. B., Verner E. M., 1998, Publication of the Astronomical Society of the Pacific, 110, 761

Ferrari C., Govoni F., Schindler S., Bykov A. M., Rephaeli Y., 2008, Science & Space Review, 134, 93

Finoguenov A., Sarazin C. L., Nakazawa K., Wik D. R., Clarke T. E., 2010, ApJ, 715, 1143

Fitzpatrick R., 2014, Plasma Physics: An Introduction. CRC Press, Boca Raton

Frenk C. S. et al., 1999, ApJ, 525, 554

Fujita Y., Takizawa M., Yamazaki R., Akamatsu H., Ohno H., 2015, ApJ, 815, 116

Gabici S., Blasi P., 2003, ApJ, 583, 695

Gardner F. F., Whiteoak J. B., 1966, Annual Review of Astronomy and Astrophysics, 4, 245

Gaspari M., Churazov E., Nagai D., Lau E. T., Zhuravleva I., 2014, A&A, 569, A67

Genel S., Vogelsberger M., Nelson D., Sijacki D., Springel V., Hernquist L., 2013, MNRAS, 435, 1426

Giacintucci S., Markevitch M., Brunetti G., ZuHone J. A., Venturi T., Mazzotta P., Bourdin H., 2014, ApJ, 795, 73

Giovannini G., Feretti L., Stanghellini C., 1991, A&A, 252, 528

Gotoh T., Fukayama D., Nakano T., 2002, Physics of Fluids, 14, 1065

Govoni F. et al., 2010, A&A, 522, A105

Griffin R. D., Dai X., Kochanek C. S., 2014, ApJ Letters, 795, L21

Gu L. et al., 2009, ApJ, 700, 1161

Guo F., Oh S. P., 2008, MNRAS, 384, 251

Guo X., Sironi L., Narayan R., 2014a, ApJ, 794, 153

Guo X., Sironi L., Narayan R., 2014b, ApJ, 797, 47

Ha J.-H., Ryu D., Kang H., 2017, ArXiv e-prints

Haardt F., Madau P., 1996, ApJ, 461, 20

Hahn O., Martizzi D., Wu H.-Y., Evrard A. E., Teyssier R., Wechsler R. H., 2015, ArXiv e-prints

Haiman Z., Mohr J. J., Holder G. P., 2001, ApJ, 553, 545

Hamaker J. P., Bregman J. D., Sault R. J., 1996, Astronomy and Astrophysics Supplement, 117, 137

Hanasz M., Kosiński R., Lesch H., 2004, APSS, 289, 303

Harten A., 1983, Journal of Computational Physics, 49, 357

Harten A., Engquist B., Osher S., Chakravarthy S. R., 1987, Journal of Computational Physics, 71, 231

Heinz S., Brüggen M., Young A., Levesque E., 2006, MNRAS, 373, L65

Hitomi Collaboration et al., 2016, Nature, 535, 117

Hlavacek-Larrondo J. et al., 2017, ArXiv e-prints

Hockney R. W., Eastwood J. W., 1988, Computer simulation using particles

Hockney R. W., Goel S. P., Eastwood J. W., 1973, Chemical Physics Letters, 21, 589

Hoeft M., Brüggen M., 2007, MNRAS, 375, 77

Hoeft M., Brüggen M., Yepes G., Gottlöber S., Schwope A., 2008, MNRAS, 391, 1511

Hofmann F., Sanders J. S., Nandra K., Clerc N., Gaspari M., 2016, A&A, 585, A130

Hong S. E., Kang H., Ryu D., 2015, ApJ, 812, 49

Hong S. E., Ryu D., Kang H., Cen R., 2014, ApJ, 785, 133

Hopkins P. F., 2015, MNRAS, 450, 53

Huber B., Farnier C., Manalaysay A., Straumann U., Walter R., 2012, A&A, 547, A102

Huber B., Tchernin C., Eckert D., Farnier C., Manalaysay A., Straumann U., Walter R., 2013a, A&A, 560, A64

Huber B., Tchernin C., Eckert D., Farnier C., Manalaysay A., Straumann U., Walter R., 2013b, A&A, 560, A64

Hudson D. S., Mittal R., Reiprich T. H., Nulsen P. E. J., Andernach H., Sarazin C. L., 2010, A&A, 513, A37

Ichinohe Y., Werner N., Simionescu A., Allen S. W., Canning R. E. A., Ehlert S., Mernier F., Takahashi T., 2015, MNRAS, 448, 2971

Itahana M., Takizawa M., Akamatsu H., Ohashi T., Ishisaki Y., Kawahara H., van Weeren R. J., 2015, Publications of the Astronomical Society of Japan, 67, 113

Ji S., Oh S. P., Ruszkowski M., Markevitch M., 2016, MNRAS

Jones F. C., Ellison D. C., 1991, Science & Space Review, 58, 259

Kaastra J. S. et al., 2008, Science & Space Review, 134, 1

Kale R., Dwarakanath K. S., Bagchi J., Paul S., 2012, MNRAS, 426, 1204

Kale R. et al., 2015, A&A, 579, A92

Kang H., Jones T. W., 1990, ApJ, 353, 149

Kang H., Jones T. W., 2005, ApJ, 620, 44

Kang H., Jones T. W., 2007, Astroparticle Physics, 28, 232

Kang H., Ryu D., 2010, ApJ, 721, 886

Kang H., Ryu D., 2013, ApJ, 764, 95

Kang H., Ryu D., 2015, ApJ, 809, 186

Kang H., Ryu D., Cen R., Ostriker J. P., 2007, ApJ, 669, 729

Kang H., Ryu D., Jones T. W., 2012, ApJ, 756, 97

Kaplan D. T., 2009, Statistical Modeling: A Fresh Approach. CreateSpace Independent Publishing Platform

Kelner S. R., Aharonian F. A., Bugayov V. V., 2006, Physical Review Letters, 74, 034018

Keshet U., Waxman E., Loeb A., 2004, ApJ, 617, 281

Khatri R., Gaspari M., 2016, MNRAS, 463, 655

Kierdorf M., Beck R., Hoeft M., Klein U., van Weeren R. J., Forman W. R., Jones C., 2017, A&A, 600, A18

Kitayama T. et al., 2016, Publications of the Astronomical Society of Japan, 68, 88

Klein U., Fletcher A., 2015, Galactic and Intergalactic Magnetic Fields

Komatsu E. et al., 2011, ApJS, 192, 18

Korngut P. M. et al., 2011, ApJ, 734, 10

Kritsuk A. G., Ustyugov S. D., Norman M. L., 2017, New Journal of Physics, 19, 065003

Kunz M. W., Schekochihin A. A., Stone J. M., 2014, Physical Review Letters, 112, 205003

Laing R. A., 1980, MNRAS, 193, 439

Landau L., Lifshitz E., 2013, Fluid Mechanics No. Bd. 6. Elsevier Science

Large M. I., Mathewson D. S., Haslam C. G. T., 1959, Nature, 183, 1663

Lau E., Kravtsov A., Nagai D., 2010, in Bulletin of the American Astronomical Society, Vol. 42, American Astronomical Society Meeting Abstracts #215, p. 534

Lazarian A., 2016, ArXiv e-prints

Lazarian A., Eyink G. L., Vishniac E. T., Kowal G., 2015, in Astrophysics and Space Science Library, Vol. 407, Magnetic Fields in Diffuse Media, Lazarian A., de Gouveia Dal Pino E. M., Melioli C., eds., p. 311

Levy D., Puppo G., Russo G., 1999, ArXiv Mathematics e-prints

Liddle A. R., 1999, An introduction to modern cosmology

Malkov M. A., 1997, ApJ, 485, 638

Mantz A., Allen S. W., Ebeling H., Rapetti D., 2008, MNRAS, 387, 1179

Markevitch M., Gonzalez A. H., David L., Vikhlinin A., Murray S., Forman W., Jones C., Tucker W., 2002, ApJ Letters, 567, L27

Markevitch M., Govoni F., Brunetti G., Jerius D., 2005, ApJ, 627, 733

Markevitch M. et al., 2000, ApJ, 541, 542

Matsukiyo S., Ohira Y., Yamazaki R., Umeda T., 2011, ApJ, 742, 47

Matsumoto Y., Amano T., Hoshino M., 2012, ApJ, 755, 109

McCarthy I. G. et al., 2010, MNRAS, 406, 822

Mee A. J., Brandenburg A., 2006, MNRAS, 370, 415

Mei S. et al., 2007, ApJ, 655, 144

Menanteau F. et al., 2012, ApJ, 748, 7

Mendygral P. J., Jones T. W., Dolag K., 2012, ApJ, 750, 166

Miniati F., 2003, MNRAS, 342, 1009

Miniati F., 2015, ApJ, 800, 60

Miniati F., Beresnyak A., 2015, Nature, 523, 59

Miniati F., Jones T. W., Kang H., Ryu D., 2001, ApJ, 562, 233

Miniati F., Ryu D., Kang H., Jones T. W., Cen R., Ostriker J. P., 2000, ApJ, 542, 608

Mitchell R. J., Culhane J. L., Davison P. J. N., Ives J. C., 1976, MNRAS, 175, 29P

Monaghan J. J., 2005, Reports on Progress in Physics, 68, 1703

Norman M. L., Bryan G. L., 1999a, in Lecture Notes in Physics, Berlin Springer Verlag, Vol. 530, The Radio Galaxy Messier 87, Röser H.-J., Meisenheimer K., eds., p. 106

Norman M. L., Bryan G. L., 1999b, in Astrophysics and Space Science Library, Vol. 240, Numerical Astrophysics, Miyama S. M., Tomisaka K., Hanawa T., eds., p. 19

Norman M. L., Bryan G. L., Harkness R., Bordner J., Reynolds D., O'Shea B., Wagner R., 2007, ArXiv e-prints

Norris R. P. et al., 2011, Publications of the Astronomical Society of Australia, 28, 215

Nuza S. E., Hoeft M., van Weeren R. J., Gottlöber S., Yepes G., 2012, MNRAS, 420, 2006

Ogrean G. A., Brüggen M., 2013, MNRAS, 433, 1701

Ogrean G. A., Brüggen M., van Weeren R. J., Burgmeier A., Simionescu A., 2014, MNRAS, 443, 2463

Ogrean G. A., Brüggen M., van Weeren R. J., Röttgering H., Croston J. H., Hoeft M., 2013, MNRAS, 433, 812

Ogrean G. A. et al., 2016, ApJ, 819, 113

Pan L., Padoan P., Haugbølle T., Nordlund Å., 2016, ApJ, 825, 30

Park J., Caprioli D., Spitkovsky A., 2015, Physical Review Letters, 114, 085003

Park J., Ren C., Workman J. C., Blackman E. G., 2013, ApJ, 765, 147

Parrish I. J., Stone J. M., 2007, APSS, 307, 77

Parrish I. J., Stone J. M., Lemaster N., 2008, ApJ, 688, 905

Peacock J. A., 1999, Cosmological Physics. p. 704

Pearce C. J. J. et al., 2017, ApJ, 845, 81

Peebles P. J. E., 1993, Principles of Physical Cosmology

Petrosian V., 2001, ApJ, 557, 560

Pfrommer C., 2008, MNRAS, 385, 1242

Pfrommer C., 2013, ApJ, 779, 10

Pfrommer C., Enßlin T. A., 2004, A&A, 413, 17

Pfrommer C., Enßlin T. A., Springel V., Jubelgas M., Dolag K., 2007, MNRAS, 378, 385

Pinto C. et al., 2015, A&A, 575, A38

Pinzke A., Oh S. P., Pfrommer C., 2013, MNRAS, 435, 1061

Pinzke A., Pfrommer C., 2010, MNRAS, 409, 449

Planck Collaboration et al., 2016a, A&A, 594, A19

Planck Collaboration et al., 2013, A&A, 550, A131

Planck Collaboration et al., 2016b, A&A, 594, A13

Planelles S., Quilis V., 2013, MNRAS, 428, 1643

Planelles S., Schleicher D. R. G., Bykov A. M., 2015, Science & Space Review, 188, 93

Porter D. H., Jones T. W., Ryu D., 2015, ApJ, 810, 93

Price D. J., 2012, Journal of Computational Physics, 231, 759

Pshirkov M. S., Tinyakov P. G., Urban F. R., 2016, Physical Review Letters, 116, 191302

Pudritz R. E., Silk J., 1989, ApJ, 342, 650

Randall S., Nulsen P., Forman W. R., Jones C., Machacek M., Murray S. S., Maughan B., 2008, ApJ, 688, 208

Rasia E. et al., 2015, ApJ Letters, 813, L17

Reichert A., Böhringer H., Fassbender R., Mühlegger M., 2011, A&A, 535, A4

Roediger E. et al., 2015, ApJ, 806, 104

Rosswog S., 2009, New Astronomy Reviews, 53, 78

Rottgering H. J. A., Wieringa M. H., Hunstead R. W., Ekers R. D., 1997, MNRAS, 290, 577

Russell H. R. et al., 2011, MNRAS, 417, L1

Ryu D., Kang H., Cho J., Das S., 2008, Science, 320, 909

Ryu D., Kang H., Hallman E., Jones T. W., 2003, ApJ, 593, 599

Ryu D., Schleicher D. R. G., Treumann R. A., Tsagas C. G., Widrow L. M., 2012, Science & Space Review, 166, 1

Sarazin C. L., 1988, X-ray emission from clusters of galaxies

Sault R. J., Hamaker J. P., Bregman J. D., 1996, Astronomy and Astrophysics Supplement, 117, 149

Schaller M., Dalla Vecchia C., Schaye J., Bower R. G., Theuns T., Crain R. A., Furlong M., McCarthy I. G., 2015, MNRAS, 454, 2277

Schleicher D. R. G., Schober J., Federrath C., Bovino S., Schmidt W., 2013, New Journal of Physics, 15, 023017

Schlickeiser R., Sievers A., Thiemann H., 1987, A&A, 182, 21

Schmidt W., Schulz J., Iapichino L., Vazza F., Almgren A. S., 2015, Astronomy and Computing, 9, 49

Schneider P., 2006, Extragalactic Astronomy and Cosmology

Sembolini F. et al., 2016, MNRAS, 457, 4063

Serlemitsos P. J., Smith B. W., Boldt E. A., Holt S. S., Swank J. H., 1977, ApJ Letters, 211, L63

Shibata R., Matsushita K., Yamasaki N. Y., Ohashi T., Ishida M., Kikuchi K., Böhringer H., Matsumoto H., 2001, ApJ, 549, 228

Sijacki D., Springel V., 2006, MNRAS, 366, 397

Sijacki D., Springel V., Haehnelt M. G., 2009, MNRAS, 400, 100

Sijacki D., Vogelsberger M., Kereš D., Springel V., Hernquist L., 2012, MNRAS, 424, 2999

Skillman S. W., Hallman E. J., O'Shea B. W., Burns J. O., 2010, in Bulletin of the American Astronomical Society, Vol. 42, American Astronomical Society Meeting Abstracts #215, p. 389

Skillman S. W., O'Shea B. W., Hallman E. J., Burns J. O., Norman M. L., 2008, ApJ, 689, 1063

Skillman S. W., Xu H., Hallman E. J., O'Shea B. W., Burns J. O., Li H., Collins D. C., Norman M. L., 2013a, ApJ, 765, 21

Skillman S. W., Xu H., Hallman E. J., O'Shea B. W., Burns J. O., Li H., Collins D. C., Norman M. L., 2013b, ApJ, 765, 21

Smith B. D., Hallman E. J., Shull J. M., O'Shea B. W., 2011, ApJ, 731, 6

Smith R. K., Brickhouse N. S., Liedahl D. A., Raymond J. C., 2001, ApJ Letters, 556, L91

Springel V., 2005, MNRAS, 364, 1105

Springel V., 2010, MNRAS, 401, 791

Springel V., 2011, in IAU Symposium, Vol. 270, Computational Star Formation, Alves J., Elmegreen B. G., Girart J. M., Trimble V., eds., pp. 203–206

Subramanian K., Shukurov A., Haugen N. E. L., 2006, MNRAS, 366, 1437

Sunyaev R. A., Zeldovich Y. B., 1972a, A&A, 20, 189

Sunyaev R. A., Zeldovich Y. B., 1972b, Comments on Astrophysics and Space Physics, 4, 173

Tasker E. J., Brunino R., Mitchell N. L., Michielsen D., Hopton S., Pearce F. R., Bryan G. L., Theuns T., 2008, MNRAS, 390, 1267

The Fermi-LAT Collaboration et al., 2013, ArXiv e-prints

Tormen G., Moscardini L., Yoshida N., 2004, MNRAS, 350, 1397

Trasatti M., Akamatsu H., Lovisari L., Klein U., Bonafede A., Brüggen M., Dallacasa D., Clarke T., 2015, A&A, 575, A45

Vacca V., Murgia M., Govoni F., Feretti L., Giovannini G., Orra E., Bonafede A., 2010, A&A, 514, A71

van Weeren R. J. et al., 2017, Nature Astronomy, 1, 0005

van Weeren R. J. et al., 2016, ApJ, 818, 204

van Weeren R. J., Röttgering H. J. A., Brüggen M., Hoeft M., 2010, Science, 330, 347

van Weeren R. J., Röttgering H. J. A., Intema H. T., Rudnick L., Brüggen M., Hoeft M., Oonk J. B. R., 2012, A&A, 546, A124

Vazza F., 2011, MNRAS, 410, 461

Vazza F., Brueggen M., Gheller C., Hackstein S., Wittor D., Hinz P. M., 2017a, Classical and Quantum Gravity, in press

Vazza F., Brüggen M., 2014, MNRAS, 437, 2291

Vazza F., Brüggen M., Gheller C., 2013, MNRAS, 428, 2366

Vazza F., Brüggen M., Gheller C., Brunetti G., 2012a, MNRAS, 2518

Vazza F., Brüggen M., Gheller C., Wang P., 2014a, MNRAS, 445, 3706

Vazza F., Brüggen M., Wittor D., Gheller C., Eckert D., Stubbe M., 2016a, MNRAS, 459, 70

Vazza F., Brunetti G., Gheller C., 2009a, MNRAS, 395, 1333

Vazza F., Brunetti G., Gheller C., Brunino R., 2010a, New Astronomy, 15, 695

Vazza F., Brunetti G., Gheller C., Brunino R., Brüggen M., 2011a, A&A, 529, A17

Vazza F., Brunetti G., Kritsuk A., Wagner R., Gheller C., Norman M., 2009b, A&A, 504, 33

Vazza F., Dolag K., Ryu D., Brunetti G., Gheller C., Kang H., Pfrommer C., 2011b, MNRAS, 418, 960

Vazza F., Eckert D., Brueggen M., Huber B., 2015a, ArXiv e-prints

Vazza F., Eckert D., Brüggen M., Huber B., 2015b, MNRAS, 451, 2198

Vazza F., Ferrari C., Bonafede A., Brüggen M., Gheller C., Braun R., Brown S., 2015c, Advancing Astrophysics with the Square Kilometre Array (AASKA14), 97

Vazza F., Gheller C., Brüggen M., 2014b, MNRAS, 439, 2662

Vazza F., Gheller C., Brunetti G., 2010b, A&A, 513, A32

Vazza F., Jones T. W., Brüggen M., Brunetti G., Gheller C., Porter D., Ryu D., 2017b, MNRAS, 464, 210

Vazza F., Jones T. W., Brüggen M., Brunetti G., Gheller C., Porter D., Ryu D., 2017c, MNRAS, 464, 210

Vazza F., Roediger E., Brüggen M., 2012b, A&A, 544, A103

Vazza F., Tormen G., Cassano R., Brunetti G., Dolag K., 2006, MNRAS, 369, L14

Vazza F., Wittor D., Brüggen M., Gheller C., 2016b, Galaxies, 4, 60

Venturi T., Giacintucci S., Brunetti G., Cassano R., Bardelli S., Dallacasa D., Setti G., 2007, A&A, 463, 937

Venturi T., Giacintucci S., Dallacasa D., Cassano R., Brunetti G., Macario G., Athreya R., 2013, A&A, 551, A24

Vikhlinin A. et al., 2009, ApJ, 692, 1060

Völk H. J., Aharonian F. A., Breitschwerdt D., 1996, Science & Space Review, 75, 279

Völk H. J., Atoyan A. M., 2000, ApJ, 541, 88

Wang T. et al., 2016, ApJ, 828, 56

Werner N. et al., 2016, MNRAS, 460, 2752

Widrow L. M., Ryu D., Schleicher D. R. G., Subramanian K., Tsagas C. G., Treumann R. A., 2012, Science & Space Review, 166, 37

Wiener J., Oh S. P., Guo F., 2013, MNRAS, 434, 2209

Willson M. A. G., 1970, MNRAS, 151, 1

Wittor D., Jones T., Vazza F., Brüggen M., 2017a, MNRAS, 471, 3212

Wittor D., Vazza F., Brüggen M., 2016, Galaxies, 4, 71

Wittor D., Vazza F., Brüggen M., 2017b, MNRAS, 464, 4448

Wright E. L., 2006, Publication of the Astronomical Society of the Pacific, 118, 1711

Xu H., Li H., Collins D. C., Li S., Norman M. L., 2009, ApJ Letters, 698, L14

Zandanel F., Ando S., 2014, MNRAS, 440, 663

Zel'dovich Y. B., 1970, A&A, 5, 84

Zhuravleva I., Allen S. W., Mantz A. B., Werner N., 2017, ArXiv e-prints

Zhuravleva I. et al., 2016, MNRAS, 458, 2902

Zhuravleva I. et al., 2014a, Nature, 515, 85

Zhuravleva I. et al., 2014b, ApJ Letters, 788, L13

ZuHone J. A., Markevitch M., Ruszkowski M., Lee D., 2013, ApJ, 762, 69

ZuHone J. A., Markevitch M., Zhuravleva I., 2016, ApJ, 817, 110